Ultrasonic joining of through-the-thickness reinforced metal-composite hybrid structures

Vom Promotionsausschuss der

Technischen Universität Hamburg

zur Erlangung des akademischen Grades

Doktor-Ingenieur (Dr.-Ing.)

genehmigte Dissertation

von

Eduardo Etzberger Feistauer

aus

Rolante

2018

Gutachter:
Univ.-Prof. Dr-Ing. Sergio de Traglia Amancio Filho
Prof. Dr.-Ing. Wolfgang Hintze

Vorsitzender des Prüfungsausschusses:
Prof. Dr.-Ing. Otto von Estorff

Tag der mündlichen Prüfung:
14. November 2018

Acknowledgments

I would like to express my sincere gratitude to those who have supported and contributed to this PhD work, which would not have been possible without any of them.

- Univ.-Prof. Dr-Ing. Sergio de Traglia Amancio Filho for the opportunity to perform this research within his group, invaluable advice, unconditional support, and encouragement throughout all stages of my PhD. His enthusiasm and motivation have significantly inspired this work.
- Prof. Dr.-Ing. Wolfgang Hintze for accepting to review this PhD work and for his contribution to the examination process.
- Dr. Jorge Dos Santos for constant support, recommendation, and all the opportunities to develop my academic career at HZG.
- Prof. Dr.-Ing Norbert Huber for support within the institute and recommendation.
- Dr. Thomas Ebel and Rafael Paiotti for their support on the development of the MIMStructing and injection molding of the first MIMStruct parts.
- Several colleagues from HZG, particularly Jürgen Knaack and Kay Erdmann, for their assistance with mechanical testing, Dr. Felix Beckmann for the µCT measurements, support on the data analysis, and related discussions and Dr. Paula O. Guglielmi for the help on the nanoindentations.
- All colleagues of the solid state joining department (WMP), for their friendship, teamwork, and helpful discussion. I would like to mention in particular the help and technical support of Luciano Bergmann, Jan Carstensen and Menno Peters, the linguistic assistance of Martin Reimann and Dagmar Koschek for the exceptional support in all issues and friendship.
- The members of the PMJoining group. I am indebted to all of you, with a special mention to my great friends Andre Abibe, Seyed Goushegir, Lucian Blaga, Natascha Zocoller, Natalia Manente, and Rielson Falck. Thanks for having contributed immensely to my professional career, for the great teamwork, cheerful company and friendship.
- Conselho Nacional de Desenvolvimento Cientifico e Tecnológico - CNPq (Brazil) for supporting the project and sponsoring my PhD scholarship.
- All my family and friends for their encouragement and support.
- My lovely girlfriend Antonella for her uninterrupted support, understanding, exceptional inspiration and patience, especially during the most difficult times.
- My beloved parents Denize and Paulo, and brothers Alexandre and Leonardo for providing unconditional love, care, and encouragement, I am grateful for having you always by my side, and I would not have made it this far without your continuous support to all my pursuits and love throughout my entire life.

Abstract

The joining of dissimilar materials, such as light metals to composites, is a rather complex engineering challenge, due to their pronounced physical and chemical dissimilarities. Furthermore, state-of-the-art metal-composite overlap joints – for example when joined by adhesive bonding – usually present brittle failure due to their reduced out-of-plane strength. Recent developments suggest that through-the-thickness reinforcement (TTR) – for example with pins or columns – integrated into the surface of the metal part can increase the mechanical performance of metal-composite overlap joints. However, there are several gaps in engineering and scientific knowledge with regards to efficient assembly routes and understanding of the joining process-microstructure-mechanical performance correlations in these new hybrid joints.

The present doctoral thesis aims at introducing Ultrasonic Joining (U-Joining), a new joining concept (co-invented by the author and patented by HZG, US 9,925,717 B2, 2018), to produce metal-composite overlap joints that have improved out-of-plane strength. U-Joining uses ultrasonic energy to join metallic parts with integrated pins – manufactured in this work by metal injection molding (MIM) - to fiber-reinforced thermoplastic composites. Joining is accomplished by two major bonding mechanisms that are activated by ultrasonic frictional heating: mechanical interlocking and adhesion forces. The first results from a TTR effect between metallic pins and the composite, wherein adhesive forces are formed at the metal-composite interface after joint consolidation of the softened polymeric matrix. A case-study joint on the aircraft material combination of glass-fiber reinforced polyetherimide laminate (GF-PEI) and MIM-structured Ti-6Al-4V was chosen to evaluate the process feasibility and joint properties.

Stop-action joining experiments were first performed, to assess the U-Joining bonding and joint formation mechanisms in a stepwise manner. By an extensive microstructural characterization using optical microscopy, scanning electron microscopy, and X-ray microtomography, the formation of a thermo-mechanically affected zone (CTMAZ) in the joint polymeric part was identified, while no microstructural changes took place in the Ti-6Al-4V part. The CTMAZ formation is a mutual effect of frictional heat at the metal-composite interface and insertion of metallic pins into the composite part. At this microstructural zone the composite underwent considerable microstructural changes, such as reorientation and local damage of glass-fiber reinforcement. Moreover, the results of physical-chemical characterization (by differential scanning calorimetry - DSC, thermogravimetric analysis - TGA and size-exclusion chromatography - SEC) showed a slight decrease in the glass transition temperature, which, coupled with a reduction in average molecular weight measured by SEC, suggests localized polymer degradation. Instrumented nanoindentation experiments showed a decrease of about 12% in hardness and 1.5% in elastic modulus, confirming that the joining process not only increased the free volume between the PEI molecules, but also promoted partial thermo-mechanical degradation by chain scission in the CTMAZ volume.

The hybrid joint's global mechanical performance was assessed by single lap shear and fatigue tests. A significant increase in ultimate lap shear force, ULSF) and toughness were observed, compared to non-reinforced reference joints, with final failure by shearing of the metallic pins. Therefore, it is possible to conclude that through-the-thickness reinforcement effectively improved the load transfer capability between metal and composite in the U-Joining joints. Moreover, the S-N curves obtained indicated outstanding results in accordance with aircraft standard procedure, and the hybrid joints produced reached their fatigue limits (i.e. 10^6 cycles) with loading levels corresponding to 30% of ULSF.

For understanding and optimization of the U-Joining process parameters a Box-Behnken design of experiments was carried out. The individual and combined effects of each joining parameter on the ULSF were evaluated with a response surfaces method and analysis of variance. As a result, a set of optimized joining parameters (E_J = 2012 J, A_0 = 52 µm, and J_p = 14.7 psi (101 kPa) were obtained to produce sound joints with above-average ULSF. This PhD work therefore succeeds in introducing and scientifically describing an alternative joining approach for metal-composite hybrid structures with TTR, addressing its fundamental characteristics and joint properties at coupon level. In addition, the results of this work contribute to filling knowledge gaps with regards to process, microstructure and mechanical performance correlations in the direct assembly of hybrid joints.

Zusammenfassung

Die Verbindung verschiedener Materialien, wie Leichtmetalle mit faserverstärkten Verbundwerkstoffen, ist aufgrund ihrer unterschiedlichen physikalisch-chemischen Eigenschaften eine komplexe technische Herausforderung. Darüber hinaus weisen moderne Überlappungsverbindung von Metall und Verbundwerkstoffen - beispielsweise, wenn sie durch Kleben verbunden werden - aufgrund ihrer geringeren out-of-plane Festigkeit in der Regel einen Sprödbruch auf. Jüngste Entwicklungen deuten darauf hin, dass mit Hilfe von „Durch-die-Dicke-Verstärkung“ (Englisch: through-the-thickness reinforcement - TTR) - zum Beispiel mit Stiften -, die in die Oberfläche des Metallteils integriert sind, die mechanische Leistungsfähigkeit von Überlappungsverbindung von Metall und Verbundwerkstoffen erhöht werden kann. Es gibt jedoch einige Lücken in den technischen und wissenschaftlichen Kenntnissen im Bezug auf effiziente Fügetechnologien und den Zusammenhang zwischen der durch den Fügeprozess veränderten Mikrostruktur der Werkstoffe und der mechanischen Eigenschaften bei diesen neuartigen Hybridverbindungen.

Ziel der vorliegenden Doktorarbeit ist es, hybride Leichtmetall-Faserverbundwerkstoff-Strukturen mit verbesserter out-of-pane Festigkeit durch die Verwendung von Ultrasonic Joining, (U-Joining), einem neuen Fügekonzept (US Patent 9,925,717 B2), herzustellen. Beim U-Joining werden metallische Teile mit integrierten Metallstiften - hergestellt im Metall-Spritzgussverfahren (MIM) - mit Hilfe von Ultraschallenergie mit thermoplastische Verbundwerkstoffe verbunden. Die Verbindung wird durch zwei Hauptverbindungsmechanismen erreicht, die durch Ultraschall-Reibungswärme aktiviert werden: mechanisches Interlocking und Adhäsionskräfte. Der erste ergibt sich aus einem TTR-Effekt zwischen den Metallstiften und dem Verbundwerkstoff, wobei Haftkräfte an der Metall- Verbundwerkstoffe-Grenzfläche nach der Verbindungsverfestigung gebildet werden. Eine Fallstudie an der Flugzeugmaterialkombination aus glasfaserverstärktem Polyetherimid-Laminat (GF-PEI) und MIM-strukturiertem Ti-6Al-4V wurde durchgeführt, um die Prozessdurchführbarkeit und die Verbindungseigenschaften zu bewerten.

Zunächst wurden stop-action Experimente durchgeführt, um die U-Joining Verbindungsmechanismen schrittweise zu bewerten. Durch eine umfangreiche Charakterisierung der Mikrostruktur mittels optischer Mikroskopie, Rasterelektronenmikroskopie und Röntgen-Mikrotomografie wurde die Bildung einer thermomechanisch beeinflussten Zone (CTMAZ) im gemeinsamen Polymerteil identifiziert, während im Ti-6Al-4V Teil keine mikrostrukturellen Veränderungen stattfanden. Die CTMAZ entstehtdurch die Wirkung von Reibungswärme an der Metall-Verbundwerkstoffe-Grenzfläche und durch das Einführen von den Metallstiften in den Verbundwerkstoff. In dieser Zone durchliefe das Gefüge erhebliche Veränderungen wie Neuorientierung und lokale Schädigung der Glasfaserverstärkung. Darüber hinaus zeigen die Ergebnisse der physikalisch-chemischen Charakterisierung (DSC, TGA und Größenausschlusschromatographie - SEC) eine leichte Abnahme der Glasübergangstemperatur, verbunden mit einer Verringerung des mittleren Molekulargewichts. Dies deutet auf einen lokalisierten Polymerabbau hin. Nanoindentationsexperimente zeigten eine Abnahme von etwa 12% der Härte und 1,5% des Elastizitätsmoduls, was bestätigt, dass der Fügeprozess nicht nur das freie Volumen zwischen den Polymerstrukturen erhöht, sondern auch den partiellen thermomechanischen Abbau durch Kettenspaltung im CTMAZ-Volumen fördert. Die globale mechanische Leistung der Verbindungen wurde durch Zug-, Scher- und Ermüdungsversuche untersucht. Im Vergleich zu nicht verstärkten Referenzverbindungen wurde ein signifikanter Anstieg der Überlappungsscherfestigkeit (ULSF) und der Zähigkeit beobachtet, mit endgültigem Versagen durch Scherung der Metallstifte. Daher ist es möglich zu schlussfolgern, dass die TTR die Lastübertragungsfähigkeit zwischen Metall und Verbundwerkstoff in den U-Joining Verbindungen effektiv verbessert. Darüber hinaus zeigen die erhaltenen S-N-Kurven hervorragende Ergebnisse,die hergestellten Hybridverbindungen erreichen ihre Ermüdungsgrenzen (d. H. 10^6 Zyklen) mit Beladungsniveaus, die 30% ULSF entsprechen.

Zum Verständnis und zur Optimierung der Prozessparameter wurde ein Box-Behnken-Versuchsplan angewendet. Die individuellen und kombinierten Effekte jedes Verbindungsparameters auf die ULSF wurde mit einer Wirkungsfächenmethode und einer Varianzanalyse bewertet. Als Ergebnis konnte ein Satz von optimierten Prozessparametern gefunden werden, mit dem Verbindungen mit einer überdurchschnittlichen ULSF erzeugt werden können. Damit gelingt es in dieser Doktorarbeit, eine alternative Fügemethode für Metall-Verbundwerkstoff-Hybridstrukturen mit TTR einzuführen und diese auf Coupon-Ebene auf ihre fundamentalen Eigenschaften und Verbindungseigenschaften hin zu untersuchen. Die Ergebnisse dieser Arbeit tragen darüber hinaus dazu bei, Wissenslücken im Bezug den Prozess, die Mikrostruktur sowie deren Zusammenhang mit der mechanischen Leistung im direkten Zusammenbau von Hybridverbindungen zu schließen.

List of Abbreviations

µCT	Micro-computed tomography
2-P WD	Two-parameter Weibull distribution
AFP	Automated fiber placement
AISI	American Iron and Steel Institute
ALT	Automated tape layup
AM	Additive manufacturing
ANOVA	Analysis of Variance
ASTM	American Society for Testing and Materials
BBD	Box-Behnken design
BM	Base material
CAD	Computer-aided design
CCD	Central composite design
CDF	cumulative density function
CFRP	Carbon-fiber-reinforced polymer
CMT	Cold-metal transfer
CNC	Computer Numerical Controlled
CP-TLOM	Transmitted-light optical microscopy with crossed polarizers
CSDF	chain scission distribution function
CSM	Continuous stiffness measurement
CTMAZ	Composite thermo-mechanically affected zone
DA	Direct assembly
DCM	Dynamic contact module
DIC	Digital image correlation
DIN	Deutsches Institut für Normung e.V.

DoE	Design of experiments
DSC	Differential scanning calorimetry
EB	Electron beam
EBM	Electron beam melting
ELI	Extra-low interstitials
FEA	Finite element analysis
FEM	Finite element method
F-ICJ	Friction-based injection clinching joining
FML	Fiber-metal laminates
FricRiveting	Friction riveting
FRP	Fiber-reinforced polymer
GF-PEI	Glass-fiber reinforced polyetherimide
GFRP	Glass-fiber reinforced polymer
GHG	Greenhouse gases
HCF	High cycle fatigue
HEMS	High Energy Materials Science
HFIP	Hexafluoroisopropanol
HIP	Hot isostatic pressing
HYPER	Hybrid penetrative reinforcement
IR	Infrared
ISO	International Organization for Standardization
LB	Laser beam
LCF	low cycle fatigue
LoP	Lack of penetration
LSCM	Scanning confocal microscopy
MH	Microhardness
MIM	Metal injection molding

MM	Micro-milling
MTTF	Mean time to failure
MW	Molecular weight
MWD	Molecular weight distribution
NDT	Nondestructive testing
OFAT	One-factor-at-time approach
PDF	probability density function
PDZ	Plastically deformed zone
PEI	Polyetherimide
PMMA	Polymethylmethacrylate
Prepregs	Pre-impregnated fibers
PTFE	Polytetrafluoroethylene
PTMAZ	Polymer thermo-mechanically affected zone
RGB	Red-green-blue
RI	Refractive index
RLOM	Reflected-light optical microscopy
RSM	Response surface methodology
RTM	Resin transfer molding
SB	Secondary bending
SEC	Size-exclusion chromatography
SEM	Scanning electron microscopy
SLM	Selective laser melting
SLS	Selective laser sintering
SR-µCT	Synchrotron radiation X-ray micro-computed tomography
TGA	Thermogravimetric analysis
T-RTM	Thermoplastic resin transfer molding
TTR	Through-the-thickness reinforcement

U-Joining	Ultrasonic Joining
ULSF	Ultimate lap shear force
UTS	Ultimate tensile strength
VARI	Vacuum assisted resin infusion
VMH	Vickers microhardness
WD	Weibull distribution

List of Symbols

a, b, and d	Fatigue regression parameters
A	Contact area
A_0	Sonotrode oscillation amplitude
c	Linear coefficient
C_0	Number of replicates of the central point
C_P	Clamping pressure
C_{opt}	Stress-optical coefficient
CV	Coefficient of variance
$d_{\parallel}$ and $d_{\perp}$	Indentation diagonals parallel and perpendicular
E	Elastic modulus, Young’s modulus
E_J	Joining energy
E_{bulk}	Elastic modulus measured in the bulk material
E_{eff}	Effective elastic modulus
E_i	Indenter elastic modulus
E_r	Reduced elastic modulus
$E_{surface}$	Elastic modulus measured on the material surface
$f(x)$	Describe the probability density function
$F_{f(x)}$	Describe the cumulative density function
F_{max}	Maximum load
F_{range}	Load range
H	True hardness
h_f	Indentation depth
h_{max}	Maximum indentation depth

h_r	Residual indentation depth
i	Failure serial number
J_F	Joining force
J_P	Joining pressure
k	Number of factors
m	Angular coefficient
M_n	Number-average molecular weight
M_{nf}	Final number average molecular weight
M_{no}	Initial number average molecular weight
M_w	Average molecular weight
MR	Bernard’s Median Rank
$MTTF$	Mean time to failure
N	Number of experiments
n	Isochromatic fringe order
n_1 and n_2	Principal refractive indices
n_R	Number of chain scissions
N_{R_x}	Fatigue life taking into consideration a defined percentage of reliability
N_R	Number of chain scissions applied to the MWD
N_f	Number of cycles calculated taking into account the reliability level
P_{max}	Maximum load
P	Power
P/S^2	Ratio of the load to the stiffness squared
PD	Polydispersity index
R^2	Coefficient of determination
R_Z	Mean roughness depth
R_a	Roughness Average

$\mathrm{R}^2_{\mathrm{adj}}$	Adjusted coefficient of determination
S	Elastic unload stiffness and Standard error of the regression
SD	Standard deviation
S_a	Load range
s_h	Structured undercut height
s_d	Penetration depth
t	Joining cycle time
T_g	Mid-point glass transition
T_{g1}	$\mathrm{T_g}$ measured in the first heating cycle
T_{g2}	$\mathrm{T_g}$ measured in the second heat cycle
v	Poisson's ratio
v_i	Indenter Poisson's ratio
x	Number of cycles
x_1 , x_2, and x_3	Normalized factors
α	Weibull's shape parameter
β	Weibull's scale parameter
β_0	Regression intercept
β_1, β_2, β_2	linear regression coefficients
β_{11}, β_{22}, and, β_{33}	Quadratic regression coefficients
β_{12}, β_{12}, and, β_{23}	Interactive regression coefficient
β_i	Inclined face angle of pyramidal indenter
Γ	Gamma function
δ	Light retardation
$\Delta\mathrm{H}$	Hardness anisotropy
E	Elastic modulus
ε_x	Strain in the X direction

θ	Impact angle
λ	Wavelength of the monochromatic light source
ξ_r	Relative residual depth
σ_1, σ_2, and σ_3	Principal stresses
σ_y	Yield stress

Contents

CHAPTER 1. INTRODUCTION

Recent scientific and technological progress in welding and joining has shown potential to revolutionize the way designers and engineers combine different materials. The possibility of fully exploring the properties of different materials in the same structure instead of relying on only one strong material, or creating material reinforcement of critical areas, opens up a range of new structural concepts. This means synergistic enhancement of structure mechanical performance, weight, chemical stability, and sustainability can be achieved. As a result, ideas based on application of the “right material at the right place” [1] have gained in attention over the last few decades, thereby improving, for instance, the way vehicles and airplanes are designed and manufactured.

In this respect, the transportation sector has been the primary booster for the development of improved multi-material structures, mainly due to strict environmental policies to decrease greenhouse gas (GHG) emissions. The European Commission recently published a White Paper [2] on the topic, and the three most important factors to ensure the sustainability of future transportation were identified as: (i) development of new clean and efficient fuels and propulsion systems; (ii) improvement of safer communications and operational systems and; (iii) improvements in vehicle efficiency with new engines, materials, and design. In the last, lightweight construction, based on materials such as fiber-reinforced polymers (FRP) and lightweight alloys, are considered the primary alternative solution to help the sector achieve emission targets. A reduction in the weight of a vehicle has a direct impact on the emission of CO_2 over its entire lifetime, which results from reduced fuel consumption [3,4]. Moreover, lighter vehicles also compensate for any additional weight required for their electrification (such as the weight of batteries), and improve the driving dynamics [4]. Lightweight structures are currently a major topic in the automotive sector, as well as for infrastructure [5] and shipbuilding [6,7], and the aerospace industries have already successfully applied lightweight concepts in the latest aircraft designs [8].

When it comes to recent developments in advanced joining technologies, a unified joining solution for multi-material structures is still not available, especially for those based on lightweight metals and FRP. Indeed, joining such materials is a rather complicated engineering challenge due to their physical-chemical dissimilarities, which result in low miscibility [9,10], thereby hindering their joining. As a consequence, joints are the most common source of premature in-service failure of hybrid structures. To remedy this, efficient joining technologies are required to fulfill increasing demand in the transportation sector and to improve the structural integrity of vehicles.

Recently, enhanced joining approaches applying through-the-thickness reinforcement have been proposed as an alternative to improve load transfer between metal and composites in hybrid structures. These new concepts are usually grouped under a class of technologies known as direct assembly joining. Typical direct assembly joints combine two manufacturing phases, that is, (i) surface structuring and (ii) assembly. In the first phase, through-the-thickness reinforcement (i.e., pins, columns or protrusions) is structured on the surface of the metallic part by an additive or subtractive manufacturing route. Subsequently, the composite is assembled on the structured surface, layer-by-layer. As a result, the through-the-thickness reinforcement is inserted in the composite, interlocking the materials. This results in a hybrid joint with improved out-of-plane strength and load capability. Direct assembly concepts are still an underdevelopment class of technologies, which exhibit advantages over conventional joining concepts, but also present some limitations. Among the disadvantages, for instance, are challenges related to the reproducibility of the individual surface-structured elements (through-the-thickness reinforcement) on the metallic part, the formation of heterogeneous microstructures, and a very time-consuming assembly phase.

In this context, this PhD thesis introduces a new direct assembly technique called Ultrasonic Joining (U-Joining). U-Joining uses ultrasonic energy to join consolidated thermoplastic composites or laminates to surface-structured metallic parts. The idea behind applying a joining-based process to assemble a hybrid joint, instead of relying on a layer-by-layer composite lamination approach, is that a considerable decrease in assembly time may be achieved. Moreover, an alternative way to manufacture surface-structured metallic parts is introduced and applied in this work, the so-termed MIM-Structuring process (a recent technology patented by Helmholtz-Zentrum Geesthacht [11]). This new concept of joining surface-structured lightweight metals and composites has been devised, patented [12–15] (see Appendix A.1) and developed over the course of this PhD project. The thesis presented herein aims to introduce the new U-Joining concept and its main features, as well as describe the properties of the hybrid joints produced as a case study using commercially available materials. This PhD thesis is consequently organized in the following way:

After this introductory chapter, Chapter 2 presents the motivation for this work and its primary objectives.

In Chapter 3, a literature review is presented on the recent scientific and technological advancements in the joining of metal-composite hybrid structures. In addition, the basics of direct assembly technologies are explored. Both process phases are addressed in detail, and the leading technologies for metal surface structuring and composite assembly are discussed. Next, the relevant mechanical properties of direct assembly joints are presented, providing insights useful for the design of future hybrid joints. At the end of this chapter, the main characteristics of the base materials used during the development of the U-Joining concept are presented.

Following this, Chapter 4 describes the experimental approach used in this work and the development phases of the thesis.

Chapter 5 discusses the materials and methods adopted during the case study. The base materials properties, joining procedures, equipment and characterization techniques applied are described in detail.

In Chapter 6, before the discussion of the experimental results, an introduction to the new direct assembly approach that is developed in this thesis is given. In this chapter, the MIM-Structuring manufacturing method is introduced and U-Joining fundamentals are discussed. In so doing, the topics of process phases, parameters, variants, advantages, limitations and potential application are systematically explored.

The experimental results obtained in this work are presented in five chapters. The first of these, Chapter 7, deals with the mechanisms involved in the formation of U-Joining joints. Stop-action joining experiments were performed to assess the process evolution in a stepwise manner and describe the material flow during joining. Thus, providing in-depth understanding of the central mechanisms involved in joint formation. After this, the general aspects of the produced joint are addressed and a typical process diagram is presented and correlated with the process phases and heat generation. In this regard, a non-contact infrared temperature measurement, coupled with digital image correlation techniques, was used to comprehend and evaluate the assembly phase, concerning temperature evolution and penetration of the through-the-thickness reinforcement.

In Chapter 8, process-induced transformations in the microstructure of the joined material are described and correlated with local mechanical properties. The use of scanning electron microscopy with backscattered electrons, transmitted-light optical microscopy and X-ray micro-computed tomography were combined to define the process-affected zone and its extent. The local mechanical changes in this zone were characterized on micro and nanoscales by indentation techniques. In addition, the physical-chemical properties of the polymeric part were investigated by thermal analysis and size-exclusion chromatography, providing a solid comprehension of the process-affected materials.

Following this, in Chapter 9, the global mechanical properties of the hybrid joints produced are assessed under quasi-static loading with single lap shear tests. Coupled with the mechanical test equipment, a digital image correlation system was used to evaluate the joint’s under-load strain fields. By combining those results with finite element modeling and fracture surface analysis, an understanding of the failure mechanism of the joints was arrived at. In addition, load/unload lap shear tests were carried out with different loading levels to assess and further understand the joint failure behavior. Finally, the metallic parts of the joint were subjected to hot isostatic pressing prior to joining, and the effect of this post-treatment on the joint’s quasi-static mechanical performance was evaluated.

In Chapter 10, the joint’s performance under cyclic loading is investigated. S-N curves were obtained using three different formulations and the U-Joining joint fatigue limit was established. In addition, the data obtained were statistically analyzed using a two-parameter Weibull distribution. Thereby providing a robust analysis of the data based on their scattering and statistical reliability. Next, the joint’s fracture surfaces are described, along with the failure mechanism under cyclic loading. Towards the end of this chapter, residual strength of the joints that survived the fatigue limit is assessed.

After an in-depth investigation into the joint formation mechanisms and the effect of the U-Joining process on the properties of the joined materials, in Chapter 11, the correlations between joining parameters and joint mechanical properties are drawn and the process is optimized to obtain joints with outstanding mechanical properties. In this respect, a Box-Behnken design was applied to understand the effects of individual and combined joining parameters on the ultimate lap shear force of joints. These discussions were supported by analysis of variance (ANOVA) and analysis of the obtained response surfaces. Moreover, reliable reduced models were obtained and validated, from which a set of optimized process parameters were achieved for the material combination investigated in this work.

Chapter 12 summarizes the main results and conclusions of this PhD work, as well as its contribution to state-of-the-art in direct assembly hybrid joints.

Finally, in Chapter 13, recommendations for future scientific and technological investigation are listed for further development of new joining concept.

CHAPTER 2. MOTIVATION AND OBJECTIVES

Over the last few years, there has been increasing demand for new metal-composite hybrid structures with improved mechanical performance and reduced weight, primarily boosted by the transportation industry. This ever-growing need for advanced hybrid structures is the motivation behind the development of the U-Joining concept and, thus, this PhD work.

Joining concepts that are traditionally used present several limitations with regard to load transfer between metal and composite, and with joint out-of-plane performance. In addition, assembly is made difficult by the substantial differences in physical and chemical properties of the materials, leading to time-consuming and laborious assembly phases. This work therefore describes an alternative assembly procedure for producing metal-composite direct assembly hybrid joints. This U-Joining concept uses ultrasonic energy to join surface-structured metallic parts that are manufactured by metal injection molding (MIM-Structuring, European patent EP 2 468 436 B1) to fiber-reinforced thermoplastic composites. The joining is accomplished by the combined effect of mechanical interlocking (due to the surface-structured through-the-thickness reinforcement) and the adhesion forces created at the metal-composite interface after reconsolidation of the polymeric composite matrix.

In order to demonstrate the feasibility of the joining process, a case study approach was chosen, using commercially available glass-fiber reinforced polyetherimide laminates (GF-PEI) and MIM-Structured Ti-6Al-4V, which are both materials of particular interest to the aircraft industry. The following objectives were established:

- Introduce the new U-Joining concept, concerning its fundamental principles, process parameters, and the bonding mechanisms involved in the formation of the hybrid joints
- Describe the effects of the joining process on the material's microstructure, physical-chemical property changes to the joined parts, and their influence on the local mechanical properties of the joint
- Investigate the mechanical properties of the U-Joining joint under quasi-static and cyclic loading, providing a fundamental understanding of its failure and fracture mechanisms
- Understand the U-Joining process parameter and property correlations and optimize the joint's mechanical strength by design of experiments (DoE) and analysis of variance (ANOVA)

CHAPTER 3. LITERATURE REVIEW

Modern lightweight design in transport structures has become a matter of success for Original Equipment Manufacturers (OEMs). Due to strict environmental policies, designers and engineers feel compelled to select lighter, recyclable, and sustainable materials to reduce fuel consumption and emissions [16,17]. Examples of the lightweight materials used in transport structures are high-strength steels, magnesium, aluminum, titanium, polymers, and fiber-reinforced polymers [4,18]. The combination of fiber-reinforced polymers with lightweight alloys for the fabrication of multi-material structures (also referred to as hybrid structures) provides an innovative range of materials with excellent mechanical properties, physical-chemical resistance, and light in weight. However, the joining of lightweight alloys to fiber-reinforced polymers is complicated, due to the differences of their physical and chemical properties, resulting in lower mutual miscibility [9]. Therefore, there is a niche for new, high-performance and cost-effective joining technologies for this purpose [10,19].

This chapter reviews the main available joining technologies for metal-composite hybrid structures, with a focus on recently developed direct assembly concepts. The chapter starts by classifying the joining methods into four distinct groups, namely: (i) adhesive bonding, (ii) mechanical fastening, (iii) welding-based technologies, and (iv) hybrid technologies. Then the two phases of a conventional direct assembly process are described (i.e., surface structuring and assembly) and the available technologies for both phases are systematically discussed. In addition, the main mechanical properties of direct assembly hybrid joints are discussed, providing useful insights for future joint design and a basic understanding of the results discussed in this PhD work. Towards the end of this chapter, the main characteristics of the base materials used in this work are presented.

3.1 Recent advances in joining methods for metal-composite lightweight structures

A variety of approaches have been recently proposed to join metal-polymer or metal-FRP hybrid structures in overlap configurations, as presented in Figure 3-1. Until now strong joints between these materials could only be achieved by means of adhesives [20,21] (Figure 3-1 (a)), fasteners [22] (Figure 3-1 (b)), a combination of both [23–26], or welding-based joining processes (Figure 3-1 (c)) [27–29]. More recently, new concepts have addressed the possibility of direct assembly of the FRP on a surface-structured metal (Figure 3-1 (d)). With this new technique the structured surface acts as a through-the-thickness reinforcement that improves the joint's out-of-plane strength [30]. As well as these joining strategies, various joint designs can be applied to improve the load transfer between the materials at the overlap area, (e.g., single-lap, double-lap, stepped-lap, and scarf geometries), as typically implemented with adhesively bonded joints [26]. Based on those approaches, several joining processes have been reported in the literature. In recent works, Amancio-Filho and dos Santos [10] and Amancio-Filho and Blaga [19] classified the available joining technologies for metal-composite structures into four groups, as illustrated in the diagram in Figure 3-2. It is important to mention that the techniques presented here are only a few examples and one could equally well list other joining methods in the classification diagram. Furthermore, these technologies may offer alternative process variants, which are also not specified, in order to keep the diagram straightforward and readable.

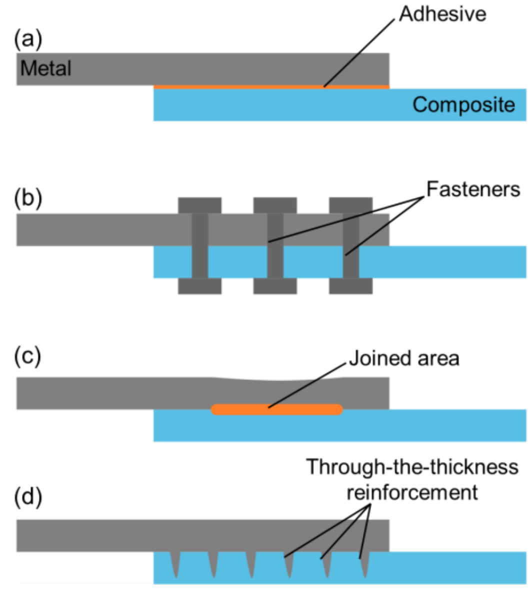

Figure 3-1: Main joining approaches for overlapped metal-composite structures: (a) adhesive bonding, (b) mechanical fasteners, (c) joining processes, and (d) direct assembly.

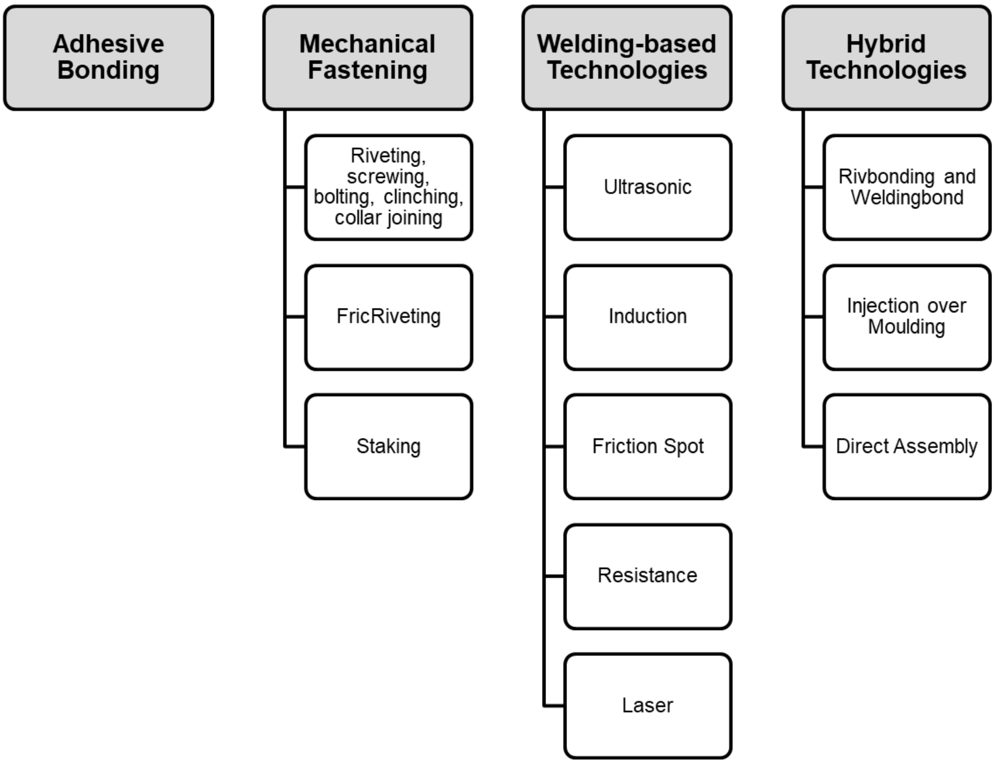

Figure 3-2: Available joining technologies for metal-composite hybrid structures. The techniques are organized into four groups according to Amancio and dos Santos [10]. Adapted from [31].

The first group of technologies is adhesive bonding, an established joining technology that has been extensively applied for joining similar structural configurations of metals and composites, as well as dissimilar configurations in several fields of application [32–34]. The second group is called mechanical fastening, which comprises traditional technologies such as riveting, screwing, bolting, clinching, collar joining and staking technologies [35], as well as recently developed technologies such as friction-based injection clinching joining (F-ICJ) [36] and FricRiveting (friction riveting) [37,38].

Intrinsic limitations of both adhesive bonding and mechanical fastening have boosted the development of alternative approaches for connecting lightweight metals to FRP. Hence, several welding-based technologies have been recently proposed to try to overcome or mitigate their process limitations. For adhesive bonding these include long curing times, limited operational temperature (due to the loss of adhesive performance), extensive surface pre-treatments, catastrophic failure of bonded areas, difficult joint disassembly, disposal of hazardous chemicals and solvents. Whereas stress concentration around the fastener, weight penalty due to the fastener, and extensive labor, are examples of the drawbacks found in state-of-the-art mechanically fastened joints. Although welding-based technologies have been investigated to tackle these issues, the adaptation of conventional metal or plastic welding technologies to join hybrid structures it is not a straightforward task, mostly due to the low thermal resistance of the matrix in most polymers. Examples of studies in this context are for ultrasonic [28,39], induction [40], resistance [41], laser welding [42,43], and friction spot joining [44,45] of metal-composite hybrid spot joints.

The last group - known as hybrid technologies - consists of a combination of two joining methods and novel joining concepts developed exclusively to produce high-performance metal-composite hybrid joints. Some of the reported technologies are Rivbonding (rivet + adhesive), Weldbonding (spot weld + adhesive) [46], injection overmolding [47] and direct assembly. Direct assembly (DA) is a relatively new concept to produce hybrid joints, with first published trials dating from 2004 and the introduction of COMELD® [48,49]. Since then, DA has been a subject increasingly investigated by the scientific community. Joints produced using this concept are mechanically interlocked by through-the-thickness reinforcements (TTR), which are usually integrated into the metallic part surface with a structured 3D pattern. After the structuring phase, the FRP is typically assembled layer-by-layer with prepregs, vacuum-assisted resin infusion or a resin transfer mold. By virtue of the mechanical interlocking between the materials, a hybrid joint with improved out-of-plane mechanical proprieties is produced. Moreover, the TTR not only increases the mechanical strength, but also the toughness and may lead to considerable improvement in damage tolerance. Furthermore, it has been reported [50,51], that such reinforcement may change the failure mechanism of hybrid joints, preventing catastrophic failure, as is commonly observed in non-TTR or adhesively bonded joints. It therefore opens up new possibilities for the designers of lightweight structures and it is now possible to monitor the structural health of such hybrid structures, preventing damage onset and evolution [49].

3.2 Fundamentals of direct assembly

DA can be divided into two phases (Figure 3-3). First, a structuring process modifies the metallic surface of the hybrid connection. Second, the composite is directly assembled onto the structured surface in a one-step assembly or manufacturing procedure. The mechanical interlocking created by the structured surface (i.e. TTR) increases the load transfer capabilities of the joined materials, thereby improving out-of-plane mechanical performance.

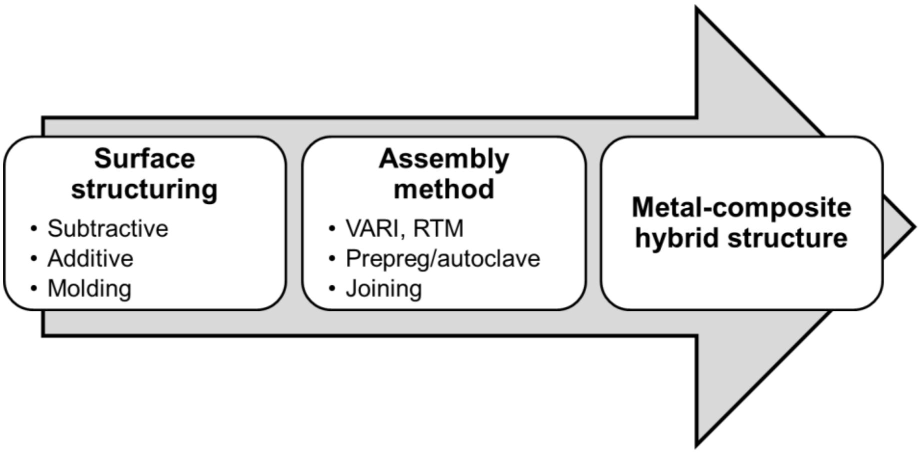

Figure 3-3: General phases of direct assembly metal-composite hybrid structures. Examples of available manufacturing technologies are also listed. VARI stands for vacuum-assisted resin infusion and RTM for resin transfer molding.

3.2.1 Surface structuring technologies

The available technologies for structuring the metal surface can be classified as subtractive, additive and molding forms of manufacturing. Although different in their nature, the primary objective of structuring processes is to locally modify the metal surface, creating three-dimensional interlocking sites, such as pins, columns or protrusions, upon which the composite will be assembled and interlocked. Currently there are different types of metal forming technologies for structuring the metallic part, and one could easily come up with alternative approaches to those presented in Figure 3-3. This is due to the rapid development of automated manufacturing processes and other forms of Computer Numerical Controlled (CNC) machining equipment. However, the emphasis here is to review some of the most relevant and available metal structuring technologies reported in the literature, rather than propose alternative strategies for metal structuring.

3.2.1.1 Surface structuring by subtractive manufacturing technologies

Micromachining

Although the term micromachining is used for a vast range of manufacturing processes that are employed to produce high-precision products, such as those reviewed by Masuzawa [52], the terminology here applied refers specifically to high-precision material removal processes by cutting tools. Therefore, in this case micromachining is regarded a subtractive manufacturing technology. The removal of surface material can be achieved by various machining processes such as turning, milling, drilling, grinding, deburring or hybrid processes [53], where two or more processes are combined to produce a particular surface structuring. Micromachining is physically equivalent to conventional machining processes, however, at small scales, size effect may have an influence on the process physics, as pointed out by Dornfeld, Min, and Takeuchi [54]. In this respect, factors such as the influence of the material microstructure (grain size and orientation) on the cutting mechanism and the edge geometry of the cutting tool should be considered [54].

Giandomenico [55] applied micro-milling (MM) to manufacture surface structured titanium parts for posterior carbon fiber-reinforced hybridization with layer-by-layer lamination using prepreg/autoclave assembly (Section 4.3). Two different, double-stepped and double-scarf, hybrid joint geometries were investigated. Different pin shapes were manufactured by the micro-milling process; sharks teeth and spike pins were tested [55]. The joint geometries were based on adhesive bonding theory and intended to improve the load transference between the joint parts.

The MM process is in principle similar to a conventional milling process, as schematically presented in Figure 3-4. The process creates a structured surface by progressive removal of chips from a workpiece with a sharp cutting tool [56,57]. The primary MM system consists at least of three components: a positioning worktable for the fixture of the workpiece, a cutting tool and an overhead spindle to clamp and a rotate the cutting tool [57]. At the beginning of the process, the cutting tool approaches the workpiece surface and starts to rotate, Figure 3-4 (Step 1). Contact under pressure and rotational movement of the sharp tool with the workpiece causes local breakage of the workpiece material, thus removing unwanted material. The tool follows a defined path along the workpiece surface and continues removing material (Step 2). The tool path in modern MM equipment is set by CNC. Thus it is an entirely automated process, which allows the direct conversion of computer-aided design (CAD) models to finished parts. After complete removal of unwanted material, the surface structured metallic element has been formed (Step 3), and the process ends with retraction of the cutting tool.

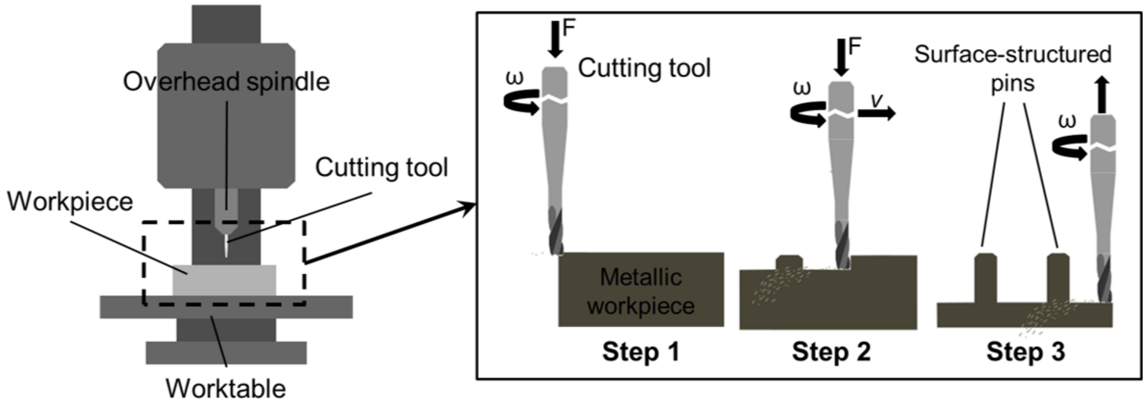

Figure 3-4: Schematic representation of surface structuring by micro-milling process.

Due to the simplicity of equipment and processing the MM process is a good solution to produce a three-dimensional structurd surface on the metallic parts of hybrid joints. However, scaling down a conventional milling process may lead to some challenges, as the average cutting depth corresponds to just a few micrometers. Consequently, chip formation may take place inside individual grains of a polycrystalline metal. For this reason, the material microstructure can affect the chosen machining process [56,58,59]. Moreover, MM tool deflection is higher at a small scale, due to its lower stiffness in comparison to conventional milling tools. Hence the machining accuracy should be considered for the MM process [60], especially with hard-to-cut materials [61]. With these the effects of cutting forces, temperature, machine vibration and tool deflection are intensified and this may lead to the cutting tool suffering premature wear or earlier failure [62–64].

Stamping

Another recent structuring process, based on forming by stamping, was introduced by Dröder *et al.* [65]. The method employs a wear resistant cutting tool with a revolving cone shape to produce undercuts on the surface of metals. The structuring process is presented schematically in Figure 3-5. At the beginning of the structuring process, the machine tool is aligned at a specific impact angle θ relative to the workpiece surface (Step 1). The tool is then impacted against the metallic workpiece surface, forming a semi-circular undercut (Step 2). After the penetration depth (s_d) has been reached, the tool is retracted from the workpiece surface, completing one structuring cycle [65]. The geometry of the structured surface undercut strongly depends on the impact force, impact angle, tool geometry and material properties [65,66]. The process feasibility has been successfully proven for aluminum alloys [65–68]. However, one must expect rapid wear of the cutting tool when it is applied to high strength steels or titanium alloys.

Müller *et al.* [67] investigated different structuring forces and impact angles during the stamping forming process and their effects on the hybrid joint's mechanical performance. In their work, a modified machining center was used, which comprised of a specially designed tool and sample holder. The tool is connected to the working axis of the machine, which allows for precise path-control of the cutting process, resulting in a completely automated structuring process. Thus, not only the geometry of the undercuts, but also different pattern layouts (undercut density and distribution) can be produced [66,68].

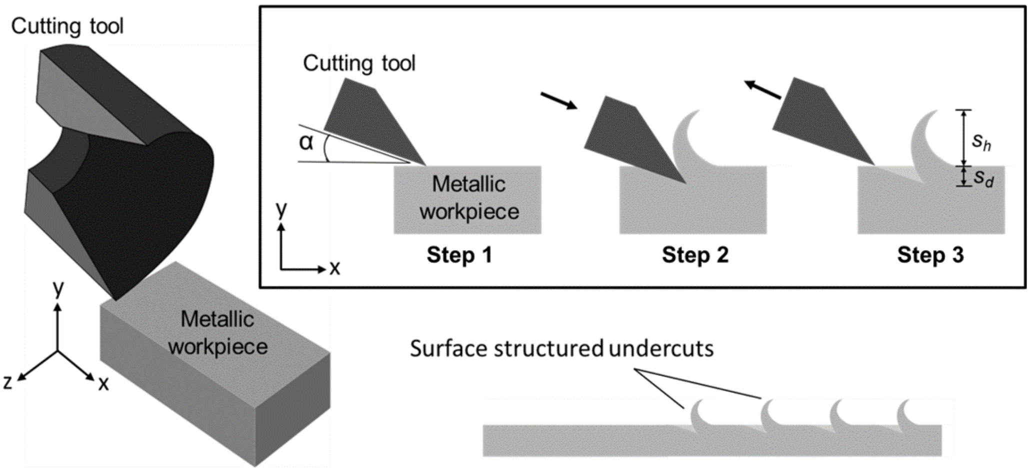

Figure 3-5: Schematic representation of surface structuring by stamping forming process, adapted from [67]. Where θ is the impact angle, s_d tool penetration depth, and s_h structured undercut height.

Surfi-Sculpt

Surfi-Sculpt is another non-additive structuring process, which was invented by Dance and Kellar at TWI (The Welding Institute) in 2002 [69,70]. The structuring process uses power beam to locally melt and move material on the metal surface, creating arrays of protrusions and intrusions. Two process variants have been introduced by TWI: in-vacuum electron beam (EB) and the laser beam (LB). Although most of the described scientific knowledge and application were reported for the former, LB-Surfi-Sculpt follows the same fundamental principles. Figure 3-6 depicts the Surfi-Sculpt process steps.

The structuring process consists in impinging an electron or laser beam against the metallic workpiece surface, as shown in Figure 3-6, Step 1. Firstly, the beam locally melts a volume of metallic material on the workpiece surface forming a molten pool at a defined start point. Secondly, the beam is rapidly deflected sideways (swiping) using computer controlled electromagnetic coils (in the case of EB) over the workpiece surface. As a result, the molten material is displaced in the opposite direction of the electron beam deflection (Figure 3-6 Step 2). At this point, combined effects of vapor pressure and surface tension allow the molten material to be piled up forming a small protrusion [71,72], (Figure 3-6, Step 3). Through a multiple-scan repetition of the EB deflection process in the same site over the workpiece surface, a structured protrusion and a corresponding intrusion are created, as shown in Figure 3-6, Step 4.

The Surfi-Sculpt process can be used to make a series of protrusions simultaneously across a metallic workpiece, instead of only one pair of protrusion/intrusion as shown in Figure 3-6. Hence the process can produce a high aspect ratio of protrusions in just a few seconds per square centimeter [73]. Moreover, by adjusting the electron beam parameters, which include beam acceleration, current, focus, scanning frequency, and process duration, it is possible to produce a wide variety of different protrusion patterns and shapes across the metal surface [74,75]. However, the size of an EB surface-modified workpiece is restricted to the dimensions of the vacuum chamber, within which the structuring process is carried out.

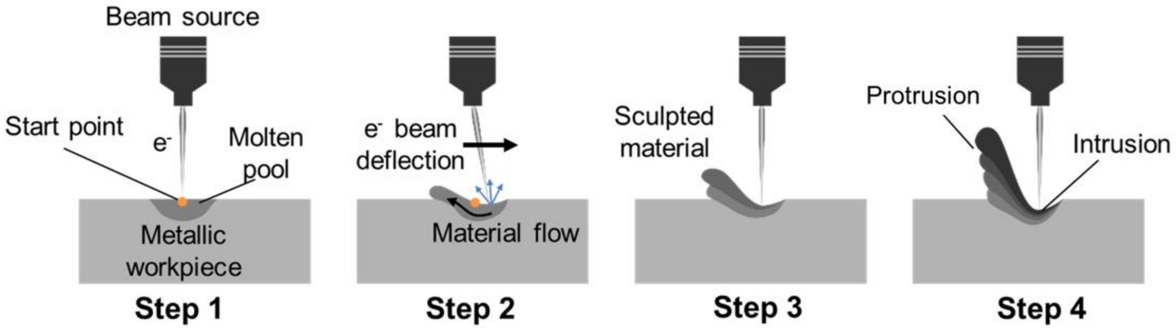

Figure 3-6: Schematic representation of the Surf-Sculpt process

TWI next introduced a laser-beam variant of the Surfi-Sculpt process in 2008 [72] to mitigate the drawbacks of vacuum chamber size and the controlled atmosphere needed to stabilize the electron beam. The dynamics of the structuring process are similar to the EB variant, but in the case of LB the swiping is achieved either by galvanometric mirror beam deflection or by rapid movement of the metallic workpiece [72]. A significant reduction in the system cost is realized by making the process possible without a vacuum chamber. Moreover, the

LB variant of Surfi-Sculpt facilitates the manufacturing of larger parts, as the size restrictions related to the chamber are removed [76]. Although still undergoing early stages of development and application, the laser beam variant has already been demonstrated with various materials such as C-Mn steel, 304 stainless steel, Ti-6Al-4V [77] and 5000 series aluminum alloys [78]. During the structuring process, the main process parameters for LB include: laser power density, laser swiping speed, swipe delay and the number of swipe repeats [76]. The most relevant works published that investigate both variants of Surfi-Sculpt are presented in Table 3-1.

Table 3-1: Relevant works carried out on Surfi-Sculpt

Authors	Process variant	Material	Description
Buxton and Dance [73]	EB	several examples	Introduction to the basics of the Surfi-Sculpt structuring process and its potential applications, as well as future trends.
Dance et al. [71]		steel and titanium	A broad introduction to the Surfi-Sculpt process, focusing on the process development stages, challenges faced and potential application
Taendl and Enzinger [79]		aluminum (AA6016)	Evaluation of different beam deflection patterns and optimization of the structuring process parameters by design of experiments.
Wang *et al.* [74,75]		Ti-6Al-4V	Investigation of scanning waveform using a new scanning control system and assessment of the structuring process on the Ti-6Al-4V microstructure.
Blackburn and Hilton [77]	LB	stainless steel (304 and 316), C-Mn steel, nickel alloy 718, and Ti-6Al-4V	Feasibility study of Surfi-Sculpt using a 200 W Yb-fiber laser on various metallic surfaces.
Earl *et al.* [78]		stainless steel (304), Ti–6Al–4V and aluminum 5000 series	Investigation of protrusion-making mechanisms by laser-based Surfi-Sculpt. Evaluation of the jet breakup theory and spatter generation equations to predict process parameters.
Earl *et al.* [80]		Ti-6Al-4V	Use of response surface methodology to statistically investigate the interactions between laser beam power, translation speed and focal distance on the structuring process.

EB – electron beam; LB – laser beam

3.2.1.2 Surface structuring by additive manufacturing technologies

Additive layer manufacturing

The manufacturing of parts by additive manufacturing (AM) has recently attracted the attention of several industry segments, including aerospace, biomedical, and electronics. AM has the potential to change the way designers and engineers think, design and manufacture products. One of the most attractive features of AM is the fast production of complex components with a high geometrical degree of freedom, especially compared with CNC machining and injection molding. Although subtractive machining process can usually remove material faster than conventional AM equipment can add it, the normally shorter manufacturing cycles of AM derives from the minimal planning, setup and tooling requirements to build a component, because the whole manufacturing process is computerized [81]. Moreover, AM technologies are by nature near net-shape techniques, thus parts do not usually require (or require lesser) post-treatment. However, to achieve high mechanical performance, AM metallic parts commonly undergo a post-manufacturing heat treatment, to remove any residual porosity and release manufacturing-induced residual stresses, which is intrinsic to most of state-of-the-art AM processes.

The manufacture of layered metallic materials by AM can be realized by several processes [82], including electron beam melting (EBM), laser beam melting (LBM), which is also known as selective laser melting (SLM), and laser metal deposition (LMD). Comprehensive literature on the various metal AM techniques can be found in [82–85]. In this manuscript, discussion is focused on the LBM process since this is later used in a case study as the surface structuring process for the realization of pins onto a metallic surface for TTR metal-composite joints.

The principles of the LBM process are presented in Figure 3-7. SLS and SLM work as do other AM processes, by creating parts directly from CAD models. Thus, before starting the manufacturing process, software virtually slices a 3D model into a series of 2D sections. Each of these 2D sections contains the x and y coordinates where the laser beam should scan and sinter (or melt) the metallic powder [81,83]. These 2D sections are then transferred to the LBM equipment where the process is carried out. During the process, the powder delivery piston moves upwards and a roller system drags powder to the building platform (Figure 3-7). After this a high-energy laser beam (LB) scans the powder bed and in accordance with the 2D slices sinters (or melts) a layer of material. After the LB has completed the whole path of each 2D slice, the building platform moves down, creating room for the next layer. The powder delivery system drags another layer of powder to the bed, and LB scanning resumes. The manufacturing process is repeated several times from bottom-up until the desired 3D model is entirely manufactured. After surface structuring is complete, the metallic part is removed from the build platform; it may then undergo further machining steps to improve surface finishing, or be heat-treated to decrease residual porosity (the latter is sometimes required to increase the part's mechanical strength) [86].

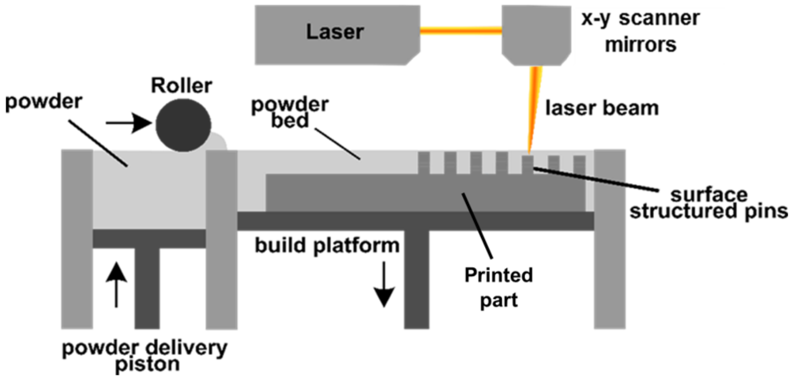

Figure 3-7: Additive layer manufacturing of a surface-structured metallic workpiece by LBM.

Due to the fact that AM concepts are able to reduce design constraints, it can be applied to produce a variety of complex geometries on the metallic surfaces of hybrid joints. For example pins can be manufactured with various tips or head features to improve the interlocking between the hybrid parts and to increase the out-of-plane strength of such joints. These are the principles of hybrid penetrative reinforcement (HYPER) technology, patented by Airbus Operations Limited [87]. Graham *et al.* [88] applied this idea to arrays of structured conical-headed pins on 3 mm thick stainless steel (316L) substrates. After the additive manufacturing process, the structured surface substrate was grit blasted with grade 60 to prepare it for the assembly phase [88]. Parkes *et al.* [89,90] and Caspari *et al.* [91] used the same principles to structure Ti-6Al-4V substrates and improve the mechanical performance of titanium/carbon-fiber reinforced hybrid joints [89,92].

Although AM concepts are flexible when it comes to design and may be faster in comparison with the traditional subtractive process, they present some drawbacks related to residual porosity, especially when complexity of the manufactured structure increases. Moreover, the microstructure of the produced part may not be homogenous and can vary through its thickness. Furthermore, high capital investment is required for the purchase of the metal AM equipment. Finally, for the industrial high-rate production of parts it may be unsuited technology, it is seen as a fast solution to rapid prototyping and small tailored components.

Cold metal transfer - CMT

Fronius recently introduced another additive surface structuring technique, known as "cold-metal transfer" or CMT [93,94] for short. This process is a variant of an arc-welding process, which applies a very well controlled source current to weld materials, thereby reducing the heat input in the melt pool. As a result, welds with smaller material affected zones are formed. Moreover, by controlling the welding parameters the filler wire can be welded to a metallic workpiece, resulting in a surface-structured pin. Figure 3-8 presents the basics of the CMT structuring process.

The process is entirely automated, that is, a robotic arm carries the welding torch and welds the filler wires on the workpiece surface. At the start of the welding process, the welding torch approaches the metallic surface and a first arc weld is created between the electrode and the workpiece (Step 1). This results in melting the filler wire, which is welded to the metallic surface. In Step 2, the current is turned off and the welded wire is left to cool down (delay time between 0.5 and 2 s [95]). Due to differential heat transfer, a temperature gradient is formed as the base of the wire has a greater mass of material to exchange heat. Thus, when the circuit is closed again and the electric current flows through the welded filler wire (Step 3) a hot spot will be formed due to a local increase in resistance and the Joule effect [95]. Finally (Step 4), a retraction force is applied to the wire, which, combined with the local increase in temperature, results in its breakage [96]. After repeating these steps according to predefined patterns, a forest of welded pins is structured on the workpiece surface.

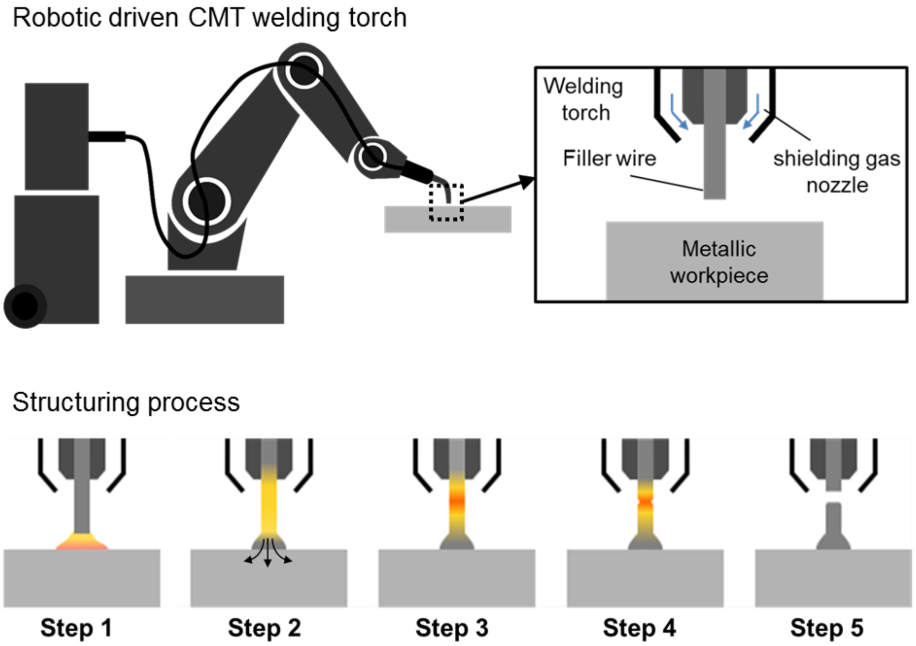

Figure 3-8: Cold metal transfer for surface-structuring pins welded on metallic parts.

By controlling the welding parameters, different pin head geometries can be achieved during the breaking-off process, such as ball-head, cylindrical and spike-like pins [93,97,98]. The main CMT process parameters include: current, retraction force, delay time between arc formation and second current pulse, and between the current pulse and retraction [95]. The CMT process is suitable for a range of metals, which includes steel, aluminum, and titanium alloys [99]. However, as a fusion welding technology, one may expect problems such as solidification cracking, hydrogen embrittlement, and alloy element evaporation. That is why shielding gases are required over the entire structuring phase, to minimize these effects.

3.2.2 Assembly strategies

Once the metallic part's surface has been structured by one of the previously mentioned techniques the fiber-reinforced composite requires assembly to form the hybrid structure. Various processes can be employed to assemble the composite. These include autoclave assisted technologies as well as out-of-autoclave concepts such as resin transfer molding (RTM) and vacuum-assisted resin infusion (VARI). Alternatively, it is possible to use energy from the joining process, as has been recently introduced [100]. Except for the latter, where established laminates were used, the other assembly processes share common steps. These are similar to the conventional polymer composite manufacturing technologies: engineering of fibers and resins, cutting of raw material laminate shapes, and curing to comply with mechanical performance requirements [101]. Mostly this could be achieved by a completely manual procedure, such as hand lay-up and spray-up [102]. However, closed-mold concepts such as RTM and VARI are preferred, to reduce volatile emissions and improve the quality of the working environment [101,102]. Closed-mold processes also result in less void formation in the composite part, thereby improving the mechanical performance of the metal-composite hybrid joint. Hence, this section will focus on these techniques.

3.2.2.1 Vacuum-assisted resin infusion (VARI)

Resin infusion of dry fiber reinforcement using a pressure gradient, such as that induced by vacuum-assisted resin infusion, is established as an industrial manufacturing process for the production of high-quality fiber-reinforced composites [101,103]. As a consequence, its use in an assembly process for surface-structured metal-composite joints is straightforward; the main difference from standard procedures is positioning the surface-structured metal inside the mold before placement of the dry reinforcement and infusion of resin. See the illustration in Figure 3-9. The VARI assembly process consists of the following stages: (1) placing the surface-structured metallic part into the mold cavity, (2) laying the dry fiber reinforcement onto the surface-structured metallic part, (3) closing the mold and sealing it with a flexible vacuum bag, (4) connecting the system to a vacuum pump and drawing the air out, (5) resin infusion to wet out the fiber reinforcement, and (6) curing the composite at room temperature.

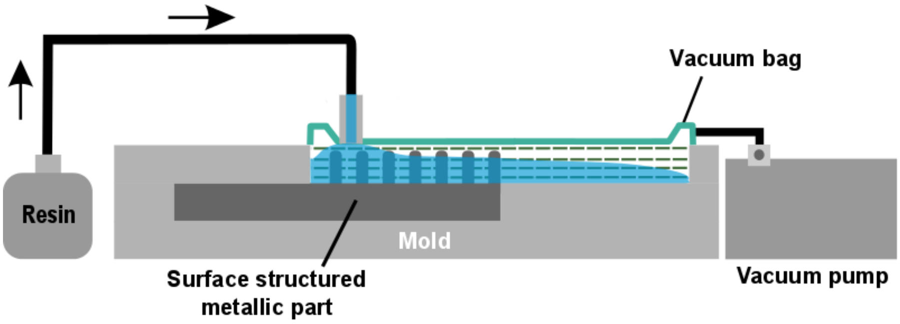

Figure 3-9: Schematic illustration of a vacuum-assisted resin infusion (VARI) assembly of a metal-composite hybrid joint.

The main advantages of VARI compared to other assembly methods are [101,103]: (i) initial capital investment of an autoclave is eliminated, (ii) simpler cold fiber storage management systems are required in comparison with pre-impregnated fibers (prepregs), (iii) shelf-life constraints are eliminated (as observed for prepregs assembly), (iv) labor-intensive lay-up is reduced in comparison with manual lay-up and spray-up. On the other hand, (i) the process is currently limited to low viscosity resins, which are required to ensure the complete infusion of the dry reinforcement, (ii) the mold production may be expensive and limit the component geometry, and (iii) void content is reduced compared to hand and spray lay-up, but this still does not meet the requirement of autoclave-manufactured high-performance composites applied, for instance, in primary aircraft structures.

3.2.2.2 Resin transfer mold (RTM)

Similar to VARI, the resin transfer molding (RTM) process is based on resin infusion of dry fiber reinforcements and thus presents similar features. RTM can be seen as a further development of the application of vacuum to improve processability and final composite properties. The difference between the methods lays in the way the pressure gradient is created. With VARI vacuum pressure is applied to parts in a flexible bag inside an open mold, whereas in RTM the pressure gradient is created inside of a stiffly closed mold. This means that higher vacuum and positive pressure are accomplished [103,104], allowing for better resin infusion and compaction of the part. Figure 3-10 illustrates the RTM process. In the same fashion as the previously described assembly process, the adaptation of RTM to manufacture direct assembly metal-composite joints only consists of positioning the structured metallic part inside the RTM mold cavity before placing the fiber reinforcement and the impregnation process. The process can be divided into the following steps: (1) mold opening and placement of the surface-structured metallic part, (2) laying-up the dry fiber reinforcement on the metallic part (Figure 3-10 (a)), (3) tightly closing the mold, (4) infusing the resin and the catalyst reagent through the mold under pressure, to impregnate the fiber reinforcement, (5) curing the resin, thermally assisted or at room temperature (Figure 3-10 (b)), and (6) mold opening releasing/demolding of the hybrid strucuture. Although conventional RTM processes are designed for a thermoset, due to its low viscosity, recently thermoplastic RTM (T-RTM) has been successfully applied using a reactive thermoplastic matrix system based on anionic polymerization of polyamides [105–107]. This represents a considerable advance towards more sustainable RTM composites.

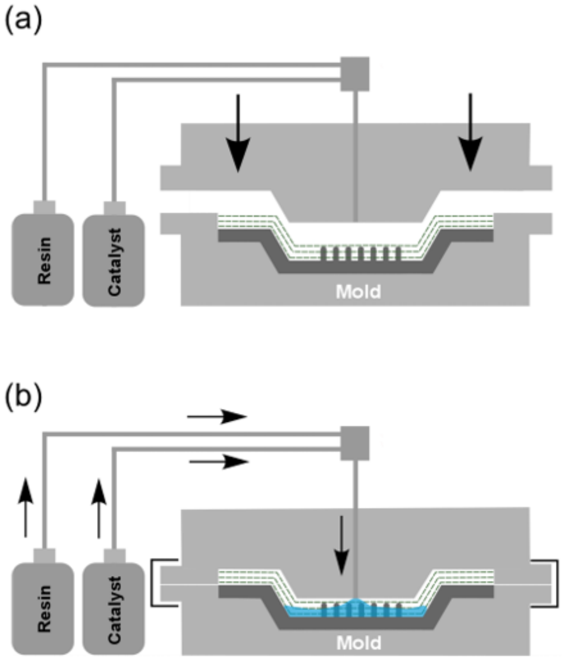

Figure 3-10: Schematic of a metal-composite structured assembled by RTM. (a) Placement of the surface-structured metallic part and dry fiber reinforcement in the mold cavity, and (b) impregnation of the fibers.

The main advantages of the RTM process are [103]: (i) Less capital investment is required, especially when compared to autoclave-based manufacturing routes. The autoclave curing can be skipped, because heating systems can be integrated directly inside the mold cavity. (ii) Reduced cycles times, (iii) low-cost of raw materials, especially when compared to pre-impregnated fibers (prepregs), (iv) production of high-performance and high surface quality components, (v) extended shelf life of fiber reinforcement, and (vi) good control of fiber/resin ratio, which usually allows to up to 70 wt.% of fiber in the composite part. The limitations usually found with RTM are: (i) more initial capital investment of the mold cavity, which tends to increase with component complexity, (ii) significantly large parts require complex tooling and vacuum systems, (iii) the impregnation process requires a tight adjustment of process parameters, and (iv) unidirectional lay-ups may result in reduced structural performance and increased weight.

3.2.2.3 Prepreg/autoclave assembly

Manufacturing of composites using prepregs and further autoclave curing is typically applied to produce superior quality composite structures with high volumes of fiber content and consequently superior strength-to-weight properties. Similar assumptions are applied for the assembly of metal-composite hybrid structures. The term prepreg refers to pre-impregnated fiber with a matrix resin in an uncured state [108]. The uncured state makes the prepreg possible to lay-up and shape the composite part. After the shaping step, the composite is cured at high temperature and pressure to reach the design requirements. Prepregs are widely applied in different industrial fields for the fabrication of composites, mostly because they eliminate the need for users to handle resin formulation and impregnation phases [101]. The pre-impregnated fibers are usually provided in unidirectional sheets or tapes, or as fabrics (woven). The latter is formed of at least two woven threads (warp and weft). These threads are usually woven or knitted in three main styles: plain weave, satin weave and twill weave [101,109]. Detailed information on the influence of weave patterns on composite mechanical strength can be found in [101,102].

The typical autoclave/prepreg assembly of surface-structured metal-composite hybrid structures is very similar to conventional vacuum bagging and VARI. However, resin curing is carried out in an autoclave to ensure complete fabric wet-out and reduce occurences of voids. To summarize, autoclave/prepreg assembly process steps include: (1) placement of the surface-structured metallic part into an open mold cavity, (2) application of prepreg plies; during this step, precaution should be taken to remove entrapped air between the plies, (3) application of release film and bleeder plies, (4) sealing of the mold with a flexible vacuum bag, (5) air removal by vacuum pump, (6) curing of the assembled hybrid structure in an autoclave under high temperature and pressure.

The advantages of prepreg and autoclave-assisted assembly are [103]: complete wet-out of the fabric by the resin, resulting in lower void content, (usually less than 1% [110,111]), thus autoclave curing of the composite part of the hybrid joint is more likely to produce high bonding strength between the metal and composite, (ii) the operator is alleviated resin chemical formulation and impregnation processes, meaning the handling and manufacturing process is facilitated, (iii) assembly automation is facilitated, such as can be seen in the automated fiber placement (AFP) and *automated tape lay-up* (ALT) processes, (iv) clean work environment. Drawbacks of prepreg processing are: (i) expensive base materials, which require (ii) low-temperature storage to avoid premature cure of the resin, (iii) limited shelf life (for thermoset composites), and (iv) an autoclave usually means high capital investment.

3.2.3 Mechanical performance of direct assembly joints

Improvements in load transfer capabilities and higher out-of-plane strength are typical features expected from direct assembly metal-composite hybrid structures. A few studies published in the literature have evaluated their properties and proposed various joining designs and optimization procedures. Some of the relevant works are briefly discussed in this section. It is important to notice that a direct comparison between different structuring process and assembly methods is a somewhat complicated task since no standardized methods have been so far introduced for such TTR metal-composite hybrid joints. Hence direct assembly joints reported were produced with different overlap areas, TTR element densities, and for a variety of geometries and distributions. As a result, one can already recognize knowledge gaps related to the selection of surface-structuring techniques and assembly methods. This is mainly due the early stage of development of this new area of knowledge. An attempt to review the relevant literature on TTR metal-composite joint properties is presented in Table 3-2. This data is compiled according to the metal surface structuring process and information about the material combination, thickness, and assembly methods are presented.

Giandomenico [55] evaluated the effect of different pin geometries and joint design, following the designs typically used for adhesively bonded joints [104]. In this work, micro-milling was applied to manufacture surface-structured titanium parts and a carbon-fiber reinforced laminate was added layer-by-layer onto its surface using prepregs followed by autoclave curing. Two different joint geometries were investigated with double-stepped and double-scarf joints, and various pin shapes (shark teeth and spike pin) were manufactured. An improvement of up to 54% was reported for the joints reinforced with shark teeth pins compared to unreinforced reference joints produced using the same assembly procedure. Brand *et al.* [68] assessed the effect of differently structured undercuts, sizes and density distribution patterns on the quasi-static strength of AlCuMg1/PA6GF30 joints assembled by injection molding. They showed that ten structured undercuts, with a projecting area of 2.9 mm^2 correspond to the optimal density for an overlapped area of 30 x 30 mm. In addition, a circular distribution layout of the undercuts resulted in joints with higher load capability [66,68]. In another work, performed with the same materials, Müller *et al.* [67] reported that the undercut orientation played a significant role in the mechanical properties of the joint. Their work indicated that an undercut oriented at 0°, counter the loading direction and produced with an impact angle of 15° and impact force of 2000 N result in improved joint quasi-static mechanical properties. In addition, by sandblasting the structured surface, further improvement in joint strength was achieved.

COMELD joints - a concept introduced by TWI - uses Surfi-Sculpt as a surface structuring process to produce metal-composite hybrid joints [48,49]. Significant improvements in the mechanical performance of hybrid joints have been reported for the COMELD concept. Smith [48] showed that such joints presented improved toughness (the energy prior to failure was shown to be more than the double), and more progressive failure compared to control references [49]. Numerical optimization of surface-structured protrusions produced by Surfi-Sculpt (i.e., protrusion height and tilt angle) for COMELD joints was studied by Tu *et al.* [112] using the FE model. Their work suggests that fabrication of protrusions with a tilt angle of 20° or 30° towards the metal end of the overlapped area could improve the load transfer between the parts. Wang *et al.* [51] evaluated the effect of circular and linear patterns on the production of Surfi-Sculpt protrusions and their influence on the joint's mechanical performance and failure mechanisms. In their work, a digital image correlation (DIC) system was used to measure the strain fields during the mechanical test. It was shown that the circular pattern results in lower mechanical performance in comparison to the linear one. Moreover, for both cases, a two-stage failure was deduced based on the DIC results. The joint failed first due to debonding of the composite metal-interface in the regions of higher strain concentration, followed by pull-out of the protrusions (for the circular pattern) or failure within the CFRP with debonding of laminate plies above the structured protrusions (for the linear pattern) [51].

The application of AM as surface structuring process to produce what are known as HYPER (hybrid penetrative reinforcement) joints have been evaluated by Parkes *et al.* [89,90,113]. They performed a broad range of experiments to assess the effect of pin design on the ultimate tensile strength (UTS) of Ti–6Al–4V/CFRP hybrid joints. Furthermore, a nondestructive testing (NDT) method was proposed to assess joint damage mechanisms. They showed that UTS was improved by 6.5 times and the joint elongation by 407% in comparison with reference joints [90]. Their NDT results suggested that the joints failed primarily by debonding of the composite, followed by fracture of the pins [113]. Similar global failure mechanisms were also observed for joints tested under cyclic load, although with a more progressive fracture of the pins with reduced load severity [89].

Ucsnik *et al.* [50,98,114] studied the effect of different pin geometries on the mechanical behavior of direct assembly hybrid joints. In their work, ball-head and cylindrical pins were welded by CMT onto stainless steel substrates, and VARI was used to assemble the CFPR (epoxy matrix). Along with a significant improvement in the load-carrying capability of joints, they observed that the pin geometry, and especially their tips, influenced the fracture mode of the joints. Cylindrical pins tended to fail by pullout mode, whereas ball-headed pins increased the interlocking and out-of-plane strength. Hence, after adhesive failure from the non-reinforced metallic surface areas, the pins bearing the transferred loads subsequently shearing off [97]. Thus, the quasi-static lap shear strength of the latter was improved. Furthermore, CMT has also been applied to manufacture composite-composite joints with a through-the-thickness metallic reinforcement in AISI 304, 316L, and Ti-6Al-4V [96,115,116] as well as being introduced as a new technology for the reinforcement of fiber-metal laminates (FML) of GFRP (epoxy matrix) and stainless steel AISI 430 [117].

Table 3-2. Relevant selected works on the properties of direct assembly overlapped metal-composite hybrid joints

Author	Material combination and Material thickness	Surface structuring	Assembly	Description
Giandomenico [55]	Titanium/CFRP (epoxy matrix) 6 mm / ~10 mm	Micro-milling	prepreg/autoclave	Effect of different pins and joint geometry on the mechanical performance of TTR joints. An improvement of up to 54% was reported for a sharks teeth pin reinforced joint in comparison with non-reinforced reference joints.
Müller *et al.* [67]	AlCuMg1 / GF-PA6 2 mm / 2 mm	Stamping	injection over molding	Evaluation of different structuring patterns. The maximum tensile strength was found for a combination of surface treatments of the aluminum by undercut structuring and sandblasting.
Brand *et al.* [68]	EW AW 2017A / PA6GF30 2 mm / 2 mm			Effect of structure size, number and distribution pattern of undercuts on the quasi-static mechanical performance.
Dröder *et al.* [66]				The effect of the structuring distribution pattern was investigated. A circular pattern of surface-structured undercuts was found to improve the load transfer between the materials significantly.
Smith [48]	Stainless steel / GFRP (polyester matrix) 8 mm / 8 mm	Surfi-Sculpt	vacuum assisted resin infusion	Introduction to COMELD technology for the fabrication of metal-composite hybrid joints. Advantages and limitations are described, as well as, joint mechanical properties.
Xiong *et at.* [118]	Ti-6Al-4V / CFRP (epoxy matrix) 1.8 mm / 1.8mm			The effect of three different composite lay-ups on quasi-static mechanical properties, damage initiation and failure of COMELD joints are described.
Kellar and Smith [49]	SS/GFRP and Ti/CFRP (matrix not informed) no thickness available		vacuum assisted resin infusion and manual lay-up	Quasi-static mechanical performance of COMELD joints with a focus on their damage-tolerance properties.
Tu *et al.*[112]	Ti–6Al–4 V / CFRP (epoxy matrix) 6 mm / 6 mm		prepreg/autoclave	Numerical optimization by FEM of surface-structured protrusions with respect to height and tilt angle.
Li *et al.*[119]	titanium alloy TC4 / CFRP (epoxy matrix) 6.5 mm / 6.5 mm			Application of FEM to predict the quasi-static mechanical performance and failure modes of COMELD joints.
Wang *et al.*[51]	Ti-6Al-Qu4V / CFRP (epoxy matrix) 11 mm / 11 mm			Quasi-static mechanical properties of hybrid joints and strain field characterization by DIC.
Graham *et al.* [88]	stainless steel (316L) / GFRP (epoxy matrix) 3 mm / 2.5mm	ALM	vacuum assisted resin transfer molding	The effect of additive layer manufactured pins on stainless steel/glass-fiber reinforced composite hybrid joint strength, toughness and damage tolerance investigated.
Parkes *et al.* [89,90,113]	Ti–6Al–4V / CFRP (epoxy matrix) 5 mm / 5 mm	SLM	prepreg/autoclave	Introduction to the HYPER concept to produce TTR hybrid joints. Joint damage evolution characterized by immersion pulse-echo ultrasound, and the fatigue life assessed.
Ucsnik *et al.* [97]	stainless steel 304 / CFRP (epoxy matrix) 8 mm / 11 mm	CMT	vacuum assisted resin infusion	Introduction of the CMT concept to produce TTR joints. Two different pin reinforcement geometries were evaluated and significant improvements in joint strength and toughness achieved.
Ucsnik *et al.* [98,114]	304L / CFRP (epoxy matrix) 9 mm / 5 mm			Evaluation of three CMT pin geometries (ball-headed, cylindrical and spike pins) on the mechanical performance of metal-composite hybrid joints.

3.3 Main properties of the materials used in this work

3.3.1 Metal injection molded Ti-6Al-4V

Titanium and its alloys are the backbone material for several industries, including chemical, energy, biomedical and aerospace [120,121]. This is owed to their high strength-to-weight ratio mechanical properties, which are maintained at elevated temperatures, combined with fracture resistant characteristics, excellent corrosion resistance and biocompatibility [120,122,123]. In this respect, the Ti-6Al-4V is by far the most commonly applied of the titanium alloys [120,121]. However, the use of Ti-6Al-4V is limited to some applications due to the high costs of the raw material and some geometry design constraints [124].

Recently, powder-based manufacturing concepts, such as metal injection molding (MIM) have gained attention as candidates to overcome production drawbacks associated with the waste of raw material and its cost. This is due to the net-shape or near net-shape fabrication route of MIM, which allows for the fabrication of complex shaped parts in large production volumes [124,125]. The MIM process is an established technology for the fabrication of small and complex geometries, especially when it comes to hard metals, such as high-speed tool steels [125,126]. A detailed description of the MIM process and its fundamentals can be found in [125], and further on (Section 6.1), where a detailed description of the MIM-based manufacturing route used to produce the titanium parts for this work will be given.

In the case of Ti-6Al-4V, MIM has been reported as an ideal route for the production of large quantities with low production costs, mainly due to its high material utilization compared with machining [127]. Indeed, machining of Ti-6Al-4V is considered an expensive and slow process. Nowadays, Ti-6Al-4V parts produced by MIM present reasonable strength levels and plastic elongation [128,129]. When an adequate MIM process is designed, Ti-6Al-4V parts can be produced with chemical composition, yield stress, and elongation in the range of ASTM B348-2 standards [130]. Despite its fatigue performance is limited in comparison to wrought alloys and corresponds to a range of 350 - 400 MPa [127,131,132], whereas for wrought material it is between 450 – 800 MPa [133].

According to Ferri [131], such an inferior performance in fatigue strength is due to residual porosity, a coarser microstructure after sintering, and superficial defects (i.e., open pores and high surface roughness). The latter can be improved by a post-treatment using, for instance, shot peening, which can increase the fatigue performance by up to 500 MPa [127,131]. In addition, hot isostatic pressing (HIP) is usually required after the sintering phase if high-performance MIM-processed Ti-6Al-4V parts are required, because residual porosity ranges from 2% to 4% is usually presented in as-sintered parts [127]. Nevertheless, the control of the injection molding parameters, binder, and alloy composition also play an essential role in the MIM process and the parts it produces [127,131].

Ferri, Ebel, and Borgmann [134] reported that a small addition of boron to the conventional MIM-processed Ti-6Al-4V alloys could promote significant transformation in the part's microstructure and mechanical properties. For instance, the addition of 0.5 wt.% leads to considerable microstructure refinement, thereby increasing by up to 12% the yield and ultimate tensile strengths. Moreover, they showed that the fatigue limit was increased by to up to 640 MPa [134].

Due to its biocompatibility properties, MIM-processed Ti-6Al-4V has also been considered for application in surgical implants [128]. As a result of the increasing attention for this kind of application, an ASTM standard has been implemented to regulate the chemical, mechanical, and metallurgical requirements of MIM-processed Ti-6Al-4V for surgical implants (ASTM F2885-11 [135]). Compelling evidence for the growth of industrial interest in MIM-based products [128]. As there are still no standard for MIM in structural applications, this standard is often adapted for other engineering applications. Part of the new regulation concerns the mechanical properties of Ti-6Al-4V alloys, because they present strong dependence on interstitial gases such as oxygen and nitrogen.

Figure 3-11 displays the effect of oxygen content on the quasi-static mechanical performance of MIM-processed Ti-6Al-4V [125]. The ASTM standard classifies two grades: Grade 5 and Grade 24, which differ in their oxygen limits [125], namely 0.2 wt.% and 0.13 wt.%, respectively. The latter is also known as ELI (extra low interstitials). Apparently, the values in the standard are considered conservative, as its elongation drop occurs around 0.45 wt.% (Figure 3-11 (b)). However, according to Ebel [125], systematic studies are still missing that evaluate precisely the effect of oxygen content on MIM-processed Ti-6Al-4V.

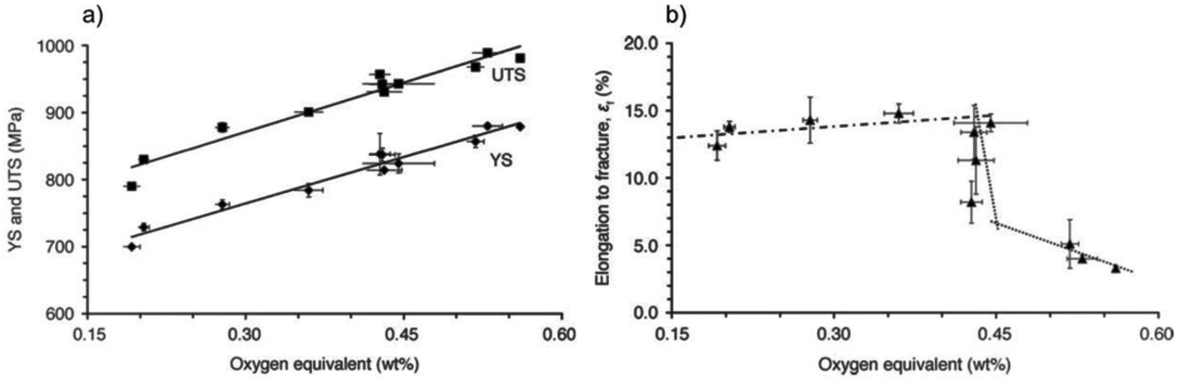

Figure 3-11: Effect of oxygen content on the MIM-processed Ti-6Al-4V alloy (a) YS (yield strength) and UTS (ultimate tensile strength), and (b) elongation to fracture, obtained from [125]

Although MIM is still not established as an industrial manufacturing technology for the transportation sector, it has a growing potential to manufacture complex Ti-6Al-4V parts, such as the ones applied in this PhD work. By following precise production guidelines, MIM Ti-6Al-4V parts can achieve outstanding properties, which are equivalent to ASTM standards and the wrought material. As well, all raw materials and equipment necessary for production are readily available on the market, which facilitates its application [127,132].

3.3.2 Glass-fiber reinforced polyetherimide

Thermoplastic composites, such as glass-fiber reinforced polyetherimide (GF-PEI), offer several advantages in the manufacture of lightweight structures compared to using a thermoset. Even more important is the fact that thermoplastic composites can be reprocessed and are more easily recycled [136,137]. Moreover, they present excellent cost-effectiveness and short consolidation cycles when compared to the long curing phases of thermoset resins [136,138].

GF-PEI is a high-performance thermoplastic composite, which offers excellent toughness, high strength, and stiffness at elevated temperatures, combined with flame resistance and low smoke emission [136,139]. Such a composite is qualified for applications in primary and secondary aircraft structures, both by Airbus and Boeing [139]. The composite matrix, polyetherimide – PEI, is an amorphous, transparent engineering thermoplastic, which was first commercialized under the trade name of Ultem by the Plastics Division of GE (General Electric) and later acquired by SABIC Innovative Plastics. PEI is prepared from condensation polymerization of diamines and dianhydrides [104], detailed information about PEI polymerization routes are found in [140]. The monomer structure of the polymer is presented in Figure 3-12. It consists of a repeated aromatic imide, propylidene (isopropylidene) and ether groups. While ether linkages provided to the chain backbone improve processability (i.e., low viscosity when in the molten state), aromatic imides contribute to an improved stiffness and thermal resistance [104].

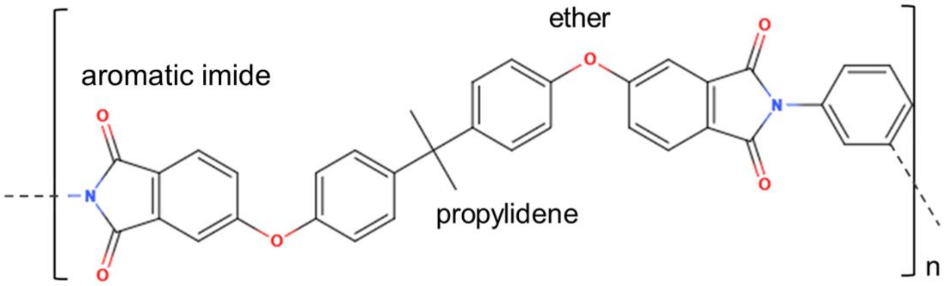

Figure 3-12: Polyetherimide monomer

PEI has a glass transition between 215 and 220°C, excellent creep properties at high temperatures, and improved chemical and rheological properties for an amorphous polymer [141,142]. When subjected to humidity, PEI presents hydrophilic behavior, absorbing a maximum of 1.45% water by weight in the range of 20 - 100°C [143,144]. Thermal degradation of PEI is reported to occur by two mechanisms, crosslinking and chain scission [145–147]. Crosslinking dominates at temperatures in the range 320 - 380°C, whereas decomposition by chain scission process starts at 450 - 600°C [145,146].

Typical PEI processing temperatures are 340 to 425°C, and it can be processed by injection molding, extrusion [104], and more recently also by additive manufacturing [148,149]. In addition, PEI and its respective carbon-fiber and glass-fiber reinforced composites can be joined by most polymer welding technologies, such as resistance [150–152], vibration [153], ultrasonic [154], laser [155], hot-tool [156], induction welding [157,158], mechanical fastening, and adhesive bonding [159].

When it comes to metal-composite hybrid structures, just a few works have explored PEI. Ageorges and Ye [160] investigated resistance welding of GF-PEI and CF-PEI to aluminum 7075-T6 for aircraft applications. In their work, hybrid joints with up to 20 MPa of ultimate lap shear strength were obtained. More recently, Blaga *et al*. [161] studied the feasibility of FricRiveting as an alternative joining technology to mechanical fastening of GF-PEI and titanium grade 2 hybrid joints.

In another study, Blaga *et al*. [162] evaluated the FricRiveted GF-PEI/titanium grade 2 hybrid joints connected to aluminum shoes (Al 2198-T851) in an overlapped configuration for future application as emergency bridges. The authors demonstrated that the friction-riveted joints, which were produced with shorter joining cycles, presented comparable or better mechanical performance as the bolted variant. Feistauer *et al*. [100] also demonstrated the joining ability of GF-PEI to MIM-structured Ti-6Al-4V by a new ultrasonic joining process to manufacture TTR hybrid joints. The results obtained are within the scope of this PhD work and are discussed in the following sections.

CHAPTER 4. EXPERIMENTAL APPROACH

In order to develop the U-Joining process and address the main properties of the hybrid joints produced, the experimental concept of this PhD work is divided into five incremental phases, see Figure 4-1. The work began with retrofitting a conventional ultrasonic welding equipment to perform the joining process. At this stage, samples holders were developed, process parameters screening was performed using a one-factor-at-time (OFAT) approach, and the feasibility of the concept was proved. Moreover, the manufacture of the metallic parts of the joint with an MIM-Structuring concept was optimized. The feasibility study, although necessary, was not the focus of the presented PhD thesis. Therefore, these related results are only briefly described in the Materials and Methods section (Chapter 5).

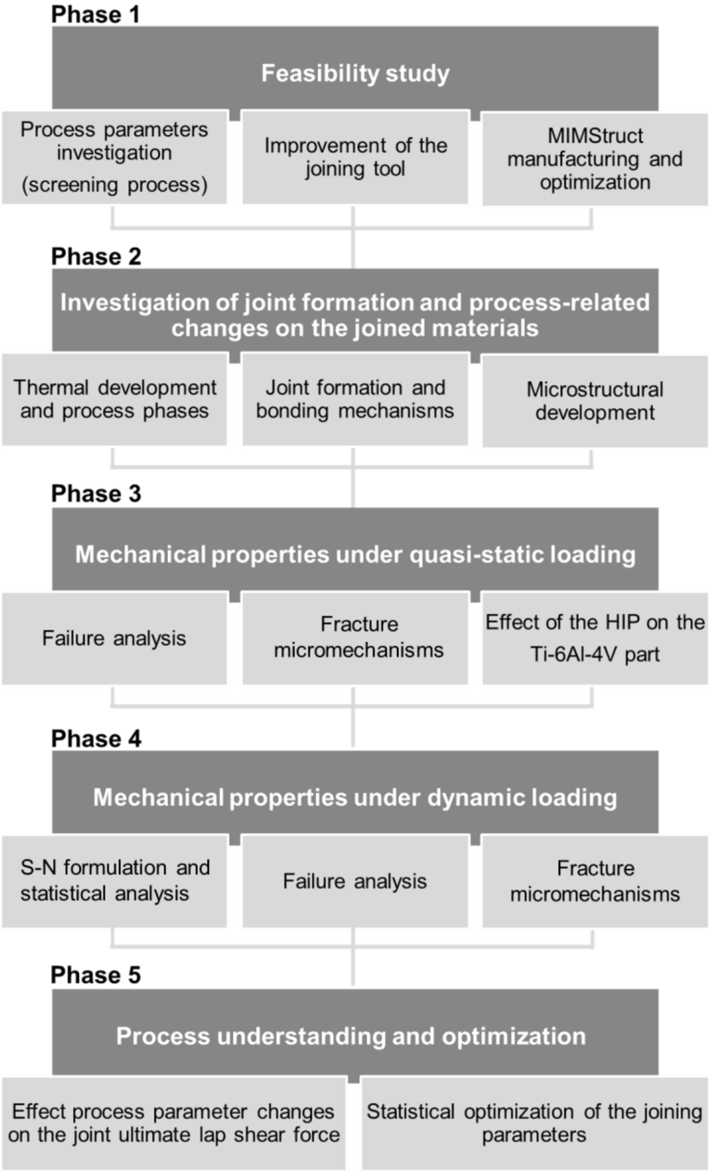

Figure 4-1: Experimental approach adopted in this PhD thesis.

In the second phase, the joint formation mechanisms and the U-Joining process-induced transformation on the joined materials were deeply investigated. This step started with a description of the joining process phases based on the changes in process parameters and thermal development. Next, a joining equipment stop-action procedure was performed, and the joint formation mechanism was evaluated in a stepwise manner. Thus, the material flow during joining was observed, and the origins of microstructural features and defects were identified. This investigation explains how the process-affected zone in the composite part is formed and how the process changes the material's physical-chemical properties. These changes were measured by thermal analysis (DSC and TGA) and size-exclusion chromatography (SEC) and were correlated with local mechanical properties, measured on micro and nanoscales by microhardness and by instrumented nanoindentation respectively. To support investigation of the polymer's process-affected zone, joining experiments with unreinforced polyetherimide were also carried out. Thus enabling qualitative measurements of residual stresses by photoelasticity and evaluation of an affected zone extent. Finally, the typical defects in U-Joining joints were addressed.

In the third phase, with the knowledge gathered on the local scale and an understanding of the process-affected volumes, mechanical performance under quasi-static loading is assessed. A customized single lap shear test was applied in this context. A digital image correlation system (DIC) linked to the testing equipment was used to evaluate the strain field of the joints under loading. Furthermore, finite element analysis (FEA) was performed to visualize stress distribution in the joints and the effectiveness of load transfer between the parts. The finite element model obtained also supported comprehension of the joint failure mechanism, which was further evaluated by scanning electron microscopy (SEM). In this way, the micromechanisms of fracture were established. In addition, the effect of hot isostatic pressing (HIP) of the Ti-6Al-4V part on joint mechanical performance was also investigated, thereby providing a strategy to further improve joint mechanical performance.

Next, in the fourth phase, mechanical performance under cyclic loading was studied. At this stage, S-N curves were obtained and the fatigue life of the produced joints was established. Three statistical models were used to fit the experimental data, providing a useful analysis for the future design of hybrid structures, based on statistical reliability. By combining an understanding of the quasi-static loading experiments and surface analysis of the fatigue-fractured specimens, the micromechanisms of failure were characterized, and an overall failure mechanism provided.

In the last phase, the joining process parameters are optimized using design of experiments (DoE) to ensure the production of joints with high mechanical performance. In order to achieve this, a Box-Behnken design (BBD) was employed and the effect of each individual and combined joining parameters on two responses (i.e., ultimate lap shear force and lack of penetration) were evaluated by plotting response surfaces and ANOVA. The statistical models obtained were validated, and the response surfaces were optimized. As a result, a set of optimized joining parameters was obtained for the material combination studied in this work.

CHAPTER 5. MATERIALS AND METHODS

5.1 Base materials

5.1.1 MIM-structured Ti-6Al-4V

The first MIM-Structured Ti-6Al-4V parts produced for the development of the U-Joining concept were the result of a collaboration work with Dr. Thomas Ebel of Helmholtz-Zentrum Geesthacht, Germany. Later, due to the necessity to produce a large volume of parts, subsequent manufacturing was performed by the Element 22 GmbH, Germany following provided specifications.

The in-house manufacturing of the metallic parts followed the MIM-Structuring concept, presented in Chapter 6. To prepare the feedstock, a pre-alloyed and gas atomized spherical powder from TLS Technik, Germany, was employed. The powder had a diameter lower than 45 µm and is grade 23 according to the ASTM B348-13 standard [130]. The titanium powders were mixed with a binder system (60 wt.% paraffin, 35 wt.% polyethylene-vinyl acetate copolymer and 5 wt.% stearic acid) in a ratio of 1:9, kneaded, and subjected to a homogenization step carried out by one injection molding cycle without filling the mold in an ARBURG 320-S machine. The injection molding parameters are summarized in Table 5-1. These parameters were also used to fill the mold cavity and produce the MIMStruct green parts.

Table 5-1: Injection molding parameters.

Volumetric Parameters	**Dose**	**Flow**	**Part Volume**	**Filling time**
	10 ccm	15 ccm/s	10.5 ccm	2 s
Injection Parameters	**Injection Pressure**	**Switchover Time**		
	440 bar	0.5 s		
Holding Time and Pressure	**Holding Time 1**	**Pressure 1**	**Holding Time 2**	**Pressure 2**
	1s	200 bar	1 s	50 bar
Barrel Temperature	**Zone 1**	**Zone 2**	**Zone 3**	**Nozzle**
	80°C	100°C	120°C	120°C
Mold Temperature	**Zone 1**	**Zone 2**		
	55°C	60°C		

Chemical debinding was carried out using a Lömi EBA-50 (Germany) chemical debinding system, with 900-minute cycles and maximum temperature of 40°C. Thermal debinding and sintering were performed in a Xerion XVAC furnace (Germany), at 600 and 1300°C, respectively. A controlled atmosphere of argon was used during thermal debinding and a high vacuum during sintering.

Figure 5-1 illustrates the as-sintered Ti-6Al-4V part (also referred to as MIMStruct) with the six round-tip conical pins used in this work. The part dimensions are 15.5 x 35 x 3 mm and the pins are 3 mm height. Detail view A (Figure 5-1 (a)) shows the pin undercuts with a radius of 0.4 mm and these were created to displace the stress concentration from bases of the pins and improve the mechanical interlocking between the materials after joining.

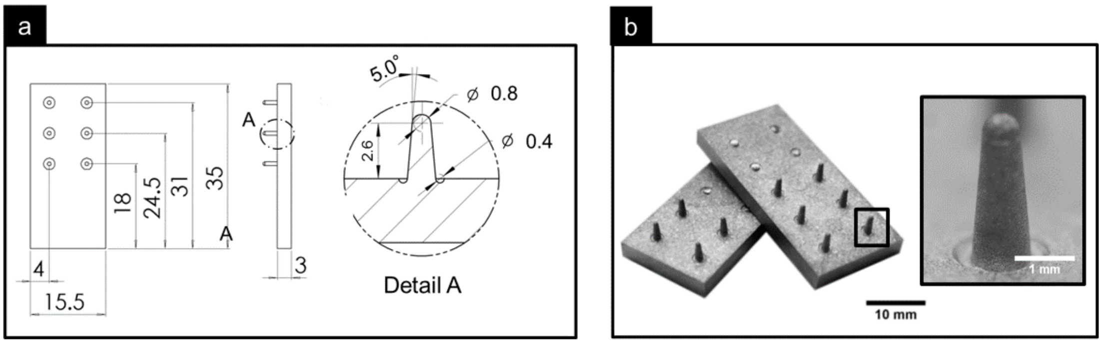

Figure 5-1: (a) Geometry of the Ti-6Al-4V parts used in this PhD work, and (b) a view of two as-sintered joint parts with four and six pins, with a detailed picture of a pin.

The as-sintered microstructure of the MIMStruct part is presented in Figure 5-2 (a). It consists of a typical microstructure of α-β Ti-6Al-4V alloy manufactured by metal injection molding [134]. The α-phase is distributed in a fully lamellar microstructure and β-phase is concentrated at the grain boundaries. After sintering, a residual porosity of 2.3 ± 0.6% was measured by digital imaging using Image J software. Such a residual porosity is typically observed in the sintering-based manufacturing of Ti-6Al-4V alloys and can be eliminated by post-treatment under high-temperature and pressure. This process is known as hot isostatic pressuring (HIP) and this was also investigated for this work.

HIP of the MIMStruct parts was carried out by Bodycote Metal Technology, Belgium**,** at 920°C and 1000 bar for 120 min. The microstructure of after HIP is presented in Figure 5-2 (b). HIP processing does not modify the microstructure of the sintered part considerably, but after treatment residual porosity was reduced to virtually zero percent.

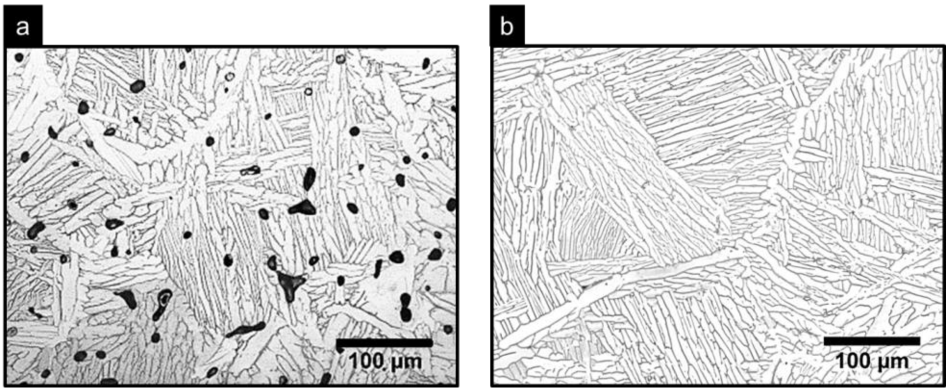

Figure 5-2: Typical microstructure of an (a) as-sintered Ti-6Al-4V, and (b) HIP Ti-6Al-4V MIMStruct part.

The chemical composition and relevant physical and mechanical properties are presented in Table 5-2 and Table 5-3, respectively. The chemical composition of the MIM-structured parts is in accordance with the ASTM F2885-11 [135]. The effect of HIP on the mechanical properties of Ti-6Al-4V is also presented in Table 5-3. An increase of up to 14% in yield stress, and 12% in ultimate tensile strength were achieved after HIP.

Table 5-2: Chemical composition of the MIM-structured Ti-6Al-4V parts.

Chemical Element	C	O	N	H	Fe	Y	Al	V	Ti
Requirement [a]	≤ 0.08	≤ 0.20	≤ 0.005	≤ 0.015	≤ 0.30	≤ 0.005	5.5-6.75	3.5-4.5	Bal.
Actual [b]	0.07	0.167	0.023	0.0019	0.18	0.001	6.61	3.96	Bal.

[a] According to ASTM F2885-11 [135]

[b] Material datasheet [163]

Table 5-3: Selected physical and mechanical properties of the MIM-structured Ti-6Al-4V parts.

Ti-6Al-4V condition	Melting point [°C]	Thermal expansion coefficient [K^{-1}]	Thermal conductivity [W.m^{-1}.K^{-1}]	Yield stress [MPa]	Ultimate tensile strength [MPa]	Elongation at break [%]
As sintered	1650 [a]	11 x 10^{-6} [a]	7.0 [a]	748 ± 3 [b]	861 ± 3 [b]	17 ± 2
HIP				872 ± 7 [b]	972 ± 4 [b]	20 ± 1

[a] Data from the literature [164]

[b] Experimentally obtained according to ISO 2740 [165]

5.1.2 Glass-fiber reinforced polyetherimide (GF-PEI)

6.35 mm glass-fiber reinforced polyetherimide laminates with a content of 50% in volume of resin (GF-PEI) and a ply stacking sequence of $[0,90]_{28}$ from TENCATE (CETEX®PEI) were used. GF-PEI is an amorphous polyetherimide thermoplastic composite qualified by the aircraft industry for primary and secondary structural applications [139,166]. Plates measuring 15.5 x 35 x 6.35 mm were machined to produce the joining parts, as shown in Figure 5-3: (a) Geometry of the GF-PEI parts used in this PhD work, and (b) its microstructure. The microstructure of GF-PEI is presented in Figure 5-3: (a) Geometry of the GF-PEI parts used in this PhD work, and (b) its microstructure. It consists of warp fiber oriented 0° (light gray) and weft fiber interlaced at 90°, following a Harness-Satin weave pattern.

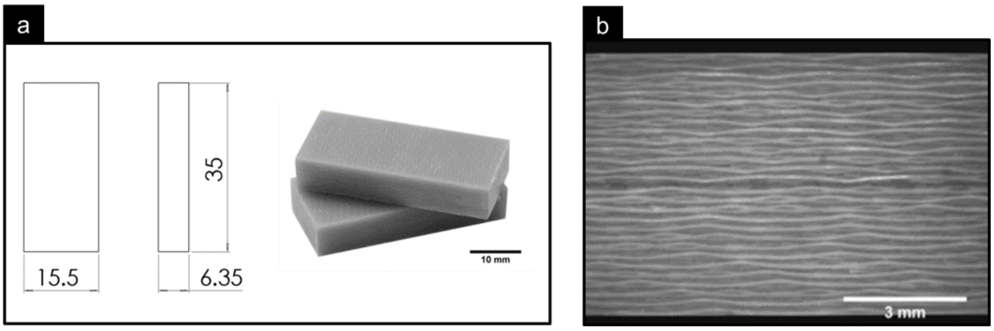

Figure 5-3: (a) Geometry of the GF-PEI parts used in this PhD work, and (b) its microstructure.

The relevant physical and mechanical properties of the GF-PEI laminates are presented in Table 5-4. GF-PEI presents outstanding mechanical performance and thermal stability, a thermal expansion coefficient roughly five times higher compared to Ti-6Al-4V, and thermal conductivity 31 times lower.

Table 5-4: Selected physical and mechanical properties of GF-PEI.

Glass transition temperature (DSC) [°C]	Onset thermal decomposition (TGA) [°C]	Thermal expansion coefficient [K^{-1}]	Thermal conductivity [W.m^{-1}.K^{-1}]	Tensile strength warp [MPa]	Tensile strength weft [MPa]
214.1 ± 0.7 [a]	531 ± 1 [a]	50 x 10^{-6} [b]	0.22 [b]	484 [b]	445 [b]

[a] Experimentally obtained

[b] Data from the literature [166,167]

5.1.3 Unreinforced polyetherimide (PEI)

To extend understanding of the process-induced changes to the polymeric matrix, joining experiments with unreinforced PEI were performed. PEI is a transparent and amorphous polymer, which presents birefringence properties. Thus when PEI is examined under transmitted light with crossed polarizers (CP-TLOM), it displays optical anisotropy. Such anisotropy originates during the polymer processing and is directly associated with residual thermal stresses, which result in the formation of a colorful fringe pattern, Figure 5-4.

The PEI base material used in this work (Duratron U1000 PEI) consists of 6.8 mm thick extruded plates from Quadrant Plastics, Switzerland. The fringe pattern observed in Figure 5-4 is, most probably, the result of differential cooling during the extrusion process. To obtain joining specimens, extruded PEI plates were cut with the same length and width used for GF-PEI laminates. The relevant physical and mechanical properties of PEI are presented in Table 5-5.

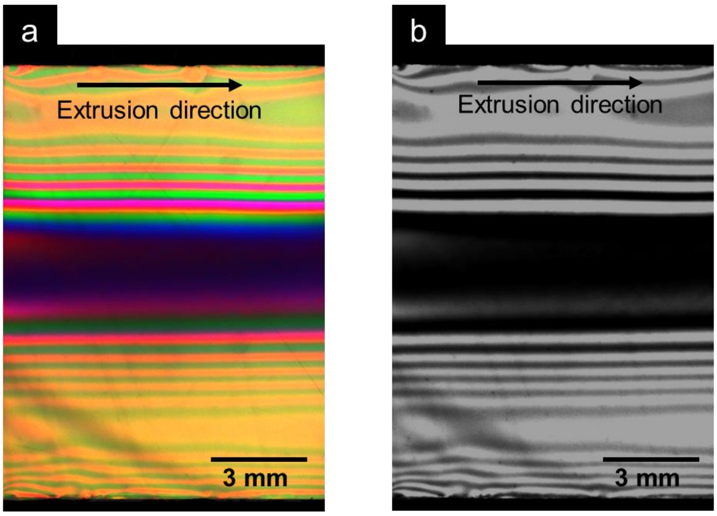

Figure 5-4: Unreinforced PEI base material optical microscopy obtained under transmitted-light with crossed polarizers. (a) Original red-green-blue color (RGB) image and (b) grayscale image with only the red component and improved contrast.

Table 5-5: Selected physical and mechanical properties of PEI.

Glass transition temperature (DSC) [°C]	Onset thermal decomposition (TGA) [°C]	Thermal expansion coefficient [K^{-1}]	Thermal conductivity [$W.m^{-1}.K^{-1}$]	Tensile yielding stress [MPa]
216.1 ± 0.1 [a]	545 ± 2 [a]	50 x 10^{-6} [b]	0.24 [b]	129 MPa [b]

[a] Experimentally obtained

[b] Data from the literature [164]

5.2 Joining equipment

The U-Joining process was carried out using a commercially available ultrasonic welding system for metals (Ultraweld L20, Branson Ultrasonics), Figure 5-5. This joining machine operates with a fixed sonotrode oscillation frequency of 20 kHz. The ultrasonic equipment is controlled by what is termed energy mode - i.e., the sonotrode vibration is kept constant until a user-preset energy value is delivered. The following joining parameters can be adjusted: joining energy (E_J), clamping and joining pressures (C_P and J_P, respectively), and sonotrode oscillation amplitude (A_0). Under this control mode, the joining system will operate in a closed-loop. The joining cycle is automatically adjusted by the control unit, Figure 5-5(b) to deliver the pre-set value of energy (E_J) according to Equation 5-1 [168].

$$E_J = P \times t \tag{5-1}$$

where P is the power and t is the joining cycle time. The joining system integrates the power used in intervals of one millisecond and adjusts the remaining joining cycle to deliver the energy value. Power is a function of resultant force and velocity of the sonotrode vibration, while force is determined by multiplying the cylinder surface area by the sonotrode manometric pressure (i.e., the joining pressure, J_P). Velocity, on the other hand, can be derived from the frequency and amplitude (A_0) [168].

The joining system is capable of applying amplitudes of sonotrode oscillation in the range 1 to 52 µm, joining power can be increased up to 4 kW, joining energy levels can be adjusted between 1 and 10000 J, and joining and clamping pressures between 7 and 552 kPa (1 and 80 psi). After system upgrades, the joining equipment allows for up to 30 seconds of consolidation phase. At this step, the last registered sonotrode position is kept constant for the determined consolidation time. In addition, the specimen can be cooled down after the joining process by blowing a pressurized air stream onto it.

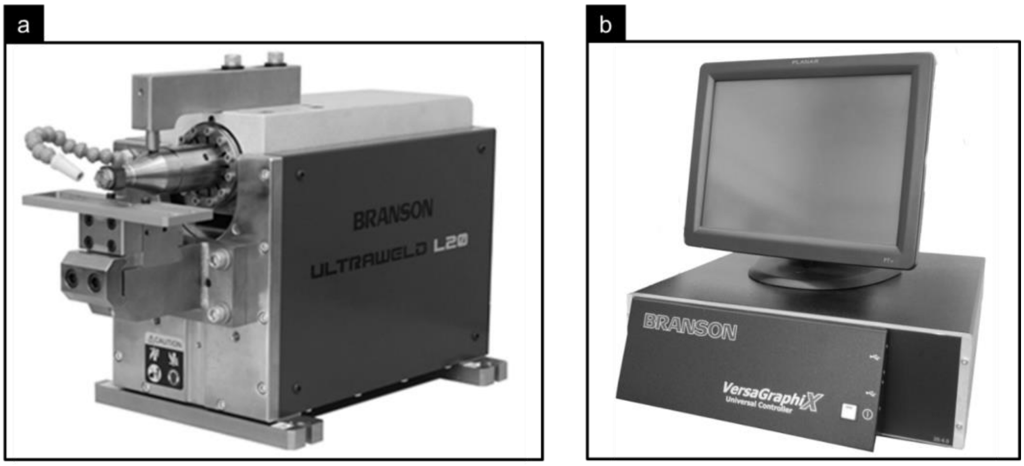

Figure 5-5: (a) Ultraweld L20 equipment, and (b) VersaGraphiX controller.

The joining pressure was mainly set in psi (pound-force per square inch) during the development of this PhD work. However, its conversion to force (newtons) was carried out using a load cell. The resultant calibration curve is presented in Appendix A.2. Although this calibration was carried out for the entire equipment capability range, the U-Joining process is usually performed under low forces. The pressure level used during the development of this work was between 69 and 138 kPa (10 and 20 psi) and this corresponds to joining forces (J_F) in the range 669 and 1147 N. The force-pressure calibration curve is presented in Appendix A.2.

5.2.1 Joining tool

The Ultraweld L20 sonotrode allows for a replaceable tip. So when it is worn it can be easily replaced. This tip is commonly referred as the joining tool in the U-Joining process. The geometry of the joining tool used in this work is presented in Figure 5-6 (a) and a detailed picture of it assembled in Figure 5-6 (b). The tool geometry was conceived during the process feasibility study and has a wavy surface pattern, which is designed to grip the metallic part of the joint, preventing slippage between the joint metallic part and the tool. However, this provides improved wear resistance compared with a knurled pattern, which is typically applied in conventional ultrasonic welding processes. In addition, the wavy pattern avoids the metallic part becoming stuck on sharp edges after sonotrode retraction. The material used to manufacture the tools is made of a maraging steel (UHB Marax ESR steel [169] - DIN 1.6358). This low carbon hardenable martensitic steel was heat-treated after tool machining to reach high hardness values (54 HRC). Subsequently, it underwent a nitriding surface treatment to further improve its wear resistance. The chemical composition of the tool material is presented in Table 5-6.

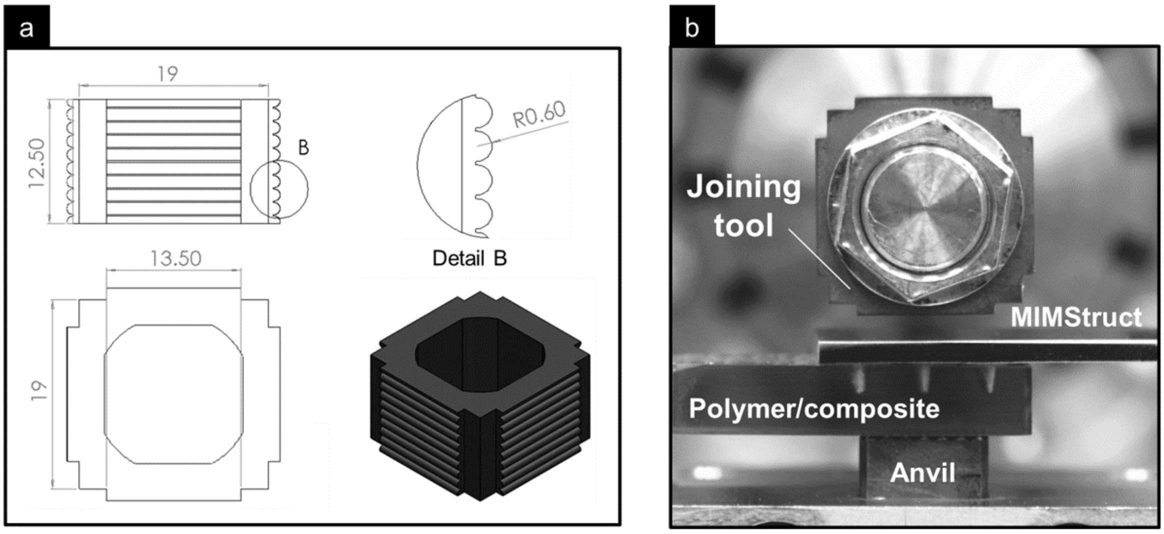

Figure 5-6: (a) Joining tool geometry, and (b) detailed picture of its assembly.

Table 5-6: The chemical composition of joining tool material, UHB Marax ESR [166].

Chemical element	C	Ni	Mo	Co	Ti	Al
%	0.03	18.5	5	9	0.7	0.1

5.2.2 Sample holder

To hold the parts between the joining tool and the anvil a specific sample holder was designed. It consists of two parts: a fixed holder, and an adjustable holder. The composite part of the joint is placed in the fixed holder slot, as shown in Figure 5-7. Then the surface-structured metallic part is placed on top of the composite, with its pin tips in contact with the composite surface. The adjustable section of the sample holder can slide across the fixed holder and thereby adjust the overlap area between the composite and metallic parts. Thus, joints with different pin numbers and overlap areas can be produced, while keeping it well clamped beneath the joining tool. This ensures the pressure applied by the sonotrode is homogeneously distributed over all the surface-structured pins.

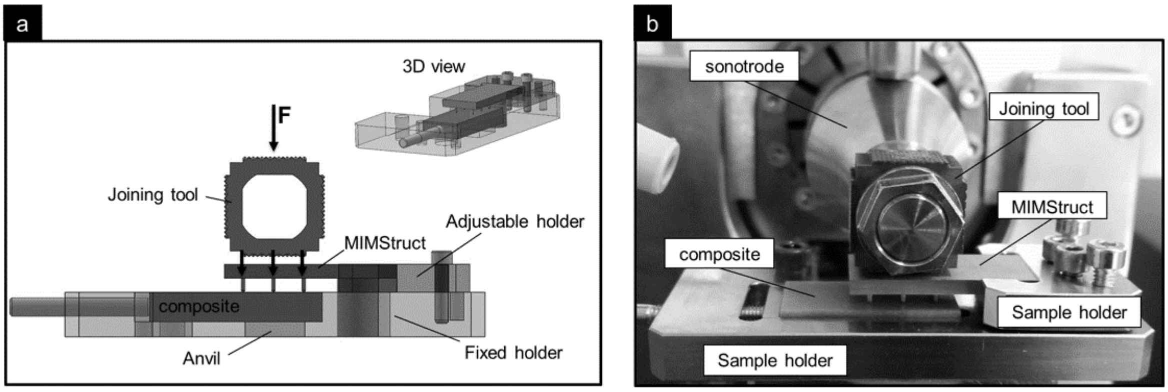

Figure 5-7: (a) Sample holder used to produce the U-Joining joints, and (b) a detailed picture of its assembly in the joining system.

5.3 Methods

5.3.1 Joining procedure

The U-Joining procedure comprises the following steps: Prior to the joining, the Ti-6Al-4V and GF-PEI parts are cleaned in an ethanol ultrasonic bath for 3 minutes and dried in air. After this washing stage, the workpieces are placed in an overlap configuration on the specially designed sample holder (presented in Section 0). The adjustable component of the sample holder aligns the Ti-6Al-4V piece on top of the composite, defining an overlapping area. Next, process parameters E_J, A_0, J_P, and C_P are defined in the VersaGraphiX control unit, and a starting pedal used to start the process. The sonotrode next moves down and applies the preset C_P, which is held for one second. After that, the sonotrode starts to vibrate in a back and forth motion under the defined A_0 and J_P. The joining process is continued until the joining equipment delivers the preset amount of E_J, which usually took less than two seconds in this work. Next, a consolidation phase begins. At this stage, the final sonotrode position is kept constant for 30 seconds, and pressurized air is blown continuously over the joint with a pressure of 0.5 MPa (5.5 bar). This procedure is employed to accommodate any shrinkage of the composite part. It is important to note that the consolidation phase applied in this work was intentionally overestimated to reduce the number of process variables and thereby simplify the experimental investigation. Such overestimated consolidation phase helps to ensure that most shrinkage effects were accommodated within this phase and joint’s temperature is well below the polymer Tg before sonotrode retraction. Finally, the joined materials are removed from the sample holder, labeled and submitted for analysis.

5.3.2 Joint geometry

Customized single lap joints were used for development of the U-Joining process as there was no technical standards available in the literature for this type of hybrid joint. The hybrid joint geometry is presented in Figure 5-8. The joints are through-the-thickness reinforced with six-pins structured on surface of the metallic part, as previously described in Section 5.1.1. The geometry proposed was defined by an injection molding tool available at HZG facilities, which was a first design for preliminary development of the U-Joining process and proof of concept. All the joints produced in this work were first joined according to this geometry, and after joining, specific regions of interest were machined from the joints for further characterization. The joints have an overlap area of 21 mm and dimensions of 15.5 x 49 mm. In addition, the nominal thickness of the overlapping area is 9.35 mm.

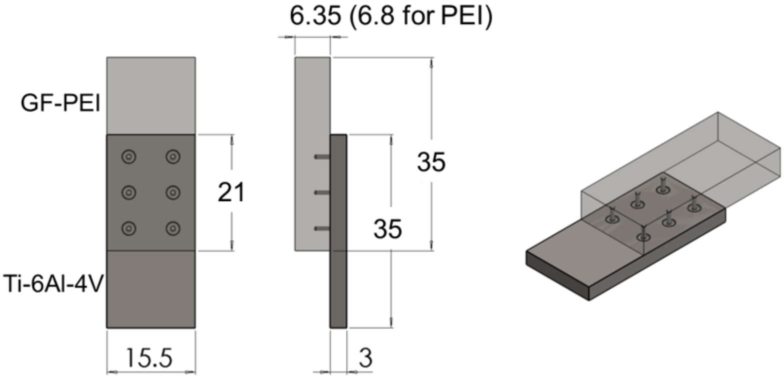

Figure 5-8: U-Joining joint geometry. All dimensions are millimeters.

5.3.3 Joint formation mechanisms

Stop-action joining experiments were performed to assess the formation of the joints in a stepwise manner and the material flow during the joining process. Stop-action studies are usually induced by a forced quick stopping of the joining process at a defined process time or stage. After the forced stopping, the frozen state of the joint is observed, and its microstructural features are characterized. As the U-Joining process was entirely controlled by energy in this work and the operator sets a preset value of joining energy, joints with incremental values of this parameter were produced to create a stop-action effect. Thus, a progression in the delivery of energy could be investigated. In these experiments, the joining parameters A_{0}, C_{P}, and J_{P} were kept constant at 52 µm, 15 psi, and 15 psi, respectively. As a result, an incremental effect in joining cycle time (t) is also achieved, as shown in Table 5-7, as well as the peak power (P) recorded by the joining equipment and sonotrode displacement (Δd).

Table 5-7: Energy levels used for the stop-action experiments.

E_J [J]	P [W]	t [s]	Δd [mm]
400	1740	0.30	0.4
800	1840	0.56	0.8
1200	2040	0.64	2.9
1600	2880	0.86	3.1
2000	2880	1.10	3.2
2400	2540	1.20	3.2

5.3.4 Statistical modeling of joining parameters and process optimization

Design of experiments (DoE) is a statistical tool extensively used to understand, develop and optimize joining processes [19]. It consists of designing experiments or series of tests with a specific structure so that the effects of changes in input variables can be identified from the output response [170]. For example, it is possible to optimize the input variables or factors (i.e., process parameters) to increase the output responses (e.g., mechanical performance).

In the U-Joining process there is a series of process variables, which are used to adjust and control the joining process and these can significantly affect the mechanical properties of the joints produced. Due to the experimental complexity of the system under analysis, the joining experiments were designed according to response surface methodology (RSM). RSM uses a collection of statistical and mathematical techniques to assess the influence of several variables (i.e., process parameters) in a process with proposals for optimizing them [170]. In addition, RSM accounts for changes in the output response caused by interaction between the input variables. In this work, a variant of RSM was used, namely Box-Behnken design of experiments.

5.3.4.1 Box-Behnken design of experiments

Box-Behnken design (BBD) is a tool for multivariable optimization comprised of incomplete three-level factorial designs. In BBD the sample size is kept to a value sufficient for the estimation of second-order polynomial functions [171,172]. Thus offering the maximum efficiency for optimization involving three factors and three levels [173] comparable with central composite design (CCD). An essential feature of BBD is that with experiments under extreme conditions, combining factors at their highest or lowest levels is avoided [174]. This corresponds to an experimental advantage in the case of joining processes, because combinations of process parameters at these levels usually result in extreme operating conditions for joining equipment. The number of experiments required for BBD is defined by Equation 5-2.

$$N = 2k(k-1) + C_0 \tag{5-2}$$

where k is the number of factors and C_0 is the number of replicates at the design central point. In this PhD work, three factors were considered for the DoE, joining energy (E_J), sonotrode oscillation amplitude (A_0), and joining pressure (J_P). In order to simplify the statistical modeling, the factor clamping pressure (C_P) was kept always at the same level as J_P. This meant it could be removed from the experimental investigation. The selected factors were varied on three different levels and three replicates were derived at the central point in order to estimate the experimental error. In total, according to Equation 5-2, 15 runs were performed of the BBD.

The effect of the process parameters mentioned on two responses was investigated, namely joint ultimate lap shear force (ULSF) and lack of penetration (LoP) of the surface-structured reinforcement in the composite. The first response is a parameter measured by single lap shear testing, as described in Section 5.3.10.1, and the second response was measured by a non-destructive test, prior to the lap shear test, using micro-computed tomography, as described in Section 5.3.7.1. Table 5-8 presents the complete set of factors and variation levels investigated in this work.

Table 5-8: BBD factors and their variation levels.

Factors	Symbol	Levels
Joining Energy [J]	E_J	1200, 1800 and 2400
Amplitude [µm]	A_0	32, 42 and 52
Joining pressure [psi / kPa]	J_P	10, 15 and 20 / 69, 103 and 138

The complete matrix of BBD experiments is set out in Table 5-9. Although the tests in this table are presented in sequential order, all runs were adequately randomized before the joining. Thereby ensuring that the observation and errors are independently distributed random variables [170].

The response Y (i.e. ULSF or LoP) is estimated from a non-linear quadratic model as follows:

$$Y = \beta_0 + \beta_1 x_1 + \beta_2 x_2 + \beta_3 x_3 + \beta_{12} x_1 x_2 + \beta_{13} x_1 x_3 + \beta_{23} x_2 x_3 \\ + \beta_{11} x_1^2 + \beta_{22} x_2^2 + \beta_{33} x_3^2 \tag{5-3}$$

where Y is the measured output, β_0 is the intercept, β_1, β_2, and β_3 are linear regression coefficients, β_{12}, β_{12} and, β_{23} are the interactive regression coefficient β_{11}, β_{22} and, β_{33} are quadratic regression coefficients. x_1 , x_2 and x_3 are the normalized factors, coded from factors E_J, A_0 and J_P, respectively [174–176].

Table 5-9: BBD matrix of experiments

Experiment	**Factors**			**Normalized factors**		
	E_J [J]	**A_0 [µm]**	**J_P [psi / bar]**	**E_J**	**A_0**	**J_P**
J1	1200	32	15 / 1.05	-	-	0
J2	2400	32	15 / 1.05	+	-	0
J3	1200	52	15 / 1.05	-	+	0
J4	2400	52	15 / 1.05	+	+	0
J5	1200	42	10 / 0.7	-	0	-
J6	2400	42	10 / 0.7	+	0	-
J7	1200	42	20 / 1.4	-	0	+
J8	2400	42	20 / 1.4	+	0	+
J9	1800	32	10 / 0.7	0	-	-
J10	1800	52	10 / 0.7	0	+	-
J11	1800	32	20 / 1.4	0	-	+
J12	1800	52	20 / 1.4	0	+	+
J13	1800	42	15 / 1.05	0	0	0
J14	1800	42	15 / 1.05	0	0	0
J15	1800	42	15 / 1.05	0	0	0

5.3.4.2 Statistical modeling, optimization, and validation

Multiple regression analysis of the BBD non-linear quadratic model and an analysis of variance (ANOVA) were performed using Minitab software. Backward elimination of insignificant terms in the model was used to obtain a reduced model, without superfluous predictors [170,176]. The procedure consists of starting model evaluation with all predictors and then removing the least significant ones in a stepwise manner based on their p-values. To perform this a removal criterion was set at p-values smaller than 0.05. After each removal step, the adjusted coefficient of determination (R^2_{adj}), and standard error of the regression (S) were recalculated, and their variation was assessed. The model with a combined highest coefficient of determination and lowest standard error was chosen. In addition, residual plots were analyzed to examine goodness of fit of the model and to ensure model adequacy. The reduced regression models obtained were validated using additional experiments. In this respect, five validation points were chosen, and the tests were performed in triplicate. The validation results obtained were then compared against model prediction. In Table 5-10 the validation points are presented.

The resultant BBD quadratic model was optimized for each factor (E_J, A_0, and J_P, or x_1 , x_2 and x_3 in Equation 5-3) to obtain the factor levels that result in the highest ULFS. To do this the stationary point of the quadratic model was found [176]. This point is described by the partial derivatives of x_1 , x_2 and x_3 (i.e., $\frac{\partial \mathrm{ULSF}}{\partial \mathrm{E_J}} = 0$ $\frac{\partial \mathrm{ULSF}}{\partial \mathrm{A_0}} = 0$ and $\frac{\partial \mathrm{ULSF}}{\partial J_P} = 0$). Theoretically, such a stationary point can represent three hypotheses; (i) it can represent a point of maximum response, (ii) a point of minimum, or (iii) a saddle point. To identify the nature of the stationary point, one can simply characterize the surface response and identify the immediate vicinity of the point or perform further mathematical tests [176].

In addition, by fixing the factors at their central point, contour plots were obtained and overlaid to define windows of the process parameters that could satisfy both responses of ULSF and low LoP at a high level.

Table 5-10: BBD validation experiments and optimized condition.

Experiment	E_J [J]	J_P [psi / kPa]	A_0 [µm]	t [s]	Δd [mm]
1	800	15 / 103	52	0.63 ± 0.10	0.66 ± 0.35
2	1200	15 / 103	52	0.78 ± 0.15	2.22 ± 0.64
3	1600	15 / 103	52	0.85 ± 0.07	3.05 ± 0.04
4	2000	15 / 103	52	1.05 ± 0.09	3.12 ± 0.03
5	2400	15 / 103	52	1.24 ± 0.07	3.12 ± 0.04

5.3.5 Process temperature measurement

An accurate measurement of U-Joining process temperature is a somewhat complicated task. This is mostly due to the fact the maximum temperature occurs predominantly at the interface between the materials, which difficult to access. In addition, the polymeric material is in a molten/softened state during joining. This creates a problematic environment for temperature monitoring with thermocouples, as they tend to move during joining. As a result, their measurement positions are usually hard to determine. To overcome these drawbacks, non-contact infrared thermography imaging was used. Such a measurement approach has been widely used for process temperature monitoring during joining, producing reliable results that can be correlated with the microstructural changes, the physical-chemical transformation, and heat input to the process [37,147,177,178]. In this work, the temperature during U-Joining was evaluated at the interface between the MIM-structured pins and GF-PEI upper surface, as schematically shown in Figure 5-9 (a) - (c). For obtaining these measurements, a high-speed infrared thermo-camera model ImageIR® 8300 hp, from Infratec, Germany, was employed, and temperature was measured in the range 150 to 700°C. The IR camera was placed about 0.5 m from the measurement area and tilted 45° (Figure 5-9 (b)) so that the IR camera could record the temperature of all the pins during their insertion in the composite part. A frame rate of 80 Hz was used to acquire thermographs with a resolution of 640 x 512 pixels during the whole process. Figure 5-9 (c) depicts a thermograph of the measurement system at room temperature.

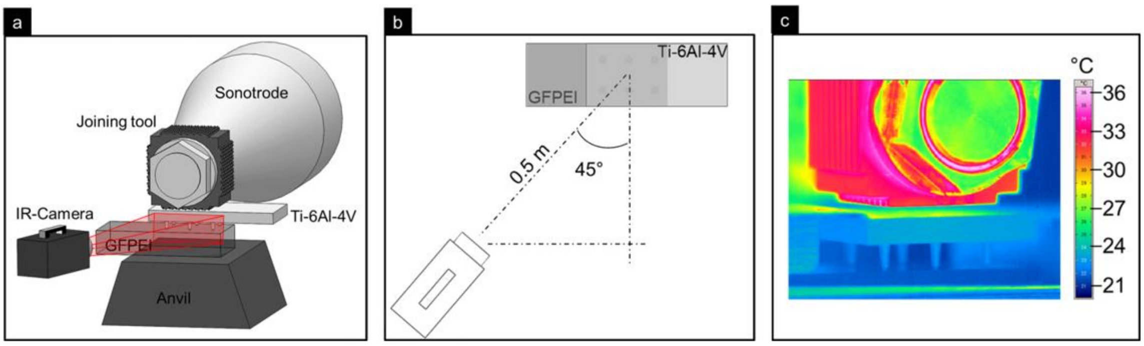

Figure 5-9: (a) Temperature measurement area assessed by infrared thermography, (b) positioning of the IR camera in relation to the joints, and (c) an IR thermograph at room temperature.

5.3.6 Microstructural analysis

Samples for microstructural analysis were cut from the hybrid joints with the cross-sectional cut shown in Figure 5-10. The cross-section samples were mounted, ground, and polished up to 0.05 µm colloidal silica suspension. The Ti-6Al-4V microstructure was revealed with Kroll's reagent (96 mL H_2O, 6 mL HNO_3 and 2 mL HF) and examined by reflected-light optical microscopy (RLOM) using a Leica DM IRM optical microscope (Leica Microsystems, Germany). The microstructural features of the GF-PEI and PEI were assessed using scanning electron microscopy (SEM), using a Quanta^{TM} 650 FEG, from Thermo Fischer Scientific Inc., USA. The measurement was carried out with 10 kV, spot size of 3.5 and working distance of 10 mm, combining secondary and backscattered electrons. Prior to the SEM analysis, the polished samples were gold sputtered using a Q150R ES coating system from Quorum Technologies Ltd., England, with a current of 60 mA for 30 s.

Birefringence patterns of the unreinforced PEI joint were revealed by transmitted-light optical microscopy using crossed polarizers (CP-TLOM) with the same Leica DM IRM microscope mentioned above. For this analysis, the cross-sectioned samples were ground down to about 1 mm thickness and both sides were polished using the same procedure as previously mentioned. Thus, polarized light could be transmitted through the samples, permitting semi-qualitative analysis of the thermal-mechanical stresses induced by the process.

The surface finishing of joints and the surface roughness of as-sintered and HIP Ti-6Al-4V parts were characterized by laser scanning confocal microscopy (LSCM, model VK-9700, Keyence, Japan). Non-contact surface roughness measurement was carried out with a 20x magnification lens and the results processed with VK-Analyzer software, version 3.8.0.0. This software calculates surface texture parameters (i.e., roughness Average - R_a, and mean roughness depth - R_z) according to ISO 4287: 1997 [179].

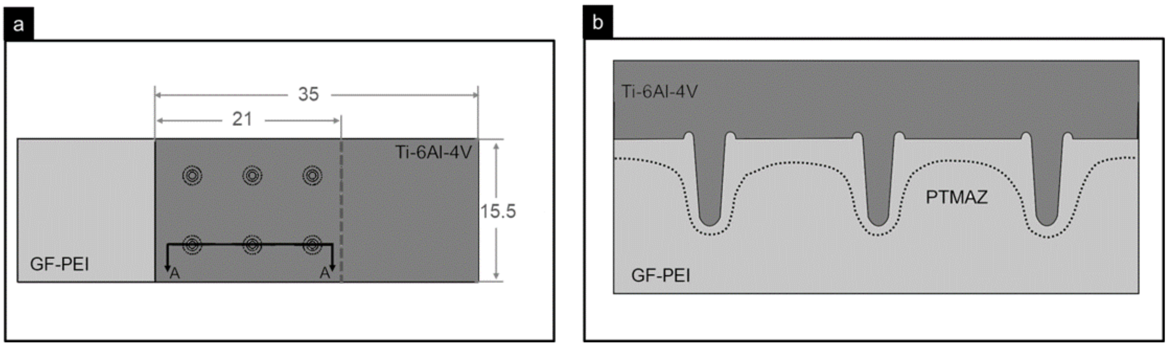

Figure 5-10: (a) Schematic representation of the cross-sectional cut performed to obtain samples for microstructural analysis, and (b) the detail view A.

5.3.7 Non-destructive characterization

5.3.7.1 X-ray micro-computed tomography (µCT)

Prior to mechanical testing, non-destructive micro-computed tomography (µCT) was used to evaluate the integrity of the through-the-thickness reinforcement. The equipment used was a Y.Cougar FeinFocus X-ray system from XYLON International, Germany. The measurement parameters were set as follows: quality scan mode, number of projections equal to 360, integration time 1 second, voltage 65 KV and current 70 µa. The reconstructed µCT 3D models were obtained and analyzed using VGStudio MAX 3.0 software from Volume Graphics, Germany. The metallic part of the joints was segmented by a thresholding approach using the 3D model gray-level histogram.

5.3.7.2 Synchrotron radiation X-ray micro-computed tomography (SR-µCT)

The overlap area of the optimized U-Joining joint was evaluated by SR-µCT to obtain a high-resolution segmentation of its internal features, such as process-induced defects. The experiments were performed by the High Energy Materials Science (HEMS) beamline at PETRA III in Hamburg, Germany [180]. The overlap area of the U-Joining joint (i.e. within the 21 x 15.5 x 9.35 mm samples) was machined from the joints, and their edges were manually ground to produce a cylindrical µCT sample. 3D-volume segmentation, visualization and rendering were performed by the VGStudio MAX 3.0 from Volume Graphics, Germany.

5.3.8 Physical-chemical changes in the polymeric parts

5.3.8.1 Thermal analysis

Process-induced physical-chemical variations in the composite were evaluated by using differential scanning calorimetry (DSC) and thermogravimetric analysis (TGA). Samples were extracted with the aid of a scalpel from the flash material. Although flash formation in U-Joining is relatively small, this volume of material is a good representation of the process-affected region. The influences of the joining process on properties were identified by a comparative study with as-received GF-PEI and PEI materials.

DSC analyses were performed in a heat flux DSC 200 F3 Maia (Netzsch, Germany). Samples of 15 ± 0.1 mg were placed in an Al crucible and submitted to a heating and cooling rate of 10 $K.min^{-1}$ between 30 and 300°C. Two heating and cooling cycles were carried out under an N_2 inert atmosphere, and the mid-point glass transition (T_g) was recorded [181] during the heating cycles. The T_g obtained during the first heating cycle usually reflects the thermal history that the as-received materials underwent during manufacturing (lamination, extrusion for the base materials, and U-Joining). Thus, affecting their property values. However, after the first heating-cooling cycle the manufacturing thermal history is eliminated or substituted by a well-known thermal history. Thus subsequently observed changes in the measured properties can be attributed to the polymer physical-chemical transformation, such as thermal degradation.

The onset of polymer thermal decomposition was identified by TGA. The equipment used was a TG 209 F3 Tarsus from Netzsch, Germany. 15 ± 0.1 mg samples were prepared using the same procedure previously described and placed in alumina crucibles. The samples were submitted to a heating cycle with a heating rate of 20 $K.min^{-1}$ from 30 to 900 °C under an inert N_2 atmosphere.

5.3.8.2 Size-exclusion chromatography (SEC)

SEC is one of the primary analytical methods used to study degradation in polymeric materials. With this technique the polymeric material being studied is completely dissolved in a solution, and its individual molecules are separated by their hydrodynamic volume [182,183]. This separation occurs in a column filled with porous packed beads and based on molecule retention time (i.e., the time needed for a specific size of molecule to pass through the column), and molecular weight distribution diagrams are created. From these diagrams, the average molecular weight (Mw) of a polymer is defined. This property has a significant influence on many of the physical and mechanical properties of the polymer. Hence, the U-Joining thermal effect on the Mw of the joined polymer can be evaluated by comparing the base material’s Mw with that of the material removed from the process-affected zone.

The extraction of material for SEC followed the same procedure described for DSC and TGA analysis. Measurements were performed in triplicate and prior to the injection the samples were diluted in Hexafluoroisopropanol (HFIP) with a concentration of 2500 ppm (mg/g) for 24 h. After complete dissolution, the eluted polymer was filtered through a 0.2 µm

PTFE filter. The column used was two PSS PFG Linear XL (300 x 8 mm and particle size of 7 µm), and injection was performed by a Dionex ASI100 injector assisted by a Gynkotek M300 pump with a flow of 1 ml/min. The collected fraction was examined by refractive index (RI) using an ERMA ERC-7512 ultra-high sensitivity RI detector. The molecular distribution diagrams obtained were calibrated against polymethylmethacrylate (PMMA) standards, also dissolved in HFIP eluent.

5.3.9 Local mechanical properties

5.3.9.1 Microhardness

Vickers's microhardness mapping was applied to assess the mechanical properties of the joined materials at local scales. Thus defining the effect and the extent of the process affected zone. To evaluate changes in the composite matrix, an unreinforced PEI was used, because the fiber reinforcement of the GF-PEI hindered the microhardness indentation. Therefore, hybrid joints with unreinforced PEI were joined using the same optimized process parameters used for the Ti-6Al-4V/GF-PEI joints and cross-sectional samples were obtained as mentioned earlier (Section 5.3.6).

PEI microindentations were performed in accordance with the ASTM E384 [184] using a load of 0.495 N for 15 seconds. The tests were carried out with a Zwick/Roell ZHV microhardness machine equipped with a hardness measuring head and a fully automated x/y table. Eight lines with 100 indentation points were performed. The indentations were separated from each other, within the same line, at a distance of 200 µm and each line was vertically displaced by 500 µm, avoiding any possible border effect. To evaluate PEI local viscoelastic properties, especially in the process-affected zone, the profile of a selected indentation was measured by laser scanning confocal microscopy, using the same equipment previously described in Section 5.3.6.

For hardness mapping of the Ti-6Al-4V parts, 20 lines with 70 indentation points were made with an indentation distance of 300 µm. The indentations were carried out using the same microhardness equipment previously described, and an indentation load of 2 N was applied for 10 seconds. The microhardness experiments were also carried out in accordance with the ASTM E384 standard [184].

5.3.9.2 Nanoindentation

Typically, hardness measurement in fiber-reinforced composites using microhardness results in considerably high variations in the measured properties. Such an outcome is an unavoidable feature of the technique, because the indenter has a relatively large area, which will interact with fibers and the polymer matrix at the same time. Thus, microindentation of fiber-reinforced composites is highly sensitive to regions with different fiber or resin content. This means the average hardness value is usually accompanied by a high standard deviation. To overcome this drawback, nanoindentation experiments were carried out in the process-affected zone of the joints, in order to evaluate the local mechanical properties of the polymer matrix.

The nanoindentation was performed using a Nano indenter® XP from MTS Systems Corporation, USA, equipped with a Berkovich diamond indenter. During the experiments a DCM (dynamic contact module) indenter head was used, which provides improved resolution in both force and displacement and decreases the sensitivity to environmental noise. The DCM indentation head assembly has a displacement resolution of 0.0002 nm and load capability of 10 mN with a resolution of 1 nN. The elastic modulus and hardness were obtained by the continuous stiffness measurement (CSM) method.

Three regions of the joined GF-PEI and PEI materials were selected for measurement, as illustrated in Figure 5-11 (a). Two regions were performed in the polymer thermo-mechanically affected zone (PTMAZ) with one of these close to the central pin (A1) and the other near to the interface (A2). The first area (A1) was positioned 1.5 mm from the parts interface and 50 µm from the pin-polymer interface. The second (A2) was positioned 1.0 mm from the pin undercut and 200 µm from the joint interface. The third area chosen (A3) was placed far from the PTMAZ and used for comparison. Such an area is not affected by the process and presents the base material properties. Lines with 10 indentations separated 10 µm from each other were made in each area in order to obtain statistically reliable measurements.

Thermal-drift corrections were performed for all indentations. This procedure seeks to adjust the measured displacement and accounts for thermal expansion and contraction of the polymer tested and/or the equipment used. To achieve this, close to the end of the indentation tests, the indenter is held at a constant load for 50 seconds. The displacement during this period is associated with thermal expansion or contraction of the material [185]. At this point the drift rate is calculated and the measurements are corrected. The load-displacement curve presented in Figure 5-11 (b) indicates the thermal-drift correction area. The complete measurement parameters used in this work is presented in Table 5-11.

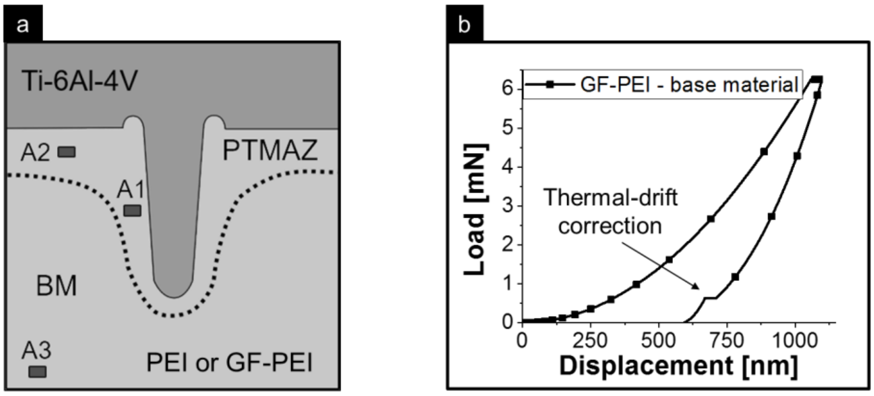

Figure 5-11: (a) Schematic of the indentation position, and (b) an example of a loading-unloading nanoindentation curve obtained for the GF-PEI base material (A3).

Table 5-11: Nanoindentation parameters.

Surface Approach Velocity [nm/s]	**Depth Limit [nm]**	**Strain Rate Target [1/s]**	**Harmonic Displacement Target [nm]**	**Frequency Target [Hz]**	**Surface Approach Distance [nm]**
10	1000	0.05	1	75	1000

5.3.10 Global mechanical properties

5.3.10.1 Single lap shear testing

A customized lap shear test was performed to assess the global mechanical properties of the hybrid joints produced. The single lap shear tests under quasi-static loading were carried out based on ASTM D3163-01 [186]. However, the geometry of the specimens as presented in Figure 5-8 does not follow the recommendation of this standard to accommodate the limitations in size of the available MIM mold. Tests were performed by a Zwick/Roell universal tensile test machine with a load capacity of 100 kN and a constant crosshead speed of 2 mm/min. The clamping area corresponded to 8 x 15.5 mm and the resultant distance between grips was 33 mm.

Linked to the tensile test machine, a GOM digital image correlation system (DIC) was used to assess the local strain field of the joints under loading. During the measurement, trigger signals were sent with an acquisition rate of two pictures per second to a 4 MP camera with a focal length of 50 mm. The complete management of analysis, evaluation of the data, and documentation was performed with the integrated ARAMIS software.

For loading-unloading experiments, selected tests were performed with three loading levels (i.e., 1000, 2000, and 3000 N), using a universal testing machine (Instron 1195) with 50 kN load capacity. Coupled with the testing system, an FOE WS 160 laser extensometer from Fiedler Optoelektronik GmbH, Germany, was employed. In order to create reference points for the laser beam measurement, white stripes were applied on the specimen surface with a gage length of 30 mm. Prior to the load/unload tests, a pre-load of 500 N was used to eliminate any stiffness adjustment due to the grip system and testing equipment.

5.3.10.2 Fatigue experiments

Within the framework of cyclic loading, fatigue tests were performed to evaluate the fatigue limit of the U-Joining joints and obtain the S-N curve. The tests were performed using a servo-hydraulic fatigue test machine with a load capacity of 25 kN in accordance with the ASTM E466 standard [187] with the same geometry of quasi-static single lap joints. In total, 15 specimens were tested with five different loading levels until final failure or until the specimen reached the fatigue endurance limit. This was defined as the load level below which no fatigue failure would occur after $1x10^6$ cycles. The experiments were performed under pure cyclic tension load with a sine-wave loading form, frequency of 5 Hz, and stress ratio of 0.1. To align the specimens in the gripping system, end tabs were machined from aluminum and attached to the grips as illustrated in Figure 5-12. Prior to the fatigue tests, all the screws used to fix the U-Joining specimens within the grip were tightened with a controlled torque of 16 N/m.

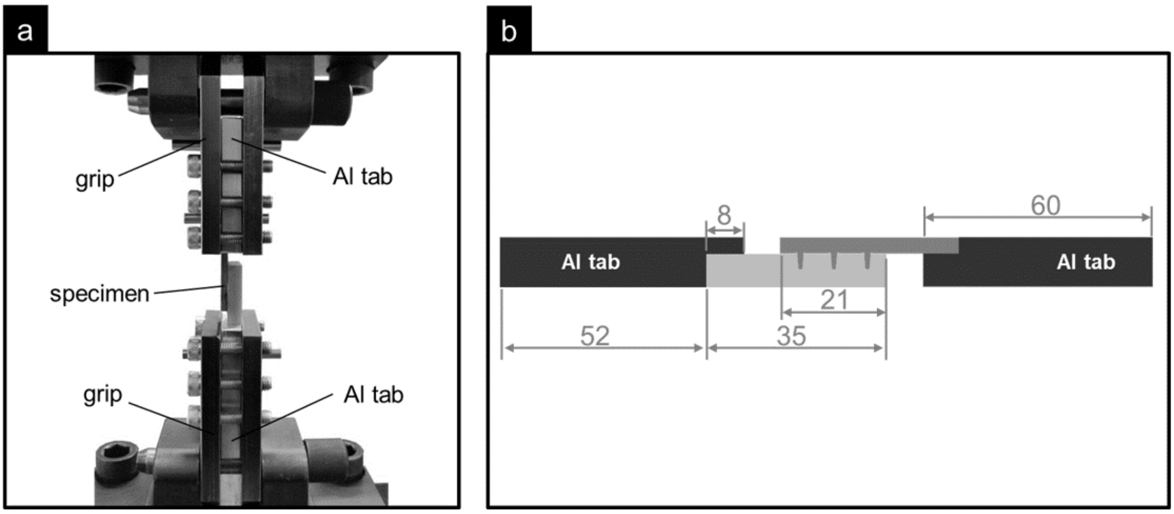

Figure 5-12: (a) Gripping system used during the fatigue test, and (b) schematic representation of the Al tabs used to compensate for the thickness difference between the materials.

The fatigue data were statistically analyzed as recommended by the ASTM E739 standard [188] and a two-parameter Weibull distribution was also applied for statistical analysis of the fatigue data. The specimens that survived the fatigue endurance limit were subsequently tested under quasi-static loading as explained in Section 5.3.10.1., to obtain the joint residual strength after one million cycles of fatigue.

CHAPTER 6. INTRODUCTION TO THE U-JOINING CONCEPT

In this chapter, the new U-Joining concept used for the direct assembly of metal-composite hybrid structures is introduced. This assembly concept was devised, patented [12–15], and further developed during the course of this PhD work. U-Joining, as the previously described direct assembly technologies, is divided into two stages. However, a modified metal injection molding route is used to manufacture the TTR metallic part instead of obtaining it through a surface-structuring phase as earlier described (Section 3.2.1). This alternative route is called MIM-Structuring and it has several advantages compared to other state-of-the-art structuring concepts. After manufacturing of the MIMStruct part the composite is joined to the metallic part. The joining of the consilidated composite or laminate to the surface-structured metal significantly decreases the assembly cycle time, when compared with the assembly methods previously discussed in Section 3.2.2.

To present the fundamentals of the U-Joining concept, this chapter is divided into three sections. Two sections are dedicated to the two stages of the direct assembly concept, firstly the MIM-Structuring process and secondly the assembly (joining) phase. The third section of this chapter briefly discusses the advantages, limitations and potential applications of the concept.

6.1 Surface structuring by metal injection molding: The MIM-Structuring process

As a solution to overcome the typical drawbacks of welding-based structuring techniques previously described, in 2010 a new structuring approach, based on metal injection molding (MIM), was invented and patented by Helmholtz-Zentrum Geesthacht [11]. This process is known as MIM-Structuring and it enables the production of surface-structured metallic parts with excellent dimensional tolerance, surface finishing, and the improved geometrical reproducibility of individual pins. Such advantages are typically observed in an MIM-based manufacturing route [125], because it results in parts with only a variation of between 0.08% to 0.65% in size and from 0.5% to just over 1% in mass [129].

The MIM-Structuring manufacturing route is similar to a conventional MIM process, and its principles are presented in Figure 6-1. First a polymeric binder and atomized metallic powders (1) are mixed and kneaded (2), producing a feedstock (3). The polymeric binder works as a medium for shaping and holding the metallic particles together, adjusting the feedstock viscosity during the injection molding phase (4) [125]. During this phase the feedstock is plasticized inside the injection barrel and subsequently injected into a mold cavity. The mold has a negative, oversized shape of the desired part, which is known as MIMStruct. The oversized geometry, which corresponds to 12% of the final sintered part, is intended to accommodate eventual shrinkage of the MIMStruct part during sintering. After the injection molding phase and demolding, the MIMStruct part is named “green” (5), and it next undergoes a two-stage debinding process to remove the polymeric binder and prepare it for the sintering phase. These debinding methods are known as chemical and thermal debinding (6 and 8, respectively).

The first debinding stage removes with solvents the nonpolar content of the green MIMStruct, which usually consists of paraffin and low molecular weight polymers. These are responsible for improving feedstock flowability inside the injection molding barrel and mold [131]. After this phase, the part is named “brown” (7) and it is ready for thermal debinding. This stage is carried out under a controlled inert atmosphere, and at this point all the remaining polymeric material is removed from the MIMStruct part (8). Finally, the part is sintered, usually in the same furnace where the thermal debinding was carried out, under high vacuum and temperature, which results in a solid and dense surface-structured metallic part (9).

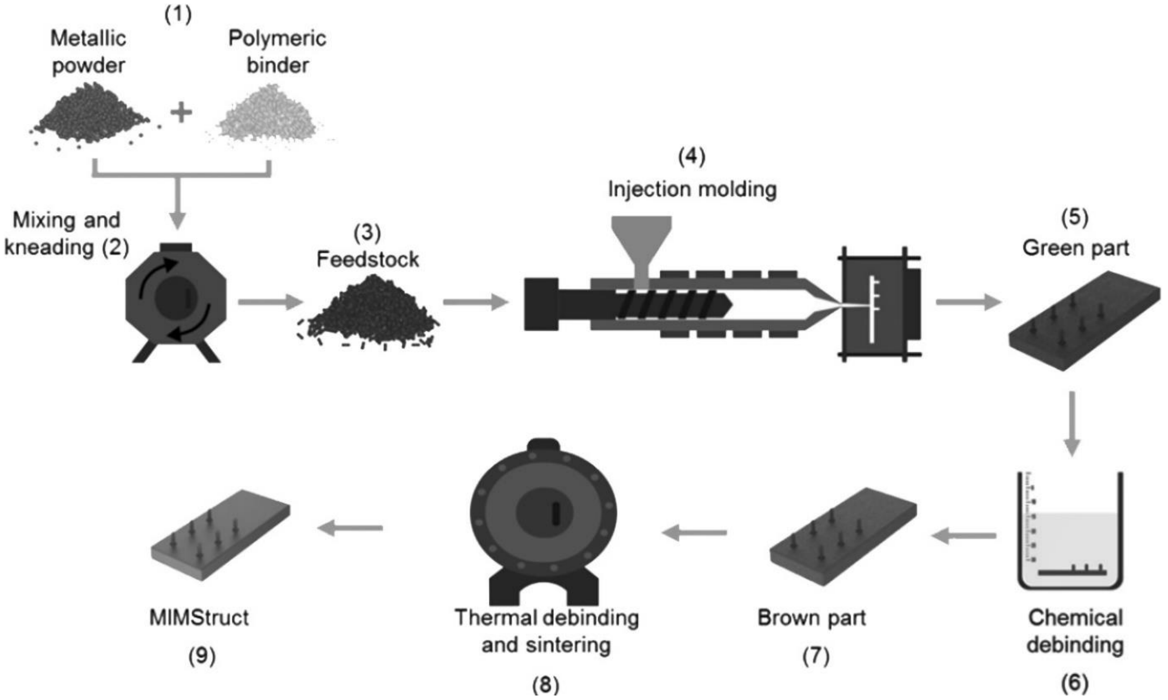

Figure 6-1: Schematic illustration of the MIM-Structuring manufacturing route.

The MIM-Structuring process is applicable to a broad range of metal alloys and considered a near net-shape technique. Thus, in essence no post-treatment is required. However, MIMStruct parts usually have a residual porosity that lies between 2 and 4%, similar to conventional MIM processes [125]. Therefore, if high mechanical performance is required, especially high fatigue strength, a hot-isostatic pressing (HIP) phase may be necessary to remove the residual porosity.

During the MIM-Structuring route, the base materials (i.e., metallic powder and polymeric binder) undergo several process-induced transformations. Figure 6-2 presents the surface morphological changes on the materials during the various MIM-Structuring phases obtained by SEM. The pre-alloyed and gas atomized powder used presents a spherical shape with diameters under 45 µm, as shown in Figure 6-2 (a) and (b). After injection, the spherical powders are held together by the binder medium, Figure 6-2 (c) and (d). It can be observed that the Ti-6Al-4V particles are well mixed with the polymeric binder, forming a homogeneous compressed MIMStruct green part. The binder consists mainly of a mixture of polyethylene-vinyl-acetate and paraffin. The paraffin is removed predominantly during the chemical debinding. As a result, a porous MIMStruct brown part is formed, as presented in Figure 6-2 (e) and (f). Such an open-pore structure allows for the gases formed during the thermal debinding to diffuse out of the part without increasing the internal vapor pressure. This avoids internal cracking of the part during the debinding process [125,131,189].

Figure 6-2 (f) clearly shows that the Ti-6Al-4V particles were exposed after the chemical debinding and that the pore channels were successfully formed for further outflow diffusion of the polyethylene-vinyl-acetate. It is also worth mentioning that the remaining polymer acts successfully as a backbone structure [131,189], holding the particles and maintaining the shape of the part prior to the thermal debinding phase. Owing to the fact that thermal debinding and sintering were carried out in the same furnace in a combined cycle, the morphology features directly after thermal debinding were not obtained. Besides, after thermal debinding the part is expected to be extremely fragile, because the backbone component of the binder is completely removed prior to the onset of sintering.

The SEM morphological features of the as-sintered part are presented in Figure 6-2 (g) and (h). It is possible to note that some spherical particles on the sintered surface present necking growth with adjacent particles. However, in the direction of material thickness, a sufficiently dense material is formed. Generally, in MIM-based processes the surface finish depends on powder size and chemistry, sintering conditions, and post-treatment [125]. The average surface roughness (Ra) measurements of the as-sintered part were relatively high and corresponded to 1.5 ± 0.2 µm, as shown in Figure 6-3 (a). However, high surface roughness has been reported to improve microinterlocking between metal and composite, enhancing the mechanical performance of hybrid joints [190–192]. This surface roughness could be tailored by additional surface processes, for instance smoothed by employing bead blasting or tumbling post-treatment, or further roughened by a sandblasting or chemical etching.

The HIP process does not affect the surface morphology of the Ti-6Al-4V, as observed in the 3D reconstructed images of the HIP MIMStruct part surface in Figure 6-3 (b). However, it tends to virtually remove all sintering-related residual porosity, as previously presented in Figure 5-2. In addition, it closes the open pores present on its surface, as shown by the black arrows in Figure 6-3 (b). The HIP MIMStruct R_a was 1.6 ± 0.2 µm, corresponding statistically to the same value as the as-sintered condition. The same trend was observed for the R_Z values Figure 6-3 (a).

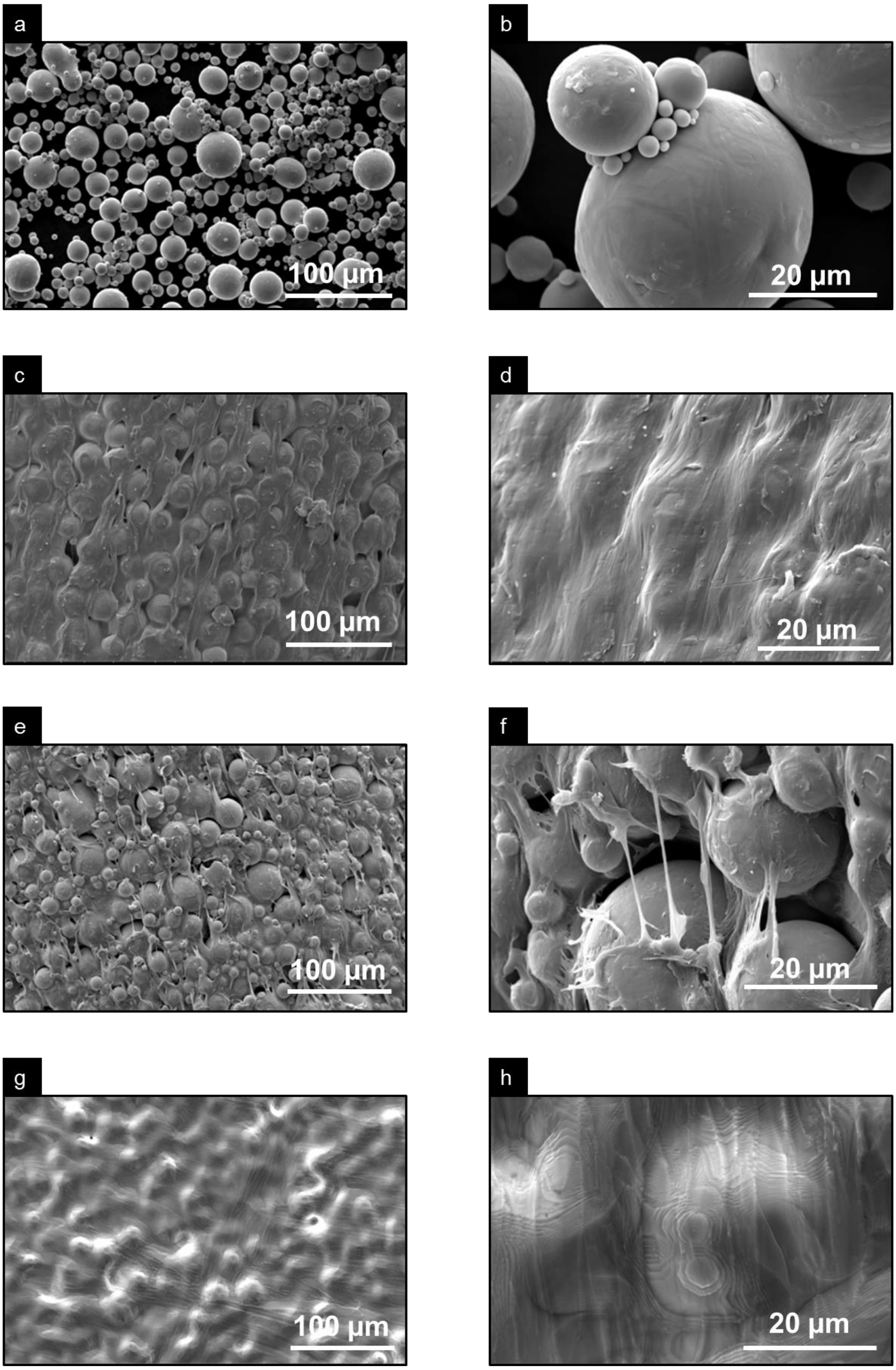

Figure 6-2: SEM surface morphology of the Ti-6Al-4V MIMStruct part during its manufacturing route. (a) Ti-6Al-4V gas-atomized powder particles, (b) detailed view of the spherical particles, (c) MIMStruct green part, (d) detailed view of the green part, (e) MIMStruct brown part, (f) detailed image showing the effect of chemical debinding on the brown part, (g) as-sintered MIMStruct part, and (h) high magnification image of the as-sintered surface.

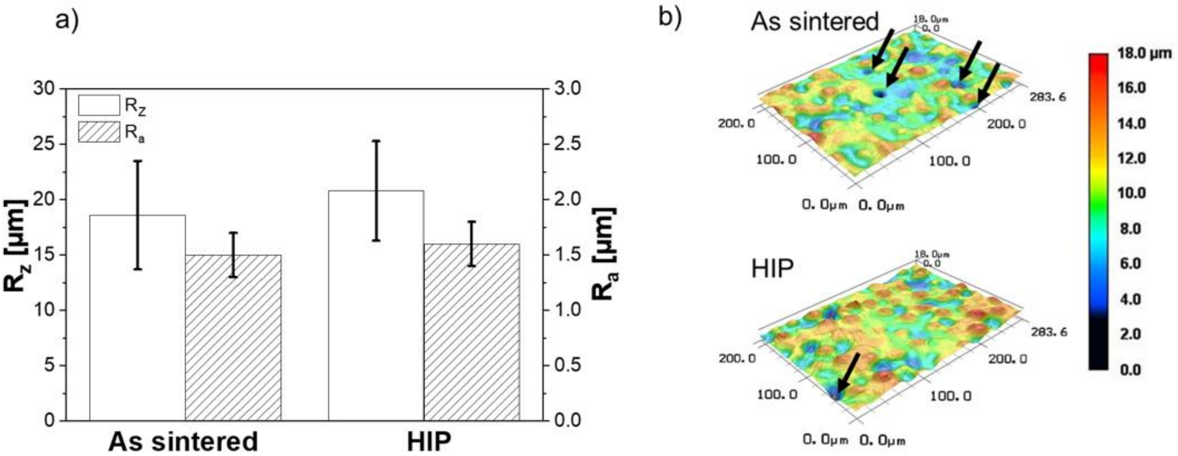

Figure 6-3: Surface roughness measurements of (a) the as-sintered and HIP Ti-6Al-4V parts, and (b) a 3D reconstructed image of the surfaces of the part obtained by LSCM.

6.2 U-Joining-based direct assembly

The application of thermal energy from the joining process as an alternative strategy for the assembly of surface-structured metals to composites has been introduced by the author and collaborators in the course of this PhD work [15,100,193]. U-Joining has the potential to decrease significantly the assembly cycle times of direct assembly hybrid joints, which has represented one of its principal drawbacks. The U-Joining process uses ultrasonic energy to create frictional heat at the material interface and locally melt/soften the polymeric matrix. It therefore allows the surface-structured reinforcement to be inserted within the composite, creating a TTR hybrid joint [100].

The mechanical interlocking provided by TTR works by distributing the load between the materials during service. Hence, it improves the joint’s out-of-plane strength and load capabilities. In addition, the reinforcement increases the toughness of the hybrid joint and has the potential to slow down failure propagation. As a result, it can prevent catastrophic failure from happening in service. In the next sections, the main features of the U-Joining as an alternative assembly method are discussed.

6.2.1 Principles of the assembly process

At the beginning of the assembly process, the joining parts are placed between the anvil and a non-consumable joining tool, as shown in Figure 6-4 (Step 1). The joining tool is attached to the equipment sonotrode and has a specifically designed surface for the purpose of preventing slippage between the metallic part and the tool during joining. When the part is initially positioned the tip of the MIM-structured pins are in contact with the upper surface of the composite. As soon as the sonotrode starts to vibrate (Step 2) frictional heat is created at the interface formed between the pins and composite. The combined effect of frictional heat and pressure applied vertically by the sonotrode locally melts/softens the composite matrix below the pins. As a result, the TTR starts to penetrate the composite (Step 3).

Typically, the ultrasonic vibration is implemented in a back-and-forth motion parallel to the contact surface. However, vertical and torsional vibration could equally well be applied. In the vertical U-Joining variant, the placement of the parts are inverted. Whereby the composite is placed upon the MIM-Structured pins. During the pin insertion phase, a compressed molten flow of polymer forms, as shown in the detailed image of Figure 6-4 (Step 3). This volume of material flows upwards, and when the pins are completely inserted, it wets out the metallic surface, forming a molten polymer layer. Hence, after the consolidation phase, the softened layer solidifies, and the joints are held by two fundamental bonding mechanisms: mechanical interlocking due to the TTR and adhesive forces created by consolidation of the molten or softened layer. In addition, mechanical interlocking at microscale has also been reported [100] at the interface between metal and composite due to the high surface roughness of the MIMStruct part after sintering, as previously shown in Figure 6-3.

The consolidation phase of the joints can be either performed under pressure or not. However, a consolidation cycle under pressure is recommended to compensate for any differential shrinkage of the materials. For instance, in the case of materials used in this PhD work, the composite presents a thermal coefficient of expansion 4.5 times higher than the Ti-6Al-4V (see Table 5-3 and Table 5-4). Thus a consolidation pressure should be applied at last before the composite part reaches temperature levels below its glass-transition temperature. In the final stage of assembly, the sonotrode is retracted (Step 4) and the process ended.

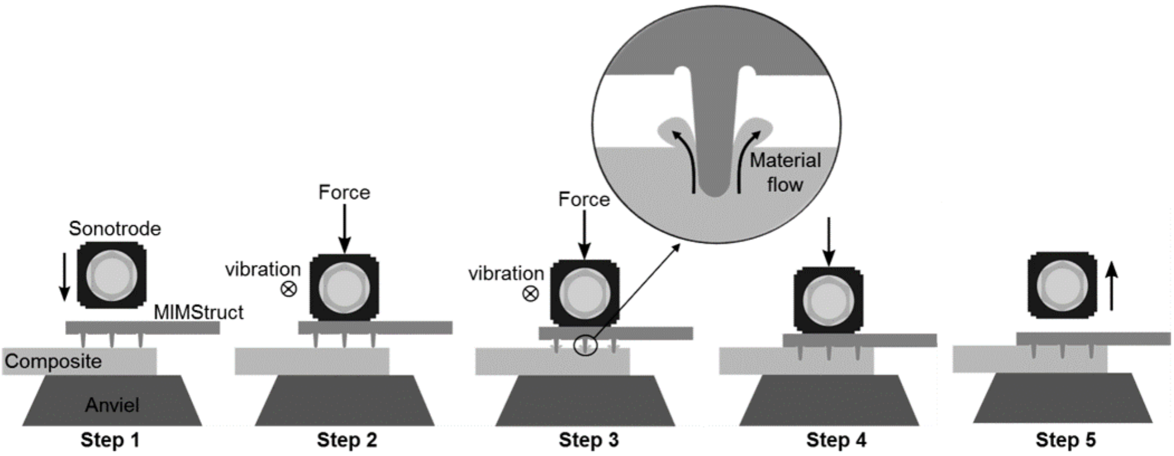

Figure 6-4: Schematic representation U-Joining process steps. The process steps are: (1) placement of joining parts between the sonotrode and anvil, (2) application of ultrasonic vibration and axial force, (3) softening of the composite matrix and onset of pin penetration, (4) consolidation phase, and (5) sonotrode retraction. Adapted from [100].

6.2.2 Process parameters and variables

The U-Joining process parameters play a significant role in joint formation and its resultant mechanical performance. Process parameters depend on the joining equipment used and assembly variant, but are similar to those described for ultrasonic welding of similar metals [194] or thermoplastics [195,196]. The core set of process parameters includes joining energy (E_J), sonotrode oscillation amplitude (A_0), joining pressure (J_p), clamping pressure

(C_p), and joining cycle (t). Additionally, the properties of the materials (such as composite fiber content or mechanical properties of the TTR), thickness, density, geometry and distribution of through-the-thickness reinforcement elements can be expected to have a significant influence on the joining process.

The conventional control modes available for U-Joining depend on the capability of the specific equipment used and may include joining energy, time, collapse distance and peak power. These control modes are selected mainly to control the duration of the applied ultrasonic vibration. The microprocessor-controlled ultrasonic welding machines available on the market permit precise control of joining parameters, usually operating in a "closed-loop" system [196]. This allows the feedback of parameters recorded by the system to adjust the joining parameters during the joining process. For instance, when the U-joining is carried out under energy-controlled mode, the ultrasonic vibration is maintained constant until a preset value of energy is achieved, regardless of the initial settings of other parameters. Likewise, it also occurs when time, preset displacement or peak power modes are chosen; the vibration will be kept constant until a determined preset time, collapse distance or power peak value is achieved during the joining.

Using the energy control mode is the preferred strategy for the development of U-Joining since the E_J is preset by the operator. E_J is directly proportional to the heat generation during joining and can be directly associated with phenomena such as changes in the viscosity and the volume of molten polymer, process-induced defects (e.g., polymer degradation and void formation), as observed in other friction-based joining processes [37,197]. This approach was first chosen for an understanding of U-Joining and was used in this PhD work. In addition, the joining system can easily compensate for surface irregularities arising from the weave of fiber-reinforcement. In this control mode, the energy delivery is steer during joining by the integral of power over time [195,196]. Therefore, the parameter joining cycle is a dependent variable that is automatically adjusted by the joining system to deliver the required amount of preset E_J [194], as previously described in Section 5.2. Since ultrasonic-based joining processes have a very short cycle time, the delivery is integrated over time at each millisecond.

The power required to start and maintain the sonotrode vibration depend on the preset J_P, (normal force applied parallel to the sonotrode vibration), A_0 and dynamic coefficient of friction between the materials. When the energy level integrated by the joining system reaches the specified E_J, sonotrode vibration stops. Some implications can be drawn from the control mechanisms used by the joining system, which is moderated by Equation 5-1, Section 5.2. For a fixed value of setup E_J, the higher the A_0 and J_P, the higher the power required by the system, but the joining cycles are consequently faster. Nonetheless, the product of parameters amplitude A_0 and J_P controls the power required to start and maintain sonotrode oscillation during joining, which affects energy consumption. Moreover, one must take into consideration the stiffness and mechanical properties of the TTR elements when selecting the J_P, in order to avoid their deflection by plastic deformation during joining.

Modern ultrasonic joining and welding systems usually allow for monitoring and recording of several quality variables, such as time, sonotrode displacement and supplied power. These data can be useful for post-joining evaluation, and one could use them for monitoring the production on an industrial scale at ongoing bases, ensuring joint quality and process reproducibility over time.

6.2.3 Process phases

U-Joining can be divided into five phases according to changes of process parameters and heat generation. A typical U-Joining process phase diagram is illustrated in Figure 6-5. Since the process temperatures are usually well below the annealing or phase transformation temperatures of high-strength and heat-resistant lightweight metals, such as α-β titanium alloys, the MIMStruct metal part generally does not undergo any microstructural and metallurgical transformation during the process. Therefore, the physical and chemical transformations involved are typically restricted to the polymeric part.

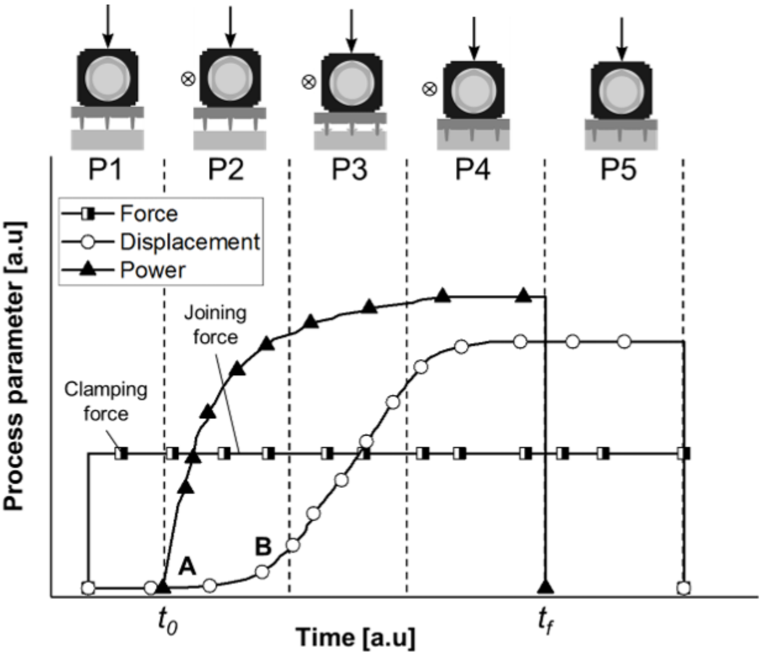

Figure 6-5: U-Joining process phases. P1 - accomplishment of contact between MIMStruct pins and the surface of the composite, P2 - Coulomb friction and unsteady-state viscous dissipation, P3 - steady-state viscous dissipation, P4 - complete pin insertion and creation of adhesion forces at the joint interface, and P5 - joint consolidation.

The heat generation mechanisms during U-Joining can be interpreted based on friction welding theories [198–201]. In the first process phase shown in (Figure 6-5, (P1) the force curve abruptly increases due to the application of normal force, when physical contact between the pin surface and composite is accomplished. In a usual joining procedure, J_F and C_F are kept at the same level, hence the force curve remains constant during subsequent process phases.

Once the sonotrode vibration begins (P2), a rapid increase in the course of the power curve is observed, while sonotrode displacement begins a more gradual increase. At this stage, electrical power is required to start the sonotrode vibration. The primary heat mechanism in this phase, which is believed to last for only fractions of a second due to the high frequency of vibration, is based on the Coulomb or solid friction phenomenon [202,203] (Region A of the displacement curve in P2). In this short period, surface microasperities of both parts are plastically deformed, generating heat, as in other friction-based welding/joining processes [199,204,205], but no detectable sonotrode displacement is usually detected. Moreover, as the matrix of the polymer is a viscoelastic material subjected to sinusoidal strain, energy is also dissipated through intermolecular friction, which can be described by polymer loss modulus (out-of-phase modulus) [206,207]. A combination of these mechanisms will increase the temperature and locally melts a small volume of polymer matrix directly below the pins. The small volume of the molten polymer this creates will accommodate and allow the MIMStruct pins to begin penetrating the composite. Owing to transition from solid to viscous heat dissipation, heat generation becomes unstable, by which the sonotrode displacement (i.e., pins penetration) increases non-linearly with time (Region B of the displacement curve in P2). Therefore, P2 is usually termed the unsteady-state of the viscous dissipation phase [208].

In the third phase (P3) heat generation becomes stable, and a more substantial molten volume of polymer matrix is formed around the vibrating pins. Due to a balance between polymer melting and molten material outflow rates (a squeeze flow of molten polymer is created) it is assumed that heat input and heat outflow are equalized. Accordingly, a steady-state viscous dissipation regime is achieved, which results in a linear displacement of sonotrode. During this phase the heat is generated and maintained by viscous dissipation, resulting from internal sinusoidal straining in the molten polymer. In case of fiber-reinforced polymers, the pins will most likely displace load bearing fibers during insertion. This means some local damage may occur during this phase, as well as the solid friction between pin and fibers. As the insertion depth of the pins increases, vibrational motion of the pins is constrained by the adjacent volume of material. To compensate for this resistance, the ultrasonic joining system needs to increase the electrical power to keep the sonotrode vibration constant, as shown in Figure 6-5 - P3.

By the end of P4, a complete penetration of the pins has been achieved and the metallic surface of the MIMStruct part is partially wetted out by the squeezed molten polymer, completing the joining process and starting the consolidation phase, P5. During this last phase, natural or forced cooling (e.g., forced air) may be applied if required to consolidate the molten polymer. In addition, a holding pressure may be used to compensate for polymer shrinkage. Finally, the sonotrode is retracted from the joint, causing all curves to return to the zero. It is worth emphasizing that the process diagram described in Figure 6-5 corresponds to an idealized joining condition. Therefore alterations to the process parameters, material properties (e.g., the volume of fibers and polymer matrix physical-chemical properties) and geometry, would significantly change the shape of the described curves.

6.2.4 Process variants and design consideration

U-Joining was first demonstrated with parallel vibration (Figure 6-6 (a)), similar to a conventional ultrasonic spot welding of metal [100]. This process variant allows for more efficient transmission of vibrational motion to the material interfaces, assuming an adequate gripping between tool and MIMStruct. In addition, as pointed out by Wagner *et al.* [209] for the conventional ultrasonic spot welding of aluminum sheets to CFRP, parallel oscillation allows for joining between metal and composite to be created without excessively damaging the load-bearing fibers. However, when the metallic surface must be preserved from marks that occur by contact with the joining tool, a perpendicular vibration variant (Figure 6-6 (b)) may be alternatively used. This variant is similar to the conventional polymer ultrasonic welding [210]. In this case, the sonotrode vibration is applied on the surface of polymeric part, perpendicular to the joining area. This means the parts are placed upside down, with MIMStruct on the anvil surface. In this case, the metallic pins of the MIMStruct would act as energy director and the heat generation should still be concentrated at the interface between the tip of the pins and composite. Similar to the first process variant, the ultrasonic vibration could also be applied in a torsional fashion as shown in Figure 6-6 (c). In such process variation, the metallic part is also placed on top of the composite part, with the surface-structured pins in contact with the composite upper surface.

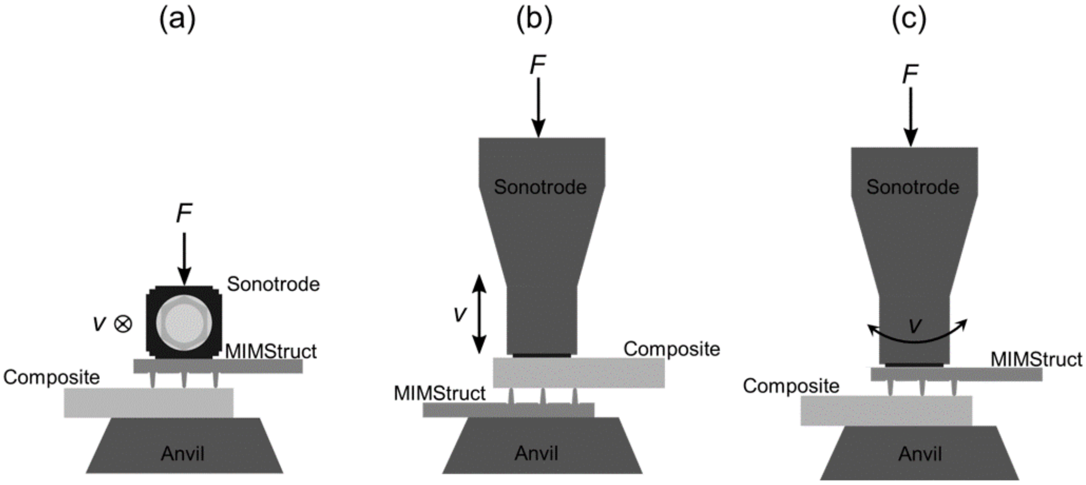

Figure 6-6: U-Joining process variations. Three variants are possible, which differ by the direction of vibration application in relation to the joining area, that is, parallel (a), perpendicular (b) or torsional (c).

The combined effect of mechanical interlocking and adhesion forces increases out-of-plane mechanical properties of the joints. By adding special anchoring features in the shape of protruding pins, such as conical, spherical, convex or arrow-like heads Figure 6-7, the mechanical performance of hybrid joints can be further improved for complex loading modes, as reported in the literature [97]. Thus, based on the application requirement one can tailor the geometry of pins necessarily. However, due to the early development stages of this technology, no design guidelines are so far available for the geometry, density and distribution of the TTR.

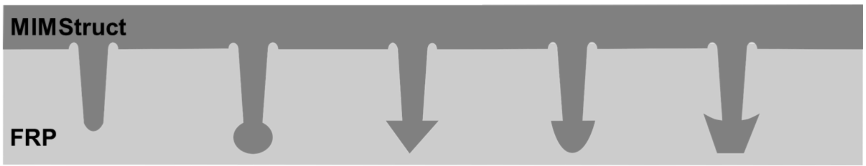

Figure 6-7: Examples of possible reinforcement elements shapes.

6.3 Advantages, limitations, and potential applications

Currently, the main advantages of U-Joining are precise control of heat generation (mainly localized at the pin surroundings), joining is clean and fast (usually joints are assembled in less than 2 s) compared to state-of-the-art composite lamination-based technologies (usually several hours). Therefore, one could expect a decrease in the final assembly costs in comparison with a complicated and time-consuming lamination process. Furthermore, ultrasonic-based joining techniques are extremely energy efficient (i.e., transformation of mechanical work into thermal energy [195,196]), environmentally friendly, safe for the operator (no spatter, sparks or fumes) and have the ability of produce hybrid joints without the use of any solvent, adhesive or additional materials, as well as not requiring any complex surface pre-treatment. After joint consolidation, the pins are anchored in the composite, generating effective bonding mechanisms that redistribute the mechanical stresses imposed during operative loading to the composite part.

In terms of limitations, U-Joining is only suitable for an overlap configuration and is not directly applicable to thermoset-based composites (use of adhesive layer may be required in this condition). Moreover, hybrid joints cannot be disassembled, which may lead to difficulties for their inspection and issues such as sonotrode wear still need to be addressed. With MIM-Structuring limitations related to the injection and sintering phases could be an issue. Both processing phases have limitations regarding part size. In addition, it consists of a multi-stage process and the high initial capital investment can be disadvantageous for the manufacturing of only a few parts. The MIM-Structuring process is therefore more appropriate when large volumes of surface-structured parts are required.

Structures designed for applications in the transportation sector require highly damage-tolerant and crash-resistant connections. Therefore, the U-Joining concept promises to satisfy a wide range of potential applications for hybrid joints in this sector. The examples presented in Figure 6-8 include potential applications for body in white automotive structures, such as hybrid metal-composite B pillars with improved stiffness and crashworthiness, Figure 6-8 (a). Other examples are envisaged, for instance in primary aircraft structural parts, such as hybrid skin stringer components (Figure 6-8 (b)), as well as applications in the infrastructure sector such as metallic connectors in construction or repair of fiber-reinforced polymer structures applied in lightweight roofs and façades (Figure 6-8 (c)).

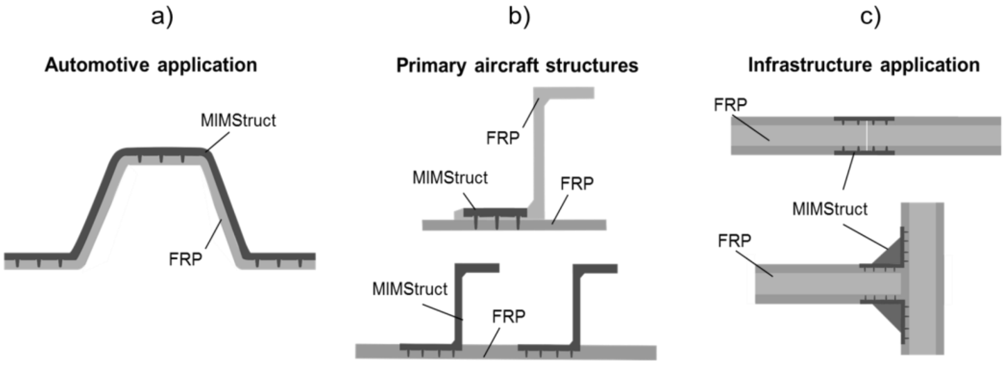

Figure 6-8: Examples of potential applications of the U-Joining concept in the automotive (a), aerospace (b), and infrastructure sectors (c).

CHAPTER 7. JOINT FORMATION MECHANISMS

The U-Joining joint is generally accomplished by applying high-frequency vibration at small amplitudes to the interface of two materials, which softens the thermoplastic composite matrix and allows its penetration by TTR elements. This phenomenon is accompanied by an intensive dissipation of heat generated by friction. In addition, TTR element penetration combined with local high temperatures changes the composite fiber disposition and matrix properties. These phenomena are correlated and happen in a fraction of a second. This means to understand and analyze it in a systematical manner is a somewhat complicated task. In order to achieve that, a stop-action study was carried out and the various process stages were analyzed separately. Thus, in this chapter a stepwise analysis of joint formation during U-Joining is discussed. Moreover, general aspects of the U-Joining joints are described and the correlation between process and heat generation is tackled using the theoretical description previously presented.

7.1 Stepwise formation of a U-Joining joint

To enable a stepwise study of U-Joining joints, nine different joints were produced with an incremental value of preset E_J. Since the joining equipment operates in a closed-loop and adjusts the joining cycle time to deliver a preset value of energy (see description in Section 5.2), it also induces an increment in joining cycle time. Figure 7-1 presents the effect of the joining condition on process variables joining cycle and sonotrode displacement – a quantitative response of pin penetration. Since the process was controlled by energy, a certain threshold of this variable is expected, to ensure the complete penetration of the pins into the composite part. This is achieved with E_J levels between 1600 and 2000 J when keeping the A_0, and J_P, at 52 µm and 15 psi (103 kPa), respectively, Figure 7-1 (a). Such energy amount is required to generate enough heat at the materials interface and thereby decrease the polymeric matrix viscosity, allowing a smooth penetration of the TTR. The heat generation, however, is mostly resultant from the partial energy dissipation through intermolecular friction, as previously described in Section 6.2.3. Although, it is worth mentioning that, part of the energy might be dissipated through friction between joining tool and MIMStruct surface. The parameter levels of A_0 and J_P used correspond to the process parameters used to produce sound joints with above-average mechanical properties (a discussion regarding joining parameters optimization is presented in Chapter 11). It is worth mentioning that changes in these parameters might considerably displace this threshold, since the strain condition to which the composite is subjected plays an essential role in the viscoelastic heating phase [206,207], as previously discussed.

In this respect, for the fixed A_0, and J_P parameters, it is likely that further considerable increases in E_J would not result in improvement to the mechanical properties of the joint, because maximum penetration is already reached. As known from another friction-based joining processes, increases in energy or heat input could lead to higher temperatures inducing, therefore, an increase of process-induced thermal flaws and thermo-mechanical degradation of the polymeric part. Such phenomena have been reported for friction riveting of PEI/aluminum joints [178,211]. However, the maximum temperature recorded by IR thermography (Figure 7-1 (a)) for the U-Joining joints showed that values of E_J above 2000 J appear not to increase the process temperature any further, which stabilizes at values around 550 °C. That occurs due to complete penetration of the pins, which impede the non-contact measurement of temperature during the whole process. Thus, one should take into consideration that this may not refer to the actual maximum temperature experienced by the materials during joining and process-related thermal flaws are still possible to be formed, as it will be discussed in the coming paragraphs.

Figure 7-1 (b) depicts the effect of stop-action experiments on the cross-sectional view of the produced joints. Once again, the effect of energy on the formation of the joints is obvious, the higher the energy for the fixed A_0, and J_P, the higher the penetration of the pins, until a complete pin penetration is achieved. Similar results have also been observed for MIM-structured Ti-6Al-4V and unreinforced PEI joints, joined by U-Joining [193]. In order to better understand the material flow during the formation of joints, the microstructural features of the central pin of the joint were further characterized by SEM and are presented in Figure 7-2.

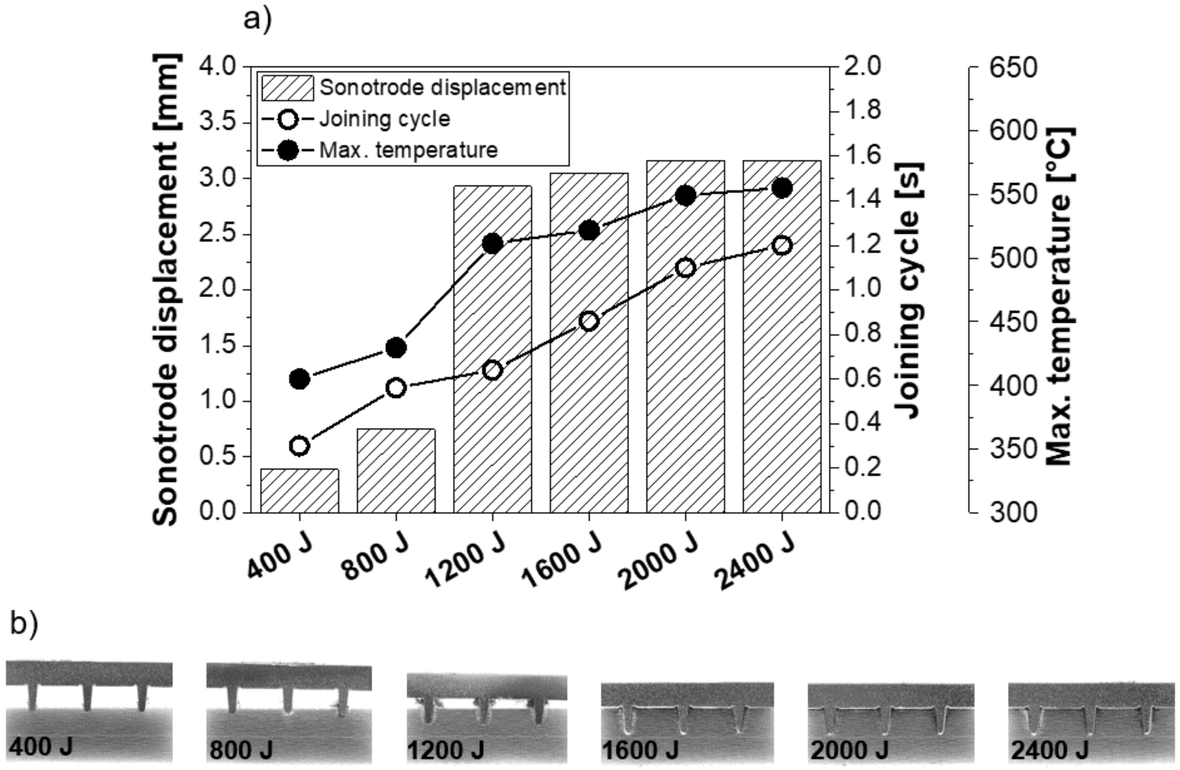

Figure 7-1: (a) Effect of the stop-action study on the U-Joining process variables: joining cycle, sonotrode displacement, and maximum recorded temperature, and (b) photographs of the crossectional view of the joints produced.

Even for very short periods, the joining process can significantly increase the temperature. After delivering only 400 J, which was carried out by the joining system in 0.3 s, the temperature at the interface had already reached 405°C. This temperature is about 190°C above the glass-transition temperature of the composite matrix. Microscopically, it means that this energy level is already high enough to increase the distance between the molecular chains, increasing the free volume of the composite matrix. The consequent thermal activation overcomes the polymer intermolecular bonds and increases the mobility of its molecules [212], in other orders softening the material. The combined effect of pressure and heat created at the pin tips therefore allows the softened polymer matrix to flow upwards, exiting the composite. This outflow of softened material is observed in Figure 7-2, for energy levels between 400 and 1200 J, and in more detail in Figure 7-3.

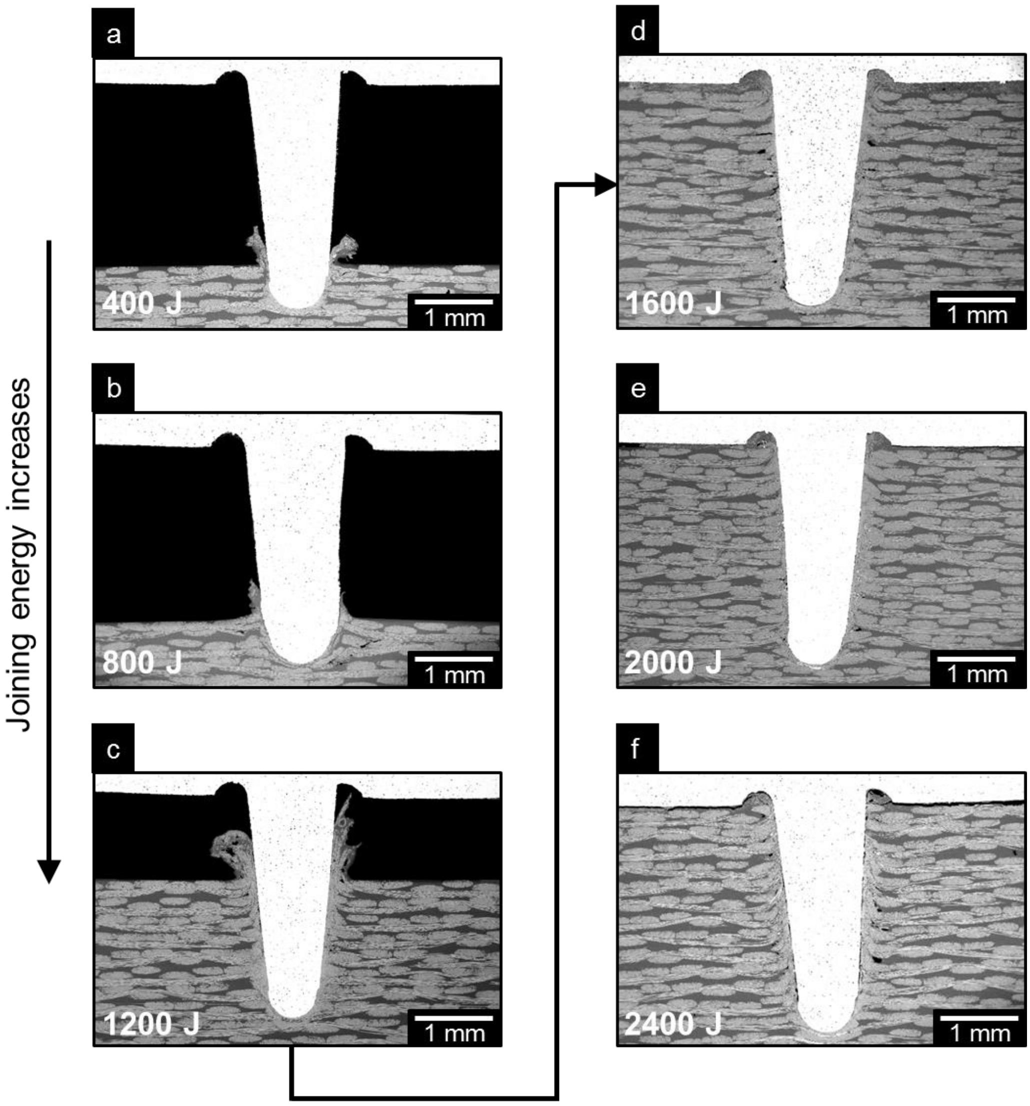

Figure 7-2: SEM micrograph of a stop-action joining of a U-Joining hybrid joint. The images were obtained by backscattered electrons from the central pin of joints produced with 400, 800, 1200, 1600, 2000 and 2400 J of E_J while keeping A_0, and J_P, at 52 µm and 15 psi (1.05 bar or 923 N), respectively.

Apart from affecting the composite matrix physically, due to pin penetration, alterations in the woven glass-fiber distribution are also induced by the U-Joining (Figure 7-4). During the process the pin insertion locally breaks the glass fibers. As a result, small fiber fragments are immersed in the softened polymer outflow, as are observed in Figure 7-3 (b) and Figure 7-4. This occurs because the pressure applied by the sonotrode and local deformation induced by pin insertion is sufficiently high to locally break the fibers. It is believed this process is not intensified by a local increase in temperature, since glass fibers are thermally stable and resistant to the temperature levels recorded by IR thermography. For instance, E-glass fibers have a liquidus temperature between 1065 and 1077 °C and soften between 830 and 860°C, while boron-free E-glass fibers are even more resistant, with a liquidus transition at 1200°C and softening at 916°C [101]. Therefore, fiber breakage is purely induced by plastic deformation.

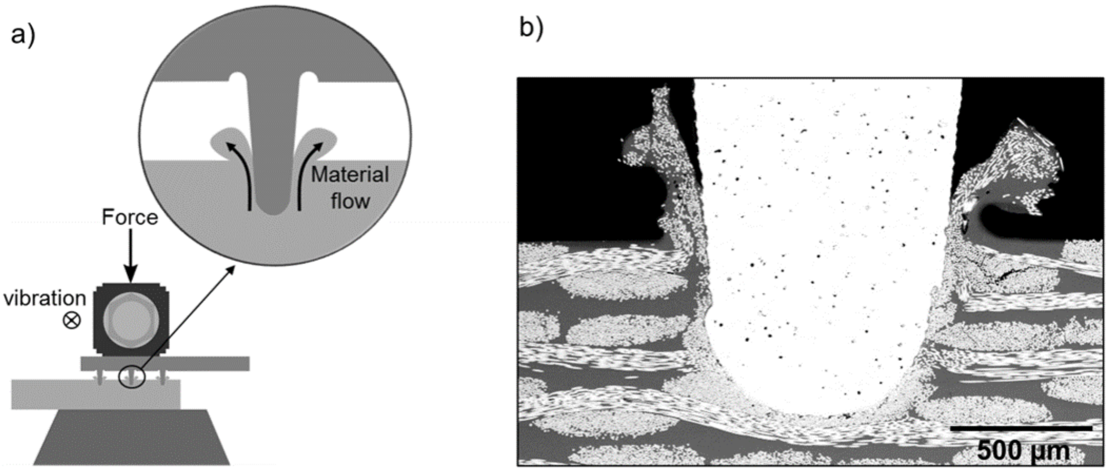

Figure 7-3: (a) Schematic of the material flow during the U-Joining, and (b) SEM micrograph of the softened polymer outflow during the joining process. The joining process was stopped after 800 J of E_J had been delivered.

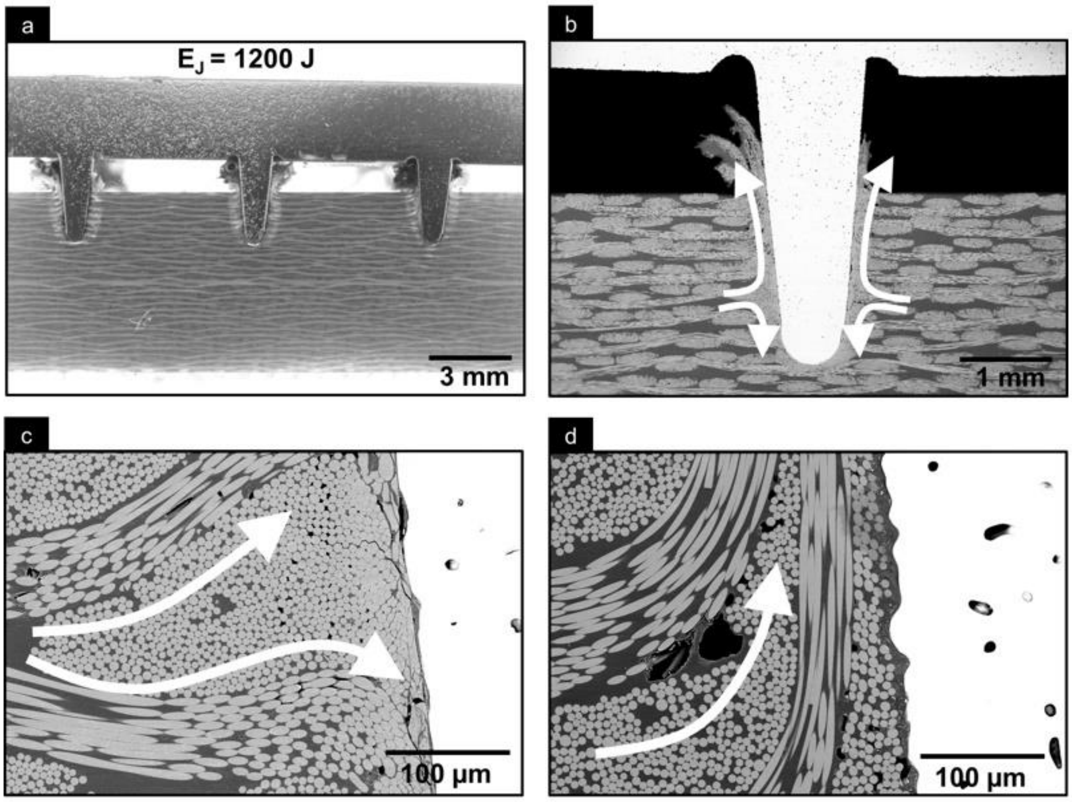

Figure 7-4. SEM micrographs of fiber reorientation due to the pin penetration during the U-Joining. For this analysis, the joining process was stopped after delivered 1200 J of E_J. The image (a) corresponds to a resultant photograph of the cross-sectional view, (b) an SEM micrograph of the central pin, (c) a detailed view, showing the upwards and downwards reorientation of fiber, and (d) a fiber reorientation effect due to the softened polymer outflow close to the interface.

The fiber networking rearrangement during U-Joining (Figure 7-4 (b)) resembles conventional drilling of fiber-reinforced laminate, when peel-up and push-out delamination are typically formed [213,214]. However, owing to the fact that the composite matrix is softened, no composite delamination is preferentially observed, since the volume of material in the pin surroundings has mobility to flow. Thus, instead of creating an internal pressure high enough to exceed the laminate inter-ply bonding strength, which would cause delamination, the fibers of the composite are just broken locally to permit pin insertion and the surrounding polymeric matrix is rearranged.

In this respect, the fiber aligned upwards results from the outflow of molten polymer, as previously mentioned, and the downward orientation is most likely caused by the pressure imposed by pin penetration, Figure 7-4 (c). The downward fiber orientation is believed to be continuously formed during pin penetration. However, as soon as a sufficient volume of softened matrix is formed and this starts to be squeezed out, the broken fibers are reoriented according to the material flow, that is, upwards. The reorientation of the fibers can be so intense that they change their orientation through 90° as shown in Figure 7-4 (d) for regions closed to the surface of the composite.

7.1.1 Primary bonding mechanisms

After complete penetration of the TTR elements (pins) in the composite matrix, two primary bonding mechanisms seems to hold the materials together: (i) macromechanical interlocking and (ii) adhesion forces. Macromechanical interlocking is conceived by the pin penetration, which will redistribute loading through the composite thickness during service. As a result, joint strength is not limited to a thin bonding layer at the material interface, as usually observed in adhesively bonded joints. Figure 7-5 (a) presents a cross-sectional view of a U-Joining joint overlap area obtained by SR-µCT, where the macromechanical interlocking achieved by full pin penetration can be observed.

During joining, when the molten material outflow reaches the composite surface and is compressed by touchdown of the titanium plate’s surface, it tends to flow radially as can be observed in slice b of Figure 7-5 (b). After the joining cycle ends, the metallic plate is wetted out by the squeezed molten polymer. The consolidation of this molten layer leads to the formation of adhesive forces between the metal and composite. Slice b (Figure 7-5 (b)) corresponds to the uppermost part of the composite and has a shape typical of a bonding mechanism based on adhesion forces. Just beneath this area, in slice c (Figure 7-5 (c)), it is possible to observe that heat developed during the process tends to induce the formation of thermal flaws; such process-induced defects will be discussed in detail in Chapter 8.

In slices d and e, which correspond to the half-heights of the pins and tips of the pins, respectively, it can be observed that the volume of process-induced defects is considerably smaller. In addition, pin insertion has not displaced the woven fibers significantly, as is typically observed in other direct assembly approaches, when the composite is laminated onto the surface-structured metallic part and subsequently cured. Such a procedure usually leads to the formation of a resin-rich area around the TTR, which has a lower content of fibers [215]. Thus, in-plane properties of the composite are locally different due to a change in fiber-volume fraction in these regions.

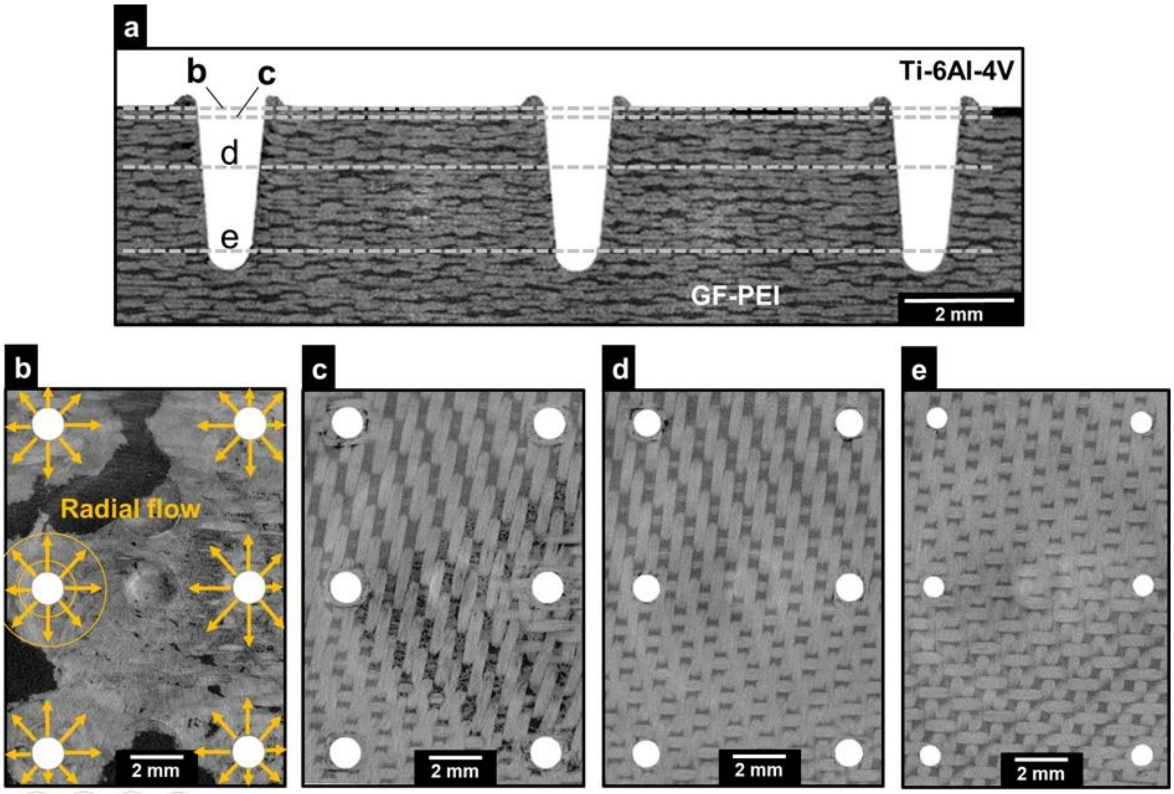

Figure 7-5: (a) Cross-sectional view of the U-Joining joint observed by SR-μCT and schematic representation of top views at different heights (b-e), as indicated in the slices in (a). Thus, (b) depicts a schematic of the radial flow of material during U-joining, (c) typical thermal-induced voids close to the metal-composite interface, and (d) and (e) correspond to top views obtained at half height, and at the tip of the pins, respectively.

Figure 7-6 shows the segmentation of the 3D reconstructed volume of each joint material. The GF-PEI surface again displays the shape of the bonding area, similar to that observed in Figure 7-5 (b). Moreover, it can be seen that the molten polymer filled the pin’s undercut completely (Figure 7-6 (a) identified with a black arrow), especially designed to decrease stress concentration at the base of pins and partially to accommodate the squeezed molten material, increasing the anchoring effect between metal and composite. In addition, a small volume of air was also found trapped between the parts during volume segmentation. This air corresponds to a lack of bonding (LoB) area, as shown in yellow in Figure 7-6 (b). Such an LoB is distributed primarily in the outer regions of the overlap area.

A detailed 3D reconstruction of the Ti-6Al-4V part (Figure 7-6 (c)) confirmed that no pin damage or deflection by plastic deformation was induced during the penetration phase. Therefore, it can be assumed that the state of molten polymer viscosity during joining was low enough to permit a smooth penetration of the pins. Similar results were also observed for joints produced with unreinforced PEI [193], indicating that the woven fiber reinforcement did not hinder pin insertion to any significant extent.

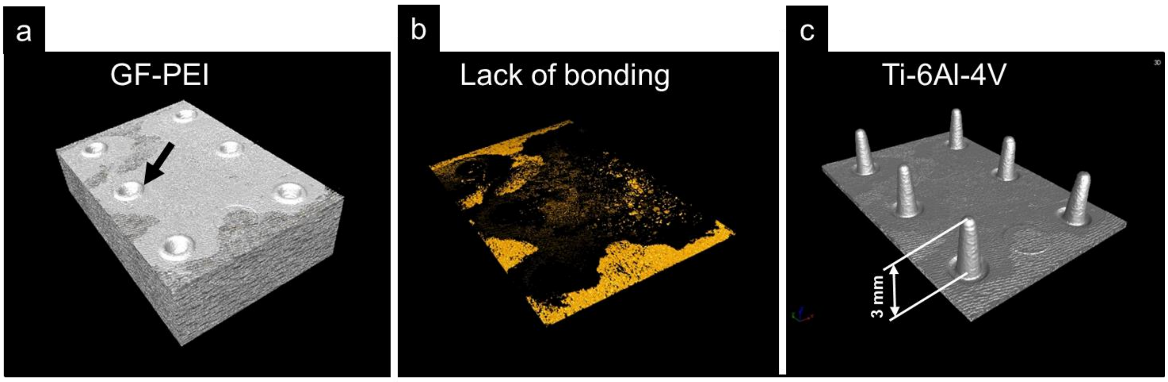

Figure 7-6: Nondestructive evaluation of the U-Joining joint via SR-μCT. Segmented composite part (a), lack of bonding at the joint interface (b), and joint metallic part (c).

7.2 General aspects of the U-Joining joints

When produced by the joining process described here, the typical appearance of a hybrid joint is shown in Figure 7-7. After the consolidation phase, the formation of a small volume of flash around the overlapping area was usually observed. The flash is formed due to touchdown of the MIMStruct on the composite surface (P4, previously described). As was observed during the stop-action study, the thermal-induced process combined with pin penetration creates a softened polymer outflow. When the TTR is completely inserted, the metallic part compresses the volume of molten polymer and part of this volume is squeezed out of the overlapping area. This creates the flash observed. In a U-Joining process, small volumes of flash formed are an excellent indication that the TTR has been completely inserted into the composite part.

The joining process is capable of locally modifying the microstructure and fiber reinforcement of the composite part and its physical properties, as previously observed. However, when the right set of joining parameters are chosen, it does not alter the metallic part's bulk properties, as addressed in Section 8.1.1 . Thus, after joining the pins are completely inserted and their geometrical integrity is preserved, as observed in the X-ray tomography of Figure 7-7. Nonetheless the contact surface between the joining tool and the upper surface of Ti-6Al-4V does undergo local plastic deformation, increasing its surface roughness. This leads to superficial marks on the surface of the metallic part, which are typically observed in the ultrasonic spot welding of metals [216,217].

The surface finish morphology of a U-Joining joint was further evaluated by LSCM, Figure 7-8. These figures may be relevant for future design purposes, such as surface finishing requirements. The marks produced on the surface of the metallic part resemble the tool surface geometry (see Figure 5-6, in Section 5.2.1). It can be observed that the tool penetrates about 0.25 mm into the metal surface (Figure 7-8 (a)). This penetration is indeed required, so that the tool can effectively clamp the metallic part during joining and transmit the sonotrode vibration to the material interface, thereby avoiding slippage between the tool and joint metallic part.

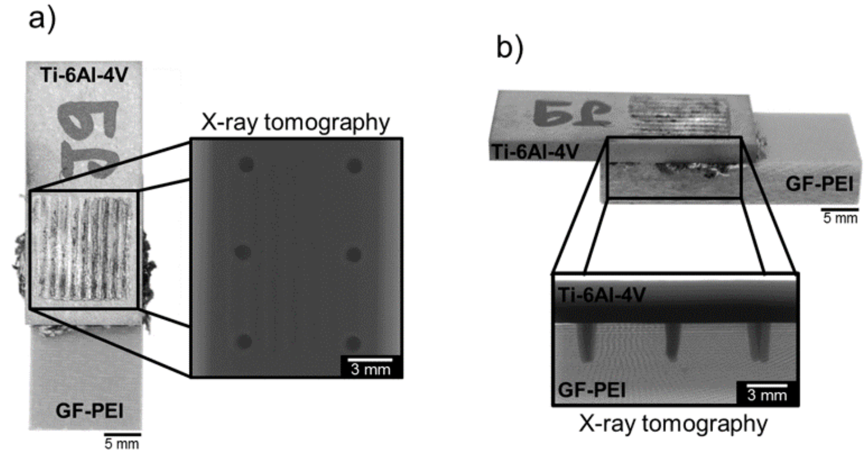

Figure 7-7: General aspects of a U-Joining joint. (a) Top view and (b) lateral view, and their respective x-ray tomography.

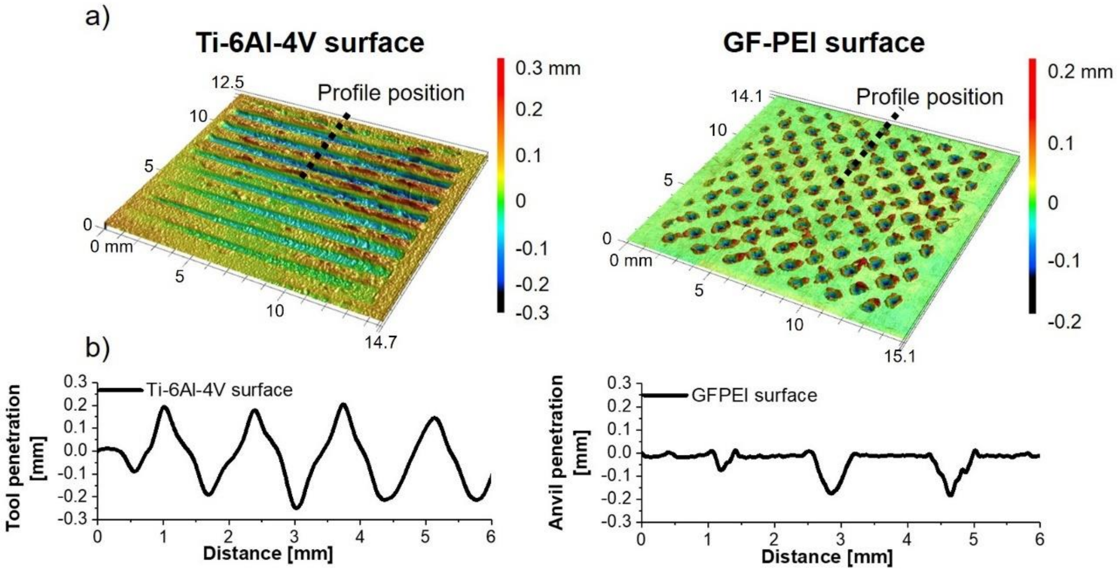

Figure 7-8: LSCM 3D reconstructed images of a joint surface finish obtained by LSCM. (a) Ti-6Al-4V surface and (b) GF-PEI button surface.

In the composite a similar effect is also observed (Figure 7-8 (b)). Due to the axial pressure applied by the sonotrode and transmitted through the metallic part to the composite, it becomes marked by the knurled surface of the anvil. The knurled surface of the anvil has a similar function as the joining tool surface, ensuring that the vibrational motion created by the sonotrode is kept only at the interface between the materials. This is necessary to avoid slippage between the composite part and the anvil. Penetration of the anvil in the composite is less pronounced than the penetration levels observed on the metallic part surface, corresponding to about 0.18 mm.

7.3 Process phases based on heat generation

The U-Joining process phases that have been described theoretically were investigated experimentally. A typical process diagram obtained by combining digital image correlation techniques (DIC) for TTR penetration measurement and IR thermography for temperature recording is presented in Figure 7-9 for a joint produced with optimized joining parameters. Selected measurement points for DIC and IR thermography, marked with stars in the diagram, are presented in Figure 7-10.

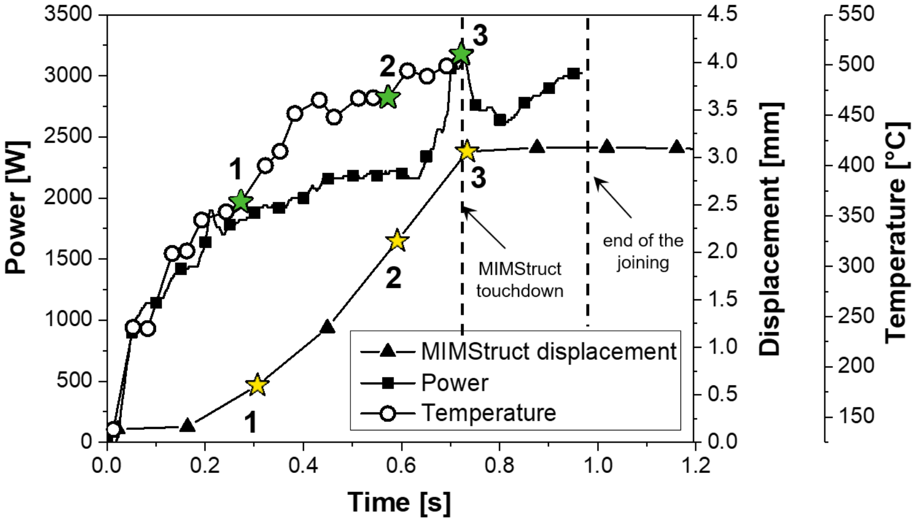

Figure 7-9: U-Joining process diagram obtained for a joint produced with optimized joining parameters: E_J = 2012 J, A_0 = 52 µm, and J_p = 14.7 psi (101 kPa). The power curve is a variable recorded by the joining system, while the MIMStruct displacement was measured by DIC and the temperature was recorded by IR thermography.

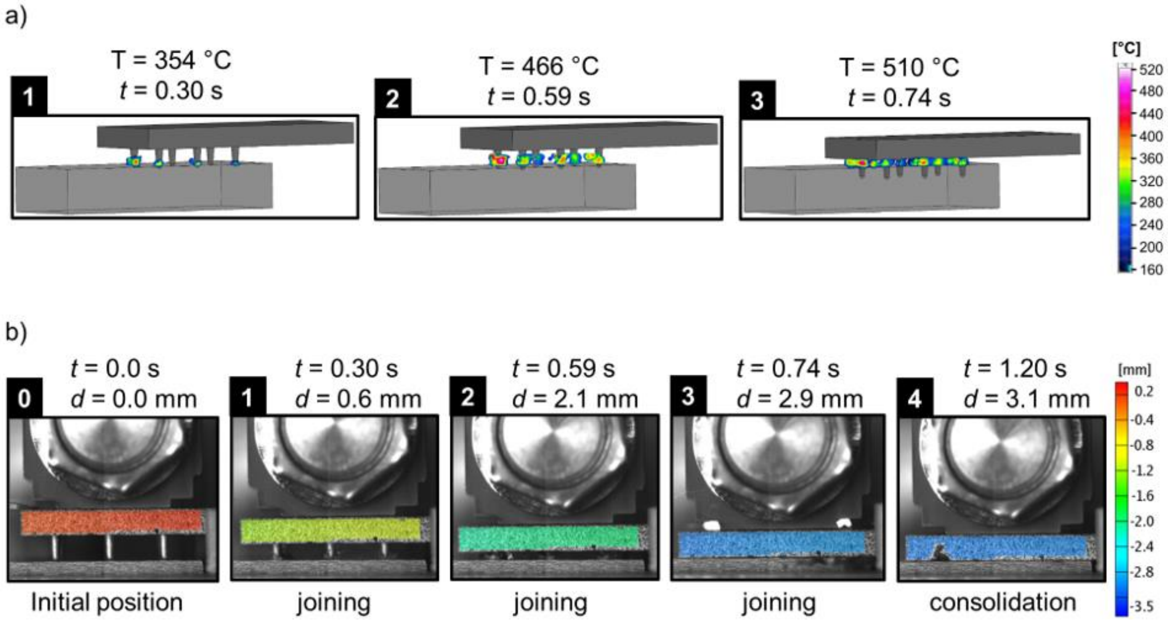

Figure 7-10: (a) Maximum temperature recorded by IR thermography at the interface between Ti-6Al-4V and GF-PEI (marked as green stars, in Figure 7-9), and (b) displacement of the metallic part during the joining procedure obtained by DIC. The images 1, 2 and 3 correspond to the selected points (marked as yellow stars, in Figure 7-9).

At the beginning of the process, high power is required by the joining system to start and maintain the sonotrode vibration. As a result, an abrupt increase in the power curve is observed, Figure 7-9. This phenomenon is accompanied by an abrupt increase of temperature, which after only 0.3 s (green star 1) is already considerably above the glass-transition temperature of the GF-PEI matrix ($T_{0.3s}$ = 354°C and GF-PEI T_g = 214°C), as shown in detail in Figure 7-10 (a). This confirms the assumption that the solid friction phase (compare Region A in P2, Figure 6-5) is extremely short during U-Joining. Indeed, temperatures above T_g were observed even earlier at 0.05 s, although transition from solid to viscous heat dissipation seems to happen at about 0.2 s. At this point, the MIMStruct displacement increases non-linearly with time (previously introduced as the unsteady-state of the viscous dissipation phase). Temperatures above the polymer T_g are required during the U-Joining since above that interchain slippage does not require high stresses [218]. As a result, the molten polymer flows easily and allows the TTR to penetrate the composite smoothly.

After 0.3 s of the process (yellow star 1), the MIMStruct pin penetration follows a quasi-linear displacement. At this joining cycle time, the heat generation becomes stable; it is believed that polymer melting and molten material outflow rates are equalized. Interestingly, the power required by the system keeps increasing. That is most probably caused by the vibrational constraint of the MIMStruct part increasing with the penetration of the pins. As the pins are inserted there is a loss of vibrational freedom due to the adjacent volume of composite material and consequently more power is required by the joining system to keep the vibration at the constant frequency of 20 kHz.

At approximately 0.74s, a peak of power is observed in the process diagram in Figure 7-9. This indicates that the MIMStruct touched the composite surface (yellow star 3). This also corresponds to the cut-off point for temperature recording by the IR camera, which happened at around 510 °C (green star 3) for this joining experiment. After the power has experienced its peak, the curve tends to decrease slightly. A possible explanation for this phenomenon may be correlated with melting of extra composite material at the interface, which might decrease the viscosity of the composite surface. Thus, it facilitates the vibration of the MIMStruct and, therefore, less power is required. Although it lasts a very short period and subsequently it returns to increase, following the same trend as previously experienced. It is worth noticing that almost no displacement of the MIMStruct is observed in this transition, corresponding to only 0.2 mm, as shown in Figure 7-10 (b), between Step 3 and 4.

The joining process lasted 0.98 s in the joining experiment discussed here. After the system has delivered 2000 J of pre-set $E_{J,}$ the consolidation phase starts. At this stage the sonotrode touchdown position was kept constant for 30 s as discussed in Chapter 11. During sonotrode retraction, no displacement was measured by the DIC. Hence, the final position of the MIMStruct corresponds to 3.1 mm, Figure 7-10 (b).

CHAPTER 8. HYBRID JOINT MICROSTRUCTURAL FEATURES AND LOCAL PROPERTIES

A thermo-mechanical-activated joining process usually results in a considerable transformation of the materials involved in terms of microstructure and local physical-chemical properties. In the case of a metal-composite hybrid joint, the polymeric part tends to undergo severe microstructural changes, due to its lower thermal resistance in comparison with most metals. U-Joining joints also follow this trend. This chapter is devoted to understand the process-induced changes in the joint materials and local mechanical properties. The knowledge generated in this chapter support the evaluation of the global hybrid joint properties in Chapter 9. The chapter starts with a description of the MIM Ti-6Al-4V part's microstructure, due to its lesser complexity, and this is followed by the process-affected zone of the composite part. Local changes in the mechanical properties induced by the process on micro and nano scales are subsequently presented and discussed. These discussions are supported by a physical-chemical characterization – i.e., glass transition temperature and molecular weight - of the polyetherimide part. To evaluate the properties mentioned, the joints produced with optimized parameters were used (the optimization procedure is discussed in Chapter 11). To conclude the chapter, common defects in the U-Joining joint are also briefly presented.

8.1 Microstructural zones

8.1.1 Microstructure of the joined Ti-6Al-4V part

Ti-6Al-4V alloys are widely applied in the transportation sector, mainly due to their high specific strength and excellent mechanical properties at high temperatures [164,219,220]. As previously mentioned its $\alpha \longrightarrow \beta$ transition phase occurs at 995 ± 15°C and liquidus transition at 1650°C [164].

In Figure 8-1 the microstructure of the joined MIM-structured Ti-6Al-4V part is presented. As was expected, the joint metallic part does not undergo any visual microstructural changes due to the relatively low process temperatures, which were well below those related to Ti-6Al-4V phase transformation. In addition, no significant changes were observed in its α colony size, distribution, and volume of pores, which remained similar to the as-delivered base material, previously presented in Figure 5-2 (a). Three representative microstructure images of this behavior, obtained from different thickness depths, are presented in Figure 8-1 (b) to (d).

Even the microstructure at the tip of the pin (Figure 8-1 (d)), where frictional heat development is expected to be most intense, remained unchanged. It can therefore be assumed that the temperature during joining, combined with axial pressure, was not severe enough to induce metallurgical and microstructural transformation in the MIM-Structured Ti-6Al-4V part. Hence, it indicates that the actual process temperature did not greatly exceed the 511 ± 3°C temperature level that was recorded by the IR thermography system during joining with optimized process parameters.

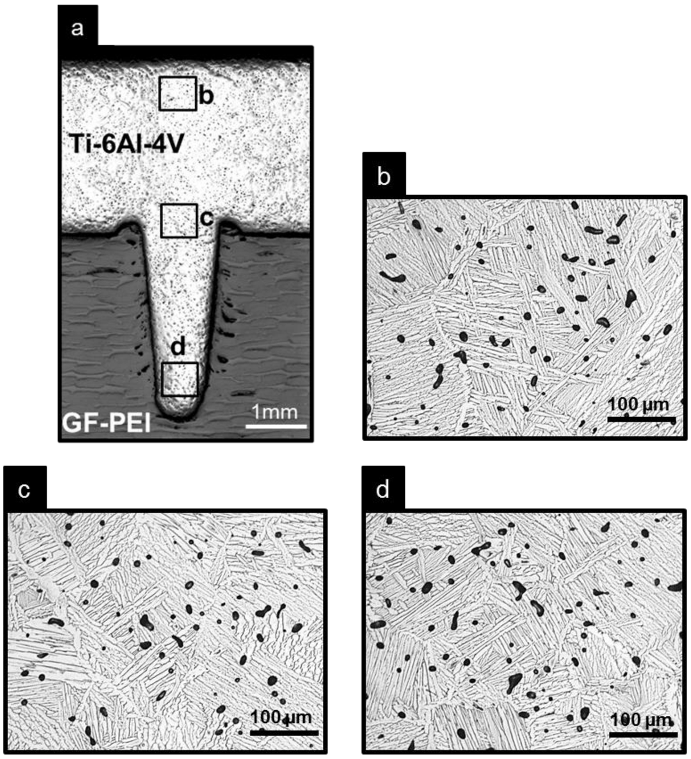

Figure 8-1: Microstructure of the MIM-structured Ti-6Al-4V part after U-Joining obtained by RLOM, where (a) corresponds to an overview of a through-the-thickness reinforcement element, and (b), (c) and (d) are microstructure images from the Ti-6Al-4V part at different thickness depths indicated in (a).

8.1.2 Microstructure of the joined GF-PEI part

Figure 8-2 presents the microstructural features of a U-Joining joint. Typically, the matrix of PEI composite is characterized by outstanding mechanical strength and thermal stability [139,141,221]. However, the heat and strain rate associated with the pin insertion and ultrasonic vibration inevitably created a process-affected region in the composite part of the joint. This region is referred to as the composite thermo-mechanically affected zone (CTMAZ).

The CTMAZ is a thin layer formed at the joint interface and distributed around the pins, as schematically illustrated in Figure 8-2 (b), whose shape is strongly influenced by the joining parameters. Such a zone is visually characterized by its softening and reconsolidation and a mixture of polymer matrix with pieces of broken fiber, which are formed during the steady-state viscous dissipation phase, P4. During this phase, broken fibers are embedded in the molten polymer and this flows upwards filling the undercuts of the pins (Figure 8-2 (c)). After complete penetration of the pins, part of the CTMAZ glass-fiber weave becomes reoriented upwards from its original plane, (Figure 8-2 (d)). Internal flaws could be found in the CTMAZ, which consists primarily of voids (as indicated by the white arrows in Figure 8-2 (c) and (d)) and local composite delamination (as indicated by the white arrows in Figure 8-2 (e)).

These process-induced voids might be related to gas evolution from polymer matrix thermal degradation – to be addressed in Section 8.2.4 - or with entrapped air bubbles in the viscous softened polymer and structural water evolution, as is typically seen in other metal-polymer joining processes [37,42,191]. The composite delamination may be a result of the significant differences between Ti-6Al-4V and GF-PEI thermal expansion coefficients. Such defects were observed primarily close to the interface of the parts and they are believed to be formed during the consolidation phase, because no evidence of them was found during the stepwise analysis of the formation of joints, as previously presented in Section 7.1.

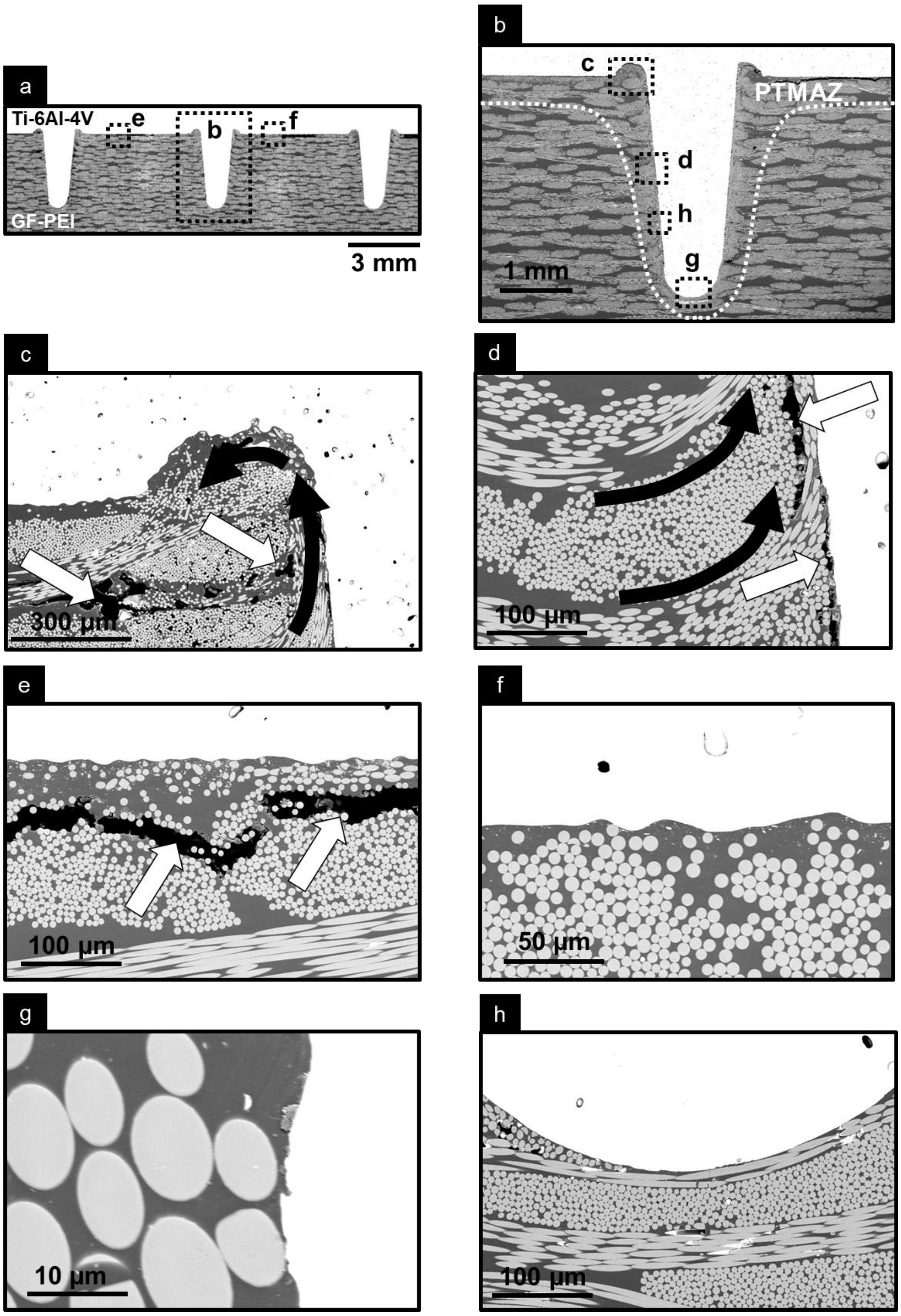

Figure 8-2: Microstructural characterization of an optimized U-Joining joint. (a) cross-sectional overview of the overlap area obtained by SR-µCT, and (b-h) SEM micrographs: (c) of the central pin showing fiber reorientation due to the upwards molten flow, (d) undercut filling and formation of thermal-induced voids, (e) localized composite delamination, (f) close contact between metal and composite at the interface, (g) interface quality between pin and composite, and (h) at the tip of the pin. Joining conditions: E_J = 2012 J, A_0 = 52 µm, and J_p = 14.7 psi (101 kPa).

Apart from the formation of few thermal flaws in the CTMAZ, confined to small regions close to the pins, a very close contact between the composite and metal was observed all over the interface (Figure 8-2 (f) – (h)). The softened polymer tends to fill asperities distributed over the Ti-6Al-4V surface and pins (Figure 8-2 (g) and (h), respectively). Consequently, a mechanical interlocking mechanism on the microscale is achieved, which can positively contribute to the bonding resistance, and thereby increase the out-of-plane mechanical properties of joints. After joining it was also observed that the pin tip is in close contact with composite fiber weave (Figure 8-2 (h)), indicating that the consolidation phase was mostly efficient in compensating for differential shrinkage between the molten polymer and metal.

The presence and distribution of the flaws mentioned are undesirable in U-Joining joints and should be kept to the lowest possible level as they can directly affect a joint's mechanical performance, especially under cyclic loading. In order to characterize three-dimensionally the presence and distribution of thermal-induced voids, synchrotron radiation X-ray µCT was applied. Figure 8-3 displays a 3D reconstructed image of a pin area.

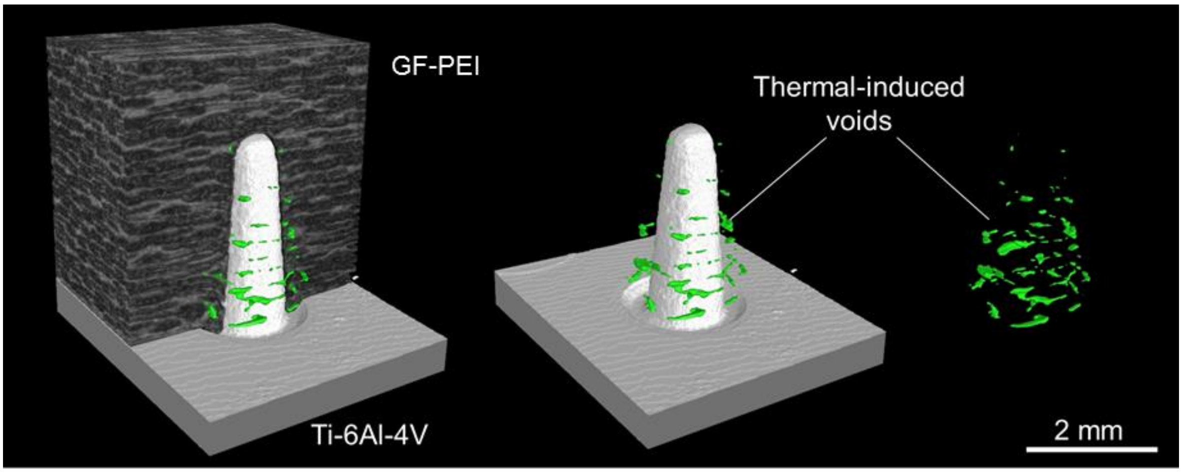

Figure 8-3: Nondestructive evaluation via SR-µCT of the thermal-induced voids formed in the CTMAZ of the U-Joining joint that was joined with optimized joining parameters (E_J = 2012 J, A_0 = 52 µm, and J_p = 14.7 psi (101 kPa).

The thermal-induced voids were found distributed mainly around the pins, owing to the fact that a pin acts as an ultrasonic energy director and heat generation is concentrated in this area. In order to visualize the voids their volume was separated from the joint and a green filter was applied, Figure 8-3. It can be observed that the voids have differences in shape and size, and some of them seem to be connected, in agreement with the previously presented SEM micrograph Figure 8-2 (d). This occurs because during the process the voids in the softened volume are mobile [218]. Due to the squeezed flow they tend to merge to form larger voids, being distributed mainly around the base of the pins, as observed by the segmented volume. Such a phenomenon was also systematically observed around the other pins.

Fiber breakage, reorientation, and thermal-induced defects are clearly observed by SEM and SR-µCT in the CTMAZ, as previously presented. However, how the joining process affects the polymer matrix and the extent of this effect is not easily observed by these characterization techniques. Therefore, to preliminarily evaluate the changes in the polymeric matrix, joints produced with the same joining parameters were performed using unreinforced PEI as the joint polymeric part. PEI is transparent to visible light and has birefringence properties. Thus, any changes to the birefringence pattern that are induced by the joining process can be assessed under transmitted light with crossed polarizers. This was done to support an understanding of the microstructural changes in the CTMAZ. A similar approach was adopted by Abibe [198] to qualitatively evaluated the residual stress in the plastically deformed zone (PDZ) of Friction-based Injection Clinching Joining (F-ICJ) of a hybrid joint of PEI and AA6082 aluminum alloy. In this work [198] compressive deformation imposed by the joining tool in the F-ICJ process made changes to the fringe order density close to the PDZ, which is directly comparable with an increase in residual stress.

Birefringence patterns are formed due to the separation of polarized light into two wave fronts oriented parallel to the principal stresses σ_1 and σ_2, assuming plane stress ($\sigma_3 = 0$) [222]. Depending on the stress state each specimen was subjected to, the light transmits through with a different velocity. This is usually described in terms of light retardation:

$$\delta = (n_1 - n_2)y = C_{opt}(\sigma_1 - \sigma_2) \tag{8-1}$$

where n_1 and n_2 are the principal refractive indices of a light wave propagating parallel to the principal stresses, y is the specimen thickness, and C_{opt} is known as the material stress-optical coefficient. Principal stress at any point is directly proportional to the isochromatic fringe order (n):

$$n = \frac{\delta}{\lambda} = \frac{C_{opt}y(\sigma_1 - \sigma_2)}{\lambda} \tag{8-2}$$

where λ is the wavelength of the monochromatic light source used. These equations are correlated with residual stresses in the material under analysis and are usually described as the stress-optic law or Brewster's law [222–224]. Although to calculate the stress concentration in birefringent material such as polyetherimide requires adequate equipment and calibrations [225,226], that is not in the scope of this work. Here, a qualitative analysis is simply carried out, based on observing increases in the number of fringes, which reflects an increase in residual stress, as stated by the stress-optic law (Equation 8-2).

Figure 8-4 (a) presents an SEM micrograph of a Ti-6Al-4V/PEI hybrid joint pin overlaid with a typical birefringence pattern. The RGB image of the central pin was filtered, so that only the red component was retained (the colored image is presented in Appendix A.3). This was then converted to grayscale and its contrast improved, resulting in a somewhat enhanced image. The overlaid birefringent pattern reveals precisely the shape and extent of the process-affected zone. That is caused by changes in light retardation (δ) induced in this region by the thermo-mechanical process that introduces residual stresses to the polymeric material. The transition between the area affected by the process and the material volume, which remains with the same properties as the base material, is sharp and easily visualized by this technique (Figure 8-4 (b)). At the tip of the pin (Figure 8-4 (c)), high compressive pressure is transmitted by the pin to the PEI due to the axial joining pressure applied by the sonotrode during the joining process. In this region there is an increase in the number of fringes from the right-hand side of the image (Figure 8-4 (c)), with a first-order fringe towards the tip of the pin. The first-order fringe has a brighter contrast and reflects low stressed material, whereas the lighter shades in the PTMAZ indicate a high residual stress (high-order fringes) [226,227]. The fringe order is not clearly identified due to the low resolution of the image at the tip of the pin, where the fringe order is considerably higher, and higher residual stresses levels coexist.

Similar behavior was also observed in the interface between the Ti-6Al-4V and PEI plate; however it is clear that the stresses in this region (white arrow Figure 8-4 (a)) are much lower than the compressive stresses observed at pin tips, owing to the fact that a higher fringe density was found in this region hence a higher retardation compared to the interface of the plates. The residual stresses – most probably of compressive nature - observed at the interface are created by the metal touchdown effect and the consolidation pressure. In addition, it was observed that the high compressive stresses beneath the pin tips induce the formation of shear bands in the PEI, which were observed at the limits of the PTMAZ, (indicated by white arrows in Figure 8-4 (d)). This is a reliable indicator that such material volume locally underwent compression yielding [228].

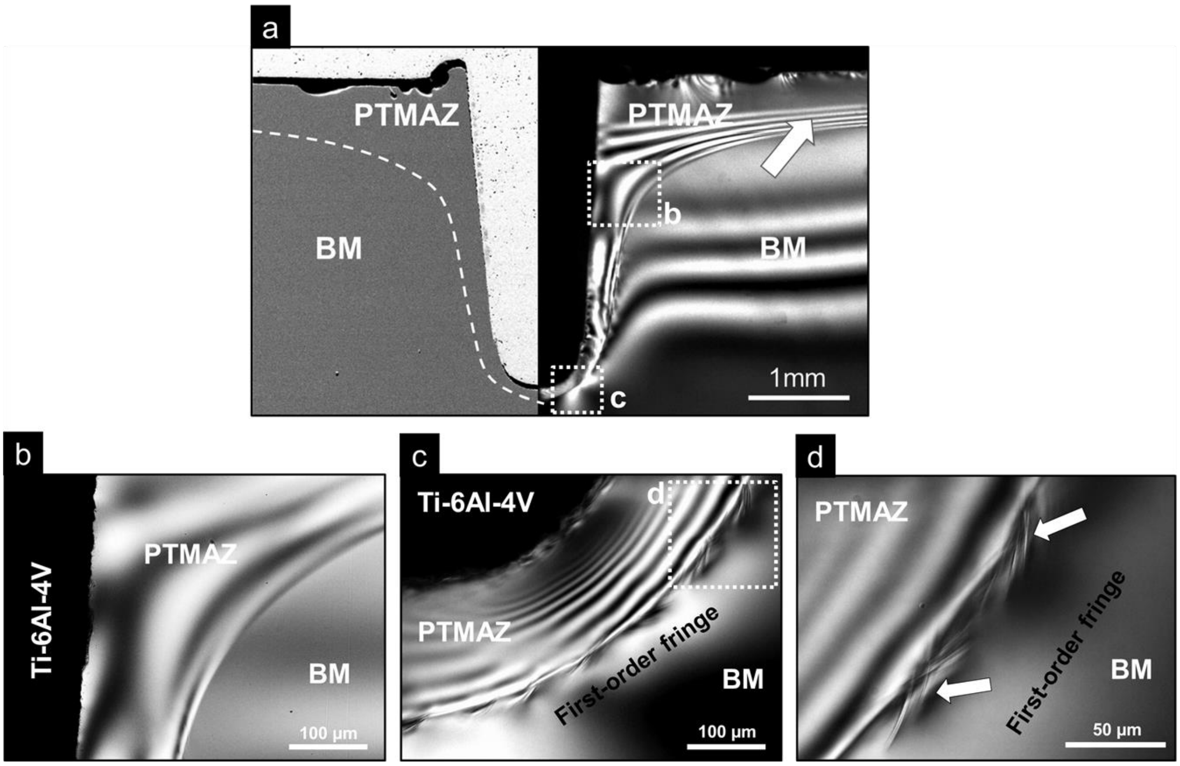

Figure 8-4: (a) SEM micrograph overlaid with a typical birefringence pattern observed in Ti-6Al-4V/PEI hybrid U-Joining joints. This joint was produced with the same optimized joining parameters used to produce the Ti-6Al-4V/GF-PEI hybrid joint. (b) A detail of the PTMAZ shape at the pin half-height, (c) birefringence patterns showing an increase of fringe order towards the pin tip and thus stress concentration, and (d) the formation of shear bands at the PTMAZ limits.

The birefringence pattern herein observed for the unreinforced PEI hybrid joints are believed to reflect in a similar manner the process-affected zone of a joint produced with glass-fiber reinforced PEI. Therefore, it is assumed that shape and extension of such zone, as well as, the thermo-mechanically induced stresses should be very similar. However, fringe density might be slightly affected by the glass fiber reinforcement in the composite. All in all, the birefringence analysis provided a qualitative but rather thorough observation of the PTMAZ shape and internal stresses.

8.2 Process-induced changes in the joined material and local properties

The microstructural changes induced by the joining process described have a significant effect on local material properties, especially in the polymeric part. To establish this connection, the next section addresses these effects on micro and nanoscales, and this is followed by a physical-chemical characterization of the PEI and GF-PEI volumes affected by the process.

8.2.1 Local mechanical properties of the joined Ti-6Al-4V part

Local mechanical properties of the Ti-6Al-4V part were assessed by Vickers microhardness (VMH) tests. Measurement maps were performed on cross-section samples of the joint (see Figure 8-5 (a) and (b)), and these compared with the base material (Figure 8-5 (c)). By comparing both VMH maps, no apparent process-related changes in hardness distribution is detected. These results agree with the microstructural observation, previously discussed, where no visual microstructural changes induced by joining were seen in the MIM-structured Ti-6Al-4V part.

Although no process-related changes were registered by VMH mapping, it can be seen that significant variations of the hardness values are present all over the metallic parts. These variations are primarily related to residual porosity. The as-sintered MIM-structured parts presented a residual porosity of 2.3 ± 0.6 %. Hence, when indentations are performed over pores, the hardness values tend to vary, as seen in the microhardness maps. These residual pores could be closed by a HIP stage after sintering, which results in a pore-free and virtually 100% dense material.

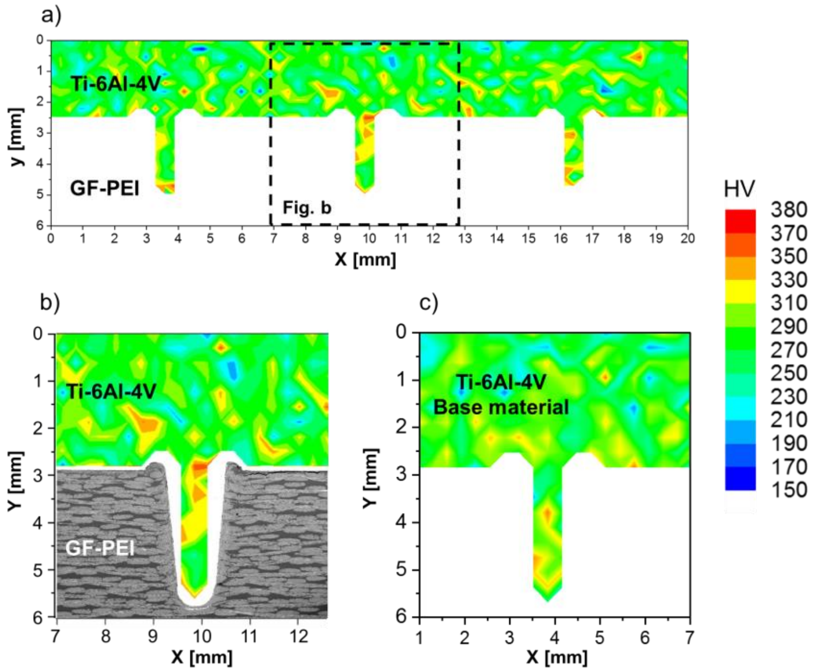

Figure 8-5: Vickers microhardness mapping, (a) hybrid joint produced with optimized joining conditions, (b) overlaid SEM micrograph with the measured microhardness map, and (c) base material microhardness map.

8.2.2 Local mechanical properties of the joined PEI part

Local characterization of the mechanical properties of the polymers has extensively been performed by VMH [229]. VMH is a powerful tool for mapping the surface properties of inhomogeneous polymers, and modifications induced for instance by physical aging, weathering, changes in molecular weight (MW), and local viscoelastic properties [230,231].

Figure 8-6 shows a typical U-Joining VMH map for a hybrid joint produced with polyetherimide as the polymeric part. Hardness distribution revealed the formation of a polymer thermo-mechanically affected zone (PTMAZ),

Figure 8-6 (a), where a decrease of 10% in average in hardness (217.5 ± 21.2) was observed in comparison with the base material (240.4 ± 6.2). The shape and distribution of this zone follow the trends observed in the birefringence patterns, as shown in the overlay CP-TLOM micrograph and VMH map in

Figure 8-6 (b). The PTMAZ is concentrated in the pin surroundings, and regions close to the interface of the materials. Its extent is limited to approximately 1.5 mm from the joint interface towards the PEI thickness and no more the 1 mm radially distributed around the pins for the investigated joining conditions.

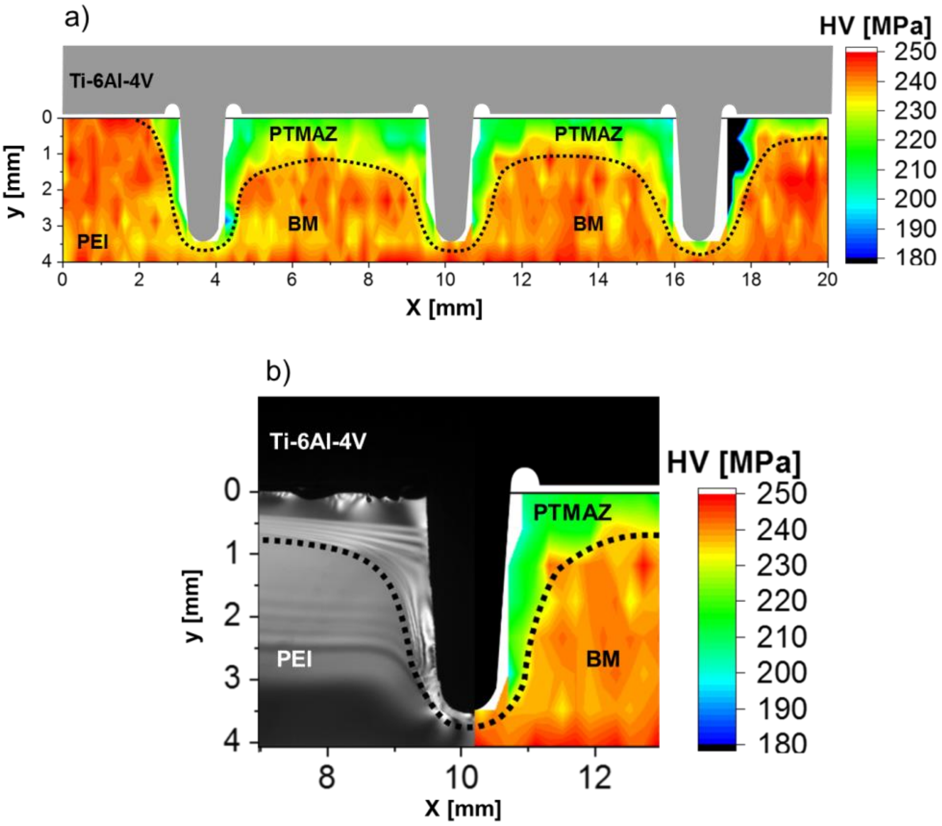

Figure 8-6: (a) Vickers microhardness mapping performed on the Ti-6Al-4V/PEI U-Joining joint, and (b) central pin image obtained by CP-TLOM (left) overlaid on a microhardness map (right). Joint produced with the same optimized joining parameters used for the fiber reinforced configuration (i.e., E_J = 2012 J, A_0 = 52 µm, and J_p = 101 kPa (14.7 psi)).

At the PTMAZ, competing phenomena such as changes in molecular weight induced by partial polymer degradation, chain packing density, and orientation might influence its mechanical properties [198,229]. Due to the pins' penetration, as earlier stated, squeezing flow of molten polymer takes place and the molten polymer wets out the metallic surface, forming adhesion forces between the metal and composite after consolidation. The softened polymer that consolidates around the pins is able to preserve some of the chain orientation it acquired during the joining. This orientation might be upwards, following the squeezing flow direction. Such a phenomenon might also have contributed to the changes observed in the birefringence pattern in Figure 8-6, evidencing the PTMAZ formation, since changes in chain orientation may lead to optical anisotropy [218]. Nonetheless, VMH is sensitive to molecular orientation and can be evaluated in terms of hardness anisotropy (ΔH). ΔH is usually influenced by the orientation of molecular chains and elastic recovery, which tends to mainly occur in the chain orientation direction [229,232]. VMH indentation parallel to the oriented chain, such as in the PTMAZ, would result in higher values of hardness [230,232,233] since during Vickers' indentation the stresses imposed are higher in this direction, due to higher stiffness and resistance of oriented chains [233]. ΔH can be defined as follows [229,234]:

$$\Delta H = 1 - \left(\frac{d_{\parallel}}{d_{\perp}}\right)^2 \tag{8-3}$$

where $d_{\parallel}$ corresponds to parallel indentation diagonals and $d_{\perp}$ those perpendicular to the orientation direction. Figure 8-7 presents ΔH calculated for an indentation line performed at the half height of the pins. Although one can see a weak tendency of ΔH increasing close to the pins (e.g., indentations at distances of about 15 to 17 mm observed for the pin 3) the calculated values are very low when compared, for instance, to injection molded semi-crystalline polymers [229,232] (up to 30% for high molecular grade PE, depending on the processing condition [232]). Therefore, the competing phenomena such as the increase in free volume (i.e., decrease in chain packing density) and partial polymer degradation seem to contribute with greater significance to the mechanical properties in the PTMAZ, as their VMH values are lower than in the BM.

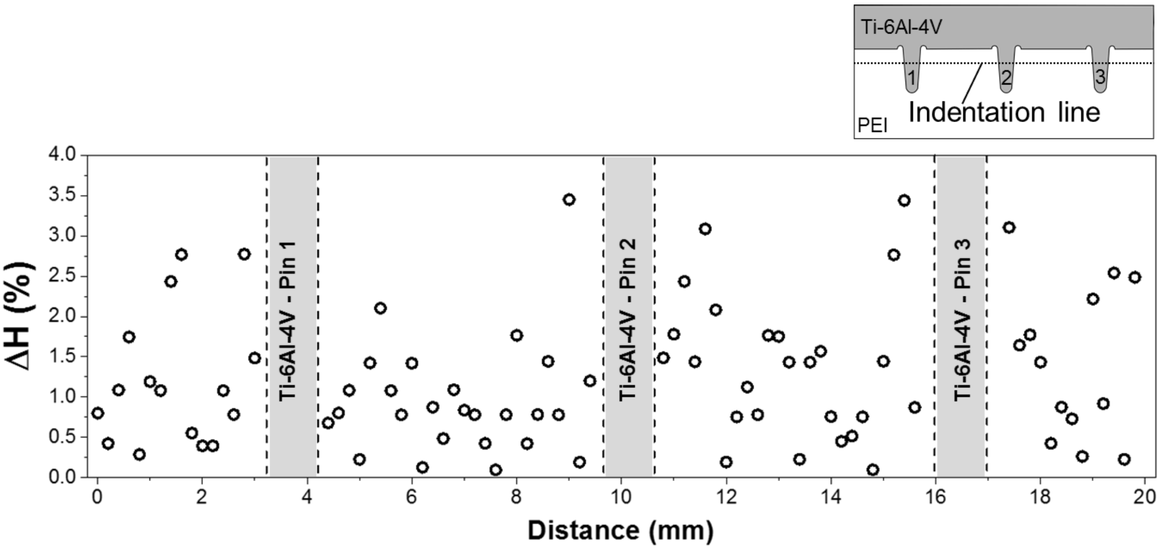

Figure 8-7: Hardness anisotropy (ΔH) assessment on a Ti-6Al-4V/PEI hybrid joint. The indentation line position of the cross-section sample is indicated in the detailed right-hand side image.

When a glassy polymer such as PEI is heated above its T_g, the entangled macromolecules acquire a certain level of mobility. This results in an increase in volume and system enthalpy, usually attributed to physical quantities such as free volume and configurational entropy [235]. Depending on the cooling rate to which the molten polymer is subjected below T_g, its structure will be frozen, retaining from the glassy state thermodynamic quantities (volume and enthalpy) that exceed the equilibrium [235]. This increase in free volume and entropy is therefore associated with decreases in hardness [198,229,230].

Furthermore, based on the maximum recorded process temperature, two competing phenomena are able to contribute to the changes in VMH during the U-Joining, crosslinking and chain scission [229,236]. PEI experiences these two phenomena as part of its thermal-degradation mechanism. According to Kuroda *et al.* [237], the first and dominant mechanism is the formation of crosslinking, which occurs at temperatures ranging from 320 to 380°C [146,147,237]. The second mechanism (chain scission) starts above 400°C, with a maximum rate of decomposition between 510 - 540°C [147,237]. The latter mechanism is associated with a decrease of VMH, since it results in large volumes of low MW molecules and chain ends [236]. By contrast, crosslinking increases the stiffness of the polymeric chains and this results in higher polymer strength [218]. In conclusion, previous observation suggests that chain orientation and crosslinking contributed less to PTMAZ local mechanical strength, since it has values lower than the BM. Thus, it is believed that the VMH reduction is correlated mainly with changes to the polymer free volume, due to its fast cooling rate during U-Joining, and possible alteration in MW (i.e. thermo-mechanical degradation), which will be discussed in Sections 8.2.4.

Analysis of the shapes of VMH indentation provides useful insights into the changes in local viscoelastic properties of the polymer, which can be correlated with changes in free volume. Such an analysis can be performed by correlating the relative residual depth and pile-up volume, as reported by Abibe [198]. In order to assess these properties, selected indentions in each microstructural zone (i.e., BM and PTMAZ) were scanned by laser scanning confocal microscopy (LSCM), and 3D reconstructed topographic images were obtained. Figure 8-8 (a) presents the indentation shapes and typical measurement profiles performed along the indenter diagonal and along the side-faces formed by the pyramidal indenter.

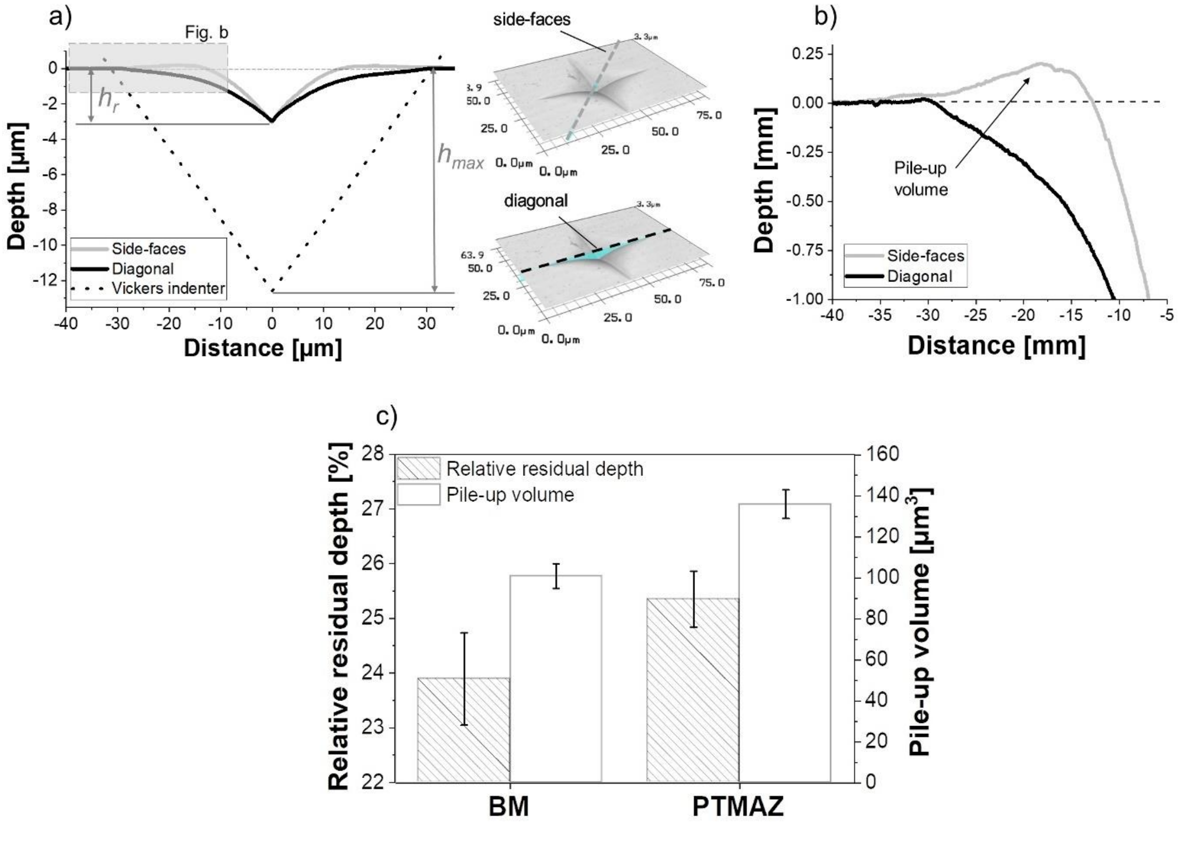

Figure 8-8: (a) Typical indentation profile obtained by LSCM of the PTMAZ measured according to the side-faces of the pyramidal indenter and diagonals, as illustrated in the 3D reconstructed images; (b) detailed view of the pile-up effect and, (c) measured values of relative residual depth and pile-up volume for the BM and hybrid joint PTMAZ.

During a Vickers indentation a glassy polymer typically undergoes a small amount of elastic deformation in the loading cycle, followed by a viscoelastic flow. After unload, some of the elastic deformation imposed instantaneously recovers while some is time-dependent [238]. Such a viscoelastic recovery depends upon several polymer properties such as MW, chain orientation, free volume, and state of internal stresses [229,235,238]. The elastic recovery after unloading usually leads to formation of pile-up, observed as an upwards extrusion of indented material, as shown in Figure 8-8 (b). Such a phenomenon is mostly observed on the side-face of the pyramidal indentation, while a negligible amount of elastic recovery is observed in the diagonals [238], as confirmed by the measurement profiles of Figure 8-8 (b). Thus, permanent plastic deformation occurs mainly at the diagonals, due to intense stress concentration. Based on that assumption, the original geometry of the Vickers' indenter was projected in relation to the diagonals of the indentation and their relative residual depth, ξ_r ($\xi_r = h_r/h_{max}$) was estimated. Where h_r is residual depth and h_{max} the maximum depth achieved by the indenter, as shown in Figure 8-8 (a). In addition, the volume of pile-up material was measured by LSCM, Figure 8-8 (c). To achieve this a baseline was established from the non-deformed, polished surface of the specimen and the volume above this was measured, similar to [198] and [239].

The relative residual depth depends upon material and indenter properties, and can be estimated by the following formula [240]:

$$\xi_r = \frac{1}{1 + 2H/(E_r \ tan\beta_i)} \tag{8-4}$$

where H is the true hardness, defined as the mean contact pressure for a plastic material under indentation [240,241], E_r is the reduced elastic modulus, which is a function of indenter and specimen material properties, and β_i is the inclined face angle of the pyramidal indenter. Assuming the variables related to the indenter are constant while measurements are carried out in the BM and PTMAZ, it can be assumed that ξ_r depends on the $E \ tan\beta/H$ [240]. As the value of H is direct correlated with material yielding stress (σ_y) [229,230,242], ξ_r has a dependency on ratio E/σ_y, which in other words describes the strain experienced by the material during indentation [198]. Thus, small strains (low values of ξ_r) represent highly elastic materials, while large strains correspond to more plastic behavior, that is with less elastic recovery.

In this respect, as higher values of ξ_r where measured in the PTMAZ compared with the BM (Figure 8-8 (c)) two hypothesis can be drawn: the joining process is either increasing the material elastic modulus or decreasing the yielding stress. In addition, the increase in ξ_r in the PTMAZ is coupled with a decrease in H. As established earlier, in Figure 8-6, this is most probably a result of fast cooling and an increase of free volume, since thermo-mechanical degradation would decrease E resulting in the opposite effect on the ξ_r. This means that the process-affected material in the PTMAZ was more prone to dissipate the energy from the indentation load than recover it elastically after unloading, which also resulted in increasing the pile-up volume Figure 8-8 (c). This implies time-dependent properties of this material volume, which might, for instance, induce premature failure under cyclic and creep loading in the material with a high free volume. In addition, changes to free volume have been reported to affect creep compliance, stress relaxation dynamic moduli, and the loss tangent [235]. However, these changes are seen as reversible, with no permanent modification of the polymer structure or physical-chemical properties [235]. Therefore, a controlled annealing of the joint to move the polymeric structure to an equilibrium state, with less free volume, could improve the long-term properties of the process-affected material volume, as shown by Abibe for the same polymer [198].

8.2.3 Local viscoelastic properties by instrumented nanoindentation

Although examination of the indentation shape provides some insight into the viscoelastic properties of the PTMAZ volume, VMH data are mainly related to irreversible plastic processes, and most of the information related to elastic release after indenter unloading is lost [230]. Although VMH was useful to describe the local mechanical properties of a hybrid joint produced with unreinforced PEI, the high glass-fiber content of the joints produced with GF-PEI hinder reliable measurements of the polymer matrix in the process-affected zone [229]. Therefore, in order to further understand the local viscoelastic properties of the polymeric material used in this work, especially material in the GF-PEI joints, instrumented nanoindentation experiments were performed. In addition, experiments carried out with the unreinforced PEI joint configuration were intended to confirm the results that were previously discussed, whereas those on the GF-PEI joint configuration were aimed at obtaining new information about the effects of the process on this material.

Measurement of hardness and elastic modulus by instrumented nanoindentation was developed in 1992 by Oliver and Pharr [243] and nowadays is considered an established technique, which has been extensively applied to characterize materials at small scales [229,244], including polymeric composites [245,246]. The technique consists of driving an indenter into the material under analysis and continuously monitoring the indentation depth as a function of the applied load. As a result, a load versus displacement (*P-h*) curve is obtained. When the indenter is withdrawn from the indented material (unloading), at the initial unloading stages it experiences a pure elastic recovery, hence the elastic unload stiffness ($S = dP/dh$), can be calculated [243,244]. Other important quantities recorded during the measurement are the maximum load (P_{max}), the maximum displacement (h_{max}), and the final indentation depth (h_f), as presented in the quasi-static *P-h* curve of the PEI base material in Figure 8-9.

From the quantities previously presented, hardness is obtained by dividing the P_{max} by the contact area (A) of the indenter impression and the elastic modulus, using the following equation [244]:

$$S = \beta_i \frac{2}{\sqrt{\pi}} E_{eff} \sqrt{A} \tag{8-5}$$

where E_{eff} corresponds to the effective elastic modulus, which considers the Poisson's ratio (v) and Young's modulus (E) of both material and indenter, and β_i is a constant that depends on the indenter's geometry. The E_{eff} is defined as [244]:

$$\frac{1}{E_{eff}} = \frac{1 - v^2}{E} + \frac{1 - v_i^2}{E_i} \tag{8-6}$$

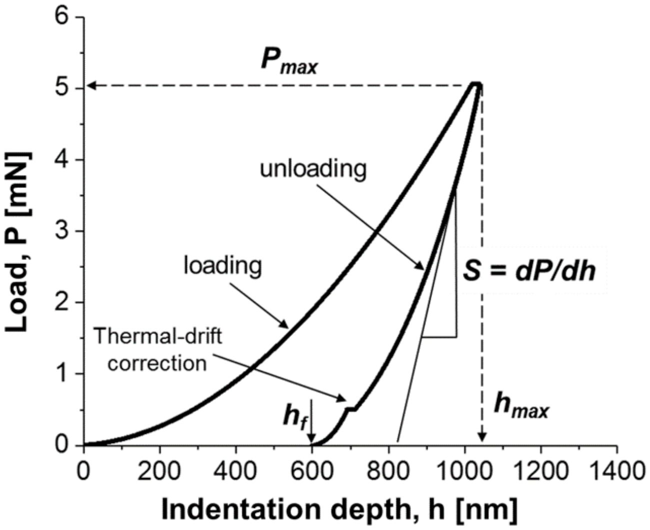

Figure 8-9: Quasi-static *P-h* curve obtained for the PEI base material and illustration of the important quantities measured by nanoindentation (adapted from [244]).

where E and v are respectively the elastic modulus and Poisson's ratio of the base material and E_i and v_i these properties for the indenter. The determination of both hardness and the material's elastic modulus by the described equation presents some drawbacks. In the case of materials that possess time-dependent properties, such as PEI, the estimation of S is not usually reliable, due to non-linear elastic recovery during unloading [244,247,248]. In addition, when the material under indentation presents pile-up, the estimated contact area is larger, and consequently the values of both H and E are overestimated [244,248]. To overcome these limitations, advanced techniques have been proposed, such as continuous stiffness measurement (CSM). With CSM a dynamic oscillation is imposed in the force applied during indentation and stiffness is measured continuously for the complete loading phase [244,246]. Thus by imposing a high-frequency oscillation to the applied force, one can acquire reliable measurements of stiffness, reducing the effect of time-dependent plasticity. Further, both H and E are measured as a function of the indentation depth with this technique. For further information on instrumented nanoindentation see [243–248].

Figure 8-10, presents the *P-h* curve obtained by CSM of a hybrid joint joined with PEI as the polymeric part. As described in Section 5.3.9.2, three measurement regions were selected; two in the PTMAZ and one in the BM. The first area in the PTMAZ, A1, corresponds to a group of indentations performed close to the interface that formed between the pin and PTMAZ. The second area, A2, is located close to the materials' interface, as shown in Figure 8-10 (a). The *P-h* curve obtained clearly shows that the joining process affected the local performance of the PTMAZ volume. As all of the experiments were performed with a prescribed displacement, or indentation depth, of 1µm, the P_{max} reading in the *P-h* curves is directly correlated with the material's nanohardness. Thus, it can be assumed that the PTMAZ has lower values of hardness, which agrees with the VMH results. In addition, the h_{max} and h_f are greater for process-affected material, also in perfect agreement with the relative residual depth analysis, as described earlier. Thus, it is again clear that the PTMAZ material is more prone to dissipate energy from indentation load than recover it elastically after unloading. As expected, the PEI also has pile-ups under nanoindentation, Figure 8-10 (a). Therefore, the measurement of hardness value is expected to be overestimated, as previously mentioned, due to dependence of this property on the indentation contact area.

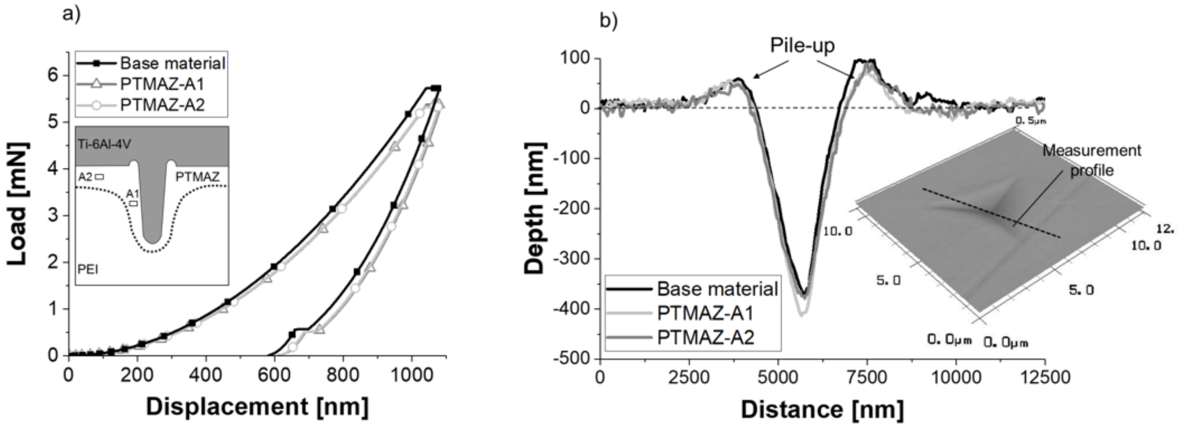

Figure 8-10: (a) Nanoindentation *P-h* curves obtained from the BM and PTMAZ for a PEI joint configuration, and (b) LSCM measurement of a nanoindentation profile at the PTMAZ.

In order to correct the measured hardness values, a procedure based on the ratio of load to stiffness squared (P/S^2) was used. Such a parameter, P/S^2, is a material characteristic that is independent of the contact area, which is experimentally recorded during the CSM indentation mode, and it was first reported by Joslin and Oliver [249]. Therefore, if the material's elastic modulus is known, even under a considerable pile-up condition, one can accurately calculate the material's true hardness by the following equation [244,249,250]:

$$\frac{P}{S^2} = \frac{\pi}{4{\beta_i}^2} \frac{H}{E_{eff}^2} \tag{8-7}$$

where E_{eff} corresponds to the effective elastic modulus (Equation 8-6) and β_i is a constant that depends on indenter geometry (for a Berkovich indenter β_i is equal to 1.034 [250]). Examples of harmonic contact stiffness curves and the indenter information that were used to correct the hardness values are presented in Appendix A.4.

Figure 8-11 presents examples of elastic modulus and corrected hardness, measured as a function of the indentation depth in the BM and PTMAZ. It can be observed that at shallow indentation depths (lower than 250 nm) the elastic modulus measured tends to increase. Such a behavior is typically observed in dynamic nanoindentation experiments and this is associated with an indentation size effect (ISE) [248,251,252]. It has been reported that the elastic modulus measured on a polymer surface is usually lower than the one measured in the material bulk ($E_{surface} > E_{bulk}$). This is most commonly correlated with inaccuracies in the determination of the contact point between indenter tip and surface, and the function of the tip area [245]. In addition, the signal-to-noise ratio decreases at low displacements and loading levels [248,253]. Taking this into account, the average elastic modulus and the true hardness values were calculated between indentation depths of 300 and 900 nm, a region where the ISE is assumed negligible and the properties constant, as observed in Figure 8-11 (a) and (b). The average values of elastic modulus and true hardness are presented in Table 8-1.

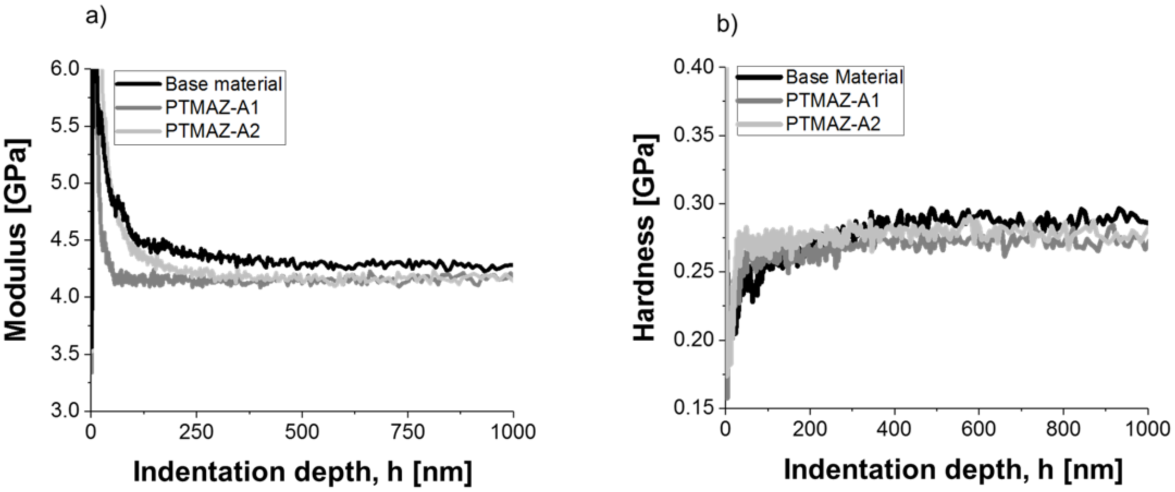

Figure 8-11: (a) Example of the elastic modulus, and (b) corrected hardness; variation in CSM indentation mode as a function of the indenter displacement into the surface of the BM and PTMAZ (A1 and A2).

Table 8-1: Average values of elastic modulus and corrected hardness measured by nanoindentation for the PEI BM and PTMAZ.

Measurement area	Average modulus [GPa]	Average corrected hardness [GPa]
BM	4.234 ± 0.038	0.286 ± 0.004
PTMAZ – A1	4.146 ± 0.035	0.278 ± 0.001
PTMAZ – A2	4.120 ± 0.032	0.274 ± 0.002

The joining process not only changes the values of hardness, as stated earlier, but also the elastic modulus of the PTMAZ volume. A reduction of up to 2.7% was measured by nanoindentation. This suggests that the thermo-mechanical process is irreversibly changing the physical-chemical properties of the polymeric material close to the interface and pins. In glassy polymers, Young's modulus has a dependence on the polymer MW. That is because the viscosity of a glassy polymer is directly affected by the polymer structure, in other words how its chains are entangled (looping around each other) [254]. In general, thermal degradation of polymers leads, among other mechanisms, to chain scission and this results in lower MW [255]. That has an effect on the entanglement state of the polymer structure, which a polymer with a low MW tends to possess less entanglement points. These points are usually seen as virtual crosslinking points and these act to increase viscosity and elasticity of the polymer [254]. In order to evaluate the degree of thermal degradation of the PTMAZ material, physical-chemical characterizations were performed and these will be discussed in the sections that follow.

The size of the resultant indentations corresponds to just a few micrometers, as shown in the measurement profile of Figure 8-10 (b). Such a small size (profile length of about 8 µm) allows for indentation between the network of fibers. Therefore, it is possible to assess the local mechanical properties of the GF-PEI polymer matrix. Following the same approach employed for evaluation of the Ti-6Al-4V/PEI joint, the GF-PEI matrix of a Ti-6Al-4V/GF-PEI joints were investigated as a part of this work. The results are presented in Figure 8-12, Figure 8-13 and Table 8-2.

The results obtained are similar to those observed for unreinforced PEI joints. *P-h* curves reveal that the process-affected matrix (CTMAZ) is less prone to recover elastically (i.e., it has a higher h_f), and lower loads were required for the indenter to reach the prescribed indentation depth of 1µm (lower P_{max}). These are characteristics of a material with high free volume and possibly with lower MW. In addition, a tendency of the material to pile-up was observed, as previously reported for the unreinforced PEI joints.

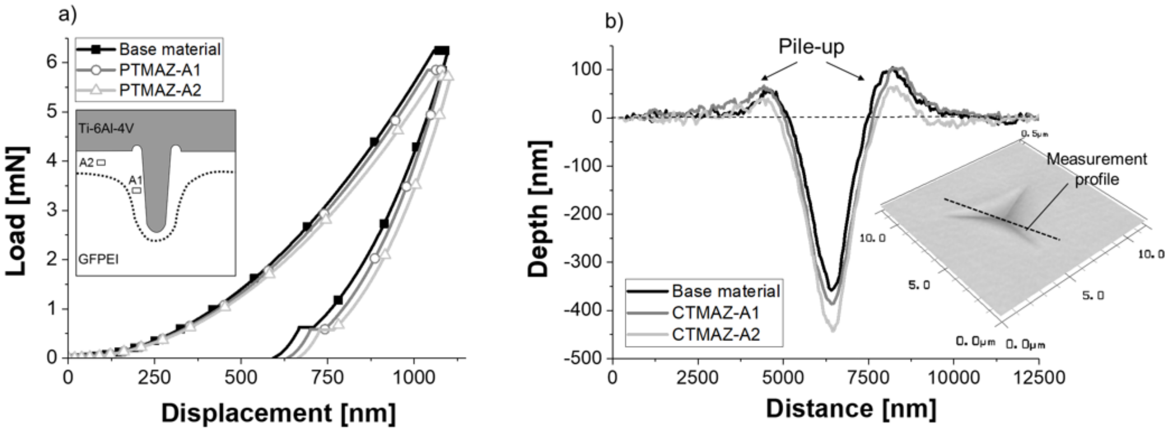

Figure 8-12: (a) Example of nanoindentation *P-h* curves obtained from the BM and CTMAZ for a GF-PEI joint configuration, and (b) measurement of a CTMAZ nanoindentation profile acquired by LSCM.

Figure 8-13 presents the values for the elastic modulus and hardness over the indentation depth, and Table 8-2 lists their average values calculated between 300 and 900 nm. It can be observed that there is a tendency of decreasing elastic modulus in CTMAZ A1 and A2 when compared with the BM, Figure 8-13 (a), which is also reflected in the calculated average values, Table 8-2. However, some indentations presented an unstable variation between 300 and 900 nm, as observed for the example curve of CTMAZ-A1 in Figure 8-13 (a). For this indentation, the modulus value tends to increase with the increase on indentation depth. This could be related to an adjacent volume of fiber beneath the indenter, which would locally increase the stiffness of the material under the indentation. Such phenomena might also explain the higher standard deviation for region A1, which was three times greater than for the BM.

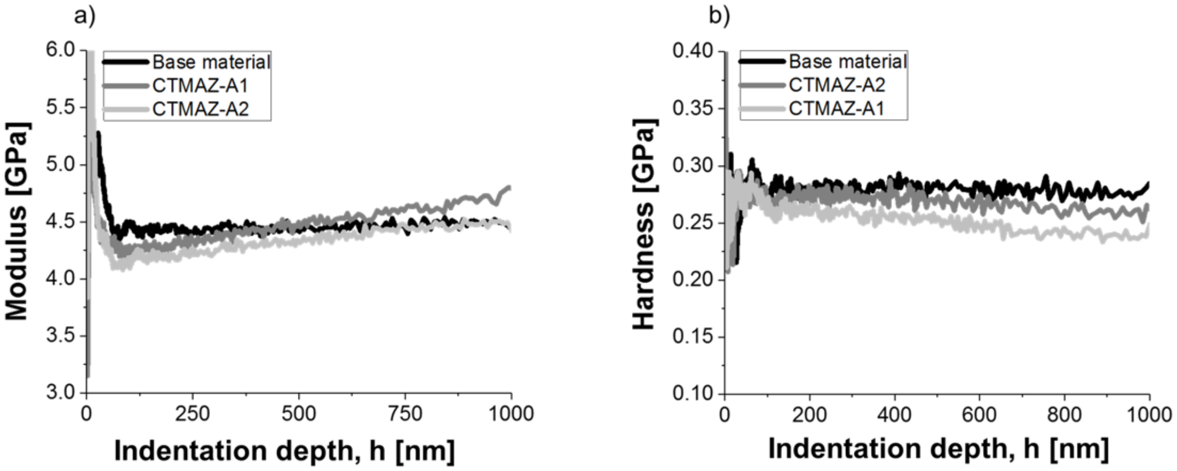

Figure 8-13: (a) Example of the elastic modulus, and (b) corrected hardness; variation in CSM indentation mode as a function of indenter displacement into the surface of the BM and CTMAZ (A1 and A2).

Table 8-2: Average values of elastic modulus and corrected hardness measured by nanoindentation for the GF-PEI BM and CTMAZ.

Measurement area	Average modulus [GPa]	Average corrected hardness [GPa]
BM	4.460 ± 0.021	0.280 ± 0.001
CTMAZ – A1	4.439 ± 0.066	0.239 ± 0.007
CTMAZ – A2	4.352 ± 0.014	0.250 ± 0.005

Similar to the unreinforced PEI joint configuration, an elastic modulus reduction of up to 2.4% and hardness reduction of 14.6% were measured for the composite matrix in the GF-PEI joint configuration. These results are also in agreement with the results obtained by VMH, although the corrected hardness measured by nanoindentation was relatively higher. An overestimation of the true values of hardness might be correlated with the pile-up behavior observed during the indentation, as previously discussed. The implication of these local mechanical changes in the CTMAZ is also similar to that earlier discussed, which suggested that the polymer matrix presents a higher free volume in relation to the BM. As a result, one could also expect a slight degradation in creep resistance, stress relaxation properties, and loss tangent [235], but it is believed that some of this effect could be reversed by a further controlled annealing process, as shown by Abibe in F-ICJ of AA2024/PEI hybrid joints [198]. However, the changes in elastic modulus are not related to a reversible process and are most probably a result of polymer thermo-mechanical degradation.

8.2.4 Physical-chemical changes in the polymeric parts

Amorphous polymers have temperature-dependent physical and chemical properties, which at a certain threshold can start to degrade. Therefore, in a thermo-mechanical-induced joining process such as U-Joining it is essential to investigate and understand the physical-chemical changes induced by the process on the polymeric part, because it can considerably affect the joint's mechanical performance. In this respect, thermal analysis (TGA and DSC) was employed to assess changes of the PTMAZ and CTMAZ of unreinforced PEI and GF-PEI joint configurations, and to support an understanding of local mechanical properties.

Figure 8-14 (a) presents the TGA curve of an as-received PEI sample before the joining process overlaid with a range indication of the process temperature recorded during U-Joining of the unreinforced PEI joint configuration. The onset of thermal decomposition was measured as 545 ± 2°C (with a maximum rate of decomposition at 561 ± 1°C) and the maximum recorded process temperature for this configuration was 456 ± 89°C. Considering the high standard deviation of the IR thermography measurements, it can be assumed that the joining process temperature is already within the onset of thermal decomposition. In addition, as earlier discussed, the temperature recording was stopped after the metallic part touched down, and so this value might be slightly underestimated. However, as previously stated, the joining cycle time is very short and the material experienced high temperatures for only a few fractions of a second. In order to investigate if the recorded process temperature levels had an effect on polymer chain structure (i.e., the chain length), the glass-transition temperature of the PTMAZ was evaluated by DSC and compared with the as-received BM, Figure 8-14 (b).

Commonly with glassy polymers, a reduction in the MW or chain length results in fewer points of polymeric chain entanglement. Thus it also decreases the thermal energy required for the polymer to achieve its T_g during heating or plastic deformation [254,256]. The T_g recorded during the first heating cycle (T_{g1}) and the second heating cycle (T_{g2}) are presented in Figure 8-14 (b). Apparently the process does not affect the measured properties significantly, since variations of less than 1°C on average were observed for both T_g measurements. Such a variation might also be related to the sample extraction procedure of scalpel cutting, which inevitably induces residual stresses in the samples [181]. Therefore, based on the TGA and DSC results, it can be concluded that the U-Joining did not induce extensive physical-chemical changes to the polymeric structure. Nonetheless, localized thermo-mechanical degradation in the PTMAZ may take place and should be therefore investigated, as they can affect joint properties.

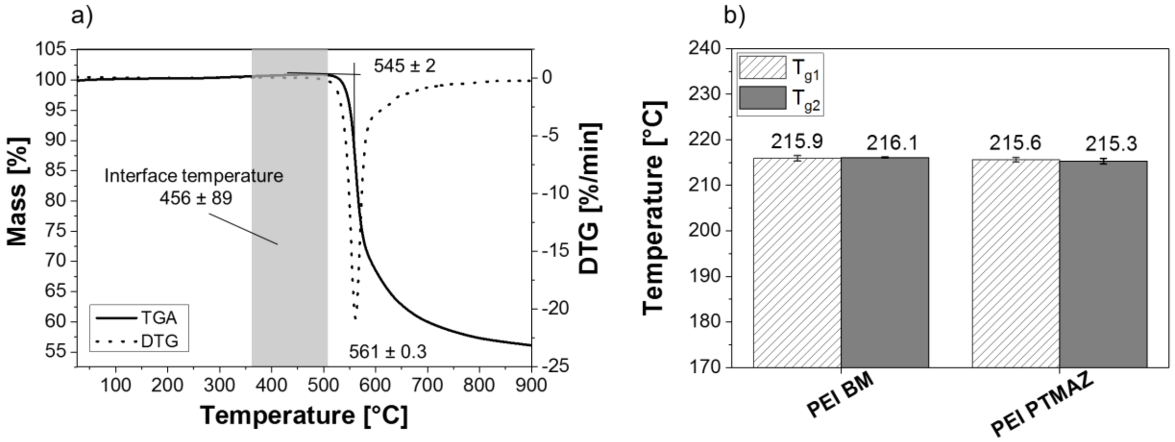

Figure 8-14: (a) Thermogravimetric curve of the PEI base material and representation of the maximum process temperature recorded by IR thermography for the optimized joint condition, and (b) glass transition temperatures of the PEI base material and material removed from the PTMAZ.

In contrast to the observations previously made for the unreinforced PEI joint configuration, the process-affected zone of the GF-PEI joint had significant changes in the measured properties. Figure 8-15 (a) presents the thermal analysis results for this joint configuration. The TGA curve reveals a slightly lower value (531 ± 2°C) for the onset of thermal decomposition in the as-received GF-PEI than that observed for PEI, which may be correlated to differences in grades of the base material [166,257]. The process temperature recorded (511 ± 3°C) was slightly below the onset of thermal decomposition, although one should consider that this value may be an underestimate, as earlier discussed.

However, the changes in T_g of GF-PEI (Figure 8-15 (b)) seem to have a significant dependence on the heating rate imposed during the DSC measurement and joining process. An increase of about 21°C in the T_g for the as-received GF-PEI base material was measured during the second-heating cycle. Such an increase is attributed to the thermal history of the GF-PEI laminate during manufacturing. The laminate is cooled down during production with a rate 5°C/min (lower than in the DSC experiments) and as a result a lower T_g is measured. After the first cooling cycle with the DSC cooling rate imposed, the thermal history of its manufacturing and the effects of sample preparation were eliminated, and the T_g values thereafter reflect the pure physical-chemical properties of the material [181], which corresponds to a value of 214.1 ± 0.7°C. When comparing T_{g1} of the BM (obtained in the first heating cycle) with that measured for the CTMAZ, a similar behavior is observed. This is probably caused by a similar effect, because after joining the CTMAZ material undergoes a cooling process with a cooling rate significantly higher than the 10°C/min applied during the DSC analysis. The dependancy of heating and cooling rates on the T_g of a glassy polymer are well-known phenomena and the faster the heating or cooling rate the higher the T_g measured [181,212,258,259]. This is because a faster cooling rate results in shorter relaxation times [258]. Therefore, when the polymer cools down from above T_g, its structure is frozen in a state of high free volume [224,235] as not enough time is given for the polymer to achieve a thermodynamically stable structure. This finding is in line with the hardness decrease measured by nanoindentation.

Apart from changes in T_{g1}, the joining cycle induced a slight decrease in T_{g2} as can be seen in Figure 8-15 (b). The second T_g measured refers to physical-chemical properties of the material, as the thermal and mechanical history (i.e., caused by the joining process) were already eliminated after the first heating cycle. Therefore, it can be assumed that to certain degree of degradation took place in the chemical structure of the polymer, such as chain scission (reduction of MW).

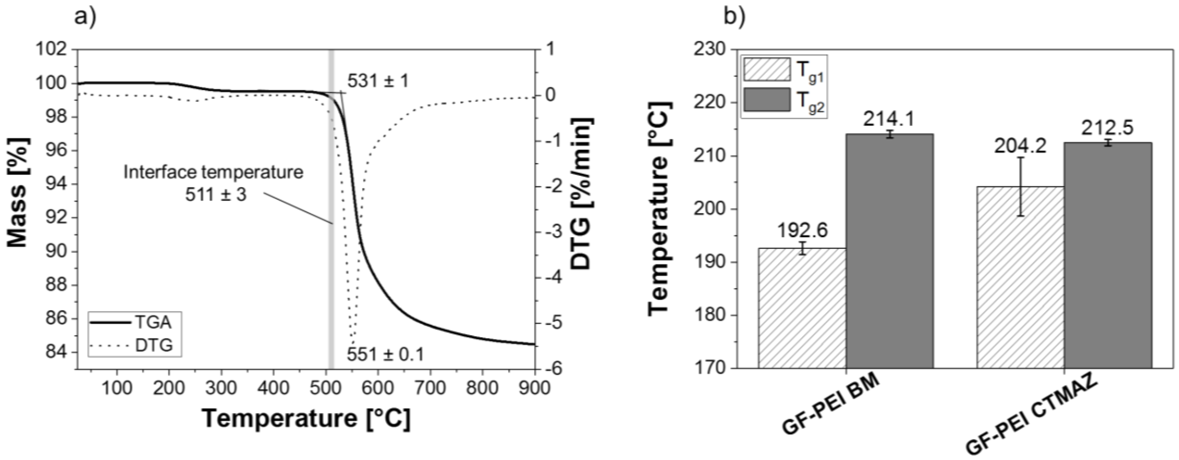

Figure 8-15: (a) Thermogravimetric curve of the GF-PEI base material and representation of the maximum process temperature recorded by IR thermography for the optimized joint condition, and (b) glass transition temperature of the GF-PEI base material and material removed from the CTMAZ.

To determine whether the described changes in U-Joining joint local mechanical properties and T_g result from process-induced thermomeachanical degradation, size-exclusion chromatography (SEC) was applied. The MW has a direct correlation with several properties of glassy polymers, such as yield strength, glass transition, elastic modulus, creep compliance, viscosity, stress relaxation [224,254,256]. In addition, fracture strength, yield stress and the transition between ductile and brittle in PEI has been reported to depend on the MW [260]. These phenomena are a response to the entanglement state of the polymer structure. High MW allows for more entanglement points between the polymeric chains (connectivity points between chains). As a result increasing the polymer viscosity [254], or decreasing the mobility [261]. On the other hand, a decrease in MW (for instance, induced by thermal degradation) will result in more and smaller chains, thereby increasing the number of chain ends. This has considerable influence on the polymer free volume, for example, since chain ends offer higher mobility. Thus, polymers with shorter chains have a higher free volume compared with polymers with longer chains [262].

Figure 8-16 (a) presents the molecular weight distribution (MWD) curves and Figure 8-16 (b) the calculated molecular weight parameters for the as-received PEI base material and material extracted from the PTMAZ (unreinforced PEI joint configuration). The results for the GF-PEI joint configuration are presented in Figure 8-17 (a) and (b) in the same fashion.

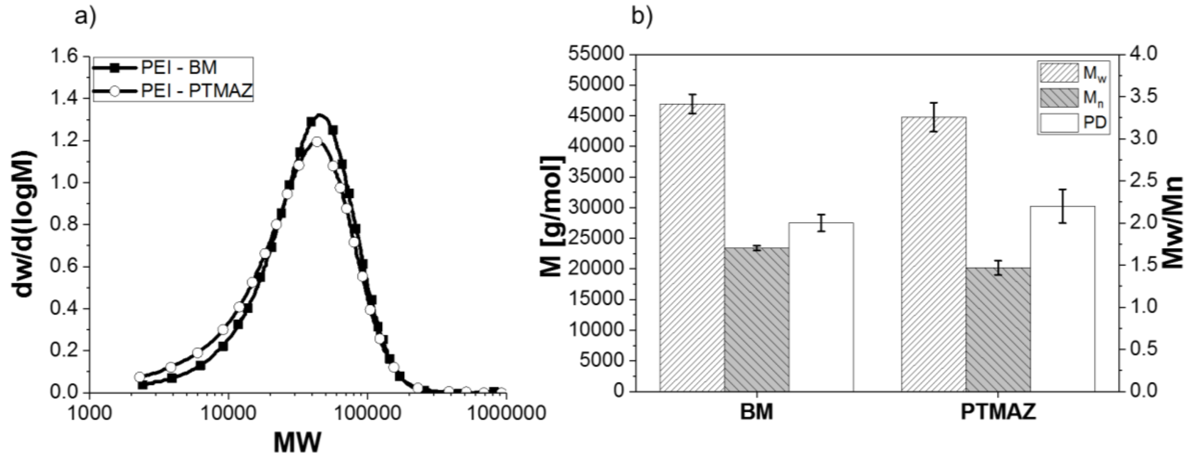

Figure 8-16: (a) Comparison of molecular weight distribution for as-received PEI base material and the PEI material extracted from the joint PTMAZ, and (b) their respective weight-average molecular weight (M_w), number-average molecular weight (M_n) and polydispersity index (PD = M_w/M_n). (Joining parameters: E_J = 2012 J, A_0 = 52 µm, and J_p = 14.7 psi (101 kPa)).

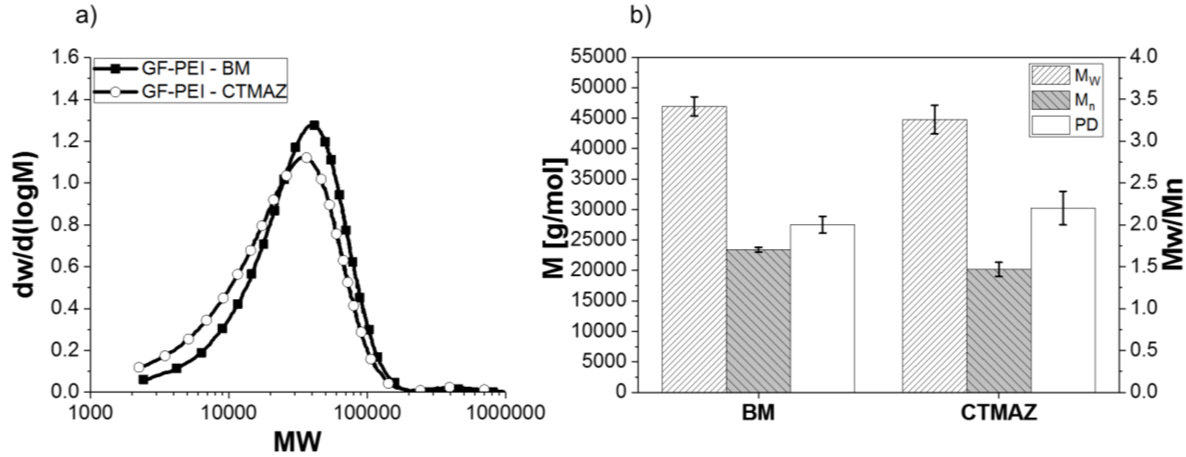

Figure 8-17: (a) Comparison of molecular weight distribution for as-received GF-PEI base material and the GF-PEI material extracted from the joint CTMAZ, and (b) their respective weight-average molecular weight (M_w), number-average molecular weight (M_n) and polydispersity index (PD = M_w/M_n) (Joining parameters: E_J = 2012 J, A_0 = 52 µm, and J_p = 14.7 psi (101 kPa)).

Both the MWD curves for the PTMAZ and CTMAZ visually reveal a tendency to shift towards the lower molecular weight side (i.e., a displacement to the left compared with the BM). In addition, this shift seems not to be constant across the whole MW scale, indicating that the joining process may have induced non-random chain scission mechanisms. This effect would have been the opposite, if crosslinking acted as the primary degradation mechanism [263]. Comparing the BMs (PEI 46933 ± 1573 g/mol and GF-PEI 40234 ± 2559 g/mol) with the material extracted from PTMAZ and CTMAZ, an average reduction of 5% (44758 ± 2372 g/mol and 38265 ± 3645 g/mol for the extracted PEI and GF-PEI, respectively) in weight-average molecular weight (Mw) was measured, as observed in Figure 8-16 (b) and Figure 8-17 (b). In addition, a reduction in number-average molecular weight (Mn) of 14% was observed for the PEI Joint (i.e., 23403 ± 413 g/mol and 20176 ± 1180 g/mol for the PEI BM and PTMAZ extracted material, respectively), whereas a reduction of 24% was observed for the GF-PEI joint (i.e.,19113 ± 262 g/mol and 14612 ± 280 g/mol for the GF-PEI BM and

CTMAZ extracted material, respectively). A reduction in M_n is directly correlated with polymer chain scission and therefore this clearly indicates that the joining process thermo-mechanically degrades locally the structure of the polymeric parts.

In order to further understand the chain scission mechanism induced by U-Joining and its dependence on MW, the chain scission distribution function (CSDF) was applied [263–265]. The CSDF was introduced by Canevarolo [263] as an extension to the number of chain scissions (n_R) [266]. This number describes a numerical average between the polymer's original number-average molecular weight (M_{no}) and its final number-average molecular weight (M_{nf}), that is:

$$\frac{\overline{M_{no}}}{\overline{M_{nf}}} - 1 \tag{8-8}$$

Based on Equation 8-8 and extending the average value n_R to the whole MWD spectrum, Canevarolo defined the CSDF as follows [263,264]:

$$CSDF = logN_R + 1 \tag{8-9}$$

where N_R corresponds to the value n_R applied to the WMD, represented by Equation 8-9. In this manner, the average value of the original M_{no} is substituted by the initial MWD curve ($\mathrm{WMD_i}$) and the final M_{nf} by the final MWD curve ($\mathrm{WMD_f}$) [263]. Thus N_R is written as:

$$N_R = \frac{MWD_i}{MWD_f} - 1 \tag{8-10}$$

In this analysis, the initial WMD refers to the base material curve, while the final WMD corresponds to the PTMAZ or CTMAZ curve. In terms of a qualitative explanation, the CSDF compares the molar fraction of both samples (BM and PTMAZ), characterized by the area under the MWD curve, as shown in Figure 8-18 (a). For a defined molar fraction (A1), referring to the base material, a typical molecular weight MW1 is defined in the MWD of sample 1. The process-induced degradation shifts its MWD to the left side, thus for the same defined molar fraction defined in the MWD of sample 2 (A2) a shifted MW2 is observed and $\mathrm{N_R}$ is calculated for one cumulative point [263,267]. This analysis is extended for the whole MWD and as a result the CSDF is computed [263,264].

Figure 8-18 (b) displays the CSDF obtained for both PTMAZ and CTMAZ. Based on the CSDF shape, conclusions about degradation mechanisms can be drawn. When the MWD is shifted to the low MW side, it yields positive CSDF values, which therefore correlate with chain scission [263,267]. An opposite behavior would be expected when crosslinking acted as the primary degradation mechanism. In addition, the CSDF shows a higher variation for low MW and a tendency to decrease with an increase of MW (negative slope), Figure 8-18 (b). Therefore, the joining process induces a non-random chain scission mechanism, which mainly forms low MW chains rather than degrading the high MW chains. This result is coupled with an increase in polydispersity index (Figure 8-16 (b) and Figure 8-17 (b)), which suggests that a possible degradation pathway in the PTMAZ and CTMAZ is induced by a multiple chain scission mechanism [267,268]. That occurs when a chain undergoes an initial breakage and its fragments continue degrading. As a result, it produces significant proportion of smaller chains (with lower MW). A similar degradation mechanism has been described for PEI/AA6082-T6 hybrid joints joined by friction-based injection clinching [267]. In addition, similar thermal degradation levels to those presented in this study have been reported for friction riveted AA2024-T351/PEI hybrid joints [147].

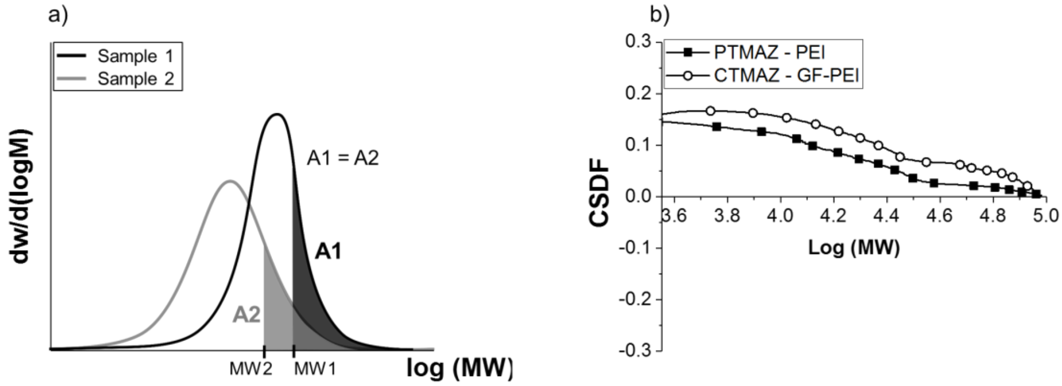

Figure 8-18: (a) Illustration of a MWD and the parameters used to extend the chain scission number to a CSDF, and (b) the CSDF curve obtained for the PTMAZ and CTMAZ for PEI and GF-PEI joint configurations, respectively.

The degraded volumes presented chains with M_w of 44.8 ± 2.3 and 38.3 ± 3.6 kg.mol^{-1} for the PTMAZ and CTMAZ, respectively. Sanner *et al.* [260], studied the effect of M_w ranging from 36.6 to 52.3 kg.mol^{-1} on the mechanical properties of PEI. According to their results, the M_w did not play a significant role in the yield strength for the studied range, although an increase in fracture strength was observed with the increase in M_w. Thus in terms of joint application the level of thermo-mechanical degradation seems not to affect the joint properties significantly. The degradation levels measured by SEC explain precisely the previously reported changes in T_g since lower thermal energy levels (temperature) are required to promote mobility in polymers with low molecular weight. Hence, the CTMAZ had its T_g, shifted to a lower temperature. In addition, the thermo-mechanical process slightly changed the elastic modulus of the process-affected zone, which is now explained as local thermo-mechanical degradation of the PEI matrix induced by multiple chain scission.

8.3 Typical defects in the U-Joining joints

The quality of U-Joining joints, as with most manufacturing processes, is closely related to precise control of the joining parameters. Changes in the joining parameters could, for instance, increase the process-affected volume, resulting in undesirable degradation of the composite and metal properties. The most common source of defect in U-Joining is related to over or underestimation of preset joining parameters, such as E_J, A_0 and J_P.

Under the energy-controlled mode, the preset level of E_J dictates the duration of the ultrasonic vibration and thus the length of the ultrasonic heat generation phase. Hence, overestimated E_J levels (i.e. above 2012 J for the current case-study materials) may lead to higher temperatures at the material interface and consequently a more aggressive thermal joining condition for polymeric or composite part. Such a higher temperature at the interface can increase the extent of the PTMAZ or CTMAZ and the number of volumetric flaws present in this region, as shown in Figure 8-19 (a). In the same manner, overestimated values of J_P (i.e. above 101 kPa) can result in deflection and damage of the TTR elements, as illustrated in the view of a joint cross-section in Figure 8-19 (b). Therefore, one must take into account the stiffness and mechanical properties of TTR elements during process optimization and selection of J_P and C_P values.

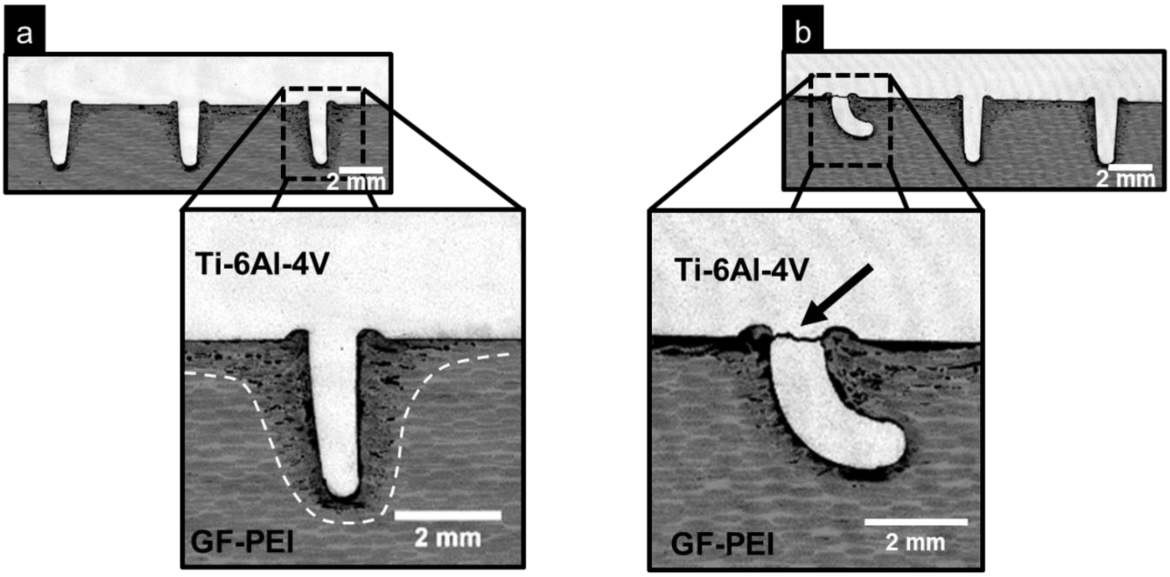

Figure 8-19: Examples of U-Joining of joints produced with overestimated values of (a) E_J, and (b) J_P.

Pin deflection is usually related to higher J_p values, but it does not always result in total damage, as shown in the µCT 3D reconstructed images of Figure 8-20 (a). In some cases it may even contribute positively to the mechanical properties of the joint. For example, Tu *et al.* [112] suggested that fabrication of a protrusion with a tilt angle of 20° or 30° towards the metal end of the overlapped area could improve load transfer between metal and composite in COMELD joints. However, from the current knowledge, the direction of pin deflection seems to not depend on the joining parameters entirely and so it is difficult to predict.

While overestimated values of the parameters typically result in excessive damage to one part of the joint, underestimated values can result in incomplete formation of the joint. Low values of E_J (below 2012 J in this work) induce a shorter joining cycle (with fixed values of A_0 and J_P), which might not ensure complete penetration of the TTR elements. This results in a joint with a lack of penetration (LoP) as shown in the X-ray µCT of Figure 8-20 (b). In addition, insufficient axial pressure (below 101 kPa) applied by the sonotrode during joining can result in slippage and rotation of the MIMStruct part relative to the composite surface, as shown in Figure 8-20 (c).

These defects are undesired in the U-Joining joint and have a direct correlation with the mechanical properties of the joint. In Chapter 11 this correlation is explored more deeply by statistical analysis on joints produced with optimized joining parameters to minimize the formation of defects and consequently improve the mechanical performance of joints.

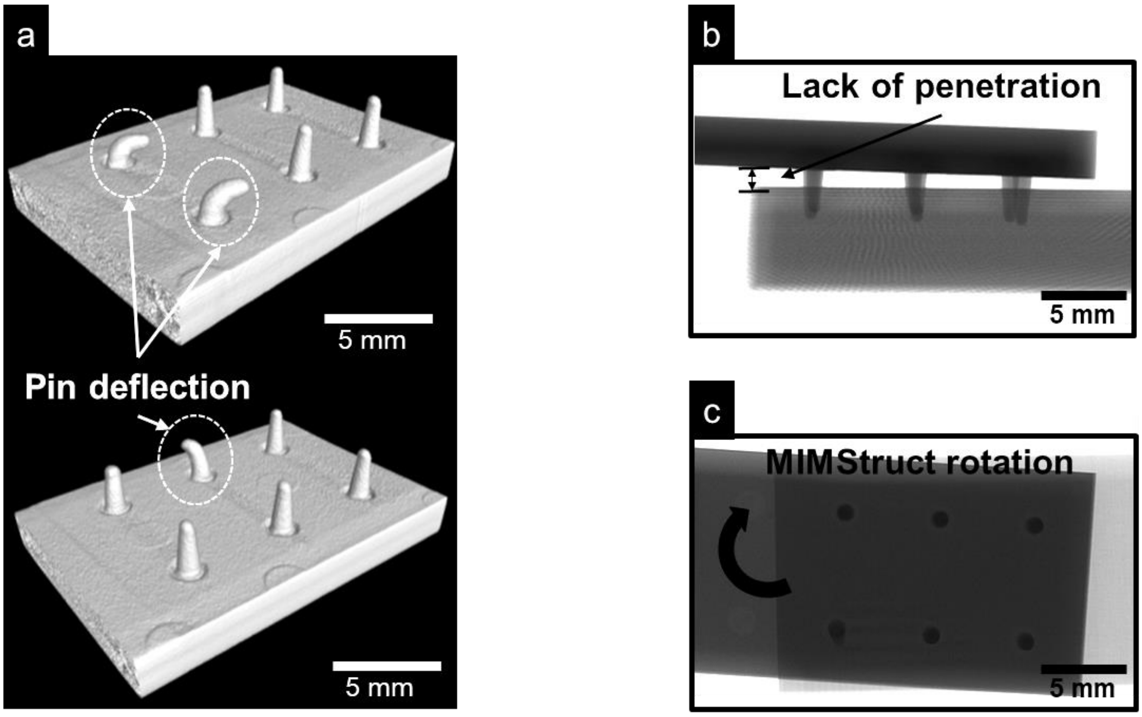

Figure 8-20: (a) Examples of pin deflection measured by µCT (joining condition: 2400 J, 52 µm and 138 kPa), (b) lack of penetration of the MIMStruct part (joining condition: 1200 J, 42 µm and 69 kPa), and (c) MIMStruct rotation (joining parameter 1200 J, 42 µm and 69 kPa).

CHAPTER 9. MECHANICAL PROPERTIES UNDER QUASI-STATIC LOADING

This chapter is devoted to the mechanical properties of joints evaluated under lap shear quasi-static loading. These mechanical tests were performed using a customized geometry according to Section 5.3.10.1., which emulates the application of the U-Joining joint as small connectors. In addition, it replicates the overlapped joint configuration that is typically used to assess adhesively bonded and mechanically fastened joints. In this chapter, not only is joint mechanical performance evaluated, but also critical areas of stress concentration and joint failure micromechanisms. Such analyses were supported by finite element analysis (FEA) and analytical modeling of loading scenario. In this context, the chapter starts with a general description of the loading scenario followed by the single lap joint mechanical properties. Subsequently, its fracture mechanisms are identified and explained. Towards the end of the chapter, the effect on mechanical properties of the joint by HIP treatment of the MIMStruct part prior to joining is investigated.

9.1 Mechanical properties under lap shear loading

The joint’s asymmetric geometry and material stiffness mismatch play significant roles in the loading bearing behavior during lap shear testing. When a shear loading F is applied to the overlapped materials, due to the eccentric load path an out-of-plane displacement is observed in both plates, with respect to their neutral line, Figure 9-1 (a). Such a phenomenon is typically observed in an overlap joint configuration and is commonly known as secondary bending (SB) [269,270]. The resultant moment M_R induced by F, which creates the SB, is transmitted to the pins, as shown in Figure 9-1 (b). For analysis reference the pins inserted in the composite plates within the same row are numbered from 1 to 3, from left to right, as shown in Figure 9-1 (a). Furthermore, perfect contact between the pins and composite volume is assumed (no clearance), as was reported in microstructural characterization of the hybrid joint. Thus, from the beginning of the loading experiment, load is transmitted to the pin and the adjacent volume, and there is no extensive load transfer due to friction.

In this respect, M_R induces a local moment M_1, to which the first pin is subjected, resulting in asymmetric pressure distribution along the pin and the surrounding composite volume. This induces tensile and compressive stresses at the base of the pin as illustrated in Figure 9-1 (c). In addition, M_1 bends pin 1 towards the loading direction, resulting in compressive stresses in the adjacent volume of the composite. The eccentricity analysis presented here was adapted from single lap bolted joints [271]. The local stresses concentrated at pin 1 and the surrounding volume of composite are believed to be similar in all pins, although their intensity and distribution may vary along the overlap area. To investigate further the stress distribution in this region, FEM was applied. The FE model proposed and its validation are presented in Appendix A.5.

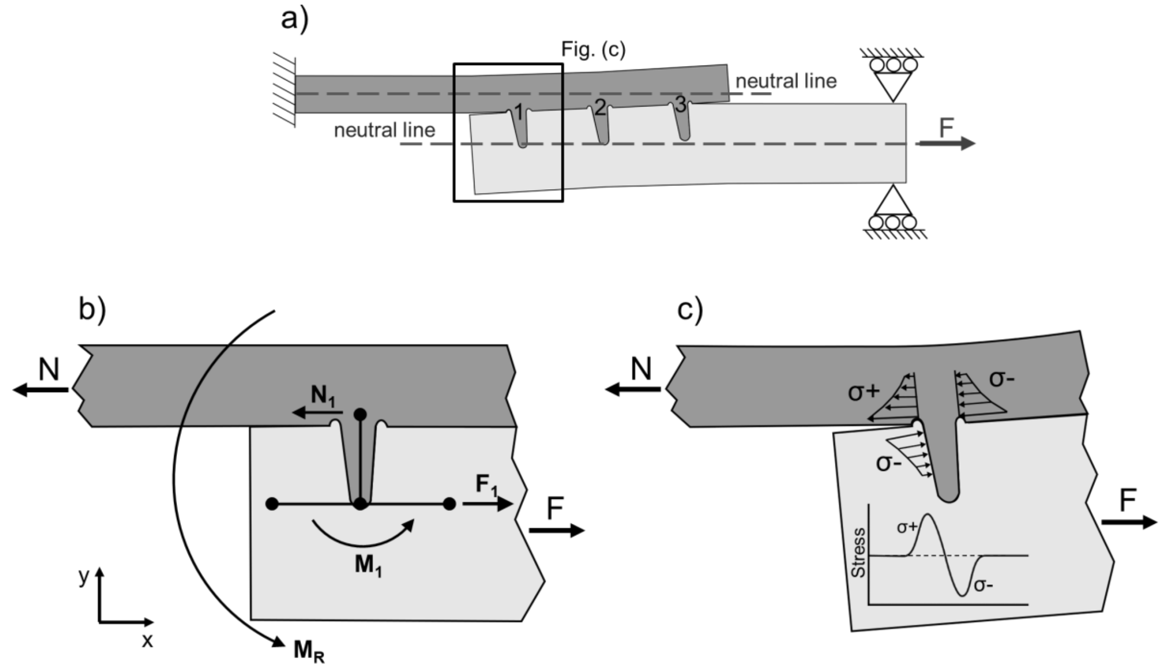

Figure 9-1: (a) Out-of-plane displacement in a U-Joining metal-composite overlap joint due to an eccentric loading path, adapted from [271]**, (b) bending moment (M_1) over pin 1, and (c) stress concentration at the base of the pin due to M_1.**

Figure 9-2 (a) presents the normal stress concentration along the metallic part of the joint and Figure 9-2 (b) the resultant shear stress profile as predicted by FEM. The stress concentration created in the normal direction of loading is in agreement with the previously elaborated analytical model. At its base the first pin experiences tensile and compressive stresses, Figure 9-2 (a). However, the magnitude of tensile stress is higher than the compressive. Such higher tensile stresses are created by the SB effect, as mentioned earlier. The same behavior is observed for the subsequent pins. Although stress magnitude tends to decrease from pin 1 to pin 3. This is most likely due to the out-of-plane displacement of the metallic part, which bends the pin 3 area out of the joint plane, as shown in the curve of Figure 9-2 (a). Thus, when a critical SB level is achieved, the adhesion forces between the surfaces of pin 3 and the composite are broken, and pin 3 starts to be pulled out of the overlap area, thus decreasing the stresses at its base, as shown in Figure 9-2 (a), pin 3 area.

In terms of shear stresses Figure 9-2 (b), FEM simulation showed a similar behavior to multi-fastened joints, where the outer fasteners (in this case the pins) tend to carry more load, and therefore more shear stresses, than the central fastener. In addition, the first pin bears higher tensile and shear stresses than the third. Therefore, one can expect that the failure of such joint would be caused by multiple stresses, starting from pin 1, at the higher stress concentration region Figure 9-2 (c), and for this to propagate towards pin 3.

The SB effect formed during loading of the U-Joining joint was evaluated by a digital image correlation system (DIC) and the results of this are presented in Figure 9-3. Due to the thickness of both materials (i.e., high stiffness) the maximum out-of-plane displacement measured during the test was relatively low. It corresponded to 0.33 mm for the Ti-6Al-4V part and 0.30 mm for the GF-PEI plate. That means the composite plate appears to be slightly stiffer than the titanium sheet. Moreover, shortly prior to failure during the lap-shear test the pins are partially removed from the composite material, forcing the titanium sheet to bend further. This result is also in perfect agreement with the SB observed by FEA, Appendix A.5.

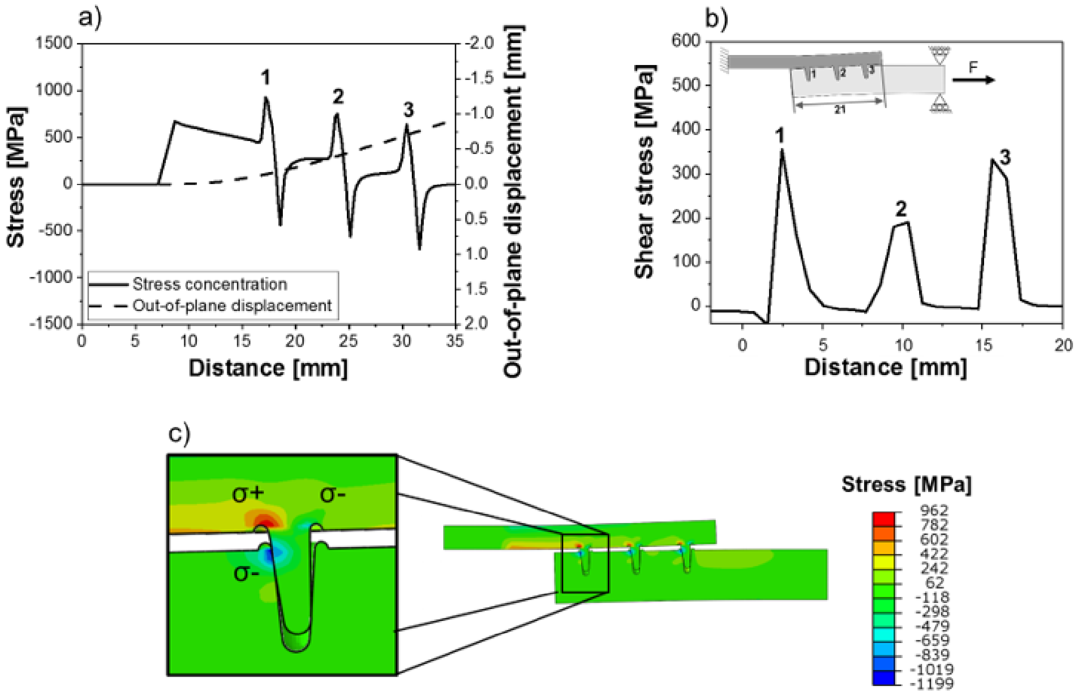

Figure 9-2: Stress analysis based on FEM. (a) Normal stresses at the pin base and out-of-plane displacement along the joint metallic part, (b) shear stress distribution along the joint overlap area (metallic side), and (c) graphical representation of the stress concentration normal to the loading direction by FE analysis.

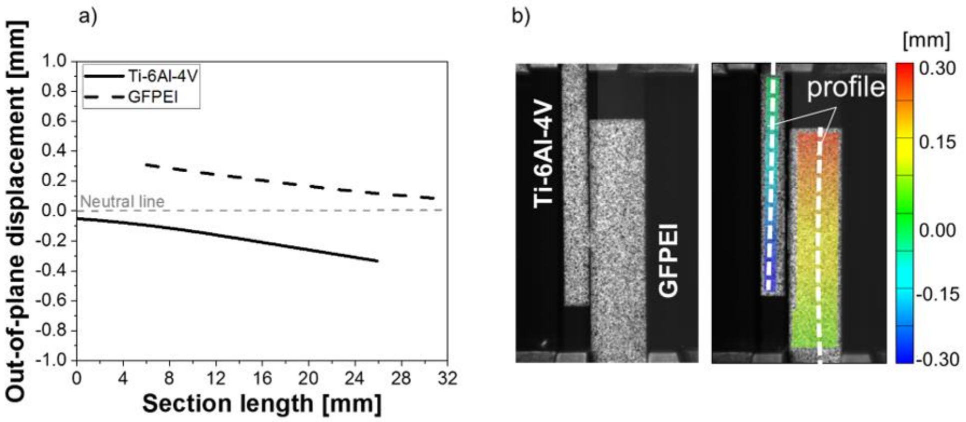

Figure 9-3: (a) Out-of-plane displacement measured by digital image correlation (DIC), and (b) images acquired during the lap shear testing, where the left picture consists of the specimen before loading and the right corresponds to a picture with the overlaid strain field as calculated by DIC. In order to acquire the strain fields a typical speckled black contrast pattern was applied over the white painted specimen surface, as observed in the picture on the left.

An example of load versus displacement curve obtained for the U-Joining joint during lap shear testing is presented in Figure 9-4. While under load the joints presented sharp transitions in stiffness due to joint damage. Initially (between Stages I and II, in Figure 9-4 (a)), deformation takes place in the elastic regime with both bonding mechanisms (mechanical interlocking and adhesion forces) contributing to load bearing. In Stage II SB starts to be noticeable as shown by the DIC results in Figure 9-4 (b). At this point the strain is mainly distributed over the outer regions of the overlap area. When the applied load surpasses the mechanical resistance of the consolidated polymer layer, adhesive failure takes place (Stage III), and the failure starts to propagate throughout the consolidated layer until the load reaches its maximum value in Stage IV. At this point the load is mainly borne by the pins, which result in failure of the first row of pins. As earlier described, due to the higher stress concentration on pin 1, the pin row that contains it should undergo the first breaking. This results in a sharp decrease in stiffness, as observed in Stage IV. After the first break, the subsequent failure of the remaining pins is observed. Therefore, after failure starts, the pins tend to slow down the propagation rate, having crack-arresting effect and increasing fracture toughness.

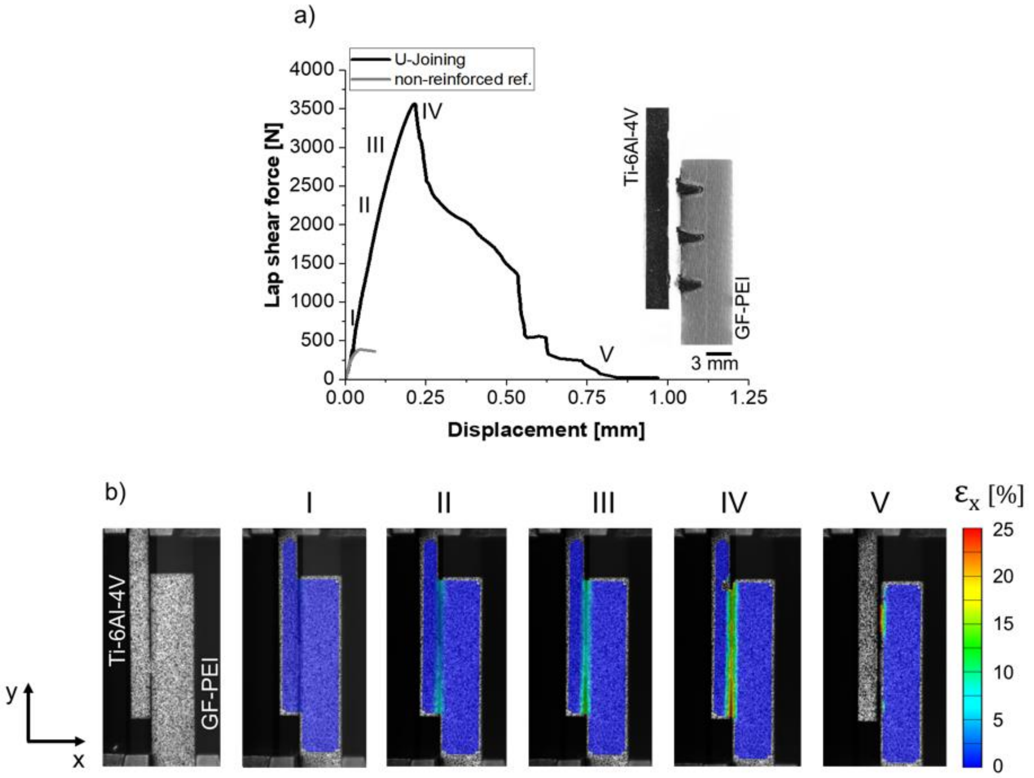

Figure 9-4: (a) Example of a typical lap shear force-displacement curves for a hybrid U-Joining joint, and (b) strain field (ε_x) measured by DIC in the out-of-plane direction.

9.2 Failure mechanism and fracture surface analyses

To evaluate damage initiation and propagation during the lap shear testing, loading-unloading experiments were performed as described in Section 5.3.10. Three loading cycles were investigated with different load levels (i.e., 1000, 2000 and 3000 N); the results are presented in Figure 9-5 (a). Each loading-unloading cycle was performed with a different replicate specimen to avoid accumulated damage from the previous cycle. After testing the specimens were characterized microscopically by SEM, and the results are presented in Figure 9-5 (b) – (g).

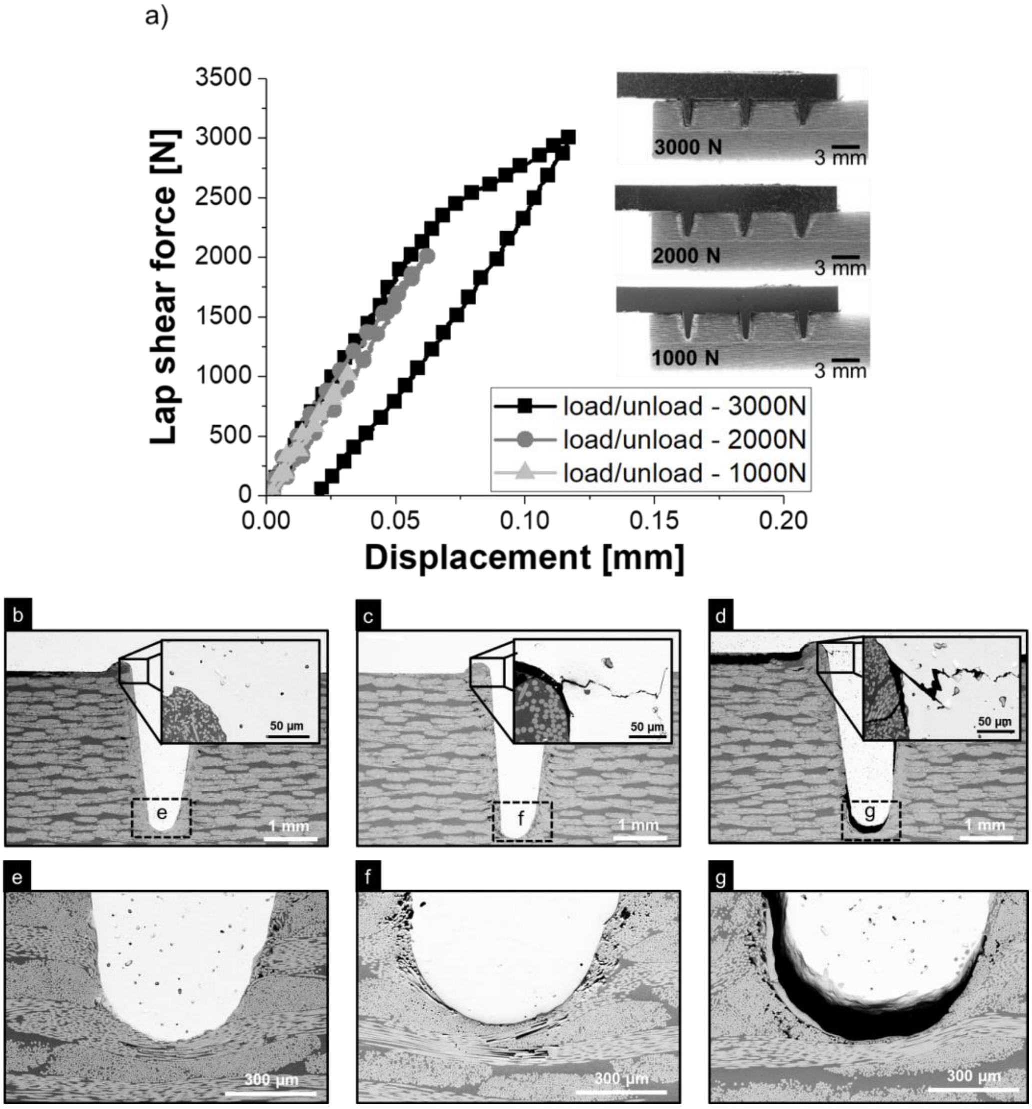

Figure 9-5: (a) Lap shear force-displacement curves obtained from the loading-unloading experiments, with SEM micrographs of the loaded-unloaded samples at loading levels of (b) 1000, (c) 2000, and (d) 3000 N, and (e), (f), and (g) the respective detail images at the tip of pin 1.

The loading-unloading curve resulting from the first loading level displays a perfect elastic behavior. All deformation to which the joint was subjected is recovered elastically. Therefore, after the joint reaches a predefined maximum load of 1000 N (with deformation of 0.03 mm), the curve returns to zero. In addition, there is no damage observed in its SEM micrographs (Figure 9-5 (b) and (e)). A similar response was observed for the joint loaded at 2000 N, where no significant damage accumulation was observed in the loading-unloading curve and the joint fully recovered elastically. However, when examining the SEM cross-section samples, it is possible to see the nucleation of a small crack at the undercut of the first pin (Figure 9-5 (c)). As stated earlier, higher stresses are concentrated in this region, which most likely suppressed the strength of the MIM-structured pin when the joint is loaded with 2000 N, therefore creating a 142 µm long crack. Although a crack is formed at this loading level, it is interesting that the adhesion forces were not broken, as observed in the detailed image in Figure 9-5 (f) along the interface between metallic pin and CTMAZ, suggesting a strong and efficient bonding between metal and composite at a small scale.

Additionally increasing the load causes considerable damage to the joint. At 3000 N, the crack that nucleated in the pin undercut propagates further, and adhesion forces between metal and composite start to break, Figure 9-5 (d) and Figure 9-5 (g) respectively. Moreover, the loading-unloading curve reveals a considerable plastic deformation, especially after 2500 N, which is not recovered after unloading. Such an unrecovered deformation combines plastic deformation of the pins and irreversible damage propagation. The latter is a combination of debonding (i.e., breakage of adhesion forces), pull out of the pins from the composite and crack propagation at the base of the pins. Although failure has already started and further propagates at this level, the joint still does not fail entirely at 3000 N loading. For the material combination studied in this PhD work, a complete failure by pin shear-off occurs at 3608 ± 417 N (for the optimized joining parameters).

Fracture analyses of a U-Joining joint are presented in Figure 9-6. The compressive zone (Figure 9-6 (c)) created by the bending moment, to which the pins were subjected, causes considerable damage to the composite, as shown in Figure 9-6 (b).

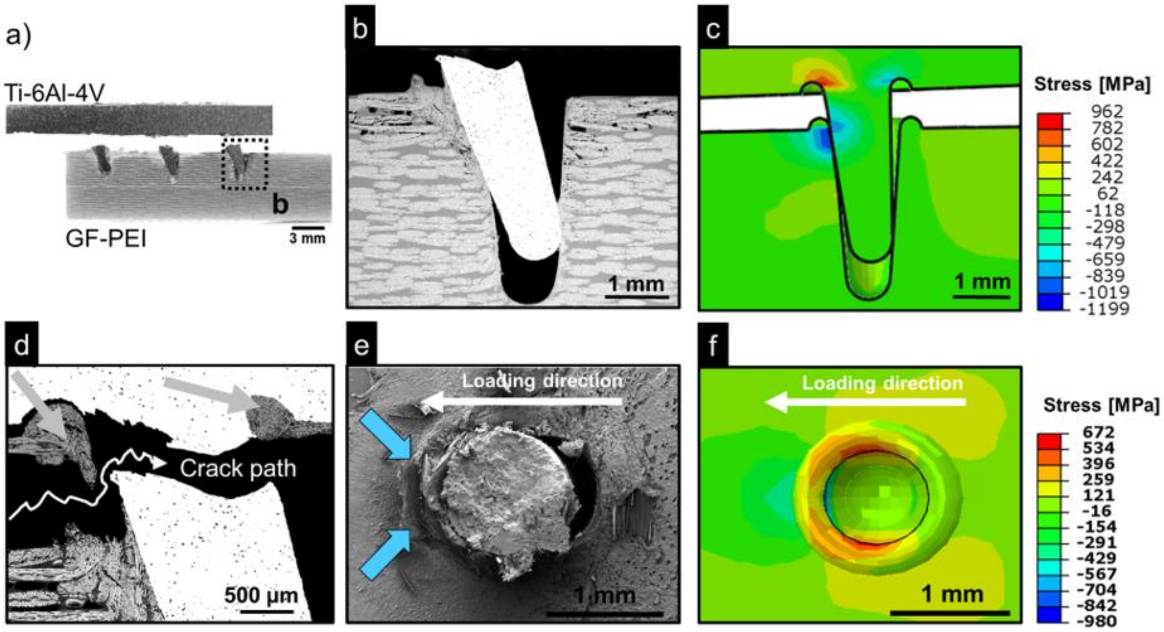

Figure 9-6: (a) Overview of a fractured hybrid joint, (b) SEM micrograph of pin 3, and (c) its respective stress field obtained by FEM, (d) crack path at the pin area and indication of cohesive failure in the composite part (grey arrows), (e) SEM image showing the composite fracture surface deformation due to load transfer by the pin, and (f) its respective stress field.

In this zone, microcracks propagated through the composites, connecting the process-induced volumetric defects. The damage induced, which is not only restricted by the reconsolidated layer of the polymer composite (i.e. the CTMAZ), is an indication of efficient load transfer through the thickness of the composite. In addition, surface analysis of a broken pin revealed considerable plastic deformation of the composite volume adjacent to the pin, as shown in Figure 9-6 (e) (blue arrows). Such a behavior agrees with the stress fields predicted by FEM (Figure 9-6 (f)) and corroborates the assumption of an effective load transfer between metal and composite due to the pin interlocking effect in the U-Joining joints.

The failure path is presented in Figure 9-6 (d). Failure is believed to start at the interface between the parts (consolidated polymeric matrix layer) and propagates from pin 1 through the overlap area towards pin 3, as previously proposed. Although it does start at the interface between Ti-6Al-4V base plate and GF-PEI, its propagation is not only characterized by adhesive failure. Regions where the failure propagates inside the composite (i.e., cohesive failure) are indicated by gray arrows in Figure 9-6 (d). This therefore suggests that failure propagation in a U-Joining joint has a more complex failure mechanism, linking a mixed cohesive-adhesive failure in the consolidated molten layer of the polymer and shear-off of the metallic pins. In order to further investigate the micromechanisms of failure, analysis of the fracture surfaces were carried out by SEM, and a discussion of these results follow.

As suggested in the previous statement, SEM surface fracture analyses of the U-Joining joint indicated complex mixture of mechanisms of failure. The micromechanisms involved in the failure will be addressed first by looking at the SEM fractographic images obtained from the surface of the metal part (Figure 9-7), followed by those of composite (Figure 9-8).

3D-rendered images obtained by LSCM of the fracture surface showed that the shear cracks initiated at and propagated from the bottom of the pins, Figure 9-7 (a), directly above the undercut feature. As a result, after failure the pins remained inserted in the composite part. The fracture surface of a broken pin reveals two distinct zones. The first is characterized by a rougher surface and the second by a flat and smoother surface. Such a behavior reflects the micromechanisms of crack propagation within the metallic pins during a lap shear test. The first zone mentioned corresponds to nucleation of the shear cracks, and it is characterized by a slow failure propagation regime. As a result, an entirely ductile behavior is observed, which allows for the nucleation, growth, and coalescence of dimples (Figure 9-7 (b) and in high-magnification detail in Figure 9-7 (c)). Due to the considerable number of residual pores distributed in the Ti-6Al-4V MIMStruct part, which typically act as failure nucleating sites, the precise site of crack nucleation n could not be identified. However, it is believed that crack initiated at multiple sites, where higher tensile and shear stresses are concentrated as previously mentioned.

When the crack reaches its critical size, the remaining metallic material in front of the crack is rapidly overloaded and fracture propagates catastrophically. This results in the formation of a flat and smooth fracture surface, thus indicating less local plastic deformation prior to final failure, as shown in Figure 9-7 (b) and in high-magnification detail in Figure 9-7 (d). Due to the fast and catastrophic propagation of this second zone, shallow dimples are formed, oriented towards the overall failure growth direction.

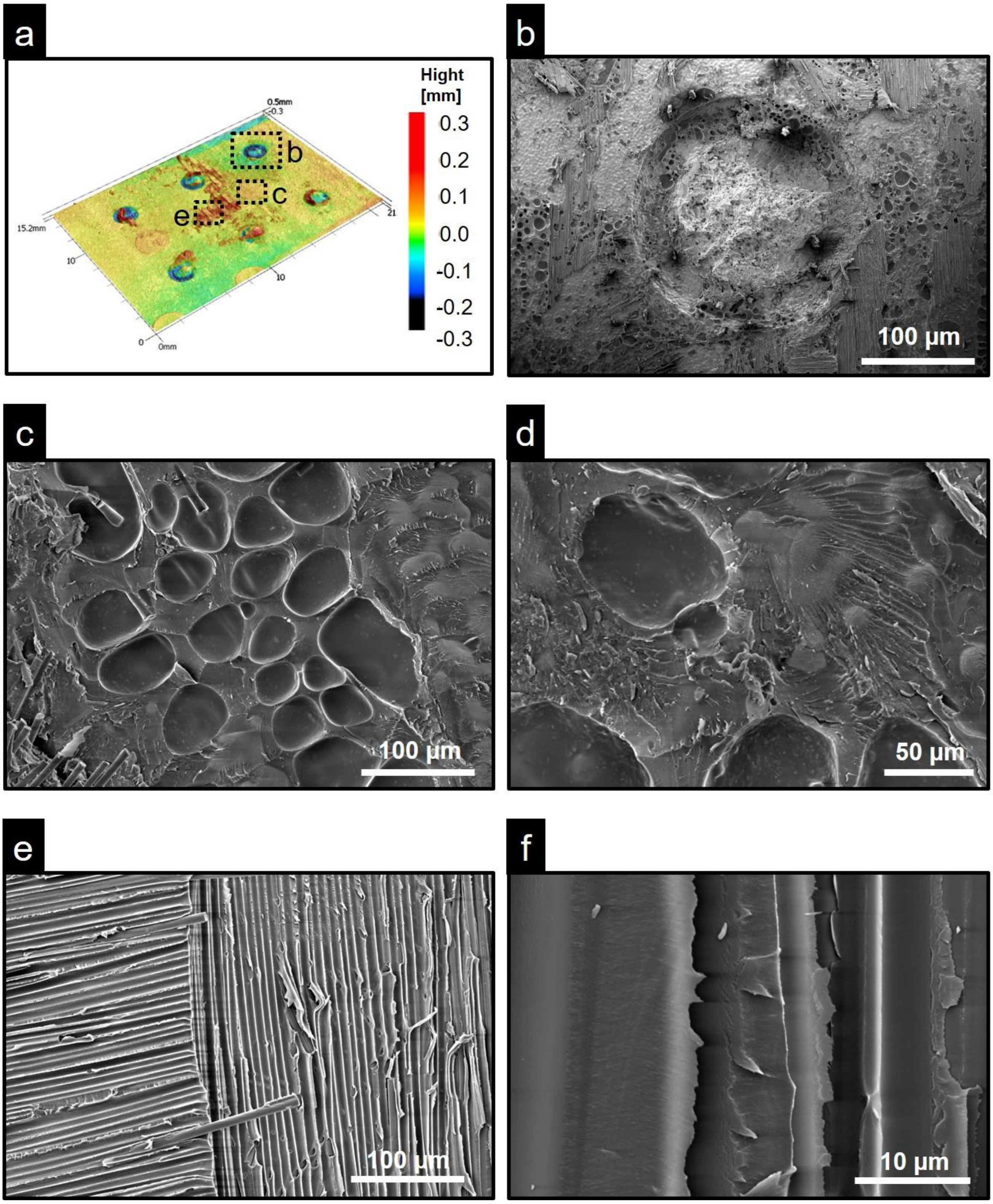

Figure 9-7: (a) 3D reconstructed image of the metal part fracture surface obtained by LSCM, (b) SEM overview of the fracture surface of a pin, (c) SEM image of the slow failure propagation region, (d) fractograph of the fast failure propagation region, (e) polymer attached to the surface of the metallic part after fracture, and (f) bundles of fiber attached to the metallic surface after fracture.

Apart from the micromechanisms of pin fracture, it was observed that on the metallic surface a considerable amount of polymer remained attached. It therefore indicates once again that the molten polymer had efficiently wetted out the Ti-6Al-4V surface, forming strong adhesion forces between the materials after joint consolidation, Figure 9-7 (e) and (f). In addition, the cohesive failure propagated either between the first layer of consolidated polymer matrix and fibers or between a deeper fiber layer and matrix. In the first case (Figure 9-7 (e)), process-induced thermal voids are exposed, suggesting that cohesive failure propagates through the voids. In the second case, however, bundles of fiber were exposed, as shown in Figure 9-7 (f)), which reinforces the assumption of strong adhesion forces at the interface between the metal and the consolidated polymeric layer.

An overview and detailed SEM fractographic images of the joint's composite part are depicted in Figure 9-8. After joint failure, fractured and considerably deformed pins remained inserted in the composite part, Figure 9-8 (b). At the adjacent zone a significant amount of broken fibers were found surrounding the pin, blue arrows in Figure 9-8 (b). These fibers were most probably broken during the joining process (i.e., pin penetration) and flowed to the undercut at the base of the pins. The overall failure is believed to start from the edge of the consolidated layer (as shown by the black arrows) and to propagate through the pins from left to right, as indicated in Figure 9-8 (b). Adjacent to the initiation region, an area with elongated fibrils, where tearing fracture at the ends of the fibrils is observed [192], Figure 9-8 (c), it therefore resembles a stable propagation failure with ductile characteristics [272].

At the center of the overlap area, where failure propagates stably, mixed regions of adhesive and cohesive failure were found, as shown in Figure 9-8 (d). The former exposes a negative of the metallic part surface roughness and is thus smoother in comparison to the latter, which exposes bundles of fibers. Besides this, the formation of morphological features known as *hackles* [101] were also observed in Figure 9-8 (e). Such features are typically observed in fracture surfaces of composites tested under mode II (i.e., shear loading). Hackles are formed by the formation of small 45° tensile microcracks in the composite matrix, as schematically shown in Figure 9-8 (f) [101].

Inside the cohesive failure region, apart from the fiber broken as observed in Figure 9-8 (d), an interfacial failure between fiber and matrix was also observed Figure 9-8 (g). Such phenomena mainly occur when warp fibers are loaded perpendicularly. In this loading direction the interface between the fibers and the composite matrix is responsible for bearing the load, and due to its lower strength, it fails. Towards the end of the failure propagation regime, a fracture surface with flat and smooth surfaces was observed, as presented in Figure 9-8 (h). Similar to the final fracture of the metallic pins, at the final stages of propagation, the consolidated polymeric layer that remains is overloaded and undergoes a catastrophic (fast) fracture. As a result, almost no plastic deformation was found.

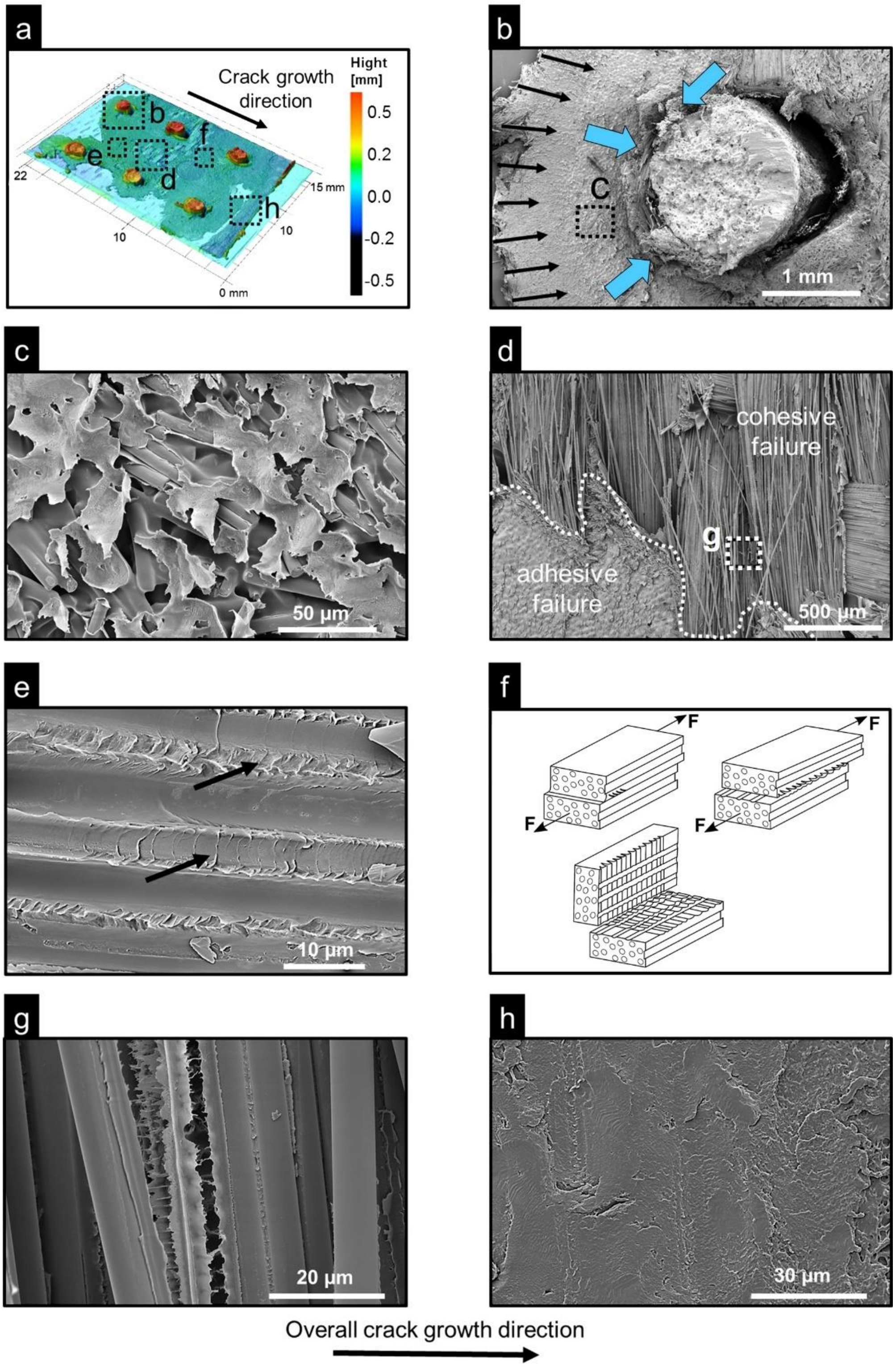

Figure 9-8: (a) 3D reconstructed image of the fracture surface of the composite part obtained by LSCM, (b) SEM overview of the fracture surface of pin 1 showing the failure nucleation site, (c) SEM image of the slow failure propagation region showing the formation of elongated fibrils, (d) adhesive-cohesive failure, (e) hackle formation at the composite matrix in a cohesive failure region, (f) illustration of the hackle formation mechanisms adapted from [101], (g) region of interfacial failure between fiber and matrix and, (h) final fracture region showing a flat and smooth failure propagation, which characterizes a catastrophic final failure.

9.3 Effect of HIP on quasi-static mechanical performance of the joint

Hot isostatic pressing (HIP) was investigated as a post-treatment strategy to further improve the mechanical performance of joints under quasi-static loading. Ferri [131] reported an increase of 17% in yield strength and 11% in fatigue performance for MIM Ti-6Al-4V parts after HIP. This suggests that residual porosity has a more significant effect on quasi-static mechanical properties than on fatigue [125,131]. However, fatigue could also be improved by a further surface smoothing treatment, such as shot peening, or by modifying the alloy composition by adding, for instance, small amounts of boron to the Ti-6Al-4V composition, as reported by Ferri, Ebel, and Bormann [134]

HIP of the MIMStruct part was carried out as described in Section 5.1.1. Similar levels of improvement to those reported by Ferri [131] were observed for the BM used in this work, which corresponded to an increase of 15% in yield strength. In addition, the residual porosity was virtually eliminated after HIP, as previously shown in Figure 5-2. However, the effect of HIP on ULSF was less pronounced (Figure 9-9 (a)), corresponding to 6.7%. The average ULSF value for the hybrid joints produced with Ti-6Al-4V parts after HIP was 3608 ± 419 N, whereas for hybrid joints produced with as-sintered Ti-6Al-4V it was 3848 ± 299 N for the optimized joining condition (i.e., E_J = 2012 J, A_0 = 52 µm, and J_p = 101 kPa (14.7 psi).

A significant increase in out-of-plane displacement was also measured by DIC, Figure 9-9 (b). The HIP Ti-6Al-4V part deforms 1.5 mm from the plane of the joining area, which corresponds to 4.5 times more out-of-plane deformation as the as-sintered part. That is mostly caused by a change in the fracture mode of joints produced with HIP parts. Due to an increase in ductility of the Ti-6Al-4V pins, pin 3 did not break during the joint failure, Figure 9-10. As explained earlier, this row of pins undergoes slight less stress concentration due to high out-of-plane displacement at this side of the overlap area. Therefore, when the joint starts to experience secondary bending, such a pin is pulled out from the overlap area. This, combined with an increase in ductility after HIP allows the pin to bend considerably without breaking, as shown in Figure 9-10 (b). During the pulling out phase, pin 3 also forces the GF-PEI plate to bend further. As a result, higher out-of-plane displacements were also registered for the polymeric part of a joint that was joined with the HIP metallic part, Figure 9-9 (b).

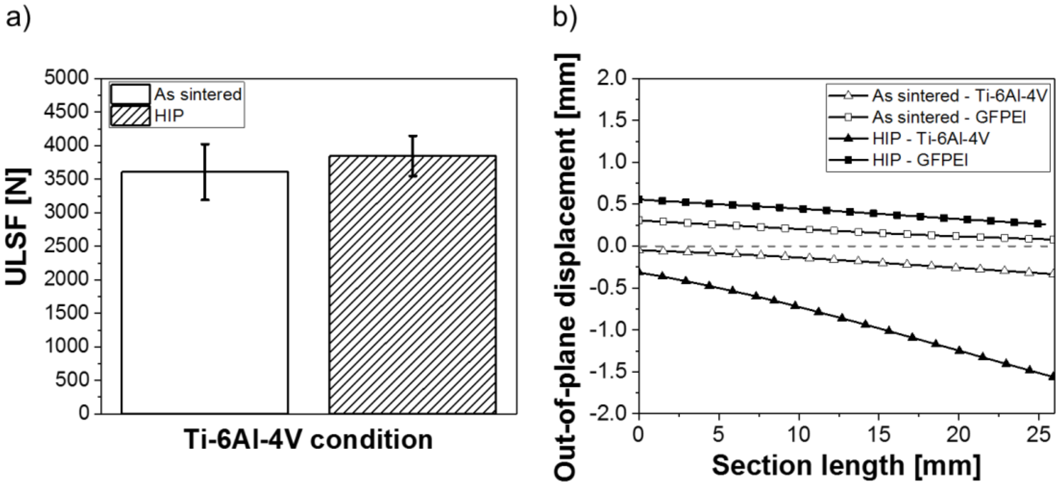

Figure 9-9: (a) Influence of the Ti-6Al-4V after HIP on the quasi-static mechanical properties of the hybrid joints, and (b) out-of-plane displacement.

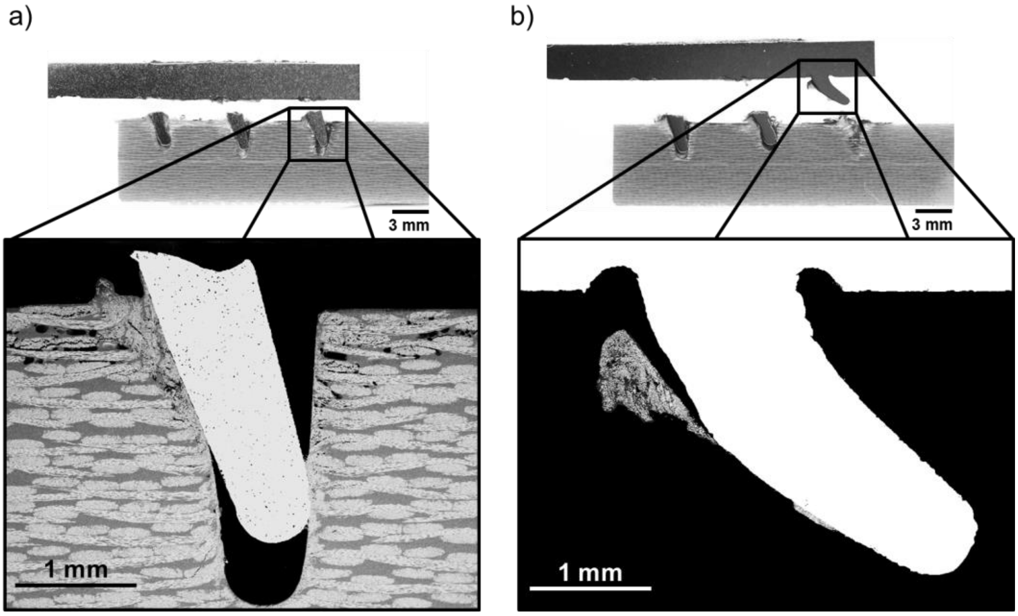

Figure 9-10: (a) Comparison between the failure modes of a hybrid joint produced with an as-sintered Ti-6Al-4V part, and (b) with a HIP Ti-6Al-4V. The joint joined with a HIP part allows pin 3 to be removed without breaking, due to improved ductility.

Apart from changing the fracture mode, especially in the pin 3 row, the fracture surface of the broken pins (i.e., pins 1 and 2) revealed much more ductile micromechanisms of failure compared to the joint condition when joined with an as-sintered Ti-6Al-4V part Figure 9-11 (a). The dimples spread all over the fracture surface are large and more profound than those observed previously, Figure 9-7 (c). Therefore, more local plastic deformation took place prior to joint failure. In addition, the HIP pins cause pronounced deformation of the composite part, as shown in Figure 9-11 (b) while bearing the lap shear test load. Hence, this suggests an improvement in load transfer between the materials after HIP.

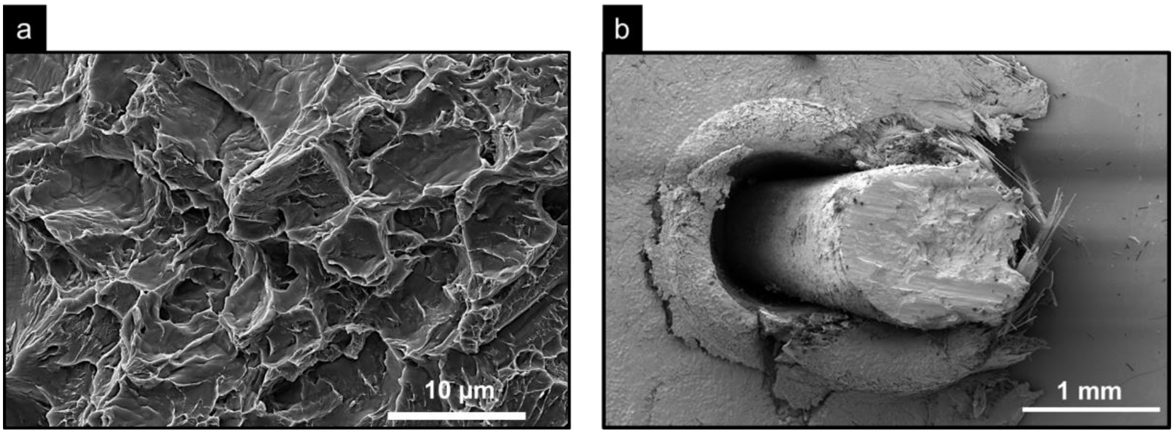

Figure 9-11: (a) SEM fractography of pin 1 of a hybrid joint produced with a HIP Ti-6Al-4V part, and (b) the effect of load bearing in the adjacent composite volume caused by a HIP Ti-6Al-4V pin.

CHAPTER 10. MECHANICAL PROPERTIES UNDER CYCLIC LOADING

This chapter deals with the fatigue performance of U-Joining joints. The joint's fatigue life assessment was performed using a two-parameter Weibull distribution. Hence, S-N curves that consider different reliability levels were obtained, providing an effective evaluation of fatigue data scattering. Moreover, a failure analysis of the U-Joining joint is provided as well as the micromechanisms of fracture under cyclic loading.

10.1 Fatigue life assessment of the U-Joining joints

Fatigue life curves (S-N curves) are derived from experimental data, which should cover a wide range of stress levels and corresponding numbers of cycles to failure. According to the guidelines provided by ASTM E739 for "research and development testing of components and specimens" [188] a percent of replication between 33 – 50 is required (percent replication = 100 [1-(total number of different stresses used in testing / total number of specimens)]). In this work, a percent replication of 66.7 was calculated, which allow the data for further use in design development [188]. The percent replication levels therefore correspond to higher levels than those required for a research and development phase. Thus, by ensuring that sufficient data was collected and adequate replication was performed a reliable characterization of fatigue behavior of the joint was achieved.

The data obtained are presented in the scatter plot of Figure 10-1. Five load levels were investigated with three replicates per level. The fatigue limit was defined as the load level below which no failure would occur before 10^6 cycles. In the scatter plot of Figure 10-1, the joints that surpassed this fatigue endurance limit (run-outs) are indicated by black arrows. The load level at the fatigue limit corresponds to 30% of the ULSF (i.e., 1082 N).

Three different models were applied to formulate the S-N curves of the obtained data. The linear models recommended by the ASTM standard, which are exponential (log-linear), power law (log-log) fit, and two-parameter Weibull distribution. It is worth noting that fatigue life data in this chapter are presented as a function of Load-Life (F-N) and not Stress-Life (S-N). Although the terminology S-N is used due to common practice in the literature. All three of the proposed models fitted well with the experimental data over the measurement range (10^3 – 10^6), as observed in Figure 10-1. However, the exponential model exhibits a more conservative prediction of fatigue life, especially at low cycle fatigue (LCF) and high cycle fatigue (HCF), at the extremes of the evaluated range, below 10^3 and above 10^6 cycles. In addition, power law fit and Weibull distribution present similar predictability at HCF, although at LCF Weibull is more conservative. Similar behaviors of these models is expected as the two-parameter Weibull distribution also obeys a power law function. The adequacy of the first two models (i.e., exponential and power-law) used to describe the fatigue data were statistically tested and validated. The procedure adopted is briefly described in Appendix A.6. A more in-depth discussion of the two-parameter Weibull distribution will be given in the next section.

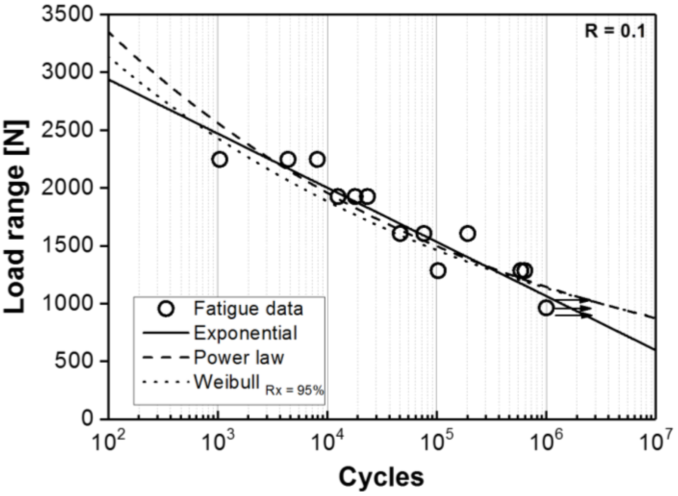

Figure 10-1: Fatigue life scatter plots for a U-Joining joint and fitted S-N curves according to the exponential, power law, and two-parameter Weibull (reliability level R_x = 95%) models.

In order to compare model predictions in the range of testing, fatigue life at 10^5 cycles was calculated for each model, Table 10-1. The fatigue life at 10^5 cycles is commonly used in the aircraft sector to evaluate and compare the performance of new designs [273]. However, here it was only investigated as a procedure to compare the predictability of the different fit formulations. In contrast to the observations previously mentioned, the exponential fit presented a less conservative prediction at 10^5 cycles, followed by the power law and Weibull. The latter was fitted with a reliability level of 95%.

Table 10-1: Fatigue life predicted at 10^5 cycles by each fitted formulation studied in this work.

Model	Max. load at 10^5 cycles [N]	% of ULSF 10^5 cycles [%]
Exponential	1724.6	47.8
Power law	1677.7	46.5
Weibull (R_x = 95%)	1623.6	40.9

10.1.1 Statistical analysis using the two-parameter Weibull distribution

The two-parameter Weibull distribution (2-P WD) was chosen for further statistical analysis of fatigue life due to its popularity in the literature, which is mainly related to its versatility and ease of determination [274,275]. Such a distribution has been applied extensively, for instance in the fatigue assessment of composite materials [274–276], magnesium alloys [277], and aluminum spot welds [278], and it provides a useful evaluation of fatigue data according to reliability curves. In addition, 2-P WD provides a more conservative prediction than comparison with three-parameters [279]. A complete description of the 2-P WD as well as the mathematical formulation, calculation, and graphical analyses used to obtain the S-N curve with different reliability levels are presented in Appendix A7.

The S-N curves obtained for the different reliability levels are presented in Figure 10-2. Such curves provide a useful tool for safe structural design, and one can adjust the reliability level to fit project requirements. For instance, in primary aircraft structural applications, where safety concerns are high, one could consider a high-reliability level, such as 99.9%. Thus, based on the obtained S-N curve and considering the experimental scattering (i.e. according to the Weibull distribution), the fatigue life at 10^5 cycles would correspond to 38.5% of the hybrid joint ULSF, Table 10-2. Here again, the characteristic fatigue life at 10^5 cycles was calculated in order to evaluate the fatigue life for different reliability levels. Such a characteristic value of fatigue life can vary between 38.5% ($R_x = 99.9\%$) and 46.8 ($R_x = 50\%$). The predicted fatigue life from the other two models considered in this work (i.e., power law and exponential) correspond to reliability levels of 50% or lower, according to the 2P-WD. Thus it shows the importance of considering data scattering when evaluating fatigue data.

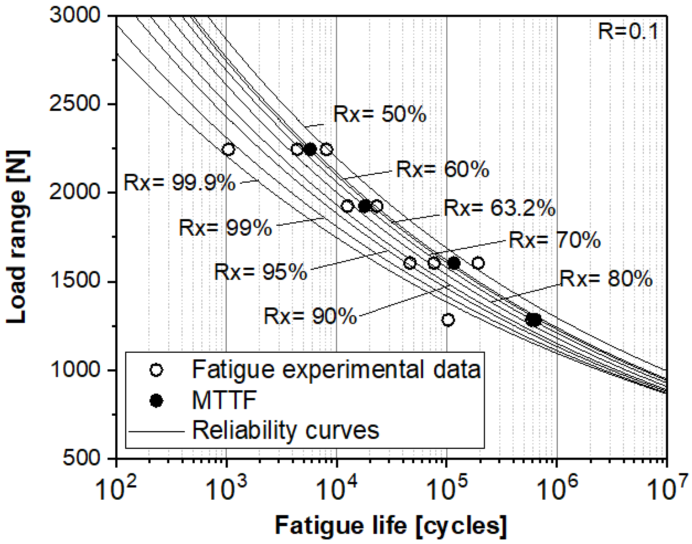

Figure 10-2: S-N curves obtained for different percentages of reliability according to the two-parameter Weibull distribution.

Table 10-2: Values of fatigue life at 10^5 cycles for different reliability levels.

Reliability [%]	Max. load at 10^5 cycles [%]	Percent ULSF [%]
99.9	1382.5	38.3
99.0	1417.7	39.3
95.0	1462.0	40.5
90.0	1491.1	41.3
80.0	1537.1	42.6
70.0	1578.2	43.7
63.2	1606.6	44.5
60.0	1620.8	44.9
50.0	1688.1	46.8

10.1.2 Residual strength after one million cycles

The fatigue limit during the experimentation phase was defined as one million cycles. After the samples have reached this characteristic value, the test is stopped, and it is assumed that the tested load would never promote failure by fatigue. To assess this hypothesis, the specimens that survived one million cycles were subsequently mechanically tested under quasi-static loading, following the same procedure as previously described in Section 5.3.10.1. Thus, the resultant residual strength after one million cycles was obtained and is presented in Figure 10-3. By comparing the residual strength values with the original mechanical performance of the optimized joint, it can be concluded that the loading level, to which the samples were subjected to reach the one million of cycles, did not promote significant fatigue damage to the joints. As a result, the average ULSF is still in the same range, considering the standard deviation of the lap shear test. The joints that survived the 10^6 cycles presented a ULSF of 3668 ± 317 N, which is in the same range as the one observed for the optimized joint condition (3608 ± 417 N).

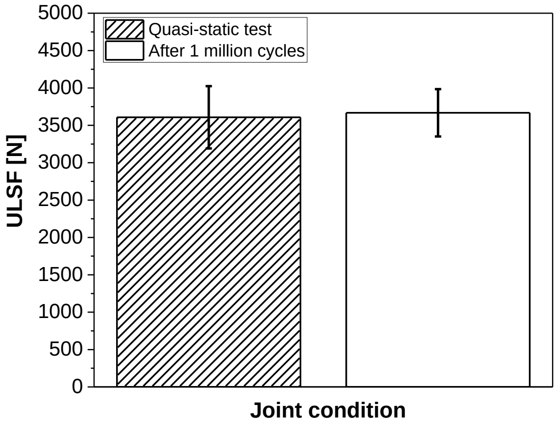

Figure 10-3: Quasi-static residual strength of the U-Joining joints after one million fatigue cycles.

10.2 Failure mechanism and fracture surface analyses

The proposed failure mechanisms of U-Joining joints under cyclic loading were similar to those previously observed for the quasi-static loading case. It is assumed that the fatigue cracks initiate at the first pin row, as shown in Figure 10-4, and propagate through the overlap area towards the third pin row. The reason for that is the higher shear and tensile stress concentration on the first pin row, as shown earlier by the FEA, Figure 9-2. The micromechanisms of fracture observed by SEM analyses of the fracture surface confirm the overall failure mechanism proposed. Following the same strategy used to discuss the micromechanisms of failure under quasi-static loading, the fracture surface of the metallic part of the joint is first analyzed (Figure 10-5) followed by the surface of the composite part (Figure 10-6).

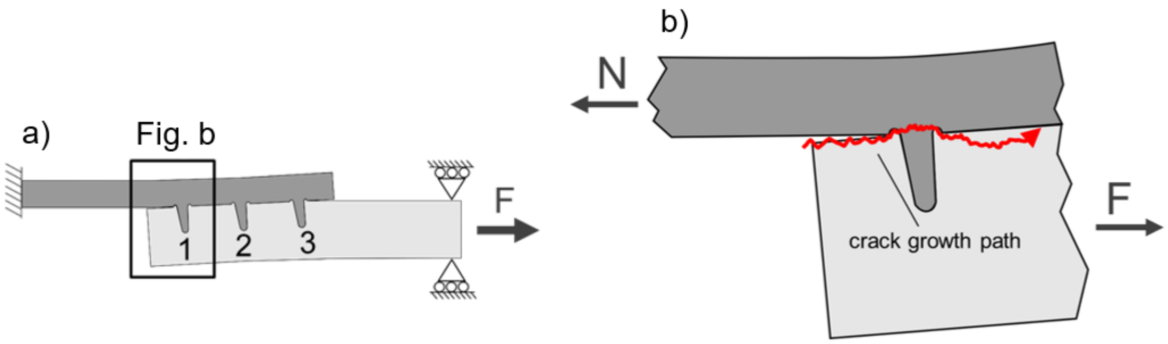

Figure 10-4: (a) Schematic illustration of the U-Joining joint, (b) and an illustration of the proposed crack growth mechanism under cyclic loading.

The overall aspects of the metallic part fracture surface resemble very much those observed for the quasi-static loading case: the fracture surface also reveals a rather complex failure mechanism, combining both adhesive-cohesive failure and shearing of the metallic pins. The former is assumed due to the high volume of composite attached to the metallic surface, which is not limited to just the matrix of the composite, but also to bundles of fiber, as shown by the black arrows in Figure 10-5 (a).

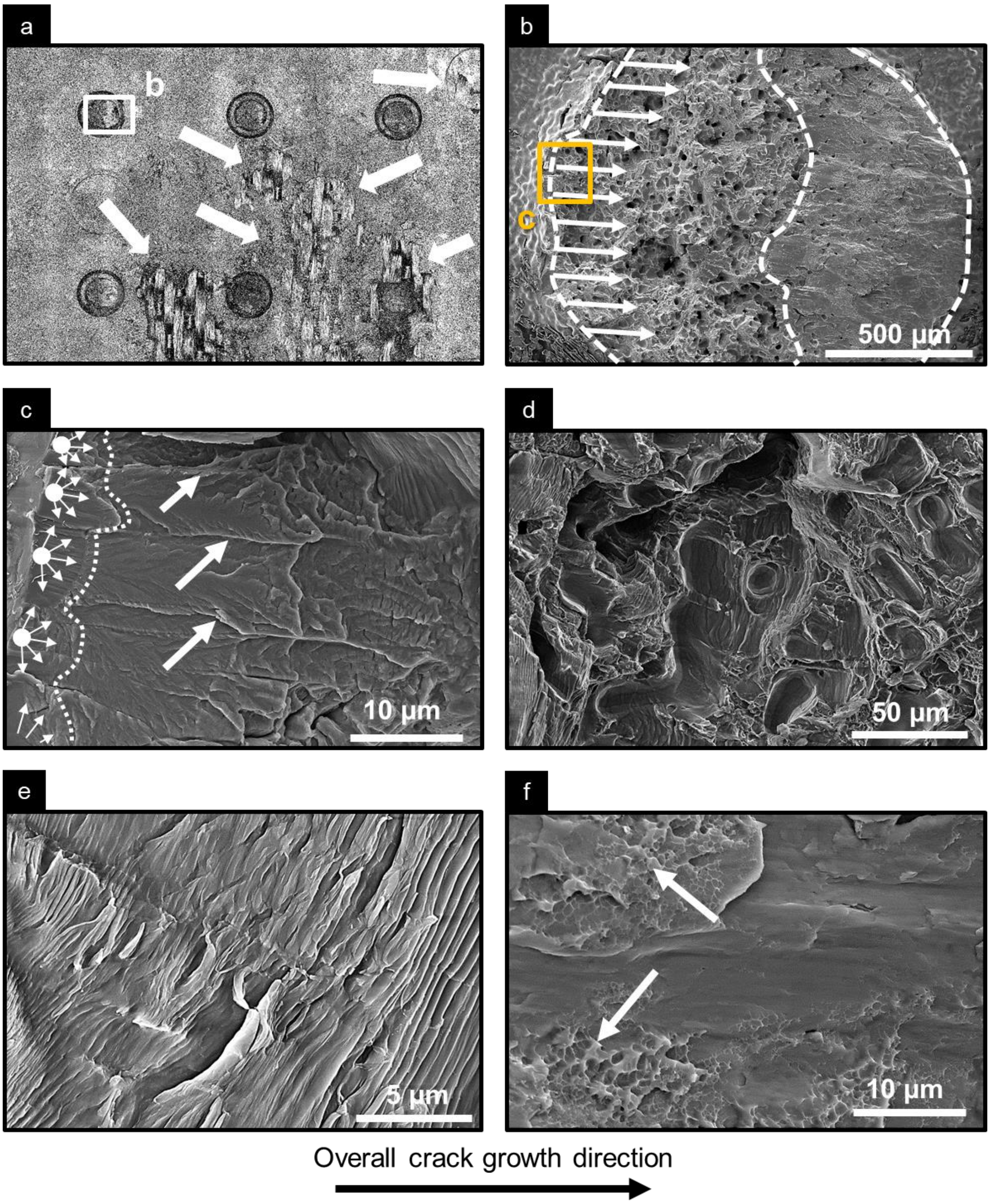

Figure 10-5: (a) LSCM overview of the joint metallic part fracture surface tested under cyclic loading, (b) SEM overview of the pin 1 fracture surface indicating the multiple cracks initiation sites, (c) high-magnification image of the cracks initiation sites, (d) detailed image of the stable crack propagation regime in different plateaus, (e) formation of fatigue striations within a plateau, and (f) crack terminal propagation phase showing dimples oriented towards the crack growth direction.

The pins also failed by shearing under cyclic loading. To provide a more in-depth investigation of crack initiation and propagation mechanism, the fracture surface of pin 1 was thoroughly investigated, Figure 10-5 (b). The morphology of its fracture surface also has features typical of a fatigue-tested specimen, with three characteristic regions: crack initiation site, stable propagation regime, and final failure, Figure 10-5 (b). Initiation of a fatigue crack is a highly surface-sensitive process [280]. Therefore, as the Ti-6Al-4V parts were used in their as-sintered state, presenting high surface roughness, it creates a favorable condition for the initiation of fatigue cracks. As a result, even the hybrid joints tested in lower load ranges presented multiple crack initiation sites as shown in Figure 10-5 (c). Due to multiple initiation, different planes of propagation are formed. When two adjacent propagation planes encounter each other, *ratchet* marks are formed [280,281], as indicated by the black arrows in Figure 10-5 (c). Such features characterize the initial crack propagation regime and point in the overall crack growth direction. Within the stable crack growth regime several plateaus of propagation were observed (i.e., cracks propagated with multiple elevations with respect to each other [280]), Figure 10-5 (d). Inside of each plateau, fatigue striations are formed, as presented in Figure 10-5 (e). Each striation is formed by one loading cycle and they are generally aligned perpendicularly to the overall crack growth direction.

When crack propagation reaches a critical size, the material retained in front of the crack tip is considered overloaded. As a result, it fractures catastrophically. This changes from a stable propagation regime, with the formation of fatigue striations, to fast growth mechanisms. As a result, an abrupt change in the morphology of the fracture surface is observed. When the crack enters its terminal propagation phase, striation formation is progressively substituted by morphological features that resemble quasi-static failure [280], such as dimples, Figure 10-5 (f). Such dimples are found orientated in the terminal propagation direction, as indicated by the black arrows. In addition, due to the fast rate of propagation, only shallow dimples were formed, indicating a lower degree of plastic deformation in this area. The propagation regimes and morphological features described for this particular pin were also observed systematically for the others.

In the framework of the composite fracture surface (Figure 10-6), similarities were also found in comparison with quasi-static failure. The fatigue crack propagates by a mixture of adhesive-cohesive failure, Figure 10-6 (a). As a result, bundles of fiber were exposed in the composite surface. The crack initiation, or debonding of the adhesion layer, is believed to start at the consolidated polymeric layer close to pin 1, as shown in Figure 10-6 (b). In this region, marks indicating the debonding direction could be found. In addition, at the center of the overlap area, Figure 10-6 (c) and (d), progressive marks were observed, which are perpendicularly oriented with respect to the failure growth direction. Such marks resemble fatigue striation, although they are most probably formed by the previously mentioned hackling mechanisms [101], as shown in detail in Figure 10-6 (e). Finally, towards the end of the overlap area (left-hand side of Figure 10-6 (a)), the terminal propagation of debonding is observed, Figure 10-6 (f). Due to the fast final propagation this region is characterized by a smooth fracture surface, which resembles a brittle fracture (i.e., the fast propagation rate does not allow for local plastic deformation) in polymers [101].

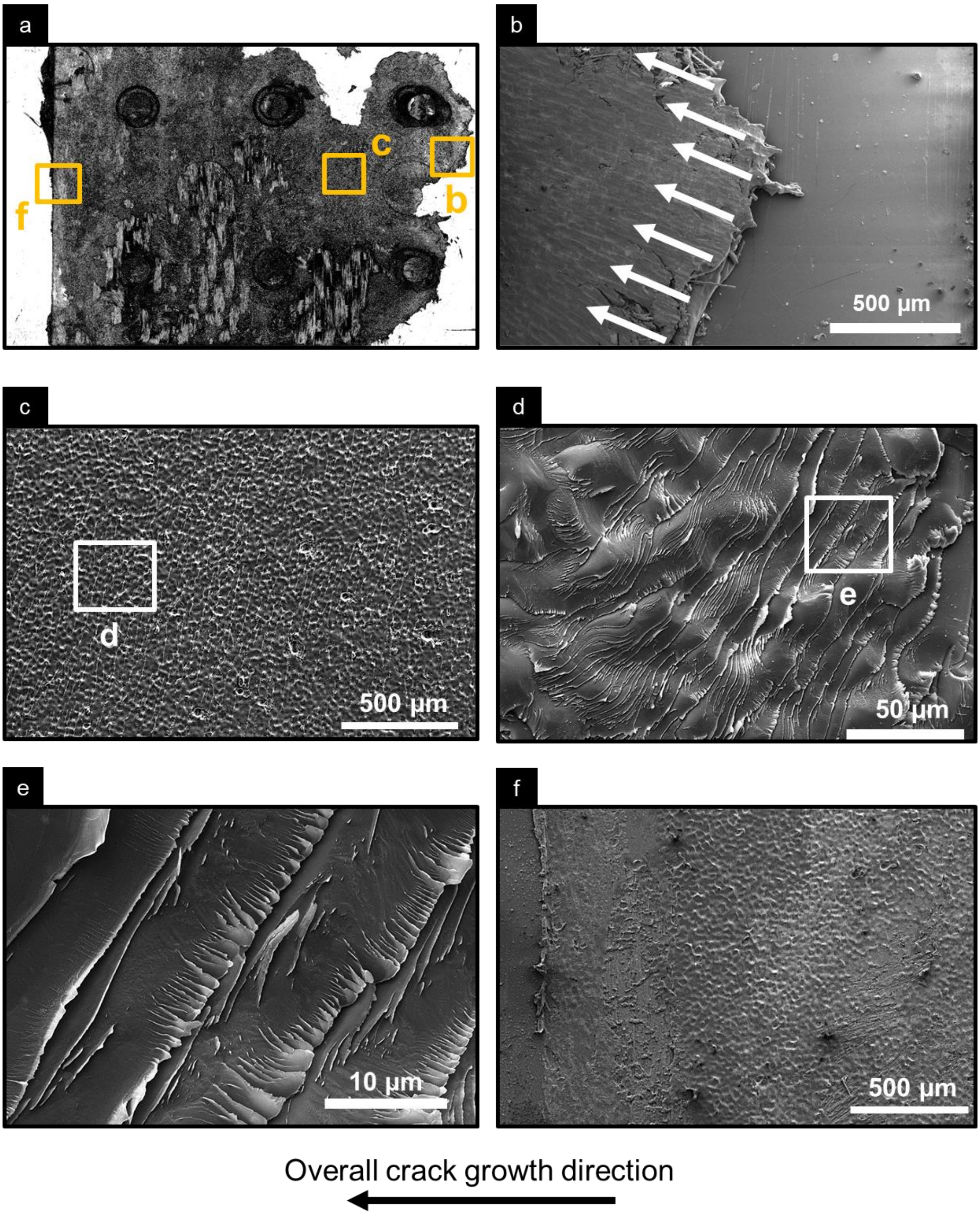

Figure 10-6: (a) LSCM overview of the fracture surface of the composite part of the joint under cyclic loading, (b) SEM overview of the probable debonding area, (c) overviews of the propagation regime at the center of the overlap area, (d) detailed image showing formation of perpendicular marks in respect to overall propagation that resemble hackles, in (e) high-magnification, and (f) terminal debonding phase, which shows a smooth surface with low plastic deformation.

CHAPTER 11. EFFECT OF PROCESS PARAMETERS ON THE JOINT QUASI-STATIC MECHANICAL PROPERTIES

In previous chapters, the main characteristics of the joints were elucidated. These included the mechanisms by which the joint are formed and the primary bonding mechanisms that act to hold the materials together. In addition, the effect of the joining process on the joined material microstructure, physical-chemical and local properties were explained and evaluated through a broad characterization of the ultrasonically joined overlap connections. In addition, the performance of joints under quasi-static and cyclic loading was investigated, fulfilling important knowledge gaps in the literature related to the joining of TTR hybrid joints. However, in this chapter the engineering objectives of this PhD work are addressed. Such objectives include further understanding the effect of U-Joining process parameters on the mechanical properties of the Ti-6Al-4V/GF-PEI joints, making it possible to optimize them to produce joints with higher ULSF. To achieve these goals, a Box-Behnken design (BBD) of experiments was applied. In this way the individual and combined effects of each joining parameter on the ULSF and lack of penetration (LoP) were evaluated by response surfaces, providing a deeper understanding of the correlation between joining process and joint mechanical properties. As a result of this study, the set of optimized joining parameters used in the previous chapter was attained for the chosen combination of materials.

11.1 Statistical analysis of the effects of process parameters on ULSF

Changing the U-Joining parameters can produce a substantial effect on the mechanical properties of a joint, as illustrated in Figure 11-1. For instance, it has been observed that the ULSF of U-Joining joints can vary from a few newtons to 3.3 kN (force-displacement curves are presented in Appendix A.8. In addition, the geometrical features of joints are affected by changes in joining parameters, which might result, for instance, in a lack of penetration (LoP) of the TTR, as previously discussed in Section 8.3. According to the results of DoE experiments, LoP can vary from high values of 2.8 mm (i.e., small penetration of TTR) to complete insertion (i.e., LoP ≈ 0 mm). Figure 11-1 presents the variation of LoP and ULSF for all the 15 experiments based on a Box-Behnken design and three replicates at the design's central point (CP). The respective µCT analyses are presented in Appendix A.9

By looking closely at the data, it can already be observed from such bar chart that high values of ULSF correlate with low LoP. For instance, if we take conditions 3 and 13 as examples, one can see that for condition 3 a low value of ULSF was observed, which is associated with a high LoP. While for condition 13, a high ULSF was observed, coupled with a low LoP. Such a trend is observed for all the conditions. Indeed, if the values of ULSF are plotted against the LoP, as presented in Figure 11-2, one can clearly see that both responses are linearly correlated. This correlation can be assessed by fitting a linear equation as shown in Figure 11-2 (a). Such a procedure results in a coefficient of correlation of 0.83, thereby characterizing a strong linear correlation between ULSF and LoP. Selected points over the experimental range were further examined by X-ray computer microtomography (µCT), thus providing better visualization of the correlation mentioned, as presented in Figure 11-2 (b). Based on this, the response ULSF was chosen in this work to describe further the effect of process parameters on properties. Moreover, choosing this response has a more engineering significance as it directly relates to the mechanical performance of the joint. Nonetheless, the LoP statistical model is additionally presented in Appendix A.10, and the same procedures described here for ULSF were applied for the LoP assessment.

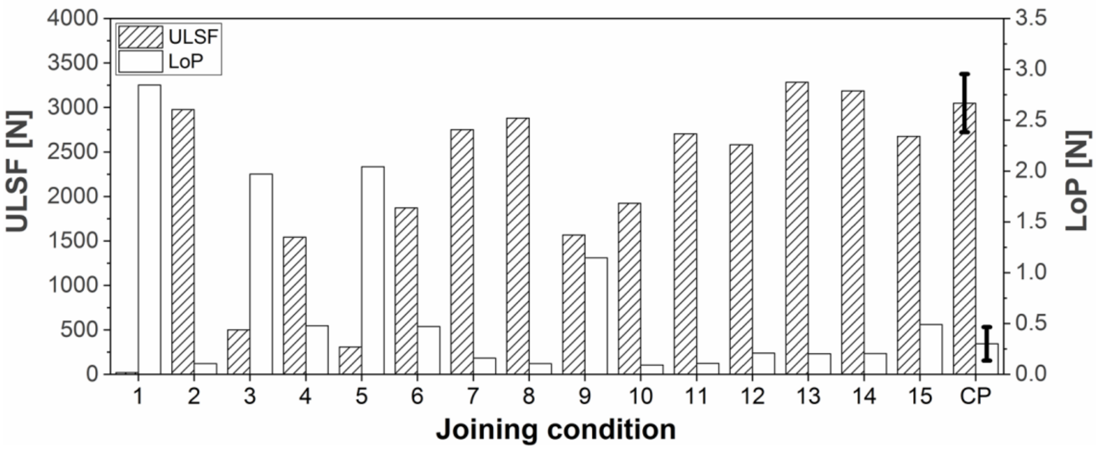

Figure 11-1: Effect of different joining conditions on the ULSF and LoP. Where 1 to 15 correspond to the experiments performed during the DoE, and CP to the replicates at the design central point.

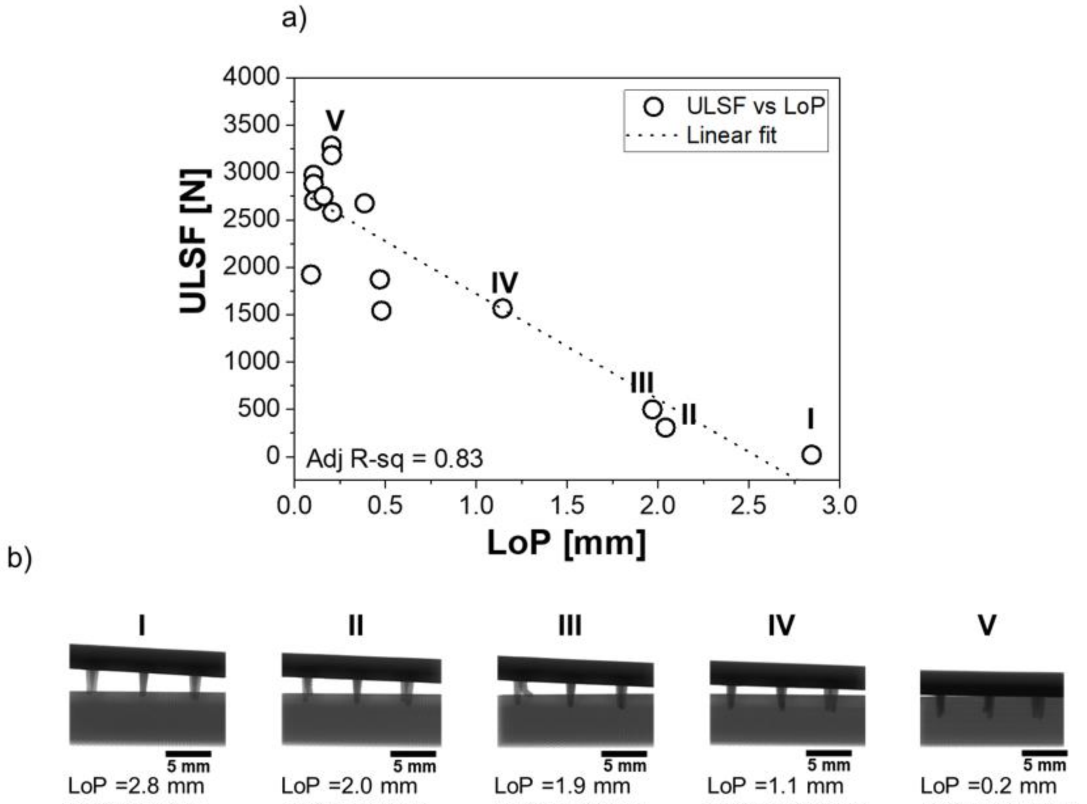

Figure 11-2: (a) Linear correlation between ULSF and LoP, and (b) X-ray tomography of five selected points distributed over the experimental range investigated, showing effect of LoP in the overlap area.

Figure 11-3 presents the validation diagram (details about the validation points are presented in Appendix A.11) of the BBD-based reduced model of ULSF, the percentage effect of each process parameter investigated in this work (i.e., E_J, A_0, and J_P), and their respective second-order significant interactions (i.e., E_J^2 and ${J_P}^{\mathbf{2}}$). The interaction between each process parameter and its second-order interaction is described by the reduced equation as follows:

$$ULSF = -17600 + 11.27 \times E_J + 903 \times J_P + 65.6 \times A_0 - 0.002801 \times E_J^2 - 30.7 \times {J_P}^2 \qquad \textbf{(11-1)}$$

The estimation of each coefficient of equation regression was obtained as described in Section 5.3.4 by a multiple regression analysis of the BBD non-linear quadratic model. In addition, the effect of each significant factor was achieved by ANOVA (Appendix A.11), applying a backward elimination procedure of insignificant terms of the model (i.e., p-values smaller than 0.05). The statistical model obtained has an R^2 of 82% and an adjusted (R^2_{adj}) of 72%. Therefore, the model is more prone to fit the data within the experimental range than predict new values outside the experimental range. Nevertheless, all points in the actual versus predicted diagram (i.e., white circles in the validation graphic, Figure 11-3 (a)) lie within the 95% confidence interval, as the average of the chosen validation points (black circles). Hence, one can conclude that the ULSF model obtained and validated presents a satisfactory explanatory power and can be applied to further understanding of the effect of process parameters in the ULSF.

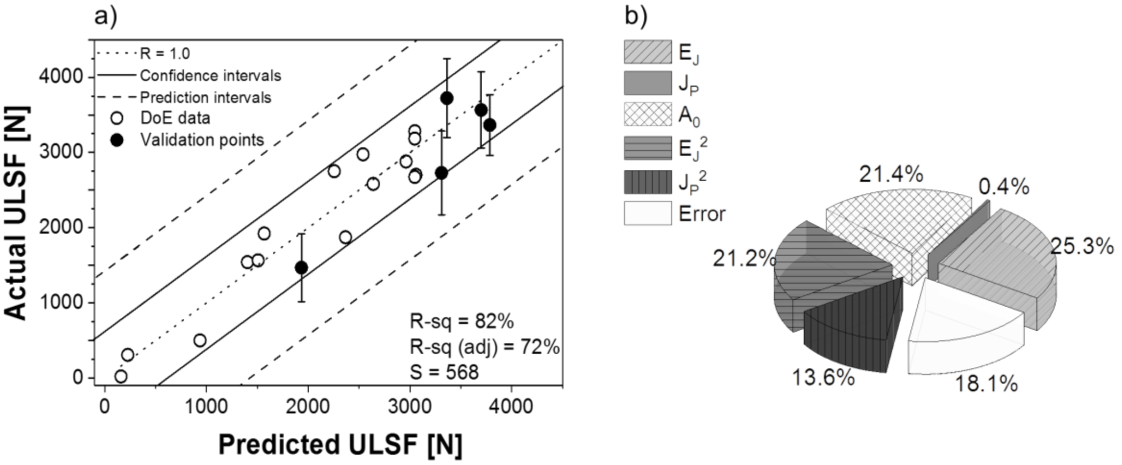

Figure 11-3: (a) Validation diagram for the ULSF reduced model, and (b) effect of each significant factor on the ULSF.

The model shows the major contributions of E_J and A_0 on the ULSF, which correspond to 25.3 % and 21.4 %, respectively. Although the individual effect of J_P was low, its second-order interaction (${J_P}^2$) showed a higher contribution (13.6%). Such a significant contribution of these three main process parameters is expected, because the joining equipment was controlled by adjusting these parameters, as presented in Equation 5-1. The average E_J shows a positive contribution to the ULSF when increased from 1200 to around 2012 J, as shown in the mean effect plot in Figure 11-4 (a). Above 2012, ULSF starts to decrease with an increase of E_J. Similarly, the individual effect of J_P also depicts a maximum, which was observed peaking around 15 psi (103 kPa), while an increase of A_0 always contributes positively to an increase of ULSF, Figure 11-4 (a). Such observations are believed to be closely related to joint formation mechanisms and the resulting microstructure, thus these correlations are further systematically confirmed.

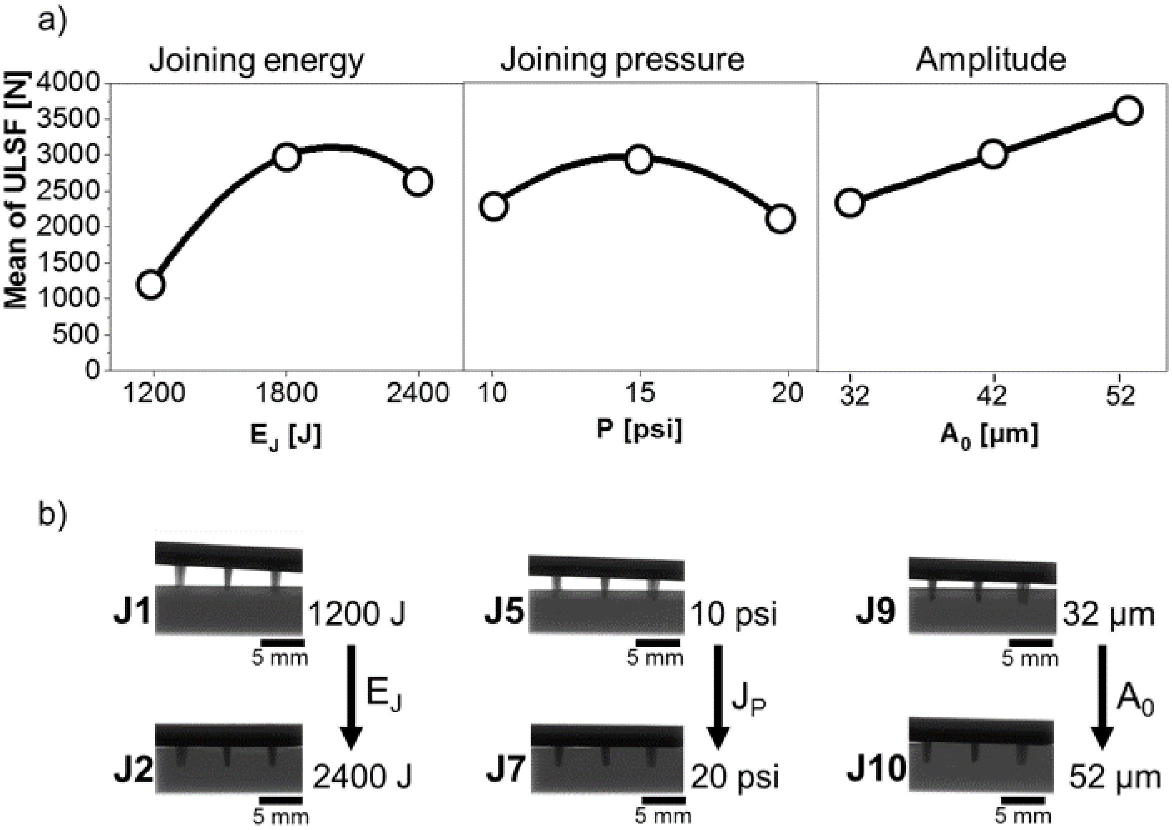

Figure 11-4: (a) Plot of the mean effect of the process parameters on the ULSF, and (b) selected X-ray tomographies of low and high limits of each individual parameter investigated within the BBD.

By the energy-controlled mode employed to adjust the E_J delivered during U-Joining (as explained in Section 6.2.2), low E_J values result in short joining cycles. Such short joining cycles does not allow for enough frictional heat at the interface between the pin tips and composite. As a result, only a small volume of composite matrix is softened during the steady-state of the viscous dissipation phase (process phase P3) and pin penetration is not completely accomplished. This phenomenon can be observed in the X-ray µCT analysis presented in Figure 11-4 (b) for joints produced with 1200 and 2400 J (i.e. conditions J1 and J2, respectively). On the other hand, the decrease in ULSF observed for E_J levels over 2012 J, Figure 11-4 (a), is most probably related to an increase in the process-affected microstructural zones in the polymeric and composite parts. As earlier presented, within this zone a fairly large volume of thermal-induced flaws are found, which could negatively affect load transfer between the materials thereby decreasing ULSF. Such an increase of thermal-induced flaws in friction-based joining processes caused by increases in heat input have been reported in the literature [35,282] for AA2024/PEI hybrid joints, which correlate with higher processes temperatures.

Although the mean effect of J_P has a similar consequence for ULSF, as observed for the E_J, its physical implications are different. Logically, the higher the J_P the higher is the pin penetration expected (i.e., lower LoP), which in turn should result in higher ULSF, as described by the linear correlation between USLF and LoP, Figure 11-2. However, it is also expected that at certain J_P levels the axial pressure applied by the sonotrode during joining may be high enough to damage the TTRs. Such a threshold is believed to lie at values close to 15 psi (1.05 bar), as shown in Figure 11-4 (a) for the combination of materials and joining parameters range studied. While E_J and J_P both display a point of maximum, the mean effect of A_0 is always positive on ULSF. This suggests that high amplitude values contribute to effective frictional heating generation at the material interface, which may soften a higher volume of the composite matrix, thus contributing to a smoother penetration of the pins.

In order to observe the combined variation of two process parameters on the ULSF, two-way response surfaces were plotted and are presented in Figure 11-5. Moreover, to deliver a visual interpretation of the experimental range limits selected, X-ray tomography and 3D reconstructed µCT of the hybrid joints produced are also shown in Figure 11-5. The response surface created by the combined effect E_J and $J_P$displays a well-defined region of maximum and its contour system consists of concentric ellipses. By combining low E_J and J_P levels (P1, Figure 11-5 (a)), while keeping the amplitude at the middle level (i.e. 42 µm), not enough frictional heat is produced, thus a complete penetration of the pins is not accomplished. Consequently, this results in low ULSF. On the other hand, a combination of high values of E_J and J_P (P2, Figure 11-5 (a)) results in a deflection of the central pin, decreasing the USLF. In addition, high values of E_J and J_P may increase the extent of the CTMAZ and the number of process-induced flaws, which contribute to a decrease in mechanical performance. Thus, in order to achieve maximum ULSF, a combination of E_J and J_P at either of the high and low levels should be avoided.

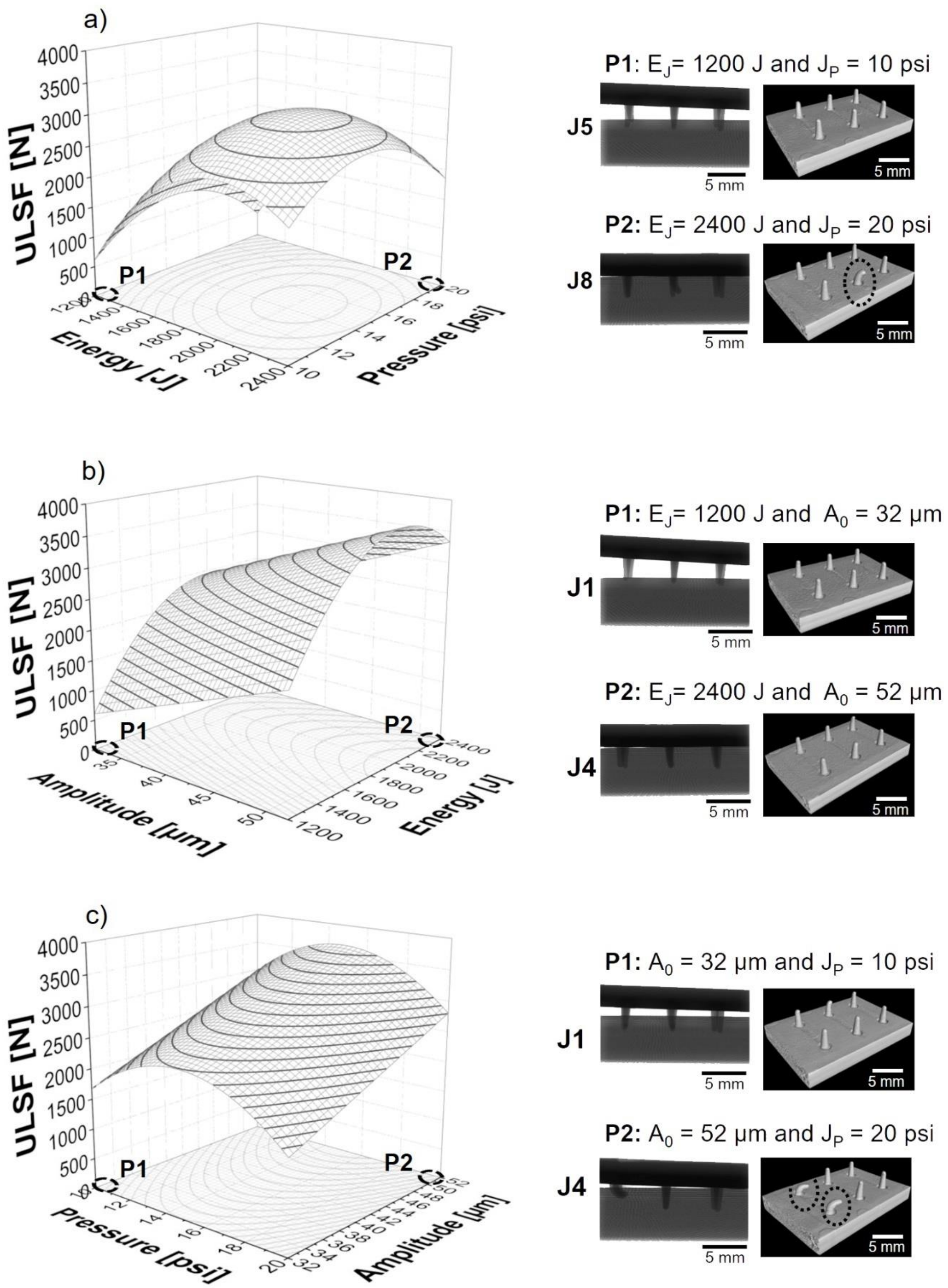

Figure 11-5: Surface responses of two-way joining parameter interactions. Where surface (a) describes the effect of energy and pressure on the ULSF, (b) amplitude and energy and (c) pressure and amplitude. At the right-hand side of each response surface, selected X-ray tomography and 3D reconstructed µCT of the hybrid joint and joint metallic part, respectively, are provided to support an understanding of process parameters on joint formation.

The combination of A_0 and E_J (Figure 11-5 (b)), as well as of A_0 and J_P (Figure 11-5 (c)), results in rising ridge response surfaces. On such surfaces the maximum ULSF is not clearly defined, which suggests that it is outside the experimental range [176]. However, it is important to mention that the joining equipment is limited to an A_0 of 52 µm. As a consequence values above this were not experimentally possible. By adopting a similar approach to describe the A_0-E_J response surface (Figure 11-5 (b), this combination of parameters at high and low limits were closely investigated. A combination of these parameters at a low level result in insufficient heat generation, thus joints with a considerably high LoP were produced, as shown in the P1 of Figure 11-5 (b). Whereas, high levels of A_0 and E_J lead to complete penetration of the pin (P2, Figure 11-5 (b)). However, such high values of E_J induce excessive heat generation, which may lead to a higher occurrence of defects in the CTMAZ. As a consequence the load transfer capacity between the materials decreases and maximum ULSF was not achieved. Therefore, a maximum is achieved by combining high A_0 with moderate E_J values.

Similar to the previous surface analysis, the response surface created by combining A_0 and J_P display a maximum ULSF results from high A_0 with moderate to high J_P values, Figure 11-5 (c). Combining low values of these parameters also leads to a joint with high LoP (P1, Figure 11-5 (c)) and consequently low ULSF. Conversely, a combination of high levels of A_0 and J_P induce an aggressive vibration on the pins. As a result, this causes considerable deflection, as shown in the 3D reconstructed µCT of the joint metallic part (P2, Figure 11-5 (c)).

11.2 Process parameter optimization

The analysis that has been performed so far has provided a detailed comprehension of the effect of U-Joining process parameters on ULSF of the joint. The strategies primarily drawn up to reach maximum ULSF were based on an analysis of each two-way surface response. Such an analysis has provided a useful tool for insights into the setting of the joining parameters for the proposed material combination. However, the exact level of each process parameter that would best provide U-Joining joints with the highest ULSF cannot be directly obtained from such an analysis. To obtain such process parameter levels the partial derivatives $\partial \mathrm{ULSF}/\partial \mathrm{E_J} = \partial \mathrm{ULSF}/\partial \mathrm{A_0} = \partial \mathrm{ULSF}/\partial J_P = 0$ of the reduced model (Equation 11-1) were calculated. In addition, joints produced with such parameter levels (the optimized condition) were produced and mechanically tested under quasi-static loading for confirmation. The optimized condition and derivation procedure are presented in Appendix A.11.

The set of parameters obtained from the partial derivative mentioned corresponds to what is known as a stationary point (or optimized condition) and its values are presented in Table 11-1. Theoretically, the position of a stationary point in a complex surface can represent three hypothesis: (i) a point of maximum response, (ii) a point of minimum response or (iii) a saddle point [170,176]. However, due to the simplicity of the responses obtained by the statistical modeling of the U-Joining process, it is clear that the values obtained correspond to the point of maximum. Such an assumption can be easily proved by a quick examination of the stationary point vicinity, drawing this point on the surfaces obtained. Based on this, it can be concluded that no additional mathematical analysis is required to investigate the nature of the stationary point, because it is clearly a point of maximum.

Table 11-1: Set of optimized U-Joining process parameters

Process parameter	Optimized level
Joining energy (E_J)	2012 J
Amplitude (A_0)	52 µm
Joining pressure (J_P)	14.7 psi / 101 kPa

To conclude, by comparing the optimized joint condition with U-Joining joints produced with the same material combination (i.e., Ti-6Al-4V and GF-PEI)., previously published [100], an average improvement of 79% in ULSF (2011 ± 530 N and 3608 ± 417 N the sound six-pin joint and optimized condition, respectively), and 91% in displacement at fracture (0.68 ± 0.14 mm and 1.30 ± 0.08) mm for the sound six-pin joint and optimized condition, respectively) is observed, as shown in Figure 11-6. Such a result emphatically shows the effectiveness of the optimization procedure employed to obtain the best set of joining parameters for the material combination used in the case study.

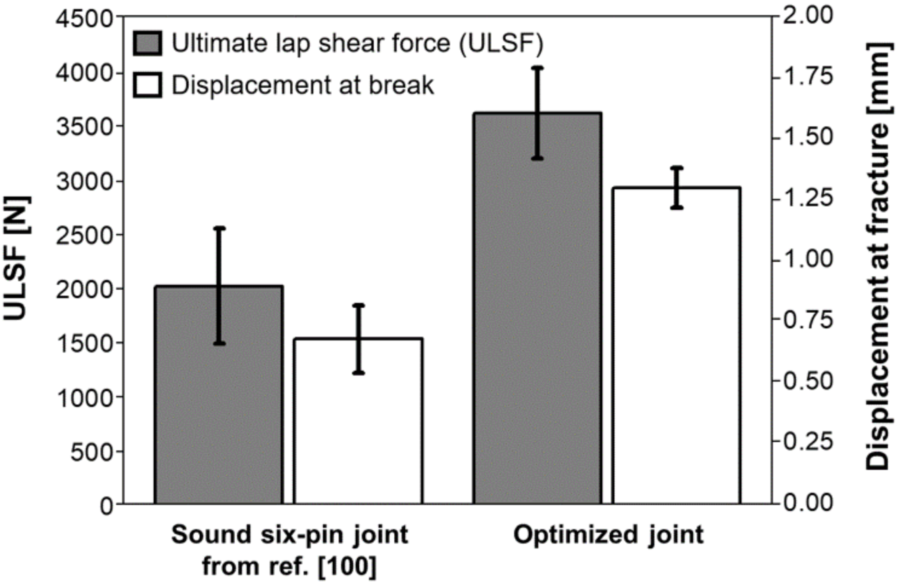

Figure 11-6: Comparison of the optimized U-Joining joint with a previously produced joint with the same material combination [100]

CHAPTER 12 . SUMMARY OF THE RESULTS AND CONCLUSIONS

The present doctoral thesis aimed at introducing the new ultrasonic Joining (U-Joining) technique for the manufacturing of through-the-thickness reinforced hybrid joints, describing its principles, process parameters, joint formation, and bonding mechanisms. Thereby, providing a fundamental understanding of the correlation between joining process-microstructure-joint properties. In this context, this chapter summarizes the main findings of this PhD work, along with the technological and scientific aspects of the joining technique.

With respect to the defined goals of the work, the following major findings were drawn from the development of U-Joining and the results obtained:

Introduction to the U-Joining process

The introduction of the new U-Joining concept was systematically divided into two parts, following the typical phases of direct assembly methods (i.e., structuring and assembly). Thus the fundamentals of the surface structuring by metal injection molding (MIM-Structuring technology) – a novel approach for manufacturing surface-structured Ti-6Al-4V parts with an improved surface finish and reproducibility - was firstly presented in Section 6.1. The assembly phase based on the U-Joining process was secondly described, providing a comprehensive overview of the key aspects of the process, such as the joining parameters (Section 6.2.2), phases (Section 6.2.3), variants (Section 6.2.4), advantages, limitations, and potential applications (Section 6.3).

Joint formation mechanisms

Based on stop-action joining experiments, the formation of U-Joining joints was evaluated in a stepwise manner, providing insights into the bonding mechanisms involved and material flow during the process. It was demonstrated by combining infrared thermography and microstructural characterization that the joining process efficiently softens the composite matrix locally, allowing the surface-structured pins to penetrate the composite. This was shown to happen during very short cycles, for instance, after the joining system had only delivered 400 J of energy (i.e., 0.3 s of joining) the temperature at the interface that formed between pin tips and composite reached 405°C (Figure 7-1). This temperature is about 190°C above the composite matrix glass-transition temperature. Therefore, it decreases the viscosity of the composite matrix and allows for a smooth penetration of the pins. During the pin penetration phase a squeezed molten polymeric matrix material flow is formed (Figure 7-3). It was demonstrated that the fiber reinforcement of the composite is locally damaged and rearranged due to the joining process and its reorientation follows the material flow (Figure 7-4). After complete penetration of the through-the-thickness reinforcement (i.e. the pins) into the composite matrix, two primary bonding mechanisms are responsible for holding the materials together: (i) macromechanical interlocking and (ii) adhesion forces, as described in detail in Section 7.1.1. The first results from a through-the-thickness reinforcement between metallic pins and the composite, wherein adhesive forces are formed at the metal-composite interface after joint consolidation of the softened polymeric matrix. In addition, it was demonstrated that the U-Joining cycles are typically very short (i.e., between 0.9 – 2.3 s for the case-study materials), reaching a maximum temperature of 510°C (Figure 7-9). Such temperatures (Figure 7-10), are within the thermal degradation temperature range of the polymer matrix and so thermo-mechanical degradation was observed and thoroughly investigated.

Hybrid joint microstructural features and local properties

Although the combination of ultrasonic frictional heat and pressure applied by the sonotrode during joining induces significant transformation in the polymeric matrix, no microstructural change was observed in the Ti-6Al-4V part (Figure 8-1). As a result, its local mechanical properties, assessed by Vickers microhardness mapping, were not affected by the process (Figure 8-5). In the case of the polymeric part, the combination of frictional heat and pin insertion created a thermo-mechanically affected zone CTMAZ in the composite part. In this region, microstructural features such as reorientation and local damage of fiber reinforcement, and thermo-mechanically induced voids were observed (Figure 8-2). Apart from the formation of such defects, which were concentrated in a small volume close to and around the pins (Figure 8-3), a very close contact between composite and metal was observed across the entire joint interface. Thereby it gave an indication of efficient joining between the materials and the formation of interlocking on the micro scale. Due to the high fiber content of the reinforced composite it was not possible to visually identify the extent of the CTMAZ by optical or electron microscopy. Therefore, unreinforced PEI hybrid joints were also produced and birefringence properties of the PEI were explored to understand better the effect of U-Joining on the polymer matrix. The birefringence patterns clearly showed the shape and extent of the process-affected zone (Figure 8-4). Moreover, a qualitative evaluation of thermo-mechanically induced stresses of the process was achieved by an investigation of fringe density. It was observed that high compressive stresses beneath the pin tips induce the formation of shear bands, which were observed at the limits of the thermo-mechanically affected zone. Thus indicating that such material volume locally underwent compression yielding.

At the CTMAZ, significant process-induced changes in the local mechanical properties of the polymer were observed, which were further characterized on micro and nanoscales. Instrumented nanoindentation experiments proved a decrease of about 12% in hardness and 1.5% in elastic modulus (Figure 8-13), suggesting that the joining process not only increased the free volume between PEI molecules, but also promoted thermo-mechanical degradation. In addition, a decrease of about 2°C in glass transition of the CTMAZ volume was measured by differential scanning calorimetry (DSC), an observation that may suggest changes in molecular weight (MW). In order to investigate the hypothesis of thermo-mechanical degradation by chain scission (i.e. decrease in MW), size-exclusion chromatography (SEC) experiments were performed (Figure 8-17). In the CTMAZ a reduction of 5% in weight-average molecular weight (M_w) and 24% in number-average molecular weight (M_n) was measured. Moreover, the mechanism by which the process degrades the polymeric chains was confirmed as based on the chain scission distribution function (CSDF). This suggested that the process-induced thermo-mechanical degradation results in a non-random chain scission mechanism, which mainly forms low MW chains rather than degrade high MW chains. This result, coupled with an increase in polydispersity index (Figure 8-16 (b)) suggested that the thermo-mechanical degradation pathway in the CTMAZ is induced by a multiple chain scission mechanism. Thus, when a chain undergoes an initial breakage its fragments keep degrading. As a result, it forms a significant number of small chains (lower MW). The degraded volumes showed chains with M_w of 44.8 ± 2.3 kg.mol^{-1} and 38.3 ± 3.6 kg.mol^{-1} for material extracted from the thermo-mechanically affected zone of the polyetherimide and glass-fiber reinforced polyetherimide joint configuration, respectively. Sanner *et al.* [260], studied the effect of M_w ranging from 36.6 kg.mol^{-1} to 52.3 kg.mol^{-1} on the mechanical properties of PEI. According to their results, M_w did not play a significant role on the yield strength for the studied range, although an increase in fracture strength was observed with an increase in $M_{w.}$ Thus, in terms of joint application, the process seems not to have degraded joint properties significantly. The degradation levels measured by SEC concur precisely with the changes in glass transition temperature by DSC, previously mentioned since lower thermal energy is required to promote mobility in low MW polymers. Hence, the CTMAZ had its glass transition shifted to a lower temperature. In addition, the thermal process only slightly changed the elastic modulus of this zone, which is in perfect agreement with the local thermo-mechanical decomposition observed in the PEI matrix.

Mechanical properties under quasi-static loading

The asymmetric geometry of the joint and material stiffness mismatch played a significant role in joint deformation under lap shear testing. Due to the eccentric load path during the mechanical test, an out-of-plane displacement (secondary bending, SB) is created (Figure 9-1). It was observed that the resulting moment, M_R, induced by loading is transmitted to the pins, resulting in an asymmetrical distribution of stresses along the pin and the surrounding composite volume. As a result, the first row of pins bore higher stresses in comparison with the other pins (Figure 9-2 (a)). Moreover, it was shown by FEM that the central pins carried lower shear stresses than the outer pins (Figure 9-2), which was in agreement with the stress distribution pattern observed in multiple-riveted joints.

In terms of overall performance, a significant increase in ultimate lap shear force (ULSF) and toughness were observed compared with non-reinforced ultrasonically joined reference. The U-Joining joint had seven times higher ULSF than the non-reinforced references. Therefore, one may conclude that the TRR effectively improved the load transfer capacity between the materials evaluated in the case study of U-Joining hybrid joints. The micromechanisms of failure were characterized by fracture surface analysis, and a mixture of adhesive-cohesive failure of the consolidated molten polymer at the joint interface was observed with final failure taking place by shearing of the metallic pins. Therefore, the process-induced defects observed in the CTMAZ were kept to a low and acceptable level, thereby not playing a significant role in the joint failure mechanism. An examination of the fracture surfaces of pins revealed that they underwent considerable plastic deformation prior to failure, which was evidenced by the high amount of dimples spread over the fracture surface.

The effect of the hot isostatic pressing (HIP) post-treatment on the Ti-6Al-4V corresponded to an improvement of 6.7% in joint ULSF. The average ULSF value for the hybrid joints produced using HIP treated Ti-6Al-4V parts was 3608 ± 419 N, whereas hybrid joints produced with as-sintered Ti-6Al-4V gave 3848 ± 299 N. Moreover, the HIP Ti-6Al-4V part deforms 1.5 mm from the plane of the joining area, which corresponds to 4.5 times more out-of-plane deformation compared with the as-sintered part. That is mostly caused by a change in the fracture mode of joints. This is because the HIP virtually removes the residual porosity of the as-sintered parts, which acts as stress concentration sites for crack initiation and facilitates failure propagation. Therefore, it provides a more ductile MIMStruct part, which can withstand higher levels of secondary bending without damaging its reinforcement elements.

Mechanical properties under cyclic loading

The fatigue performance of joints was also evaluated under cyclic tension-tension loading (R=0.1, Figure 10-1). In this study, the fatigue limit was defined as the load level below which no failure would occur until after 10^6 cycles. Based on this, it was observed that joints reached their fatigue endurance limit with a maximum load of 30% of the ULSF (i.e., 1082 N). Three S-N formulation were applied to obtain S-N curves, the linear models recommended by the ASTM standard and the two-parameter Weibull distribution. All three models fitted well with the experimental data in the measurement range (10^3 – 10^6), as shown in Figure 10-1. However, the exponential model gave a more conservative prediction of fatigue life, especially at low cycle fatigue (LCF) and high cycle fatigue (HCF) i.e., at the extremities of the evaluated range, below 10^3 and above 10^6 cycles. In addition, the power law and Weibull fit gave a similar predictability at HCF, although at LCF Weibull was more conservative. The similar behavior of these two models is expected, because the two-parameter Weibull distribution also obeys a power law function. The two-parameter Weibull distribution was applied for further statistical examination and S-N curves with different reliability levels were obtained (Figure 10-2). Such an analysis provided an accurate tool for further reliable structural design, by considering fatigue data scattering.

The joints that survived fatigue endurance limits were further mechanically tested to evaluate their residual strength. It was shown by this analysis that no considerable damage was induced by fatigue when a loading level of 30% of ULSF is applied (Figure 10-3). The failure mechanisms of U-Joining joints under cyclic loading are similar to those previously observed for quasi-static loading. It is assumed that fatigue cracks initiate at the first row of pins and propagate through the overlap area towards the third pin row. Such a mechanism was confirmed by scanning electron microscopy (SEM) fracture analysis and the various propagation regimes were characterized.

Effect of process parameters on the joint quasi-static mechanical performance

In order to understand the effect of process parameters on ULSF and optimize the process to produce stronger joints, a Box-Behnken design (BBD) of experiments was applied. During data analysis it was observed that changes in the U-Joining parameters could produce substantial effects on the mechanical properties of joints (Figure 11-1), varying from a few newtons to 3.3 kN). By applying a multiple regression analysis of the BBD and ANOVA, a reduced statistical model that described the interaction between each process parameter and its second-order interaction was achieved. The reduced model showed an R^2 of 82% and thus was considered reliable for the analysis. By a plot of the response surface, analysis of the combined effect of joining parameters was obtained and their effect on joint properties were described based on the micro-computed tomography results. These findings can efficiently assist in future development of the U-Joining process, which would include the application of different material combinations and process scale-up.

Finally, by optimizing the reduced model obtained for the ULSF, a set of joining parameters was achieved to produce a hybrid joint with above-average mechanical performance from the experiments in this PhD work. To conclude, by comparing the optimized joint condition with previous U-Joining joints that were joined with the same material combination [100], an improvement of 79% in ULSF and 91% in displacement at fracture was achieved, as shown in Figure 11-6. Such a result emphatically shows the effectiveness of the optimization strategy to discover the best possible joining parameters.

Therefore, this PhD work has not only contributed to introduce and describe the fundamentals of the new U-Joining concept, but also to filling knowledge gaps with respect to the microstructure and mechanical performance correlations of the joining process in the joining of through-the-thickness reinforced metal-composite hybrid structures. In addition, it shows the potential for the U-Joining concept in manufacturing future lightweight hybrid joints for structural applications with improved toughness and load-bearing capability.

CHAPTER 13. RECOMMENDATIONS FOR FUTURE WORK

This PhD work corresponds to the first effort to introduce, understand and further develop the U-Joining concept. Although many topics regarding the joining process and joint properties were addressed and successfully explained, some aspects remain open for future investigation. This chapter therefore recommends some important topics for further development of the U-Joining concept.

The MIM-structured Ti-6Al-4V part employed in the case study of this work had six round-tipped conical pins. Such a geometry has been shown to improve the load transfer between the materials considerably. However, a more in-depth investigation of alternative pin density, distribution, geometry, and materials would provide valuable information for successful industrial transferability. In this respect it is expected that the addition of further anchoring geometrical features to the pin tip, as presented in Figure 6-7, could improve the out-of-plane strength of joints significantly. With regards pin distribution and geometry, a topology optimization would provide useful insights on how to design the through-the-thickness reinforcement elements. Thus further improving the joint load-bearing capability and reducing the structural weight of the metallic part. Additive manufacturing techniques would be a valuable tool for this purpose.

When one considers the flexibility of the MIM-Structuring manufacturing route, different alloying compositions could also be evaluated as a strategy to improve the mechanical performance of joints, especially under cyclic loading. For example, the addition of small amount of boron to the Ti-6Al-4V [283]. The effect of a MIMStruct surface finish on fatigue performance is also an important topic for further investigation, as this has a major influence on titanium parts manufactured by MIM [127,129]. Likewise, an investigation of damage tolerance and crashworthiness of U-Joining joints would make available useful information for further manufacturing of hybrid structures applied in the transportation sector.

In regard to the assembly process, a heat development model and more accurate characterization of the temperature during joining are still required. This would better substantiate the explanation of physical-chemical changes in the joined materials. In addition, it is essential to investigate the behavior of the joining process for up-scaled part production and producing multi-spot sub-components.

References

[1] J. Staeves, The right material at the right place (BMW Group), Glob. Automot. Light. Mater. London, UK. (2013). http://www.global-automotive-lightweight-materials.com/media/downloads/99-0840-johannes-staeves-bmw.pdf (accessed July 22, 2017).

[2] WHITE PAPER: Roadmap to a Single European Transport Area - Towards a competitive and resource efficient transport system, Eur. Comm. (2011). http://eur-lex.europa.eu/legal-content/EN/TXT/PDF/?uri=CELEX:52011DC0144&from=EN (accessed May 21, 2018).

[3] A.J. Timmis, A. Hodzic, L. Koh, M. Bonner, C. Soutis, A.W. Schäfer, L. Dray, Environmental impact assessment of aviation emission reduction through the implementation of composite materials, Int. J. Life Cycle Assess. 20 (2015) 233–243.

[4] R. Heuss, N. Müller, W. van Sintern, A. Starke, A. Tschiesner, Lightweight, heavy impact, McKinsey Co. (2012). https://www.mckinsey.com/~/media/mckinsey/dotcom/client_service/automotive and assembly/pdfs/lightweight_heavy_impact.ashx (accessed September 7, 2015).

[5] V.M. Karbhari, F. Seible, Fiber Reinforced Composites – Advanced Materials for the Renewal of Civil Infrastructure, Appl. Compos. Mater. 7 (2000) 95–124.

[6] RAMSSES - Realisation and Demonstration of Advanced Material Solutions for Sustainable and Efficient Ships, RAMSSES - Realisation and Demonstration of Advanced Material Solutions for Sustainable and Efficient Ships, Chalmers, Eur. Proj. (2017).

[7] S. Ferraris, L.M. Volpone, Aluminium alloys in third millennium shipbuilding: materials, technologies, perspectives, Fifth Int. Forum Alum. Ships, Tokyo, Japan. (2005).

[8] G. Marsh, Composites and metals – a marriage of convenience?, Reinf. Plast. 58 (2014) 38–42.

[9] F. Faupel, R. Willecke, A. Thran, Diffusion of metals in polymers, Mater. Sci. Eng. R Reports. 22 (1998) 1–55.

[10] S.T. Amancio-Filho, J.F. dos Santos, Joining of polymers and polymer–metal hybrid structures: Recent developments and trends, Polym. Eng. Sci. 49 (2009) 1461–1476.

[11] T. Ebel, S. de Traglia Amancio Filho, J. Fernandez dos Santos, Method for manufacturing metal casings with structured surfaces. European Patent No. EP 2 468 436 B1., 2016.

[12] S.T. Amancio-Filho, E.E. Feistauer, J.F. dos Santos, Method for connecting a surface-structured workpiece and a plastic workpiece, U.S. patent, US 2016/0297138 A1, 2016.

[13] S.T. Amancio-Filho, E.E. Feistauer, J.F. dos Santos, Method for connecting a surface-structured workpiece and a plastic workpiece, Canadian patent, CA 2924209

A1, 2016.

[14] S.T. Amancio-Filho, E.E. Feistauer, J.F. dos Santos, Método para conectar uma peça de trabalho de superfície estruturada e uma peça de trabalho de plástico, Instituto Nacional da Propriedade Industrial, BR 102016007517-3 A2, 2016.

[15] S.T. Amancio-Filho, E.E. Feistauer, J.F. dos Santos, Method for connecting a surface-structured workpiece and a plastic workpiece, European patent, EP 3 078 480 A1, EP 3 078 480 A1, 2016.

[16] M. Redelbach, M. Klötzke, H.E. Friedrich, Impact of lightweight design on energy consumption and cost effectiveness of alternative powertrain concepts, in: EEVC Eur. Electr. Veh. Congr., Brussels, Belgium, 2012: pp. 1–9.

[17] H.E. Friedrich, Challenges of materials technology for low consumption vehicle concepts, Adv. Eng. Mater. 5 (2003) 105–112.

[18] ASM International, Market Spotlight: Global lightweight materials market to surpass $186 billion by 2020, Adv. Mater. Process. (2014) 1.

[19] S.T. Amancio Filho, L.-A. Blaga, Joining of polymer-metal hybrid structures : principles and applications, John Wiley & Sons, Inc.

[20] Y. Su, M. de Rooij, W. Grouve, R. Akkerman, The effect of titanium surface treatment on the interfacial strength of titanium – Thermoplastic composite joints, Int. J. Adhes. Adhes. 72 (2017) 98–108.

[21] M.-S. Seong, T.-H. Kim, K.-H. Nguyen, J.-H. Kweon, J.-H. Choi, A parametric study on the failure of bonded single-lap joints of carbon composite and aluminum, Compos. Struct. 86 (2008) 135–145.

[22] Y. Zhai, D. Li, X. Li, L. Wang, An experimental study on the effect of joining interface condition on bearing response of single-lap, countersunk composite-aluminum bolted joints, Compos. Struct. 134 (2015) 190–198.

[23] G. Di Franco, L. Fratini, A. Pasta, Analysis of the mechanical performance of hybrid (SPR/bonded) single-lap joints between CFRP panels and aluminum blanks, Int. J. Adhes. Adhes. 41 (2013) 24–32.

[24] P. Lopez-Cruz, J. Laliberté, L. Lessard, Investigation of bolted/bonded composite joint behaviour using design of experiments, Compos. Struct. 170 (2017) 192–201.

[25] J.-H. Kweon, J.-W. Jung, T.-H. Kim, J.-H. Choi, D.-H. Kim, Failure of carbon composite-to-aluminum joints with combined mechanical fastening and adhesive bonding, Compos. Struct. 75 (2006) 192–198.

[26] K. Bodjona, L. Lessard, Hybrid bonded-fastened joints and their application in composite structures: A general review, J. Reinf. Plast. Compos. 35 (2016) 764–781.

[27] P. Mitschang, R. Velthuis, M. Didi, Induction Spot Welding of Metal/CFRPC Hybrid Joints, Adv. Eng. Mater. 15 (2013) 804–813.

[28] F. Balle, G. Wagner, D. Eifler, Ultrasonic metal welding of aluminium sheets to carbon fibre reinforced thermoplastic composites, Adv. Eng. Mater. 11 (2009) 35–39.

[29] S.M. Goushegir, J.F. dos Santos, S.T. Amancio-Filho, Friction Spot Joining of

aluminum AA2024/carbon-fiber reinforced poly(phenylene sulfide) composite single lap joints: Microstructure and mechanical performance, Mater. Des. 54 (2014) 196–206.

[30] S. Ucsnik, M. Scheerer, S. Zaremba, D.H. Pahr, Experimental investigation of a novel hybrid metal–composite joining technology, Compos. Part A Appl. Sci. Manuf. 41 (2010) 369–374.

[31] S.M. Goushegir, Friction Spot Joining of Polymer-Metal Hybrid Structures, HZG Rep. 5 (2015).

[32] A. Higgins, Adhesive bonding of aircraft structures, Int. J. Adhes. Adhes. 20 (2000) 367–376.

[33] Y. Ciupack, H. Pasternak, C. Mette, E. Stammen, K. Dilger, Adhesive bonding in steel construction -Challenge and innovation, Procedia Eng. 172 (2017) 186–193.

[34] A. Kwakernaak, J. Hofstede, J.A. Poulis, R. Benedictus, Improvements in bonding metals for aerospace and other applications, Weld. Join. Aerosp. Mater. (2012) 235–287.

[35] A.B. Abibe, S.T. Amancio-Filho, J.F. dos Santos, E. Hage Jr., Mechanical and failure behaviour of hybrid polymer–metal staked joints, Mater. Des. 46 (2013) 338–347.

[36] A.B. Abibe, M. Sônego, J.F. dos Santos, L.B. Canto, S.T. Amancio-Filho, On the feasibility of a friction-based staking joining method for polymer–metal hybrid structures, Mater. Des. 92 (2016) 632–642.

[37] S.T. Amancio-Filho, Henry Granjon Prize Competition 2009 Winner Category A: “Joining and Fabrication Technology” Friction Riveting: development and analysis of a new joining technique for polymer-metal multi-material structures, Weld. World. 55 (2011) 13–24.

[38] N.Z. Borba, L. Blaga, J.F. dos Santos, S.T. Amancio-Filho, Direct-Friction Riveting of polymer composite laminates for aircraft applications, Mater. Lett. 215 (2018) 31–34.

[39] F. Balle, G. Wagner, D. Eifler, Ultrasonic spot welding of aluminum sheet/carbon fiber reinforced polymer – joints, Materwiss. Werksttech. 38 (2007) 934–938.

[40] P. Mitschang, R. Velthuis, S. Emrich, M. Kopnarski, Induction Heated Joining of Aluminum and Carbon Fiber Reinforced Nylon 66, J. Thermoplast. Compos. Mater. 22 (2009) 767–801.

[41] C. Ageorges, L. Ye, Resistance welding of thermosetting composite/thermoplastic composite joints, Compos. - Part A Appl. Sci. Manuf. 32 (2001) 1603–1612.

[42] K.W. Jung, Y. Kawahito, M. Takahashi, S. Katayama, Laser direct joining of carbon fiber reinforced plastic to zinc-coated steel, Mater. Des. 47 (2013) 179–188.

[43] F.I. Hussein, E. Akman, B. Genc Oztoprak, M. Gunes, O. Gundogdu, E. Kacar, K.I. Hajim, A. Demir, Evaluation of PMMA joining to stainless steel 304 using pulsed Nd:YAG laser, Opt. Laser Technol. 49 (2013) 143–152.

[44] N.M. André, S.M. Goushegir, J.F. dos Santos, L.B. Canto, S.T. Amancio-Filho, Friction Spot Joining of aluminum alloy 2024-T3 and carbon-fiber-reinforced poly(phenylene sulfide) laminate with additional PPS film interlayer: Microstructure,

mechanical strength and failure mechanisms, Compos. Part B Eng. 94 (2016) 197–208.

[45] S.M. Goushegir, J.F. dos Santos, S.T. Amancio-Filho, Influence of process parameters on mechanical performance and bonding area of AA2024/carbon-fiber-reinforced poly(phenylene sulfide) friction spot single lap joints, Mater. Des. 83 (2015) 431–442.

[46] S.T. Amancio-Filho, A.B. Abibe, J.F. Dos Santos, Joining: Mechanical Fastening of Polymers, Composites, and Polymer–Metal Hybrid Structures, Wiley Encycl. Compos. (2012).

[47] M. Grujicic, V. Sellappan, G. Arakere, N. Seyr, A. Obieglo, M. Erdmann, J. Holzleitner, The Potential of a Clinch-Lock Polymer Metal Hybrid Technology for Use in Load-Bearing Automotive Components, J. Mater. Eng. Perform. 18 (2009) 893–902.

[48] F. Smith, COMELD - An innovation in composite to metal joining, Compos. Process. (2004) 319.

[49] E.J.C. Kellar, F. Smith, Comeld - A New approach to damage control for composite to metal joints, Des. Perform. Compos. Mater. Conf. (2005).

[50] S. Ucsnik, M. Scheerer, S. Zaremba, D.H. Pahr, Experimental investigation of a novel hybrid metal-composite joining technology, Compos. Part A Appl. Sci. Manuf. 41 (2010) 369–374.

[51] X. Wang, J. Ahn, C. Kaboglu, L. Yu, B.R.K. Blackman, Characterisation of composite-titanium alloy hybrid joints using digital image correlation, Compos. Struct. 140 (2016) 702–711.

[52] T. Masuzawa, State of the Art of Micromachining, CIRP Ann. - Manuf. Technol. 49 (2000) 473–488.

[53] G. Byrne, D. Dornfeld, B. Denkena, Advancing Cutting Technology, CIRP Ann. - Manuf. Technol. 52 (2003) 483–507.

[54] D. Dornfeld, S. Min, Y. Takeuchi, Recent Advances in Mechanical Micromachining, CIRP Ann. - Manuf. Technol. 55 (2006) 745–768.

[55] V. Di Giandomenico, Surface structured bonded composite-metal joint, Ph.D Thesis, Cranfield University, 2014.

[56] E. Gandarias, Micromilling technology: Global review, P.hD. Thesis, Mondragon Unibertsitatea, Spain, 2015.

[57] D.J. Guckenberger, T.E. de Groot, A.M.D. Wan, D.J. Beebe, E.W.K. Young, Micromilling: a method for ultra-rapid prototyping of plastic microfluidic devices., Lab Chip. 15 (2015) 2364–78.

[58] E. Demir, A method to include plastic anisotropy to orthogonal micromachining of fcc single crystals, Int. J. Adv. Manuf. Technol. 43 (2009) 474–481.

[59] M.P. Vogler, R.E. DeVor, S.G. Kapoor, Microstructure-Level Force Prediction Model for Micro-milling of Multi-Phase Materials, J. Manuf. Sci. Eng. 125 (2003) 202.

[60] D. Huo, W. Chen, X. Teng, C. Lin, K. Yang, Modeling the Influence of Tool Deflection

on Cutting Force and Surface Generation in Micro-Milling, Micromachines. 8 (2017) 188.

[61] F. Wang, X. Cheng, Y. Liu, X. Yang, F. Meng, Micromilling Simulation for the Hard-to-cut Material, Procedia Eng. 174 (2017) 693–699.

[62] B.H.T. Baharudin, N. Dimou, K.K.B. Hon, Tool Wear Behaviour of Micro-Tools in High Speed CNC Machining, Proc. 34th Int. MATADOR Conf. (2004) 111–118.

[63] W.. Bao, I.. Tansel, Modeling micro-end-milling operations. Part III: influence of tool wear, Int. J. Mach. Tools Manuf. 40 (2000) 2193–2211.

[64] K. Zhu, X. Yu, The monitoring of micro milling tool wear conditions by wear area estimation, Mech. Syst. Signal Process. 93 (2017) 80–91.

[65] K. Dröder, M. Brand, A. Gerdes, T. Grosse, H. Grefe, K. Lippky, F. Fischer, K. Dilger, An innovative approach for joining Of Hybrid CFRP-metal parts by mechanical undercuts, Euro Hybrid Mater. Struct. 2014. (2014) 54–60.

[66] K. Dröder, M. Brand, M. Kühn, Numerical and Experimental Analyses on the Influence of Array Patterns in Hybrid Metal-FRP Materials Interlocked by Mechanical Undercuts, Procedia CIRP. 62 (2017) 51–55.

[67] S. Müller, M. Brand, K. Dröder, D. Meiners, Increasing the Structural Integrity of Hybrid Plastics-Metal Parts by an Innovative Mechanical Interlocking Effect, Mater. Sci. Forum. 825 (2015) 417–424.

[68] M. Brand, M. Kühn, A. Müller, K. Dröder, Enhancing the tensile strength in hybrid metal-FRP materials through various interlocking structure patterns, Conf. Proc. - Euro Hybrid Mater. Struct. 2016. (2016) 251–256.

[69] B.G.I. Dance, J.K.C. Ewen, Workpiece structure modification, U.S. Patent, 7667158 B2, (2004).

[70] TWI, Surfi-Sculpt, (n.d.). http://www.twi-global.com/services/intellectual-property-licensing/surfi-sculpt/ (accessed February 17, 2015).

[71] D.A.L.B. Bruce G I Dance, MA, A.L.B. Bruce G I Dance, An introduction to Surfi-Sculpt® technology - new opportunities, new challenges, 7th Int. Conf. Beam Technol. (2007).

[72] Paul Hilton and Lien Nguyen, A new method of laser beam induced surface modification using the Surfi-Sculpt® process, 3rd Pacific Int. Conf. Appl. Lasers Opt. (2008) 16–18.

[73] B.G.I.D. A L Buxton, Surfi-Sculpt - Revolutionary surface processing with an electron beam, ASM Int. ISEC Congr. (2005).

[74] X. Wang, J. Ahn, Q. Bai, W. Lu, J. Lin, W. Xiong, B. Blackman, J.P. Dear, X. Wang, Effect of forming parameters on electron beam Surfi-Sculpt protrusion for Ti–6Al–4V, Mater. Des. 76 (2015) 202–206.

[75] W. Xichang, G. Enming, G. Shuili, L. Bin, Realization and Experimental Analysis of Electron Beam Surfi-Sculpt on Ti-6Al-4V Alloy, Rare Met. Mater. Eng. 43 (2014) 819–822.

[76] J. Blackburn, An Overview of Laser Surfi-Sculpt ® Development, TWI Ltd, Heriot-Watt Univ. Edinburg, UK. (2012).

[77] J. Blackburn, P. Hilton, Producing Surface Features with a 200 W Yb-fibre Laser and the Surfi-Sculpt® Process, Phys. Procedia. 12 (2011) 529–536.

[78] C. Earl, J.R. Castrejón-Pita, P.A. Hilton, W. O'Neill, The dynamics of laser surface modification, J. Manuf. Process. 21 (2016) 214–223.

[79] J. Taendl, N. Enzinger, Electron beam surface structuring of AA6016 aluminum alloy, Weld. World. 58 (2014) 795–803.

[80] C. Earl, P. Hilton, B. O'Neill, Parameter Influence on Surfi-Sculpt Processing Efficiency, Phys. Procedia. 39 (2012) 327–335.

[81] I. Gibson, D.W. Rosen, B. Stucker, Additive Manufacturing Technologies, Springer USA, Boston, MA, 2010.

[82] D. Herzog, V. Seyda, E. Wycisk, C. Emmelmann, Additive manufacturing of metals, Acta Mater. 117 (2016) 371–392.

[83] M. Wang, X. Lin, W. Huang, Laser additive manufacture of titanium alloys, Mater. Technol. (2016) 1–8.

[84] E.O. Olakanmi, R.F. Cochrane, K.W. Dalgarno, A review on selective laser sintering/melting (SLS/SLM) of aluminium alloy powders: Processing, microstructure, and properties, Prog. Mater. Sci. 74 (2015) 401–477.

[85] L.E. Murr, S.M. Gaytan, D.A. Ramirez, E. Martinez, J. Hernandez, K.N. Amato, P.W. Shindo, F.R. Medina, R.B. Wicker, Metal Fabrication by Additive Manufacturing Using Laser and Electron Beam Melting Technologies, J. Mater. Sci. Technol. 28 (2012) 1–14.

[86] M. Benedetti, E. Torresani, M. Leoni, V. Fontanari, M. Bandini, C. Pederzolli, C. Potrich, The effect of post-sintering treatments on the fatigue and biological behavior of Ti-6Al-4V ELI parts made by selective laser melting, J. Mech. Behav. Biomed. Mater. 71 (2017) 295–306.

[87] J. Meyer, D. Johns, Hybrid component, U.S. Patent, 9085030 B2, (2009).

[88] D.P.P. Graham, A. Rezai, D. Baker, P.A.A. Smith, J.F.F. Watts, A hybrid joining scheme for high strength multi- material joints, 18th Int. Conf. Compos. Mater. (2011).

[89] P.N. Parkes, R. Butler, D.P. Almond, Fatigue of Metal-Composite Joints with Penetrative Reinforcement, 54th AIAA/ASME/ASCE/AHS/ASC Struct. Struct. Dyn. Mater. Conf. (2013).

[90] P.N. Parkes, R. Butler, J. Meyer, A. de Oliveira, Static strength of metal-composite joints with penetrative reinforcement, Compos. Struct. 118 (2014) 250–256.

[91] T. Caspari, D. Huelsbusch, M. Haack, A. Solbach, C. Emmelmann, F. Walther, Technological and economical aspects of novel hybrid joining strategies based on integrated fibre penetrating reinforcing elements, Euro Hybrid Mater. Struct. 2016. (2016) 81–85.

[92] P.N. Parkes, R. Butler, J. Meyer, A. de Oliveira, Static strength of metal-composite

joints with penetrative reinforcement, Compos. Struct. 118 (2014) 250–256.

[93] J. Evans, COLD METAL TRANSFER – Robotics, Fronius UK Ltd. (2012). http://www3.fronius.com/cps/rde/xbcr/SID-BBF1EF32-82E0BBF5/fronius_uk/CMTRobotics_pres_openhouse__538967_snapshot.pdf (accessed January 25, 2017).

[94] A. Schierl, The CMT Process a Revolution in welding technology, Weld. World. 49 (2005) 38.

[95] F. Bianchi, Numerical modelling of through-thickness reinforced structural joints, Ph.D Thesis, Cranfield University, England, (2012).

[96] S. Stelzer, S. Ucsnik, J. Tauchner, T. Unger, G. Pinter, Novel composite-composite joining technology with through the thickness reinforcement for enhanced damage tolerance, 19th Int. Conf. Compos. Mater. (2013) 4645–4653.

[97] S. Ucsnik, M. Scheerer, S. Zaremba, D.H. Pahr, Experimental investigation of a novel hybrid metal–composite joining technology, Compos. Part A Appl. Sci. Manuf. 41 (2010) 369–374.

[98] S.A. Ucsnik, G. Kirov, New Possibility for the Connection of Metal Sheets and Fiber Reinforced Plastics, Mater. Sci. Forum. 690 (2011) 465–468.

[99] D.P. Graham, A. Rezai, D. Baker, P.A. Smith, J.F. Watts, The development and scalability of a high strength, damage tolerant, hybrid joining scheme for composite–metal structures, Compos. Part A Appl. Sci. Manuf. 64 (2014) 11–24.

[100] E.E. Feistauer, R.P.M. Guimaraes, T. Ebel, J.F. Dos Santos, S.T. Amancio-Filho, Ultrasonic joining: A novel direct-assembly technique for metal-composite hybrid structures, Mater. Lett. 170 (2016) 1–4.

[101] ASM International Handbook Committee, ASM Volume 21 - Handbook of Composites, ASM International, 2001.

[102] S.T. Peters, Handbook of composites, 2nd ed., Chapman & Hall, Springer, US, 1998.

[103] E. Irving, C. Soutis, Polymer composites in the aerospace industry, 1st ed., Woodhead Publishing, Elsevier, 2015.

[104] C. Harper, Handbook of Plastics , Elastomers , and Composites, Mcgraw-Hill, 2004.

[105] M. Bitterlich, Thermoplastic Resin Transfer Molding (T-RTM): Tailored to Reactive Polyamide 6, Kunststoffe Int. (2014) 47–51.

[106] M. Thomassey, B.P. Revol, F. Ruch, J. Schell, M. Bouquey, Interest of a Rheokinetic Study for the Development of Thermoplastic Composites by T-RTM, Univers. J. Mater. Sci. 5 (2017) 15–27.

[107] Y. Gong, G. Yang, All-polyamide composites prepared by resin transfer molding, J. Mater. Sci. 45 (2010) 5237–5243.

[108] G. Wiedemann, H. Rothe, Review of Prepreg Technology, Dev. Reinf. Plast. (1986) 83–119.

[109] HexPly Prepreg Technology, HexPly Prepreg Technology, Hexcel Regist. Trademark. (2013) 28.

[110] H. Huang, R. Talreja, Effects of void geometry on elastic properties of unidirectional fiber reinforced composites, Compos. Sci. Technol. 65 (2005) 1964–1981.

[111] L. Liu, B.-M. Zhang, D.-F. Wang, Z.-J. Wu, Effects of cure cycles on void content and mechanical properties of composite laminates, Compos. Struct. 73 (2006) 303–309.

[112] W. Tu, P.H. Wen, P.J. Hogg, F.J. Guild, Optimisation of the protrusion geometry in Comeld^{TM} joints, Compos. Sci. Technol. 71 (2011) 868–876.

[113] P.N. Parkes, R. Butler, D.P. Almond, Growth of damage in additively manufactured metal-composite joints, ECCM 15 - 15th Eur. Conf. Compos. Mater. (2012).

[114] S. Ucsnik, R. Gradinger, Evaluation of a novel lightweight metal-composite- joint technology, 14th Eur. Conf. Compos. Mater. (2010).

[115] S. Stelzer, S. Ucsnik, G. Pinter, Fatigue behaviour of composite–composite joints reinforced with cold metal transfer welded pins, Int. J. Fatigue. 81 (2015) 37–47.

[116] S. Stelzer, S. Ucsnik, G. Pinter, Strength and damage tolerance of composite–composite joints with steel and titanium through the thickness reinforcements, Compos. Part A Appl. Sci. Manuf. 88 (2016) 39–47.

[117] I. Skhabovskyi, N.L. Batista, C.A. Damato, R.P. Reis, E.C. Botelho, A. Scotti, Appraisal of fiber-metal laminate panels reinforced with metal pins deposited by CMT welding, Compos. Struct. 180 (2017) 263–275.

[118] W. Xiong, B. Blackman, J.P. Dear, X. Wang, The effect of composite orientation on the mechanical properties of hybrid joints strengthened by Surfi-Sculpt, Compos. Struct. 134 (2015) 587–592.

[119] N. Li, P.H. Chen, X.Y. Liu, W. Ma, X.C. Wang, A micro-macro finite element model for failure prediction of ComeldTM joints, Compos. Sci. Technol. 117 (2015) 334–341.

[120] M.J. Donachie, Titanium : a technical guide, 2nd ed., ASM International, 2000.

[121] ASM International committee., ASM Handbook: Properties and Selection : Nonferrous Alloys and Special-Purpose Materials, 10th editi, ASM International, Materials Park, Ohio, 1990.

[122] E.O. Ezugwu, Z.M. Wang, Materials Processing Technology Titanium alloys and their machinability a review, J. Mater. Process. Technol. 68 (1997) 262–274.

[123] C. Veiga, J.P. Davim, A.J.R. Loureiro, Review on machinability of titanium alloys: the process perspective, Rev. Adv. Mater. Sci. 34 (2013) 148–164.

[124] G.C. Obasi, O.M. Ferri, T. Ebel, R. Bormann, Influence of processing parameters on mechanical properties of Ti-6Al-4V alloy fabricated by MIM, Mater. Sci. Eng. A. 527 (2010) 3929–3935.

[125] D.F. Heaney, Handbook of metal injection molding, Woodhead Publishing, Elsevier, Cambridge, UK ; Philadelphia, PA, 2012.

[126] N. Myers, D. Heaney, Metal injection molding (MIM) of high-speed tool steels, in: D.F. Heaney (Ed.), Handb. Met. Inject. Molding, 2012: pp. 516–525.

[127] T. Ebel, Metal injection molding (MIM) of titanium and titanium alloys, Handb. Met.

Inject. Molding. (2012) 415–445.

[128] T. Ebel, O.M. Ferri, W. Limberg, M. Oehring, F. Pyczak, F.-P. Schimansky, Metal injection moulding of titanium and titanium-aluminides, Key Eng. Mater. 520 (2012) 153–160.

[129] R.M. German, Progress in Titanium Metal Powder Injection Molding., Mater. (Basel, Switzerland). 6 (2013) 3641–3662.

[130] ASTM B348 - 13 Standard Specification for Titanium and Titanium Alloy Bars and Billets, ASTM Int. (2013).

[131] O. Ferri, Optimisation of Fatigue Behaviour of Ti-6Al-4V Alloy Components Fabricated by Metal Injection Moulding, Ph.D Thesis, Tech. Univ. Hambg. (2010).

[132] T. Ebel, MIM Processing of Titanium Alloys – Success , Limitations and Further Research, Euro Light. 2013. (2013).

[133] O.M. Ferri, T. Ebel, R. Bormann, Improvement of fatigue behaviour of Ti-6Al-4V components fabricated by MIM, Int. Congr. Exhib. EURO PM2009. (2009) 299–304.

[134] O.M. Ferri, T. Ebel, R. Bormann, The Influence of a Small Boron Addition on the Microstructure and Mechanical Properties of Ti-6Al-4V Fabricated by Metal Injection Moulding, Adv. Eng. Mater. 13 (2011) 436–447.

[135] ASTM F2885 - 17 Standard Specification for Metal Injection Molded Titanium-6Aluminum-4Vanadium Components for Surgical Implant Applications, ASTM Int. (2017).

[136] E.C. Botelho, J.C. Bravim Júnior, M. Leali Costa, M.C. Magalhaes De Faria, Environmental Effects on Thermal Properties of PEI/Glass Fiber Composite Materials, J. Aerosp. Technol. 5 (2013) 241–254.

[137] S. Boria, A. Scattina, G. Belingardi, Impact behavior of a fully thermoplastic composite, Compos. Struct. 167 (2017) 63–75.

[138] E.C. Botelho, L. Figiel, M.C. Rezende, B. Lauke, Mechanical behavior of carbon fiber reinforced polyamide composites, Compos. Sci. Technol. 63 (2003) 1843–1855.

[139] Product datasheet, Cetex® TC 1000 Premium, TenCate. (n.d.). http://www.tencate.com/emea/Images/Cetex_TC1000_Premium_DS_Web 05051428-25012.pdf (accessed December 7, 2017).

[140] S. Carroccio, C. Puglisi, G. Montaudo, Polyetherimide, in: Handb. Eng. Spec. Thermoplast., John Wiley & Sons, Inc., Hoboken, NJ, USA, 2011: pp. 79–110.

[141] R.O. Johnson, H.S. Burlhis, Polyetherimide: A new high-performance thermoplastic resin, J. Polym. Sci. Polym. Symp. 70 (1983) 129–143.

[142] M. Biron, Thermoplastics and Thermoplastic Composites - Technical Information for Plastics Users, Elsevier Ltd. (2007).

[143] I. Merdas, F. Thominette, J. Verdu, Humid aging of polyetherimide. I. Water sorption characteristics, J. Appl. Polym. Sci. 77 (2000) 1439–1444.

[144] I. Merdas, F. Thominette, J. Verdu, Humid aging of polyetherimide. II. Consequences of water absorption on thermomechanical properties, J. Appl. Polym. Sci. 77 (2000)

1445–1451.

[145] S. Kuroda, K. Terauchi, K. Nogami, I. Mita, Degradation of aromatic polymers - I. Rates of crosslinking and chain scission during thermal degradation of several soluble aromatic polymers, Eur. Polym. J. 25 (1989) 1–7.

[146] L. Augh, J.W. Gillespie, B.K. Fink, Degradation of Continuous Carbon Fiber Reinforced Polyetherimide Composites During Induction Heating, J. Thermoplast. Compos. Mater. 14 (2001) 96–115.

[147] S.T. Amancio-Filho, J. Roeder, S.P. Nunes, J.F. dos Santos, F. Beckmann, Thermal degradation of polyetherimide joined by friction riveting (FricRiveting). Part I: Influence of rotation speed, Polym. Degrad. Stab. 93 (2008) 1529–1538.

[148] J.M. Gardner, C.J. Stelter, E.A. Yashin, E.J. Siochi, High Temperature Thermoplastic Additive Manufacturing Using Low-Cost, Open- Source Hardware, NASA/TM—2016– 219344. (2016).

[149] D. Bourell, J.P. Kruth, M. Leu, G. Levy, D. Rosen, A.M. Beese, A. Clare, Materials for additive manufacturing, (2017).

[150] C. Ageorges, L. Ye, M. Hou, Experimental investigation of the resistance welding for thermoplastic-matrix composites. Part I: heating element and heat transfer, Compos. Sci. Technol. 60 (2000) 1027–1039.

[151] C. Ageorges, L. Ye, Y.-W. Mai, M. Hou, Characteristics of resistance welding of lap shear coupons. Part I: Heat transfer, Compos. Part A Appl. Sci. Manuf. 29 (1998) 899–909.

[152] M. Hou, L. Ye, Y.W. Mai, An Experimental Study of Resistance Welding of Carbon Fibre Fabric Reinforced Polyetherimide (CF Fabric/PEI) Composite Material, Appl. Compos. Mater. 6 (1999) 35–49.

[153] V.K. Stokes, Vibration weld strength data for glass-filled polyetherimide, J. Adhes. Sci. Technol. 15 (2001) 1763–1768.

[154] M.J. Troughton, Handbook of plastics joining: a practical guide, 2nd ed., William Andrew, Norwych, 2008.

[155] V. Wippo, Y. Winter, P. Jaeschke, O. Suttmann, L. Overmeyer, The influence of laser welding processes on the weld seam quality of thermoplastic composites with high moisture content, Phys. Procedia. 83 (2016) 1064–1072.

[156] V.K. Stokes, A phenomenological study of the hot-tool welding of thermoplastics Part 3. Polyetherimide, Polymer (Guildf). 42 (2001) 775–792.

[157] T.J. Ahmed, D. Stavrov, H.E.N. Bersee, A. Beukers, Induction welding of thermoplastic composites—an overview, Compos. Part A Appl. Sci. Manuf. 37 (2006) 1638–1651.

[158] O. Schieler, U. Beier, Induction Welding of Hybrid Thermoplastic-thermoset Composite Parts, Int. J. Appl. Sci. Technol. 9 (2016) 27–36.

[159] Ultem* and Siltem* resins - Products and markets guide, 2008. http://www.pod-sabic-ip.com/KBAM/Reflection/Assets/Thumbnail/14106_13.pdf (accessed June 24, 2015).

[160] C. Ageorges, L. Ye, Resistance Welding of Metal/Thermoplastic Composite Joints, J. Thermoplast. Compos. Mater. 14 (2001) 449–475.

[161] L. Blaga, R. Bancilă, J.F. dos Santos, S.T. Amancio-Filho, Friction Riveting of glass–fibre-reinforced polyetherimide composite and titanium grade 2 hybrid joints, Mater. Des. 50 (2013) 825–829.

[162] L. Blaga, J.F. dos Santos, R. Bancila, S.T. Amancio-Filho, Friction Riveting (FricRiveting) as a new joining technique in GFRP lightweight bridge construction, Constr. Build. Mater. 80 (2015) 167–179.

[163] Element22, Element 22 GmbH - As sintered Ti-6Al-4V Material Datasheet, (n.d.).

[164] Kenneth C. Mills, Recommended Values of Thermophysical Properties for Selected Commercial Alloys, Woodhead Publishing, 2002.

[165] ISO 2740:2009 - Sintered metal materials, excluding hardmetals -- Tensile test pieces, 2009.

[166] Tencate, CETEX(R) PEI Datasheet - Tencate advanced composites USA, INC., (n.d.).

[167] Duratron U1000 PEI, 2011. http://www.quadrantplastics.com/fileadmin/quadrant/documents/QEPP/EU/Product_Data_Sheets_PDF/AEP/Duratron_U1000_PEI_PDS_E_28042011.pdf (accessed September 7, 2014).

[168] UltraWeld L20, AmTech Product Manual- Special Information, (2007).

[169] UHB Marax ESR, Hochfester Kalt- und Warmarbeitsstahl - Material datasheet, (2015).

[170] D.C. Montgomery, G.C. Runger, Applied statistics and probability for engineers, 3rd ed., John Wiley & Sons, 2003.

[171] M. Cavazzuti, Optimization Methods: From Theory to Design Scientific and Technological Aspects in Mechanics, Springer Berlin Heidelberg, Berlin, Heidelberg, 2013.

[172] Preparation of Cu-Cr alloy powder by heat mechanical alloying and Box-Behnken design based optimization, Powder Technol. 321 (2017) 326–335.

[173] Application of Box–Behnken design for fabrication of titanium alloy and 304 stainless steel joints with silver interlayer by diffusion bonding, Mater. Des. 77 (2015) 161–169.

[174] Optimization of paclitaxel loaded poly (ε-caprolactone) nanoparticles using Box Behnken design, Beni-Suef Univ. J. Basic Appl. Sci. (2017).

[175] B.K. Sahoo, U. Chakraborty, J. Mukherjee, T.K. Pal, Optimization and Validation of Modulated Release Formulation of Ranitidine HCl by Response Surface Methodology, J. Biomed. Sci. Res. 2 (2010) 76–85.

[176] D.C. Montgomery, Design and Analysis of Experiments, Fourth, John Wiley & Sons, Inc., 1997.

[177] C.F. Rodrigues, L.A. Blaga, J.F. dos Santos, L.B. Canto, E. Hage Jr., S.T. Amancio-Filho, FricRiveting of aluminum 2024-T351 and polycarbonate: Temperature

evolution, microstructure and mechanical performance, J. Mater. Process. Technol. 214 (2014) 2029–2039.

[178] S.T. Amancio Filho, Friction Riveting development and analysis of a new joining technique for polymer-metal multi-material structures, HZG Rep. (2007).

[179] ISO 4287:1997 - Geometrical Product Specifications (GPS) - Surface texture: Profile method -Terms, definitions and surface texture parameters, ISO. (1997).

[180] N. Schell, A. King, F. Beckmann, H.U.H.-U. Ruhnau, R. Kirchhof, R. Kiehn, M. Müller, A. Schreyer, R.V. Martins, F. Beckmann, H.U.H.-U. Ruhnau, R. Kiehn, A. Schreyer, The High Energy Materials Science Beamline at PETRA III, Mater. Sci. Forum. 571–572 (2008) 261–266.

[181] G.W. Ehrenstein, G. Riedel, P. Trawiel, Thermal Analysis of Plastics: Theory and Practice, Carl Hanser Verlag, Munich, 2004.

[182] Z. Grubisic, P. Rempp, H. Benoit, A universal calibration for gel permeation chromatography, J. Polym. Sci. Part B Polym. Lett. 5 (1967) 753–759.

[183] M. Gaborieau, P. Castignolles, Size-exclusion chromatography (SEC) of branched polymers and polysaccharides., Anal. Bioanal. Chem. 399 (2011) 1413–23.

[184] ASTM, E384-10e1: Standard Test Method for Knoop and Vickers Hardness of Materials, West Conshohocken, PA, 2010.

[185] The Nano Indenter® XP, MTS - TestWorks ® 4 Software for Nanoindentation Systems - Operation Manual, (2002). https://eng.auburn.edu/files/acad_depts/matl/lab-manuels/113 - Nanomechanics Lab/manuals/the-nano-indenter-xp-manual.pdf (accessed October 6, 2017).

[186] ASTM D3163 - 01(2014) Standard Test Method for Determining Strength of Adhesively Bonded Rigid Plastic Lap-Shear Joints in Shear by Tension Loading, (n.d.).

[187] ASTM E466 - 15 Standard Practice for Conducting Force Controlled Constant Amplitude Axial Fatigue Tests of Metallic Materials, (n.d.).

[188] ASTM E739 - 10(2015) Standard Practice for Statistical Analysis of Linear or Linearized Stress-Life (S-N) and Strain-Life (ε-N) Fatigue Data, ASTM Stand. (n.d.).

[189] Influence of paraffin wax characteristics on the formulation of wax-based binders and their debinding from green molded parts using two comparative techniques, J. Mater. Process. Technol. 209 (2009) 5981–5989.

[190] A.-F.S. Goushegir S, dos Santos J, Friction Spot Joining of aluminum AA2024/carbon-fiber reinforced poly(phenylene sulfide) composite single lap joints: Microstructure and mechanical performance, Mater. Des. 54 (2014) 196–206.

[191] N.. Andre, S.M. Goushegir, J.. dos Santos, L. Canto, S.T. Amancio-Filho, Friction Spot Joining of aluminum alloy 2024-T3 and carbon-fiber-reinforced poly(phenylene sulfide) laminate with additional PPS film interlayer: Microstructure, mechanical strength and failure mechanisms, Compos. Part B Eng. 94 (2016) 197–208.

[192] A.-F.S. Goushegir S, Dos Santos J, Failure and fracture micro-mechanisms in metal-composite single lap joints produced by welding-based joining techniques, Compos.

Part A Appl. Sci. Manuf. 81 (2016) 121–128.

[193] E.E. Feistauer, T. Ebel, J.F. Santos, S.T. Amancio-Filho, Ultrasonic joining of through-the-thickness reinforced Ti-4Al-6V and polyetherimide hybrid joints, ANTEC® 2017 - Anaheim, Soc. Plast. Eng. Calif. - USA. (2017).

[194] Welding Handbook Committee, Welding Handbook volume 2, 9th ed., AWS - American Welding Society, 2004.

[195] D.A. Grewell, A. Benatar, Plastics and Composites Welding Handbook, Hanser Gardener, 2003.

[196] J. Rotheiser, Joining of Plastics: Handbook for Designers and Engineers, 3. Auflage, Carl Hanser Verlag GmbH & Co. KG, 1999.

[197] G. Wagner, F. Balle, D. Eifler, Ultrasonic Welding of Aluminum Alloys to Fiber Reinforced Polymers, Adv. Eng. Mater. 15 (2013) 792–803.

[198] A.B. Abibe, Friction-based Injection Clinching Joining (F-ICJ): a new joining method for hybrid lightweight structures, Ph.D. Thesis, Technischen Universität Hamburg, 2015.

[199] V.K. Stokes, Analysis of the friction (spin)-welding process for thermoplastics, J. Mater. Sci. 23 (1988) 2772–2785.

[200] S.T. Amancio-Filho, J.F. dos Santos, Preliminary analytical modeling of heat input in friction, Proc. ANTEC 2016. (2016) 1361–1368.

[201] D.A. Grewell, A. Benatar, J.B. Park, Plastics and composites welding handbook, Carl Hanser Verlag, Munich, 2003.

[202] G. Menges, Werkstoffkunde der kunststoffe, Carl Hanser Verlag, München, Germany, 1985.

[203] G. Mennig, Wear in Plastics Processing: How to Understand, Protect and Avoid, Hanser Publishers, Munich, 1995. http://www.amazon.com/Wear-Plastics-Processing-Understand-Protect/dp/3446170715.

[204] V.I. Vill, Friction Welding of Metals, American Welding Society, USA, 1962.

[205] H. Potente, M. Reinke, Welding parameters and properties of polyolefin parts, Plast. Rubber Appl. 1 (1981) 149–160.

[206] A. Benatar, T.G. Gutowski, Ultrasonic welding of PEEK graphite APC-2 composites, Polym. Eng. Sci. 29 (1989) 1705–1721.

[207] M.N. Tolunay, P.R. Dawson, K.K. Wang, Heating and bonding mechanisms in ultrasonic welding of thermoplastics, Polym. Eng. Sci. 23 (1983) 726–733.

[208] S.T. Amancio-Filho, Henry Granjon Prize Competition 2009 Winner Category A: “Joining and Fabrication Technology” Friction Riveting: development and analysis of a new joining technique for polymer-metal multi-material structures, Weld. World. 55 (2013) 13–24.

[209] G. Wagner, F. Balle, D. Eifler, Ultrasonic Welding of Aluminum Alloys to Fiber Reinforced Polymers, Adv. Eng. Mater. 15 (2013) 792–803.

[210] H. Potente, Fügen von Kunststoffen. Grundlagen, Verfahren, Anwendung, Carl Hanser Verlag GmbH & Co. KG, München, 2004.

[211] S.T. Amancio-Filho, S. Sheikhi, J.F. dos Santos, C. Bolfarini, Preliminary study on the microstructure and mechanical properties of dissimilar friction stir welds in aircraft aluminium alloys 2024-T351 and 6056-T4, J. Mater. Process. Technol. 206 (2008) 132–142.

[212] J. Rösler, H. Harders, M. Bäker, Mechanical Behaviour of Engineering Materials, 2007.

[213] C.W. Liu D, Tang Y, A review of mechanical drilling for composite laminates, Compos. Struct. 94 (2012) 1265–1279.

[214] J.H. Kavad B, Pandey A, Tadavi M, A Review Paper on Effects of Drilling on Glass Fiber Reinforced Plastic, Procedia Technol. 14 (2014) 457–464.

[215] H. Zhang, W. Wen, H. Cui, Study on the strength prediction model of Comeld composites joints, Compos. Part B Eng. 43 (2012) 3310–3317.

[216] F. Haddadi, F. Abu-Farha, Microstructural and mechanical performance of aluminium to steel high power ultrasonic spot welding, J. Mater. Process. Technol. 225 (2015) 262–274.

[217] C.Q. Zhang, J.D. Robson, P.B. Prangnell, Dissimilar ultrasonic spot welding of aerospace aluminum alloy AA2139 to titanium alloy TiAl6V4, J. Mater. Process. Technol. 231 (2016) 382–388.

[218] Z. Tadmor, C.G. Gogos, Principles of polymer processing, Wiley-Interscience, 2006.

[219] M. Boivineau, C. Cagran, D. Doytier, V. Eyraud, M.-H. Nadal, B. Wilthan, G. Pottlacher, Thermophysical Properties of Solid and Liquid Ti - 6Al - 4V (TA6V) Alloy, Int. J. Thermophys. 27 (2006).

[220] ASM International Handbook Committee, ASTM Handbook - Volume 2. Properties and Selection: Nonferrous Alloy and Special-Purpose Materials, 1992.

[221] M. Biron, Thermoplastics and Thermoplastic Composites, Elsevier, Oxford, 2007.

[222] C. Weng, W.B.B. Lee, S. To, Birefringence techniques for the characterization of residual stresses in injection-moulded micro-lens arrays, Polym. Test. 28 (2009) 709–714.

[223] N.K. Lautre, A.K. Sharma, P. Kumar, S. Das, A photoelasticity approach for characterization of defects in microwave drilling of soda lime glass, J. Mater. Process. Technol. 225 (2015) 151–161.

[224] G. Strobl, The Physics of Polymers, 3rd ed., Springer, Berlin, 2007.

[225] M. Scafidi, G. Pitarresi, A. Toscano, G. Petrucci, S. Alessi, A. Ajovalasit, Review of photoelastic image analysis applied to structural birefringent materials: glass and polymers, Opt. Eng. 54 (2015) 081206–081206.

[226] A.S. Redner, B.R. Hoffman, Measuring residual stress in transparent plastics, Med. Plast. Degrad. Resist. Fail. Anal. (1998) 45–50.

[227] A. Ajovalasit, G. Petrucci, M. Scafidi, RGB Photoelasticity: Review and

Improvements, Strain. 46 (2010) 137–147.

[228] J. Kameda, Y. Yokoyama, T.R. Allen, Strain-controlling mechanical behavior in noncrystalline materials: I: Onset of plastic deformation, Mater. Sci. Eng. A. 448 (2007) 235–241.

[229] F.J. Baltá Calleja, S. Fakirov, Microhardness of polymers, Cambridge University Press, New York, 2007.

[230] A. Flores, F. Ania, F.J.J. Baltá-Calleja, From the glassy state to ordered polymer structures: A microhardness study, Polymer (Guildf). 50 (2009) 729–746.

[231] D.R. Rueda, M.C.G. Gutiérrez, F.J.B. Calleja, S. Piccarolo, Order in the amorphous state of poly(ethylene terephthalate) as revealed by microhardness: Creep behavior and physical aging, Int. J. Polym. Mater. Polym. Biomater. 51 (2002) 897–908.

[232] D.R. Rueda, F.J. Baltá Calleja, R.K. Bayer, Influence of processing conditions on the structure and surface microhardness of injection-moulded polyethylene, J. Mater. Sci. 16 (1981) 3371–3380.

[233] F.J. Baltá-Calleja, D.C. Bassett, Microindentation hardness of oriented chain-extended polyethylene, J. Polym. Sci. Polym. Symp. 58 (2007) 157–167.

[234] D.R. Rueda, F. Ania, F.J.B. Calleja, Vickers indentation anisometry on thin cylindrical materials, J. Mater. Sci. 17 (1982) 3427–3430.

[235] J.M. Hutchinson, Physical aging of polymers, Prog. Polym. Sci. 20 (1995) 703–760.

[236] F.J. Baltá Calleja, A. Flores, G.H. Michler, Microindentation studies at the near surface of glassy polymers: Influence of molecular weight, J. Appl. Polym. Sci. 93 (2004) 1951–1956.

[237] S. -i. Kuroda, K. Terauchi, K. Nogami, I. Mita, Degradation of aromatic polymers - I. Rates of crosslinking and chain scission during thermal degradation of several soluble aromatic polymers, Eur. Polym. J. 25 (1989) 1–7.

[238] I.M. Low, Effects of load and time on the hardness of a viscoelastic polymer, Mater. Res. Bull. 33 (1998) 1753–1758.

[239] L. Blunt, P.J. Sullivan, The measurement of the pile-up topography of hardness indentations, Tribol. Int. 27 (1994) 69–79.

[240] M. Sakai, Simultaneous estimate of elastic/plastic parameters in depth-sensing indentation tests, Scr. Mater. 51 (2004) 391–395.

[241] M. Sakai, S. Shimizu, T. Ishikawa, The indentation load-depth curve of ceramics, (2017).

[242] P. Zhang, S.X. Li, Z.F. Zhang, General relationship between strength and hardness, Mater. Sci. Eng. A. 529 (2011) 62–73.

[243] W.C. Oliver, G.M. Pharr, An improved technique for determining hardness and elastic modulus using load and displacement sensing indentation experiments, Mater. Res. Soc. 7 (1992) 1564–1583.

[244] W.C. Oliver, G.M. Pharr, Measurement of hardness and elastic modulus by instrumented indentation : Advances in understanding and refinements to

methodology, J. Mater. Res. 19 (2004) 3–20.

[245] Nanoindentation in polymer nanocomposites, Prog. Mater. Sci. 67 (2015) 1–94.

[246] R.F. Gibson, A review of recent research on nanoindentation of polymer composites and their constituents, Compos. Sci. Technol. 105 (2014) 51–65.

[247] S.R. Cohen, E. Kalfon-Cohen, Dynamic nanoindentation by instrumented nanoindentation and force microscopy: a comparative review., Beilstein J. Nanotechnol. 4 (2013) 815–33.

[248] M.R. VanLandingham, J.S. Villarrubia, W.F. Guthrie, G.F. Meyers, Nanoindentation of polymers: an overview, Macromol. Symp. 167 (2001) 15–44.

[249] D.L. Joslina, W.C. Oliver, A new method for analyzing data from continuous depth-sensing microindentation tests, J. Mater. Res. 5 (1990) 123–126.

[250] X.Y. Zhou, Z.D. Jiang, H.R. Wang, Q. Zhu, A Method to Extract the Intrinsic Mechanical Properties of Soft Metallic Thin Films Based on Nanoindentation Continuous Stiffness Measurement Technique, J. Phys. Conf. Ser. 48 (2006) 1096–1101.

[251] G.Z. Voyiadjis, L. Malekmotiei, Variation of the strain rate during CSM nanoindentation of glassy polymers and its implication on indentation size effect, J. Polym. Sci. Part B Polym. Phys. 54 (2016) 2179–2187.

[252] G.M. Odegard, T.S. Gates, H.M. Herring, Characterization of viscoelastic properties of polymeric materials through nanoindentation, Exp. Mech. 45 (2005) 130–136.

[253] C.C. White, M.R. VanLandingham, P.L. Drzal, N.K. Chang, S.H. Chang, Viscoelastic characterization of polymers using instrumented indentation. II. Dynamic testing*, J. Polym. Sci. Part B Polym. Phys. 43 (2005) 1812–1824.

[254] L. Nielsen, R. Landel, Mechanical properties of polymers and composites, Second Edition, Marcel Dekker , 1993.

[255] W. Schnabel, Polymer Degradation, Principles and Practical Applications, Carl Hanser Verlag München, München, Germany, 1981.

[256] W. Brostow, R.D. Corneliussen, Failure of Plastics, Carl Hanser Verlag, Munich, 1986.

[257] Quadrant Engineering Plastic Products - Duratron(R) U1000 PEI Datasheet, Quadr. Gr. Co. (2013). http://www.nylaplas.com/plastics/pds/Duratron_U1000_PEI_PDS_E_17102013.pdf (accessed December 7, 2017).

[258] C.T. Moynihan, A.J. Easteal, J. Wilder, J. Tucker, Dependence of the glass transition temperature on heating and cooling rate, J. Phys. Chem. 78 (1974) 2673–2677.

[259] D. Simatos, G. Blond, G. Roudaut, D. Champion, J. Perez, A.L. Faivre, Influence of heating and cooling rates on the glass transtion temperature and the fragility parameter of sorbitol and fructose as measured by DSC, J. Therm. Anal. 47 (1996) 1419–1436.

[260] M.A. Sanner, G. Haralur, A. May, Effect of molecular weight on brittle-to-ductile

transition temperature of polyetherimide, J. Appl. Polym. Sci. 92 (2004) 1666–1671.

[261] A.L. Agapov, V.N. Novikov, A.P. Sokolov, Fragility and other Properties of Glass-forming Liquids: Two Decades of Puzzling Correlations, in: A.L. Greer, K.F. Kelton, S. Sastry (Eds.), Fragility Glas. Liq., Hindustan Book Agency, 2014.

[262] K. Kunal, Influence of chemical structure and molecular weight on fragility in polymers, Ph.D. Thesis, University of Akron, 2009.

[263] S. V Canevarolo, Chain scission distribution function for polypropylene degradation during multiple extrusions, Polym. Degrad. Stab. 709 (2000) 71–76.

[264] C.A. Cáceres, S. V Canevarolo, Calculating the chain scission distribution function (CSDF) using the concentration method, Polym. Degrad. Stab. 86 (2004) 437–444.

[265] L.A. Pinheiro, M.A. Chinelatto, S. V Canevarolo, The role of chain scission and chain branching in high density polyethylene during thermo-mechanical degradation, Polym. Degrad. Stab. 86 (2004) 445–453.

[266] Photodegradation of polyethylene: comparison of various photoinitiators in natural weathering conditions, Polym. Degrad. Stab. 37 (1992) 233–245.

[267] M. Sônego, Efeitos de degradação e de alterações microestruturais do polímero no desempenho mecânico estático de juntas híbridas de polieterimida (PEI) e alumínio produzidas por F-ICJ. M.Sc. Thesis, Universidade Federal de São Carlos, 2016.

[268] A. Tayal, S.A. Khan, Degradation of a Water-Soluble Polymer: Molecular Weight Changes and Chain Scission Characteristics, Macromolecules. 33 (2000) 9488–9493.

[269] L. Zhao, A. Xin, F. Liu, J. Zhang, N. Hu, Secondary bending effects in progressively damaged single-lap, single-bolt composite joints, Results Phys. 6 (2016) 704–711.

[270] J. Ekh, J. Schön, L.G. Melin, Secondary bending in multi fastener, composite-to-aluminium single shear lap joints, Compos. Part B Eng. 36 (2005) 195–204.

[271] J. Ekh, Multi-Fastener Single-lap Joints in Composite Structures, Ph.D. Thesis, Royal Institute of Technology, Stockholm, Sweden, n.d.

[272] E. Schulz, Rasterelektronenmikroskopische Untersuchungen von Kunststoffschäden, Acta Polym. 31 (1980) 273–274.

[273] H.J. Schmidt and B. Schmidt, Fatigue & Damage Tolerance and Composite Training, Geesthacht, (2017).

[274] S. Rasool, Fatigue of woven thermoplastic composites, Ph.D. Thesis, Technische Universiteit Delft, 2015.

[275] R. Sakin, İ. Ay, Statistical analysis of bending fatigue life data using Weibull distribution in glass-fiber reinforced polyester composites, Mater. Des. 29 (2008) 1170–1181.

[276] U.A. Khashaba, Fatigue and Reliability Analysis of Unidirectional GFRP Composites under Rotating Bending Loads, J. Compos. Mater. 37 (2003) 317–331.

[277] M. Sivapragash, P.R. Lakshminarayanan, R. Karthikeyan, K. Raghukandan, M. Hanumantha, Fatigue life prediction of ZE41A magnesium alloy using Weibull

distribution, (2008).

[278] P.S. Effertz, V. Infante, L. Quintino, U. Suhuddin, S. Hanke, J.F. dos Santos, Fatigue life assessment of friction spot welded 7050-T76 aluminium alloy using Weibull distribution, Int. J. Fatigue. 87 (2016) 381–390.

[279] Y.X. Zhao, H.B. Liu, Weibull modeling of the probabilistic S–N curves for rolling contact fatigue, Int. J. Fatigue. 66 (2014) 47–54.

[280] ASM International. Handbook Committee., ASM handbook - Fatigue and Fracture, ASM International®, United States of America, 1996.

[281] Janet, Understanding the Surface Features of Fatigue Fractures: How They Describe the Failure Cause and the Failure History, J. Fail. Anal. Prev. 5 (2005).

[282] S.. Amancio-Filho, J.F. dos Santos, Influence of processing parameters on microstructure and properties of a polyetherimide joined by FricRiveting: investigation of rotational speed, in: ANTEC, 2009: pp. 750–756.

[283] O.M. Ferri, T. Ebel, R. Bormann, The influence of a small boron addition on the microstructure and mechanical properties of Ti-6Al-4V fabricated by metal injection moulding, Adv. Eng. Mater. 13 (2011) 436–447.

[284] J.L. Hay, M.T.S.S. Corporation, Instrumented Indentation Testing, in: H. Kuhn, D. Medlin (Eds.), ASM Handb. Vol. 08 Mech. Test. Eval., ASM International®, n.d.: pp. 233–243.

[285] M. Ben Bettaieb, T. Van Hoof, H. Minnebo, T. Pardoen, P. Dufour, P.J. Jacques, A.-M. Habraken, Micromechanics-Based Damage Analysis of Fracture in Ti5553 Alloy with Application to Bolted Sectors, J. Mater. Eng. Perform. 24 (2015) 1262–1278.

[286] W. WEIBULL, Fatigue Testing and Analysis of Results - CHAPTER IX – ANALYSIS OF RESULTS, in: Fatigue Test. Anal. Results, 1961: pp. 184–249.

[287] D.D. Randall Pollak, Analysis of methods for determining high cycle fatigue strength of a material with investigation of Ti-6Al-4V gigacycle fatigue behavior, Ph.D. thesis, Air Force Institute of Technology Air University,OH, US, 2005.

[288] A. Bennett, G. Weinberg, Fatigue Notch Sensitivity of Some Aluminum Alloys, J. Res. Natl. Bur. Stand. (1934). 52 (1954).

List of Figures

List of Tables

APPENDICES

APPENDIX A.1. U-JOINING PATENT

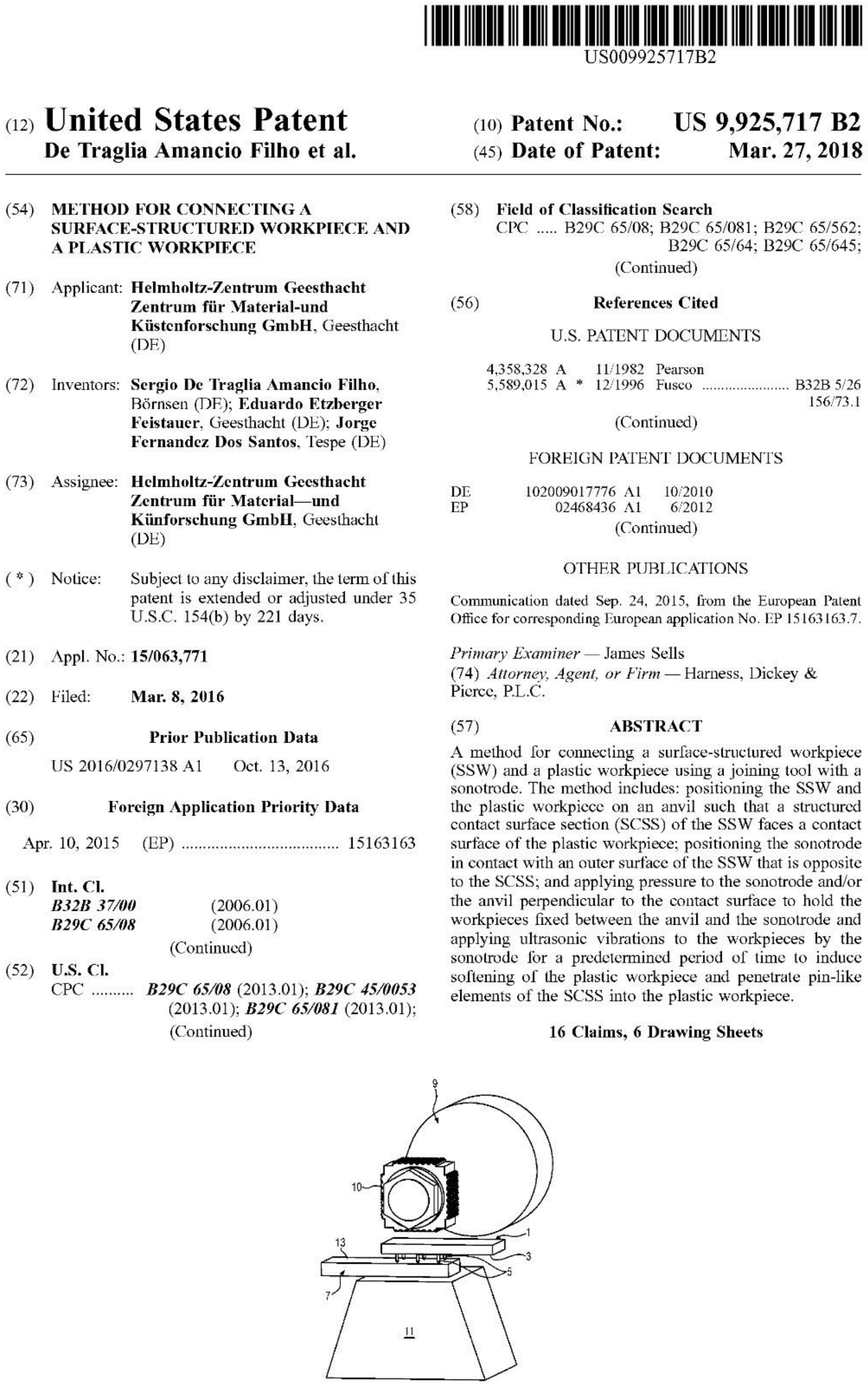

US009925717B2

(12) **United States Patent**
De Traglia Amancio Filho et al.

(10) **Patent No.: US 9,925,717 B2**
(45) **Date of Patent: Mar. 27, 2018**

(54) **METHOD FOR CONNECTING A SURFACE-STRUCTURED WORKPIECE AND A PLASTIC WORKPIECE**

(71) Applicant: **Helmholtz-Zentrum Geesthacht Zentrum für Material-und Küstenforschung GmbH**, Geesthacht (DE)

(72) Inventors: **Sergio De Traglia Amancio Filho**, Börnsen (DE); **Eduardo Etzberger Feistauer**, Geesthacht (DE); **Jorge Fernandez Dos Santos**, Tespe (DE)

(73) Assignee: **Helmholtz-Zentrum Geesthacht Zentrum für Material—und Künforschung GmbH**, Geesthacht (DE)

(*) Notice: Subject to any disclaimer, the term of this patent is extended or adjusted under 35 U.S.C. 154(b) by 221 days.

(21) Appl. No.: **15/063,771**

(22) Filed: **Mar. 8, 2016**

(65) **Prior Publication Data**

US 2016/0297138 A1 Oct. 13, 2016

(30) **Foreign Application Priority Data**

Apr. 10, 2015 (EP) 15163163

(51) **Int. Cl.**
B32B 37/00 (2006.01)
B29C 65/08 (2006.01)
(Continued)

(52) **U.S. Cl.**
CPC ***B29C 65/08*** (2013.01); ***B29C 45/0053*** (2013.01); ***B29C 65/081*** (2013.01);
(Continued)

(58) **Field of Classification Search**
CPC B29C 65/08; B29C 65/081; B29C 65/562; B29C 65/64; B29C 65/645;
(Continued)

(56) **References Cited**

U.S. PATENT DOCUMENTS

4,358,328 A 11/1982 Pearson
5,589,015 A * 12/1996 Fusco B32B 5/26 156/73.1
(Continued)

FOREIGN PATENT DOCUMENTS

DE 102009017776 A1 10/2010
EP 02468436 A1 6/2012
(Continued)

OTHER PUBLICATIONS

Communication dated Sep. 24, 2015, from the European Patent Office for corresponding European application No. EP 15163163.7.

Primary Examiner — James Sells
(74) *Attorney, Agent, or Firm* — Harness, Dickey & Pierce, P.L.C.

(57) **ABSTRACT**

A method for connecting a surface-structured workpiece (SSW) and a plastic workpiece using a joining tool with a sonotrode. The method includes: positioning the SSW and the plastic workpiece on an anvil such that a structured contact surface section (SCSS) of the SSW faces a contact surface of the plastic workpiece; positioning the sonotrode in contact with an outer surface of the SSW that is opposite to the SCSS; and applying pressure to the sonotrode and/or the anvil perpendicular to the contact surface to hold the workpieces fixed between the anvil and the sonotrode and applying ultrasonic vibrations to the workpieces by the sonotrode for a predetermined period of time to induce softening of the plastic workpiece and penetrate pin-like elements of the SCSS into the plastic workpiece.

16 Claims, 6 Drawing Sheets

Figure A. 0-1: Ultrasonic Joining (U-Joining) United State patent US 9,925,717 B2. Also published as: EP 3 078 480 - A1, BR 102016007517- A2, and CA 2 924 209 - A1.

APPENDIX A.2. FORCE-PRESSURE CALIBRATION CURVE OF THE JOINING SYSTEM

Figure A. 0-2 presented the force-pressure calibration curve obtained in-house, as well as, the calibration equation.

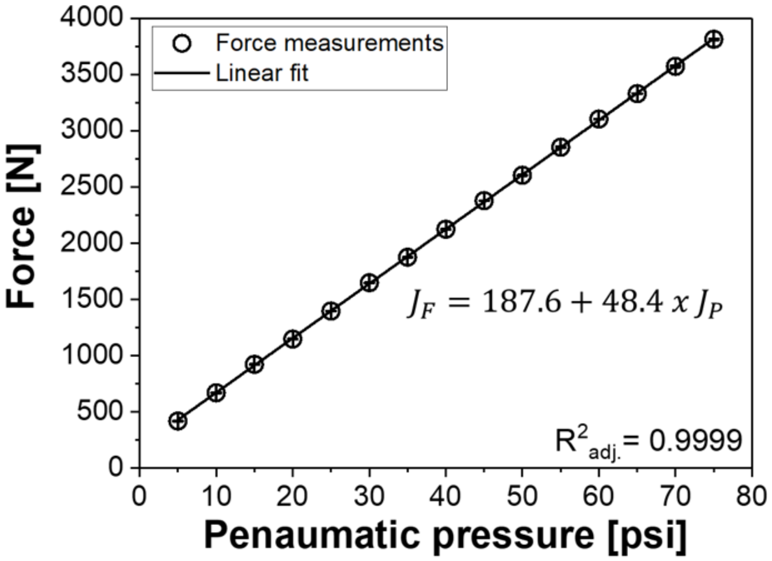

Figure A. 0-2: Force-pressure calibration curve of the joining system.

APPENDIX A.3. COLORED BIREFRINGENCE PATTERNS

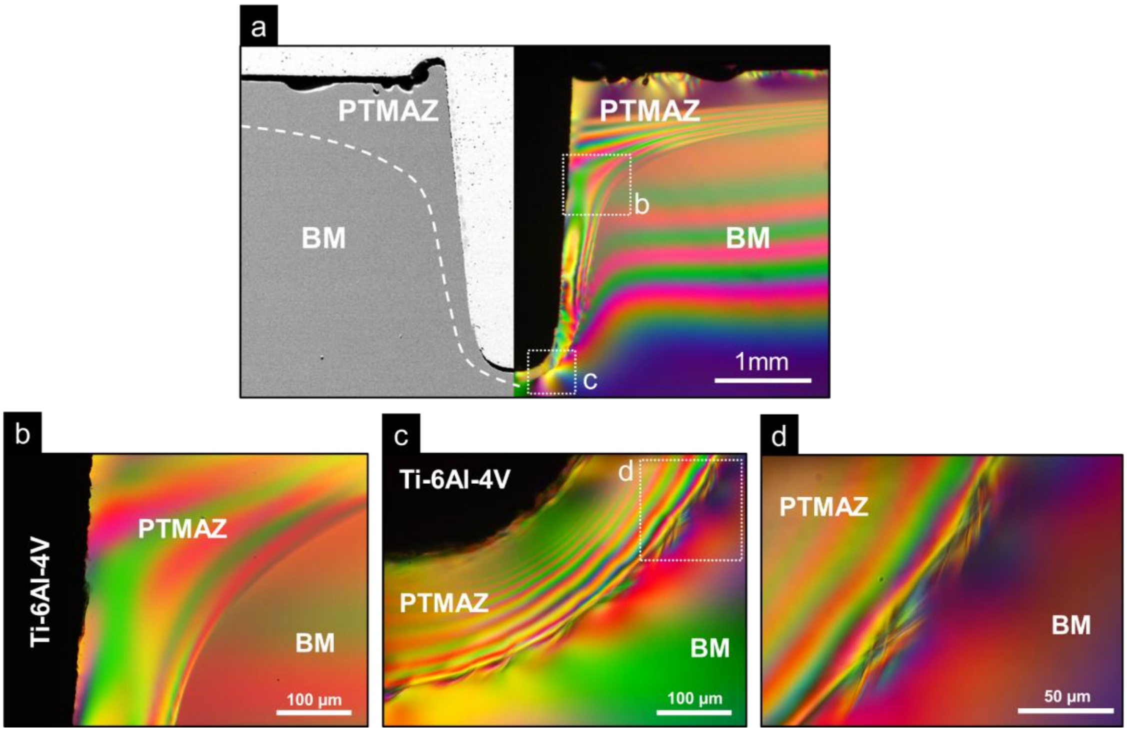

Figure A. 0-3: (a) SEM micrograph with a typical birefringence pattern observed in the Ti-6Al-4V/PEI hybrid joints. Such a joint was produced with the same optimized joining parameters used to join the GF-PEI hybrid joint. (b) Presents the shape of the PTMAZ at half the height of the pin, and (c) birefringence patterns showing the increase of fringe density towards the pin tip and thereby stress concentration, and in (d) the formation of shear bands at the PTMAZ limit.

APPENDIX A.4. NANOINDENTATION HARMONIC CONTACT STIFFNESS CURVES

Figure A. 0-4 presents the harmonic contact stiffness curves over the indentation depth during the nanoindentation tests for the joints produced with PEI and GF-PEI. Such curves are used to calculate the ratio of the load to the stiffness squared (P/S^2). This parameter is essential for correction of the hardness values according to the Joslin and Oliver [249] method.

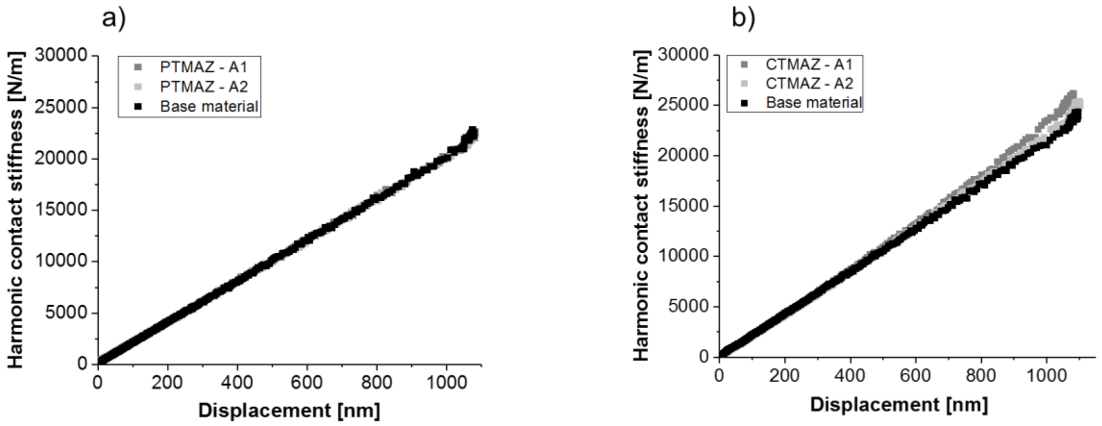

Figure A. 0-4: Examples of harmonic contact stiffness versus displacement for U-Joining joints produced (a) with PEI, and (b) with GF-PEI as the polymeric part of the joint.

As described in Section 8.2.3, the effective elastic modulus (E_{eff}) [244] was calculated by the following equation:

$$\frac{1}{\mathrm{E_{eff}}} = \frac{1-\mathrm{v}^2}{\mathrm{E}} + \frac{1-\mathrm{v_i^2}}{\mathrm{E_i}} \tag{8-6}$$

where E and v are the elastic modulus and Poisson’s ratio of the base material respectively and E_i and v_i the elastic modulus and Poisson’s ratio of the indenter. The values adopted for the diamond indenter used in this work corresponds to $\mathrm{E_i} = 141\ \mathrm{GPa}$ and $\mathrm{v_i} = 0.07$ [284]. For PEI the values were used according to the material datasheet [257] and correspond to $\mathrm{E} = 3.5\ \mathrm{GPa}$ and $\mathrm{v} = 0.38$.

APPENDIX A.5. FINITE ELEMENT ANALYSIS OF THE SINGLE LAP SHEAR TEST

The finite element (FE) method was applied to obtain the hybrid joint stress fields during the simulation of a single lap shear test. The model is presented in Figure A. 0-5. The FE analyses were performed using the Abaqus/Standard (version 6.14-2). This model uses linear hexahedron elements (C3D8H) and the dimensions of the computational problem are presented in Table A.0-1.

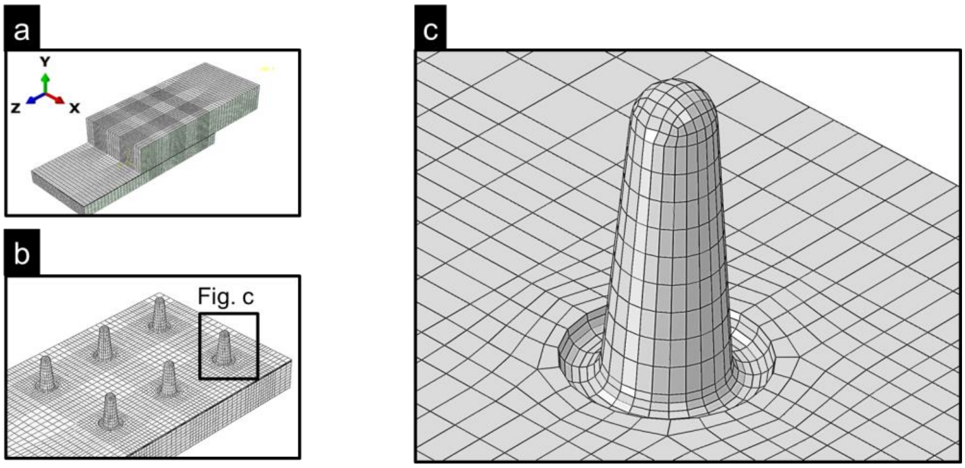

Figure A. 0-5: FE model of the single lap shear test

Table A.0-1: Problem size of the FE analysis.

Model characteristics	**Total number**
Number of elements	115918
Number of elements generated for contact	3867
Number of nodes	133154
Total number of variables	394284

To simulate the interface between the materials a cohesive surface contact was defined between the contact interface formed between the MIMStruct and GF-PEI plates. Such a contact surface was divided into three parts in order to improve the computational time as shown in Figure A. 0-6. Similarly, the cohesive surfaces were defined between each pin and adjacent composite volume, as presented in Figure A. 0-7. In both cases a set of master/slave pairs were applied, where the composite acts as a master surface.

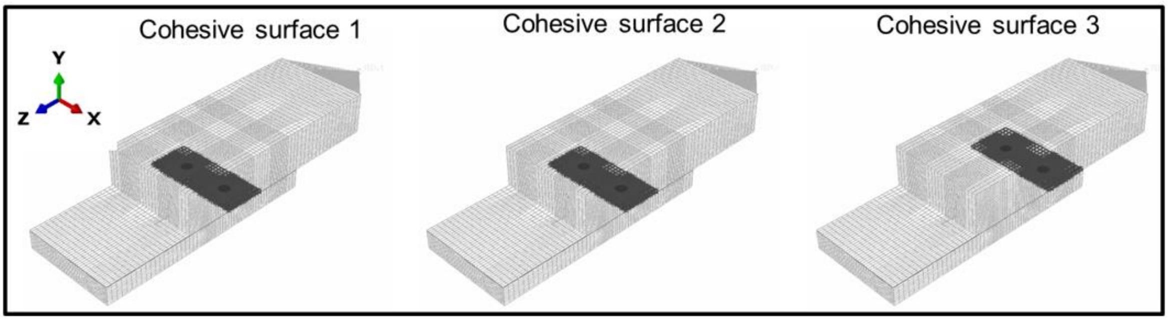

Figure A. 0-6: Cohesive surface defined at the hybrid joint interface

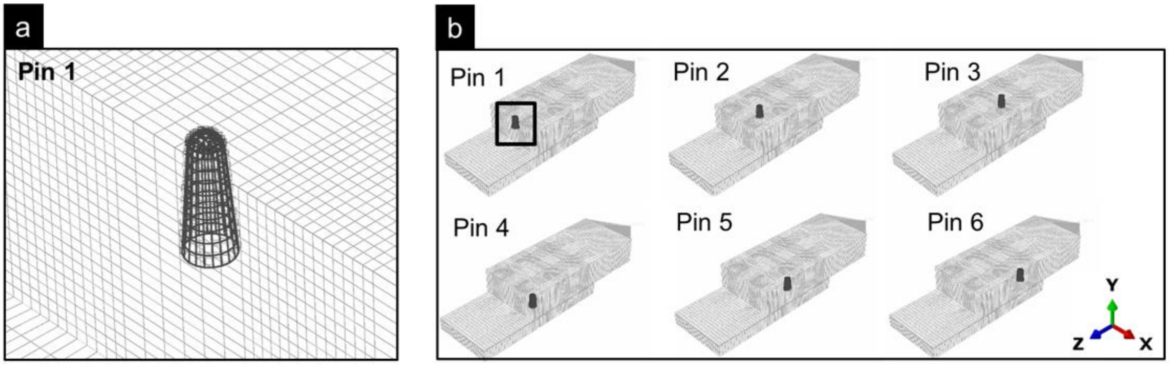

Figure A. 0-7: Detailed cohesive surface defined (a) between pin 1 - composite interfaces, and (b) for the remaining pins.

Figure A. 0-8 presents the boundary conditions applied during the FEA. The regions that represent the grip area were constrained as shown in Figure A. 0-8 (a). In addition, a prescribed displacement was applied in the load application point RP-1, to which the displacement of the GF-PEI face nodes are constrained as shown in Figure A. 0-8 (b). The prescribed displacement was applied according to the experimental data, and the reaction force on RP-1 was extracted for validation purpose.

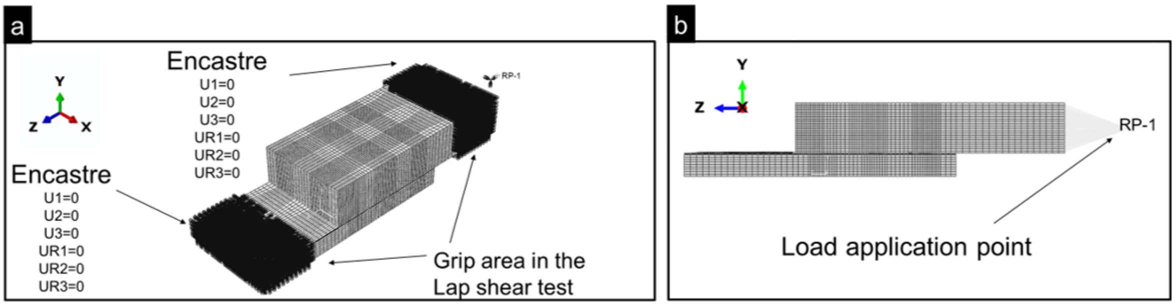

Figure A. 0-8: Boundary condition defined during the FEA

The Ti-6Al-4V part of the joint was defined as an elastic/plastic material and a ductile damage criterion was applied. The material properties were based on the MIM-structured alloy presented in Table 5-3, and a stress triaxiality curve obtained from [285] was applied to describe the ductile damage criteria. The GF-PEI material behavior was defined as elastic according to material datasheet properties (Table 5-4).

In order to validate the FE model, the force-displacement curve obtained by the FEM was overlaid with the experimental curve (see Figure A. 0-9 (a)). In addition, the predicted out-of-plane displacement was compared with that measured by digital image correlation (DIC) (see Figure A. 0-9 (b)). In both cases the FE model agrees well with overall joint behavior. The force-displacement curves overlay each other during the joint's elastic behavior. However, after maximum load is reached (first pin row breakage) a discrepancy is observed. It therefore suggests that improvements are still required to the failure description and criterion adopted. Nevertheless, the model was considered accurate to describe the joint's behavior during the elastic regime, and it predicted the joint's ultimate lap shear force with a deviation of only 6% compared with the experimental data.

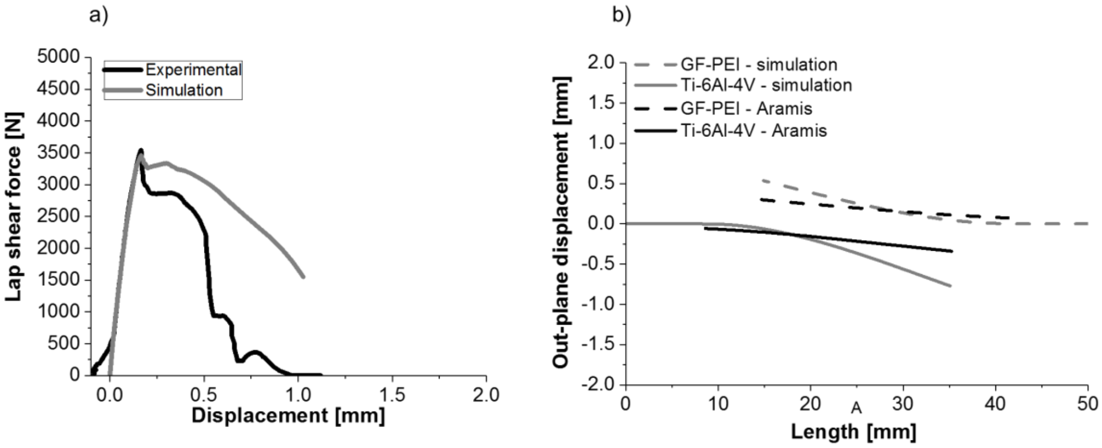

Figure A. 0-9: (a) Comparison between the force-displacement curves obtained by FEM simulation and experiment, and (b) between the out-of-plane displacement measured by DIC using Aramis and that predicted by FEM.

APPENDIX A.6. LINEAR STATISTICAL ANALYSIS OF THE FATIGUE DATA

The linear models used to obtain the S-N curves (i.e., exponential and power law) followed the procedure regulated by the ASTM E739-10 standard [188]. In this respect, the linearized S-N relationships to describe such curves consist of:

$$\log(N) = a + bF \tag{A.0-1}$$

$$\log(N) = a + dlog(F) \tag{A.0-2}$$

where N corresponds to fatigue life, F is the maximum value of constant-amplitude force, and a, b, and are the model parameters obtained by linear fitting using the exponential formulation (also known as log-linear, Equation A.0-1) and the power law (also known as log-log, Equation A.0-2). In the linear formulation proposed, the fatigue life N is the random dependent variable, whereas the F is the controlled independent variable [188]. Moreover, during the statistical analysis, no run-outs were used and it is assumed that the logarithm of N follows a normal distribution. During the experimentation phase, a consistent proportion of replication was ensured, which consisted of 67%. Thus classifying the tests as design allowable data, according to the ASTM mentioned. The estimated model parameters are presented in Table A.0-2. The models presented a reliable $R^2_{(adj)}$, which consists of 0.89 and 0.87 for exponential and power law, respectively.

Table A.0-2: Estimated exponential and power law model parameters.

Exponential		Power law	
a	**b**	**a**	**d**
4255.1	231.5	6284.3	833.1

In order to validate the linearization procedure, the linearity index was calculated for both formulation and compared with the critical linearity index (Fp) for a significance level of 5%. According to ASTM E739-10, the linearity hypothesis is valid when the linearity index is lower than the Fp. For both linear fits this hypothesis is valid as shown in Table A.0-3.

Table A.0-3: Linearity index for the exponential and power law models

Exponential		Power law	
Linearity index	**Fp**	**Linearity index**	**Fp**
0.216	4.459	0.432	4.459

APPENDIX A.7. THE TWO-PARAMETER WEIBULL DISTRIBUTION APPLIED TO THE U-JOINING JOINTS

Two-parameter Weibull distribution (2-P WD) was applied to assess the data scattering of the U-Joining joint. The 2-P WD is defined as a probability density function (PDF) of failure as follows [274,275,278,286]:

$$f(x) = \frac{\beta}{\alpha}\left(\frac{x}{\alpha}\right)^{\beta-1} e^{-\left(\frac{x}{\alpha}\right)^{\beta}} \qquad \alpha \geq 0, \qquad \beta \geq 0 \tag{A.0-3}$$

where α and β are the two Weibull parameters, which describe the characteristic life at a certain selected stress level (scale parameter) and slope (shape parameter) of the Weibull distribution, respectively [275,278], and where x is the number of cycles. By integrating the PDF, a cumulative density function (CDF) is obtained:

$$F_{f(x)} = 1 - e^{-\left(\frac{x}{\alpha}\right)^{\beta}} \tag{A.0-4}$$

Weibull parameters can be estimated by two approaches, either graphically or by using the method of moments [274]. The former is preferable though, due to its simplicity [274,275]. Hence, rearranging the CDF (Equation A.0-4) and applying a natural logarithm on both sides of the equation, the following equation is obtained:

$$\ln\left(\ln\left(\frac{1}{1-F_{f(x)}}\right)\right) = \beta\ln(x) - \beta\ln(\alpha) \tag{A.0-5}$$

Equation A.0-5 can be represented by a linear equation, such as [274,275]: $y = mX + \mathrm{c}$. In this case, y, X, m, and c are represented as follows:

$$\mathrm{y} = \ln\left(\ln\left(\frac{1}{1-F_{f(x)}}\right)\right) \tag{A.0-6}$$

$$X = \ln(x) \tag{A.0-7}$$

$$m = \beta \tag{A.0-8}$$

$$c = -\beta\ln(\alpha) \tag{A.0-9}$$

Generally, in order to simplify Weibull parameter estimation, Bernard's Median Rank (MR) approximation can be applied to estimate $F_{f(x)}$ [275,278]. Such an empirical estimator was applied in this work and is given by the following equation:

$$MR = \frac{i - 0.3}{n + 0.4} \tag{A.0-10}$$

where i corresponds to the failure serial number and n represents the total number of specimens tested by each loading level. Thus, by organizing the fatigue life (N_f) obtained by each loading level in an ascending order (Rank (i)) and giving to each of the three specimen a serial number, the MR is calculated, as shown in Table A.0-4. After that, y is calculated and plotted against the *ln* of number of cycles *x* for each loading level. This graphic, which is presented in Figure A.0-10 (a), is known as the Weibull plot [274]. From such a plot, the Weibull parameters can be easily estimated by a liner fit of each loading level, as shown in Figure A.0-10 (a). In this analysis, the angular coefficient m of the fitted equation corresponds to β, and by substituting the linear coefficient c in Equation A.0-9 the value of α is obtained. The Weibull parameters calculated for the U-Joining joints are presented in Table A.0-4. Once these parameters are known, the mean time to failure (MTTF) can be calculated as follows:

$$MTTF = \alpha\Gamma\left(1 + \frac{1}{\beta}\right) \tag{A.0-11}$$

where Γ is the gamma function [274,275,278]. The MTTF describes the expected mean life for a given loading level, according to the Weibull distribution.

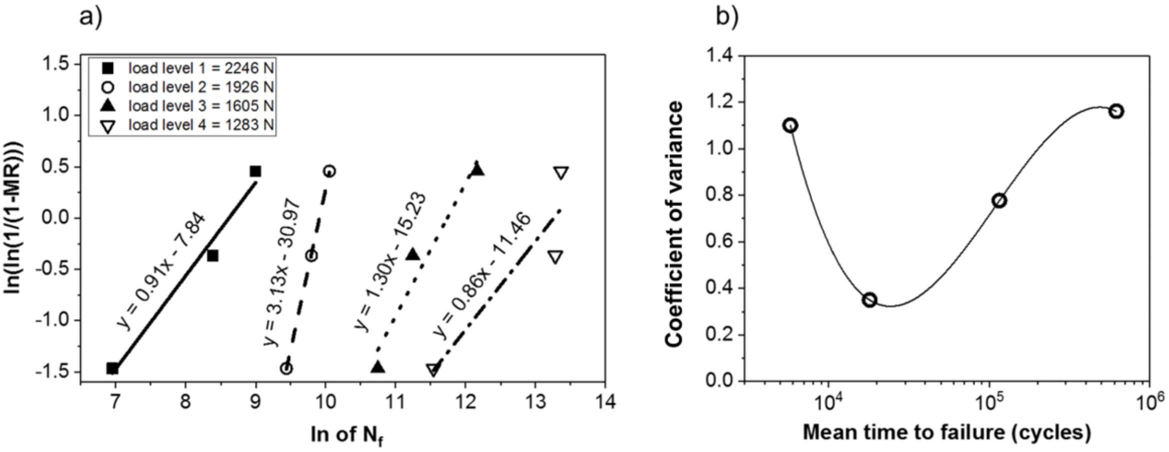

Figure A. 0-10: (a) Weibull plot used for estimation of the Weibull parameters, and (b) coefficient of variance versus calculated mean time to failure (MTTF).

Table A.0-4: Estimation of Weibull parameters for U-Joining joints.

Loading level	F_{max} [N]	F_{range} [N]	N_f	Rank (i)	MR	ln(ln(1/(1-MR))	c	β	α	MTTF (N_0)
1	2496	2246	1045	1	0.2	-1.5	-7.8	0.9	5520	5774
	2496	2246	4385	2	0.5	-0.4				
	2496	2246	8089	3	0.8	0.5				
2	2140	1926	12552	1	0.2	-1.5	-31.0	3.1	20115	17996
	2140	1926	17979	2	0.5	-0.4				
	2140	1926	23218	3	0.8	0.5				
3	1783	1605	46377	1	0.2	-1.5	-15.2	1.3	125188	115664
	1783	1605	76327	2	0.5	-0.4				
	1783	1605	191918	3	0.8	0.5				
4	1426	1283	102838	1	0.2	-1.5	-11.5	0.9	573220	617322
	1426	1283	585728	2	0.5	-0.4				
	1426	1283	636031	3	0.8	0.5				
5	1070	963	10^6							
	1070	963	10^6							
	1070	963	10^6							

F_{max}: maximum load, F_{range}: load range, N_f: number of cycles (experimental), MR: Bernard's Median Rank, MTTF: mean time to failure, β and α: Weibull parameters.

To evaluate data scattering in the MTTF a coefficient of variance (CV) was calculated. CV is defined as the ratio between standard deviation (SD) and MTTF. Figure A.0-10 (b) presents the CV calculated for each level, according to the following equation:

$$CV = \frac{SD}{MTTF} = \frac{\alpha\sqrt{\Gamma\left(1+\frac{2}{\beta}\right) - \Gamma^2(1+\frac{1}{\beta})}}{\alpha\Gamma\left(1+\frac{1}{\beta}\right)} \qquad \textbf{(A.0-12)}$$

The CV reveals two regions of high scattering in the MTTF estimation, the first is between 10^3 and 10^4 cycles and the second between 10^5 and 10^6 cycles. In addition, amid these two regions a low scattering region was observed (i.e., between 10^4 and 10^5 cycles). Data scattering in fatigue experiments is assumed to be stochastic and unavoidable. The high surface roughness of the metallic part and residual porosity of the as-sintered Ti-6Al-4V part are assumed primary factors affecting high scattering in the fatigue data. It is believed that at the higher loading rates at LCF (i.e., between 10^3 and 10^4 cycles) residual pores are subjected to higher triaxial stresses (due to the higher test loading), which can increase the data scattering. Moreover, in rough titanium alloys, fatigue life usually depends more significantly on the propagation phase, due to a fast initiation phase [120] (quasi-absent). Such a phenomenon is believed to be pronounced at LCF.

However, with lower loading rates at HCF (i.e., between 10^5 and 10^6 cycles) fatigue life is believed to be dominated by the crack initiation phase. Therefore the asperities in the high surface roughness of the MIM-structured Ti-6Al-4V (randomly distributed) can increase the scattering, as shown in Figure A.0-10 (b). Such increases in fatigue scattering at HCF have been reported in the literature [275,287,288].

Considering the scattering effect on the fatigue data, each stress level can be assessed to take into account the probability of survival (or statistical reliability (*R_x*)). Such an analysis is usually presented in survival diagrams, as shown in Figure A.0-11. The survival probability is calculated according to the following equation:

$$N_{R_x} = \alpha((-\ln(N_{R_x}))^{-\frac{1}{\beta}} \quad \textbf{(A.0-13)}$$

where N_{R_x} is the calculated fatigue life taking into account a defined percentage of reliability. As expected, for high percentages of reliability the estimated fatigue life is considerably lower. In addition, the first and fourth load level are more sensitive to the percentage of reliability. That is, its curves display a wider distribution. For instance, for a probability of survival varying from 5 to 99.9%, joints tested with 2246 N can present a fatigue life that varies from 10^3 to 10^5. Such a high scatter is in agreement with the CV plot, previously presented in Figure A.0-11 (b). Although load level 2, which presented a considerably lower CV, displays a more narrow distribution over the different reliability levels.

The concept of reliability can be extended to the entire S-N curve. To do this the mean fatigue lives for each loading level can now be described in terms of reliability (Equation A.0-13) and the S-N curve can be formulated by a power law function as follows:

$$S_a = a(N_f)^b \quad \textbf{(A.0-14)}$$

where S_a is the load range under investigation, N_f is the number of cycles calculated, taking into account the reliability level x (i.e., 50, 60, 63.2, 70, 80, 90, 95, 99, and 99.9%), and a and b are the regression parameters obtained by the power law model. 63.2% is the characteristic reliability value of the Weibull cumulative density function, calculated when x, is equal to α, Equation A.0-5.

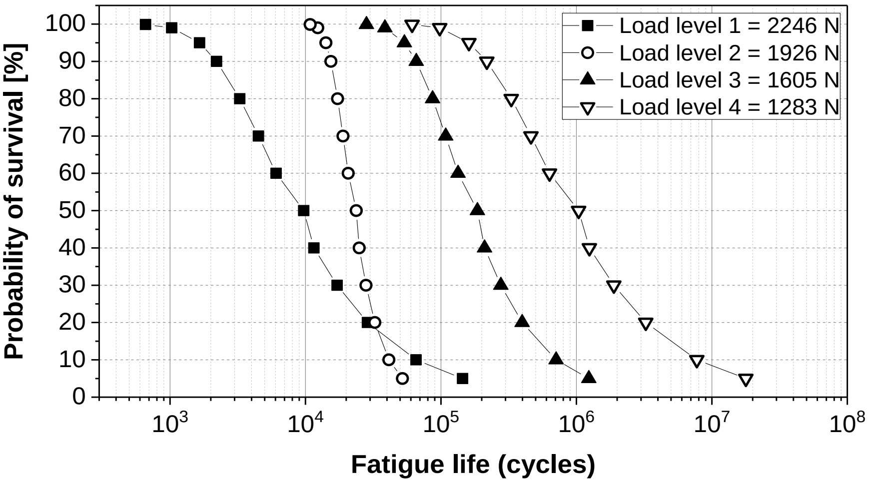

Figure A. 0-11: Assessment of fatigue life according to the probability of survival.

APPENDIX A.8. LOAD-DISPLACEMENT CURVES FROM THE SPECIMENS OF THE DOE (LAP SHEAR TESTING)

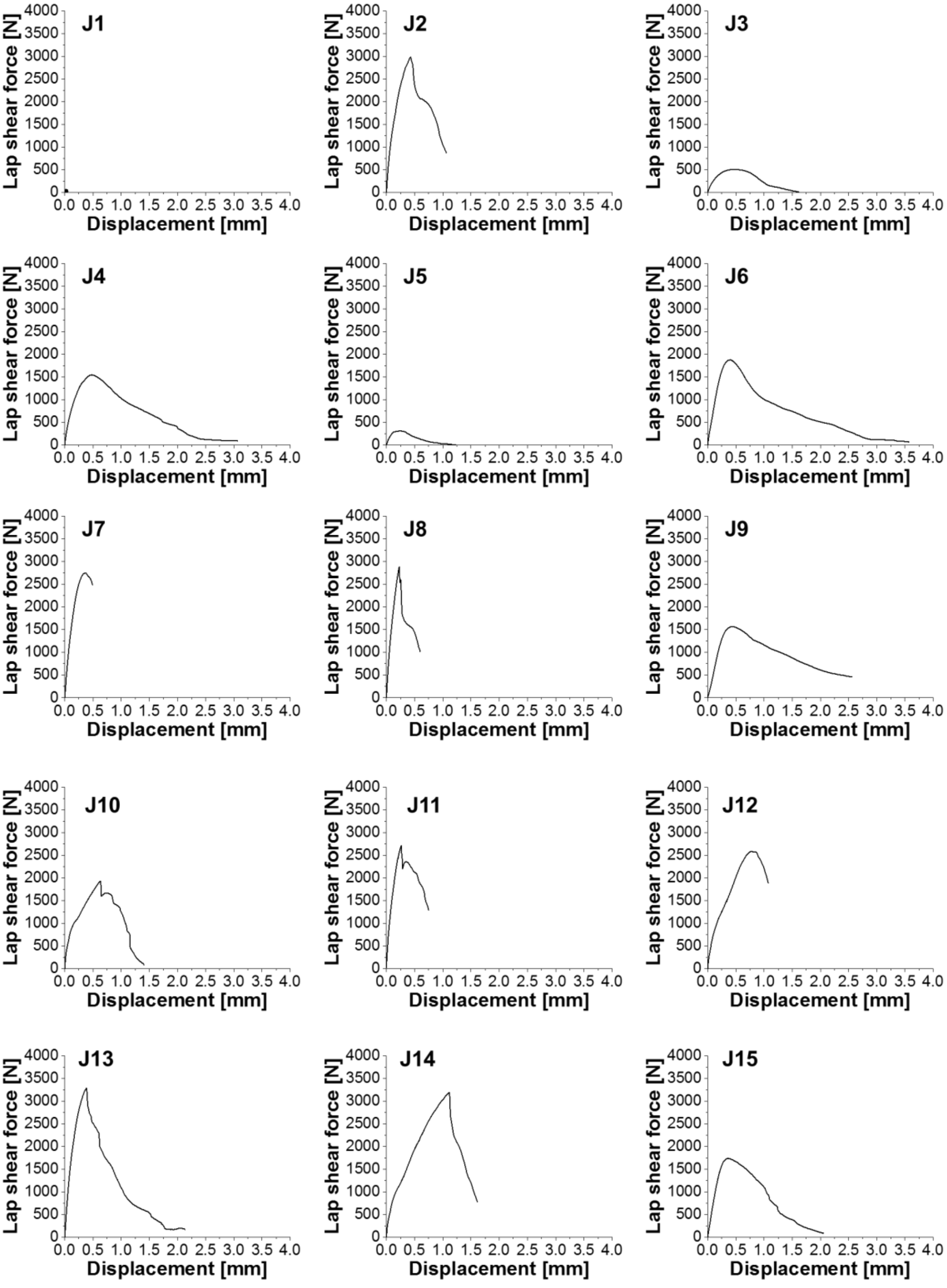

Figure A. 0-12: Force-displacement curves from lap-shear testing for all joining conditions used as input for the Box-Behnken design of experiments.

Table A. 0-5: Ultimate lap shear force (ULSF) and lack of penetration (LoP) measured for all the DoE experiments.

Joint	Parameters			Responses	
	EJ [J]	A0 [µm]	JP [psi] / [bar]	ULSF [N]	LoP [mm]
J1	1200	32	15 / 1.05	21.3	2.85
J2	2400	32	15 / 1.05	2976.2	0.11
J3	1200	52	15 / 1.05	499.8	1.97
J4	2400	52	15 / 1.05	1541.6	0.48
J5	1200	42	10 / 0.7	307.2	2.04
J6	2400	42	10 / 0.7	1872.4	0.47
J7	1200	42	20 / 1.4	2750.5	0.16
J8	2400	42	20 / 1.4	2880.0	0.11
J9	1800	32	10 / 0.7	1565.6	1.15
J10	1800	52	10 / 0.7	1923.1	0.09
J11	1800	32	20 / 1.4	2703.4	0.11
J12	1800	52	20 / 1.4	2582.1	0.21
J13	1800	42	15 / 1.05	3283.1	0.20
J14	1800	42	15 / 1.05	3184.7	0.21
J15	1800	42	15 / 1.05	2674.9	0.39

APPENDIX A.9. X-RAY MICRO-COMPUTED TOMOGRAPHY FROM THE SPECIMENS OF THE DOE

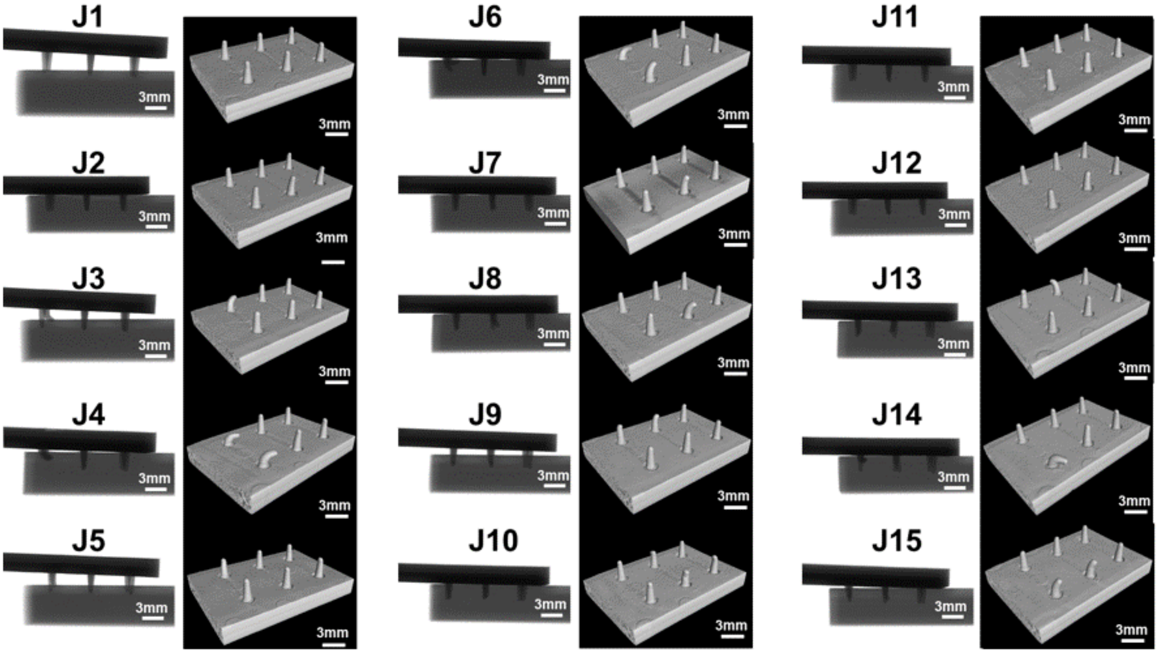

Figure A. 0-13: X-ray micro-computed tomography for all joining conditions used as input for the Box-Behnken design of experiments.

APPENDIX A.10. EFFECT OF U-JOINING PROCESS PARAMETERS ON THE LACK OF PENETRATION

Figure A. 0-14 presents the LoP validation diagram and the effect of each significant factor on the LoP. The reduced model has an acceptable explanatory power, with an R^2 of 69% and $R^2_{(adj)}$ of 57%. In addition, most of the observed actual versus predicted points lie within the 95% confidential interval. In agreement with the ULSF, joining energy showed a major contribution to LoP. The obtained reduced equation, using the same procedure as described in Section 5.3.4, is:

$$LoP = 10.8 - 0.008 \times E_J - 0.036 \times J_P - 0.040 \times A_0 + 0.000002 \times E_J^2 \qquad \textbf{(A.7-1)}$$

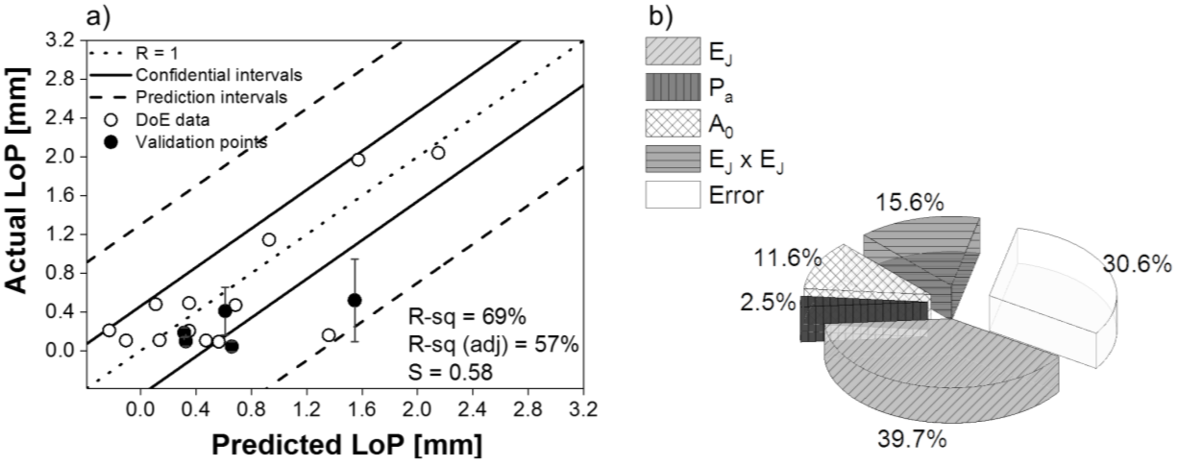

Figure A. 0-14: Validation diagram for the LoP statistical model (a) and effect of each significant factor on the LoP (b).

Table A.0-6 presents the ANOVA of the statistical model obtained for the response ultimate lap shear force.

Table A.0-6: ANOVA of lack of penetration model

Source	DF	Adj SS	Adj MS	F-Value	P-Value
Model	4	7.48984	1.87246	5.64	0.012
Linear	3	5.80563	1.93521	5.83	0.014
E_J	1	4.28806	4.28806	12.92	0.005
J_P	1	0.26463	0.26463	0.8	0.393
A_0	1	1.25294	1.25294	3.77	0.081
Square	1	1.68421	1.68421	5.07	0.048
${E_J}^2$	1	1.68421	1.68421	5.07	0.048
Error	10	3.32012	0.33201		
Lack-of-Fit	8	3.26559	0.4082	14.97	0.064
Pure Erro	2	0.05453	0.02727	5.64	
Total	14				

Figure A. 0-15 displays the mean effect of the process parameters on the LoP. The individual effect of each joining parameters presented a similar behavior as observed for the ULSF (Figure 11-4) response although inverted.

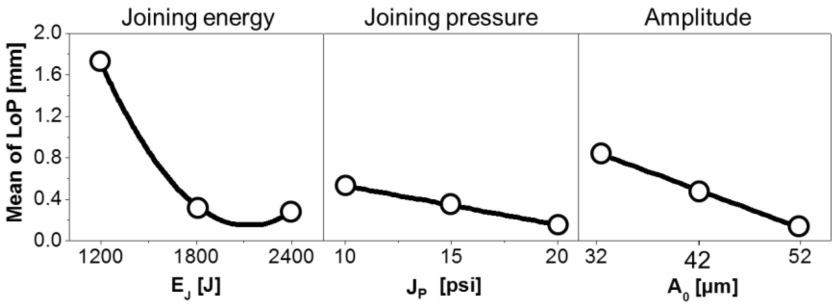

Figure A. 0-15: Plot of the mean effect of the process parameters on the LoP

The LoP response surfaces of two-ways interaction are plotted in Figure A. 0-16. The shape of the surface obtained resembles those observed for the ULSF, but are inverted, as observed previously for the mean effect. Such behavior is due to a strong linear correlation between ULSF and LoP (Figure 11-2). As discussed in Chapter 11 low values of LoP are inversely correlated with high ULSF.

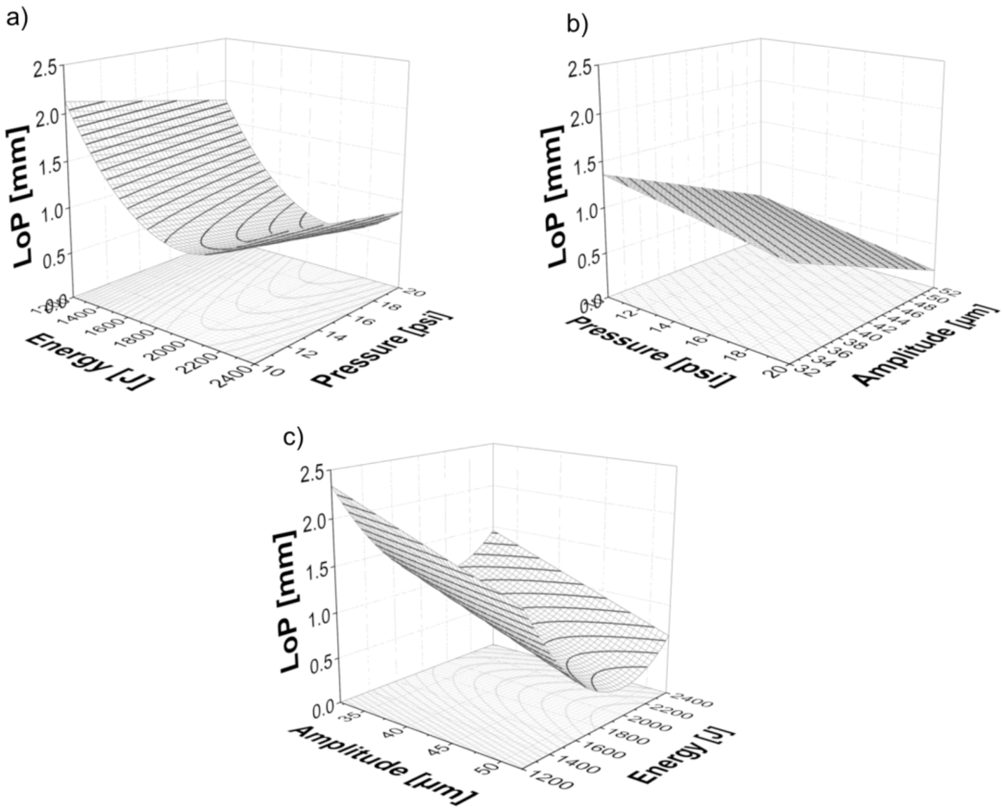

Figure A. 0-16: Surface responses of two-way joining parameters interactions. (a) Where the surface describes the combined effect of energy and pressure on the ULSF, (b) pressure and amplitude, and (c) amplitude and energy.

APPENDIX A.11. VALIDATION POINTS, OPTIMIZATION PROCEDURE, AND ANOVA

Figure A. 0-17 and Table A.0-7 present the effect of joining energy on ULSF and LoP validation experiments and the optimized joint condition.

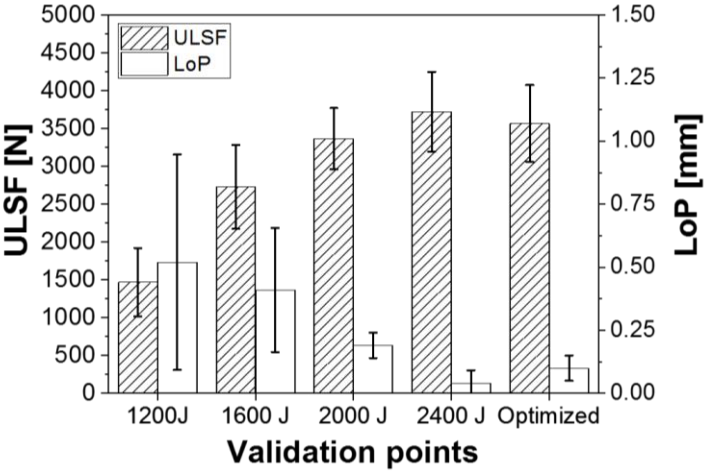

Figure A. 0-17: Effect of joining energy on the ULSF and LoP validation points.

Table A.0-7: Selected validation experiments and optimized parameters

a) Joining condition	**E_J [J]**	**J_P [psi]**	**A_0 [µm]**	**Joining cycle [s]**	**ULSF [N]**	**LoP [mm]**
V1	1200	15.0	52	0.78 ± 0.15	1466 ± 452	0.52 ± 0.43
V2	1600			0.85 ± 0.07	2729 ± 557	0.41 ± 0.25
V3	2000			1.05 ± 0.09	3366 ± 404	0.19 ± 0.05
V4	2400			1.24 ± 0.07	3723 ± 527	0.04 ± 0.05
Optimized	2012.1	14.7	52	1.09 ± 0.03	3608 ± 417	0.10 ± 0.05

In order to obtain a set of U-Joining optimized process parameters, which result in a hybrid joint with the highest ULSF, the partial derivatives $\partial \mathrm{ULSF}/\partial \mathrm{E_J} = \partial \mathrm{ULSF}/\partial \mathrm{A_0} = \partial \mathrm{ULSF}/\partial J_P = 0$ of the ULSF reduced equation (Equation 11-1) were calculated as follows:

$$ULSF = -17600 + 11.27 \times E_J + 903 \times J_P + 65.6 \times A_0 - 0.002801 \times E_J^2 - 30.7 \times {J_P}^2 \qquad \textbf{(11-1)}$$

$$\frac{\partial ULSF}{\partial E_J} = 0 \rightarrow\ 11.27 - 0.005602\ x\ E_J\ \rightarrow\ \ E_J = 2012\ \mathrm{J}$$

$$\frac{\partial ULSF}{\partial J_P} = 0 \rightarrow\ \ 903 - 61.4\ x\ P\ \rightarrow\ P = 14.7\ \mathrm{psi}$$

$$\frac{\partial ULSF}{\partial A_0} = 0\ \rightarrow A_0 = 65.6\ \mathrm{\mu m}$$

It is important to notice that the partial derivative in relation to $\mathrm{A_0}$ results in 65.6 µm, although the optimized value used in this PhD work was 52 µm. Such an amplitude level corresponds to the maximum amplitude limit of the joining system used.

Table A.0-8 presents the ANOVA of the statistical model obtained for the response ultimate lap shear force. Although the main effects of J_P presented a p-value higher than 0.05 during the backward elimination procedure, it was kept in the model so that a hierarchical model could be achieved, since its second-order interaction showed a significant contribution, p-value smaller than 0.05.

Table A.0-8: ANOVA of the ultimate lap shear model

Source	DF	Adj SS	Adj MS	F-Value	P-Value
Model	5	13135924	2627185	8.13	0.004
Linear	3	7555993	2518664	7.80	0.007
E_J	1	4048976	4048976	12.54	0.006
J_P	1	64775	64775	0.20	0.665
A_0	1	3442242	3442242	10.66	0.01
Square	2	5579932	2789966	8.64	0.008
${E_J}^2$	1	3775602	3775602	11.69	0.008
${J_P}^2$	1	2186301	2186301	6.77	0.029
Error	9	2906760	322973		
Lack-of-Fit	7	2693589	384798	3.61	0.234
Pure Erro	2	213171	106585		
Total	14	16042685			